THE UNIVERSITY *of* EDINBURGH

Orbital molecules in vanadium oxide spinels

Alexander J. Browne

Doctor of Philosophy
The University of Edinburgh
2019

Declaration

I declare that this Thesis has been composed solely by myself, and that the work contained herein is my own except where explicitly acknowledged otherwise. This work has not been submitted, in whole or in part, for any other degree or professional qualification. Publications that have resulted from a portion of this work are detailed and included.

Alexander J. Browne

December 2018

Lay summary

Materials in which transition metal elements are combined with oxygen have a wide range of electronic and magnetic properties. These properties have led to these materials finding applications in technology throughout human history, from the use of magnetic minerals as compasses in the ancient world through to the purposely-designed systems used in rechargeable batteries, solar cells and data-storage devices today.

The useful properties of transition metal oxide materials are the result of the interactions between the transition metal cations and their electrons. For example, cations with unpaired electrons have a magnetic moment, so if such cations interact with one another and align their individual magnetic moments the material itself can have a magnetic moment. Understanding the small-scale interactions that occur in materials is therefore essential for understanding their large-scale properties, and hence of developing materials with useful properties for new technological applications.

This Thesis is concerned with materials containing small clusters of transition metal cations called orbital molecules. Just as free atoms can share their electrons to form covalently-bonded molecules, so too can the cations in a transition metal oxide when suitable electronic interactions occur. The formation of orbital molecules is particularly common in vanadium oxides, where their formation often accompanies interesting behaviour such as dramatic changes in electrical conductivity. The aim of this work is therefore to understand how orbital molecules form, and the range of different orbital molecule states that can form, in vanadium oxides, with a particular focus on those that have the same structure as the mineral spinel. In this structure vanadium and oxygen are combined with one or more additional metal cations, with the choice of these allowing both the number of electrons *per* vanadium cation and the separation of neighbouring

vanadium cations to be varied. These variations affect the electronic interactions between the vanadium cations, and the different interactions – and the different orbital molecule states they give rise to – in a range of vanadium oxide spinels have been explored.

Abstract

Orbital molecules are clusters of transition metal cations, formed by orbital ordering in materials with extended structures that allow direct *d*-orbital interactions. Vanadium oxides exhibit an especially rich variety of orbital molecule states, with dimers and trimers identified in numerous systems. VO_2, in which V-V dimerisation accompanies a metal-insulator transition, is a particularly well-known example.

Materials of general composition AB_2O_4 often adopt the spinel structure. As this structure features edge-sharing chains of BO_6 octahedra it is a good motif for orbital molecule formation, and the choice of *A*-site cation allows both the *B*-site oxidation state and the *B*-*B* separation to be varied. Unusually large V_7 'heptamer' orbital molecules had been reported to form in the spinel AlV_2O_4 below an ordering transition at 700 K. Atomic pair distribution function analysis was used to investigate the V-V bonding in this material and reveals that the heptamers are actually ordered pairs of V_3 trimers and V_4 tetramers. Furthermore, these orbital molecules persist into a structurally disordered phase above the 700 K transition and remain well-defined to temperatures of at least 1100 K.

Analogous behaviour is found in GaV_2O_4, a newly-synthesised spinel. It is isoelectronic with AlV_2O_4 and crystallographic and local-structure characterisation, complemented by magnetic and transport property measurements, reveals that it has the same V_3 and V_4 orbital molecule states but with a lower ordering temperature, of 415 K. In addition, quasi-elastic neutron scattering indicates that the orbital molecules in the high-temperature phase of GaV_2O_4 have static, rather than dynamic, disorder.

By contrast, ZnV_2O_4 has an antiferromagnetic ground state without ordered orbital molecules. The nature of the orbital ordering in this state has been contentious, and has been investigated using X-ray total scattering for the first

time. The ground state has a tetragonal structure consistent with long-range ferro-orbital ordering, and V-V bonding is not evident in either its average or local structures. The variation of electronic ordering in $Zn_xGa_{1-x}V_2O_4$ solid solutions has also been explored. Whilst the structural and electronic perturbations induced by doping rapidly suppress the long-range ordering found in the two end members, local V-V bonding is remarkably stable with respect to these perturbations and is found in phases with $x \leq 0.875$. Powder neutron diffraction and magnetometry measurements suggest that disordered orbital molecules are also present in $Li_{0.5}Ga_{0.5}V_2O_4$, another newly-synthesised material.

A particularly interesting vanadium oxide is LiV_2O_4, which is one of very few *d*-electron systems in which heavy-fermion behaviour has been found. Although V-V orbital interactions have been implicated in the microscopic origin of this behaviour, no orbital molecule-like distortions are found in the local structure of the heavy-fermion phase. LiV_2O_4 also exhibits a pressure-induced metal-insulator transition, and powder X-ray diffraction under low temperature-high pressure conditions reveals a concurrent cubic-monoclinic structural distortion that may be the result of orbital molecule ordering.

Acknowledgements

First and foremost I would like to express my gratitude to my supervisor, Paul Attfield. I feel deeply privileged to have been able to spend four years benefitting from Paul's knowledge, guidance and patience, and am glad to have learnt from him why magnetism is just like a packet of chips.

I am also fortunate to have been able to work with and learn from many talented researchers. In Edinburgh, I would particularly like to thank James Cumby for his patience in answering my steady stream of questions about GSAS. I would also like to thank Calum Lithgow, who made the resistivity measurement of GaV_2O_4 in Chapter 3; Ángel Arévalo-López and Elise Pachoud, for their assistance and advice; and Paula Kayser and Elena Solana-Madruga, for their support in my final year. Elsewhere, I am grateful to Simon Kimber, who first suggested the use of PDF analysis and QENS to study AlV_2O_4 and GaV_2O_4, and to the staff at the various beamlines that I have been fortunate enough to use – Mauro Coduri, Catherine Dejoie and Andy Fitch at ID22; Gaston Garbarino at ID15B; Kevin Knight at HRPD; and Michael Koza at IN6 – who shared their knowledge and expertise.

There are numerous others whom I would like to thank for their support of my scientific development. I am indebted to Mike Hayward at the University of Oxford, with whom I first discovered solid-state chemistry and who has continued to provide support and advice, as well as my tutors at Oxford and teachers before that whose guidance has allowed me to follow the path that I have. I am grateful to my colleagues at Edinburgh Research and Innovation, from whom I learnt a lot about science outside the lab during my internship there. And I would also like to thank Gary Nichol in the X-ray lab, Xiao Wang in the Mag lab, and the technical, support and administrative staff in CSEC and the School of Chemistry, who have facilitated and supported my research endeavours. Finally, I appreciated greatly the enthusiastic feedback provided by my examiners, Simon Parsons and Andrew

Goodwin. At this point, I would also like to acknowledge financial support from the European Research Council, for the funding of my PhD studentship, and the Science and Technology Facilities Council, for the provision of access to central facilities.

On a more personal note, I would like to give a shout out to the two great families that I found in Edinburgh and who have made my time here so special. Firstly, the other Attfield group students – Giuditta Perversi, Graham McNally, Paul Sarte, Jacky Hong, Ed Pace, Kunlang Ji, Padraig Kearins and Patricia Kloihofer – whose company and support have been invaluable. Through all of the cricket, cakes and cryostat calamities, I cannot imagine a better group to have shared the PhD experience with. And secondly, my teammates and friends at Edinburgh University Kendo Club, whom it has been privilege to teach and train with, and whose dedication and effort were inspirational to me when times were tough. I leave Edinburgh a proud kendo dad.

Finally, I would like to thank my friends and family near and far, and most of all my parents, without whose support – academic, financial and otherwise – I wouldn't be handing in this Thesis.

Contents

Chapter 1: Introduction

1.1: Transition metal oxides

The solid compounds of transition metal cations and oxide anions are fascinating materials. They adopt extended structures of great variety, and exhibit a phenomenal range of electronic and magnetic properties.[1] These properties have found applications ranging from energy conversion to microelectronics and magnetic data-storage, and as phenomena such as high-temperature superconductivity and multiferroism offer great potential for future technology, transition metal oxides are at the heart of electronic materials research.

The interesting properties of transition metal oxides are displayed on the macroscopic scale, but are the result of the behaviour on the microscopic scale of the valence *d*-electrons. The electrons in a solid occupy bands formed by overlapping orbitals, and their behaviour is typically described in terms of two simple limits: metallic, when the valence electrons are itinerant; and insulating, when they are localised. According to the Mott-Hubbard model the electrons are itinerant when the width of the valence band, W, is larger than the electrostatic repulsion between valence electrons on the same atoms, U, whilst they are localised when U is larger than W. However, in many transition metal oxides U and W are approximately equal, and this is the basis of the interesting electronic properties that these materials display.[2] In such a regime the valence *d*-electrons are neither fully itinerant nor fully localised; rather, their behaviour is governed by the strong interactions, or correlations, that the electrons experience with one another. These can result in exotic electronic behaviours, such as the formation of Cooper pairs in cuprate high-temperature superconductors.[3] Furthermore, in a strongly-correlated system the forces that favour metallic and insulating behaviour are delicately balanced, so different states with different electronic properties can have very similar energies. Such a system can therefore be

sensitive to small perturbations – heating or cooling, application of pressure or a magnetic field, or variation of composition – that affect this balance and induce a phase transition. The phenomena of colossal magnetoresistance in manganite perovskites[4] and metal-insulator transitions more generally[5] illustrate how dramatic the changes of properties accompanying such a phase transition can be.

The behaviour of the electrons is also influenced by the atomic structure.[6] The structure defines how the orbitals of different atoms interact, and these interactions are responsible for property mechanisms ranging from the conduction pathways of mobile electrons to the exchange interactions that govern magnetic ordering. Coupling of the electronic and atomic structures, such that an electronic phase transition is accompanied by a structural distortion, may also be significant. This can have important implications – for example, if a magnetic ordering transition is accompanied by distortion that breaks inversion symmetry, the coupling of electrical and magnetic polarisations required for multiferroic behaviour can be realised.[7] A second important example of electron-lattice coupling is the Peierls transition, by which a one-dimensional metallic system is unstable with respect to a periodic lattice distortion that lowers the energy of the system by opening a band gap at the Fermi level.[8] This results in the formation of a charge-density wave – a periodic accumulation of electron density in phase with the lattice distortion.

The *d*-electrons responsible for the electronic behaviour of the materials studied in this Thesis are provided by vanadium. In its oxides vanadium is stable in oxidation states ranging from +2 ($3d^3$) to +5 ($3d^0$) and these materials exhibit a rich variety of electronic behaviours, including attractive lithium-ion intercalation,[9,10] supercapacitance,[11] oxide-ion conduction,[12] and catalytic[13] properties. Perhaps the two most highly-studied vanadium oxides are the binary compounds V_2O_3 and VO_2, which are canonical examples of transition metal oxides that undergo a metal-insulator transition (Figure 1.1).[14] The dramatic changes of conductivity that these materials undergo has led to them being investigated for technological uses ranging from microelectronic switches and chemical sensors[15] to random access memories[16] and thermochromic window

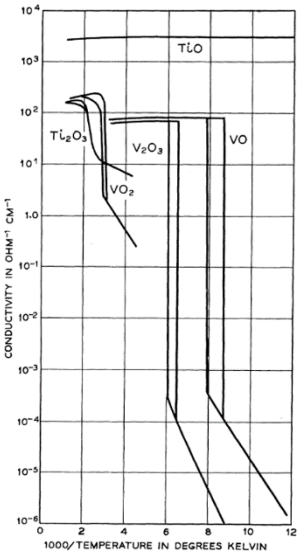

Figure 1.1: Variable-temperature conductivity measurements of oxides including V_2O_3 and VO_2 from the first report of the metal-insulator transitions that these materials undergo, at 160 K and 340 K respectively. Figure reproduced from Ref. 14.

coatings[17] but, despite decades of research, the complex electronic interactions that underpin this behaviour in these chemically simple systems are not fully understood. V_2O_3 is generally regarded as a Mott system, in which the transition is the result of electron-electron correlations, though its behaviour cannot be fully described by the simple model of U and W detailed above.[18,19] In contrast, the transition in VO_2 has a Peierls-like mechanism that couples electronic ordering to a lattice distortion through the formation of covalent V-V bonds.[20] The vanadium dimers formed by this bonding are examples of orbital molecules, and the investigation of the orbital molecule states in particular vanadium oxides is the subject of this Thesis.

1.2: Charge, spin and orbital ordering

In transition metal oxides, the valence *d*-electrons are localised or near-localised at particular cation sites by strong electron correlations. The local electronic structure of these cations can therefore be described by well-defined electron configurations.[2] As every electron in a solid has a charge, -*e*, a spin, $S = \pm ½$, and

an orbital symmetry, these configurations determine the charge, spin and orbital degrees of freedom afforded to the system[21]:

- The charge degree of freedom accounts for delocalised *d*-electrons, and charge ordering localises these electrons, or the equivalent holes, at periodic positions within the lattice. This occurs most commonly in mixed-valence systems, in which crystallographically-equivalent sites with the same non-integer charge may separate into two or more inequivalent sites with different, integer charges.
- A spin degree of freedom is found when the cations have unpaired electrons. This gives each site a magnetic moment, and those of different sites can couple through exchange mechanisms to form magnetically ordered states. The two simplest are ferromagnetic order, where all of the atomic moments align in parallel to give a net macroscopic moment, and antiferromagnetic order, where different moments align in opposition such that the net moment is zero, though many more complex states are known.
- The orbital degree of freedom describes the spatial distribution of the electrons. The coordination of the transition metal cations in oxides causes them to experience a ligand field that splits the five *d*-orbitals into symmetry-related sets; in an octahedral field, these are a low-energy t_{2g} triplet and high-energy e_g doublet. If the electron configuration leaves one of these sets with an orbital degeneracy the system is unstable with respect to a Jahn-Teller distortion that lifts the degeneracy. This localises the electrons into particular orbitals such that their distribution becomes spatially ordered.

The electronic states of transition metal oxides can therefore be described in terms of the charge, spin and orbital degrees of freedom of the cation sites, and if those of different sites correlate with one another, an ordered state is established. If several electronic degrees of freedom are available they can couple to and compete with one another, resulting in complex ordering schemes like those found in the $La_{1-x}Ca_xMnO_3$ perovskites.[22] As transition metal oxides have

extended, and typically crystalline, structures, the atomic positions are themselves ordered. The atomic structure is therefore important in determining the correlations between ordering species, and hence the ordered states that can form. Furthermore, the electronic degrees of freedom can couple to those of the lattice, so an electronic ordering transition may be accompanied by a structural distortion. Structural probes are therefore important tools for the characterisation of electronically-ordered states.

The length-scales over which ordering correlations are present can vary significantly. At one extreme, of short-range order, correlations exist solely between nearest neighbours, so ordering exists locally but becomes averaged at greater distances. Short-range correlations can be static, as in a glass, or dynamic, as in a liquid. Conversely, in a regime of long-range order, correlations exist over an infinite range – the short-range order between nearest-neighbours is repeated throughout space, as in a crystal. Typically, the ground states of transition metal oxides are characterised by the formation of long-range order from a high-temperature disordered state, such as the emergence of ferromagnetic order from a paramagnet below the Curie temperature, but transitions between low-temperature states with long-range order and high-temperature states with short-range order are also found. As such, the characterisation of both the crystallographic and local structures of a material may be important for the determination of its electronic states. For example, in $LaMnO_3$, Mn^{3+} is susceptible to a Jahn-Teller distortion. The distortions of the MnO_6 octahedra occur cooperatively in the ground state of this perovskite and locally in its high-temperature phases, evidencing a transition between states with long- and short-range orbital ordering.[23]

In some structures, it is impossible to simultaneously satisfy all of the preferred correlations between all of the ordering species. This geometric frustration is typified by the incompatibility of antiferromagnetic ordering on a triangular lattice,[24] though it can also apply to charge, orbital and structural ordering. Frustrated systems have a manifold of degenerate states; they may undergo a structural distortion, such that the frustration is relieved and a unique ground

state with long-range order can be established, or may adopt a ground state with a high degeneracy. In the latter case, short-range order may still be significant and can result in exotic ground states, such as spin glasses and spin liquids, being formed.

In systems such as the manganite perovskites, the separations between transition metal cations are too large for their *d*-orbitals to interact directly. However, in certain structures, direct interactions can occur. For example, the t_{2g} orbitals of a cation in an octahedral environment are directed towards the edge of the octahedron, so in a structure in which octahedra share edges direct t_{2g}-t_{2g} interactions are possible. The extent of the interaction is dependent on the metal-metal separation, and when this separation is sufficiently short the electrons occupying the directly-interacting orbitals become delocalised. An empirical model developed by Goodenough provides estimates of this critical distance for different transition metal cations.[25] In the delocalised regime the t_{2g} electrons should be itinerant, but they can be stabilised by forming pairs with antiparallel spins that localise between neighbouring cations.[26] This pairing is effectively the formation of a metal-metal covalent bond, and as it requires an orbital ordering such that the electrons specifically occupy the directly-interacting orbitals rather than a degenerate t_{2g} set, the clusters of cations formed by this bonding are known as orbital molecules.[27]

1.3: The spinel structure

All of the materials studied in this Thesis crystallise with the spinel structure. Named after the mineral $MgAl_2O_4$, this structure type is commonly adopted by solid materials of general composition AB_2X_4, where *A* and *B* are cations and *X* is a divalent anion.

The spinel structure (Figure 1.2(a)) has cubic $Fd\bar{3}m$ symmetry, and there are eight formula units *per* unit cell. The atomic arrangement consists of a cubic close-packed anion lattice in which cations occupy one-eighth of the tetrahedral interstices and one-half of the octahedral interstices, and is defined by three

independent crystallographic sites. The tetrahedrally- and octahedrally-coordinated cations occupy sites conventionally referred to as the *A*-site and the *B*-site, respectively; the *A*-site has fractional coordinates (⅛, ⅛, ⅛), corresponding to the Wyckoff position 8*a*, whilst the *B*-site has coordinates (½, ½, ½) and the Wyckoff position 16*d*. The anion site has the Wyckoff position 32*e* and this is the only one of the three sites with a variable coordinate, (*x*, *x*, *x*). This coordinate, and the cubic lattice parameter *a*, are the only two parameters required to define the geometry of a spinel unit cell. In general, *a* is dependent on the average of the ionic radii of the *A*-site and *B*-site cations whilst *x* varies according to their radius ratio.[28] When $x = 0.25$ the anions form a perfect cubic close-packed lattice; displacements away from this position manifest as a trigonal distortion of each BO_6 octahedron along a ⟨111⟩-type direction of the cubic cell.

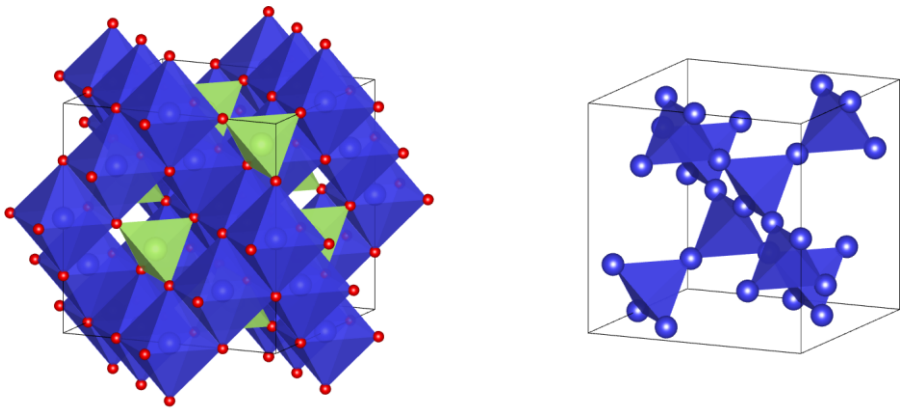

Figure 1.2: The AB_2X_4 spinel structure, with *A*-site cations in green, *B*-site cations in blue, and *X* anions in red. Shown in **(a)** are the cation-anion coordination polyhedra – AX_4 tetrahedra, and edge-sharing BX_6 octahedra. Shown in **(b)** is the pyrochlore lattice of corner-sharing tetrahedra formed by the *B*-site cations. These, and all other crystal structures in this Thesis, were produced using VESTA3.[29]

An important feature of the spinel structure is the sublattice of *B*-site cations. Each BO_6 octahedron shares edges with six others, such that chains of edge-sharing octahedra run along the six ⟨110⟩-type directions of the cubic structure. This allows the t_{2g} orbitals of neighbouring *B*-site cations to interact directly, so the *B*-site sublattice can be a template for orbital molecule formation.

Furthermore, the *B*-site cations are arranged such that they form a network of corner-sharing tetrahedra known as a pyrochlore lattice (Figure 1.2(b)). As this network can be broken down into two-dimensional triangular and kagome lattice layers that stack in alternation along a ⟨111⟩-axis of the cubic unit cell, and as the distances from each *B*-site cations to all six of its *B*-site nearest neighbours are equivalent, the pyrochlore lattice arrangement means that the interactions between *B*-site cations are subject to geometric frustration.

Another important structural consideration for spinels is the distribution of the available cations over the *A*- and *B*-sites. For a '2-3' spinel such as $MgAl_2O_4$, in which there are one divalent cation and two trivalent cations *per* formula unit, there are two extremes of distribution. These are designated as the 'normal' distribution, in which the divalent cations occupy the *A*-site and the trivalent cations occupy the *B*-site, and the 'inverse' distribution, in which the *A*-site is occupied by trivalent cations and the *B*-site is occupied by divalent and trivalent cations in equal proportion. Several factors – the electrostatic potential of the lattice, the sizes and charges of the cations, and possible ligand-field stabilisation – influence which distribution is adopted.[28] Ligand-field stabilisation is particularly important when transition metal cations with unpaired *d*-electrons are present, as illustrated by a comparison of the structures adopted by the binary spinels Co_3O_4 and Fe_3O_4. To maximise the ligand-field stabilisation Co_3O_4 crystallises with the normal cation distribution, $[Co^{2+}]_A[(Co^{3+})_2]_BO_4$, but as Fe^{2+} (high-spin $3d^6$) can benefit from ligand-field stabilisation whilst Fe^{3+} (high-spin $3d^5$) cannot, Fe_3O_4 has the inverse distribution, $[Fe^{3+}]_A[Fe^{2+}Fe^{3+}]_BO_4$. Ligand-field stabilisation also determines the cation distribution in the materials studied in this Thesis, which all consist of closed-shell metal cations, such as Li^+, Zn^{2+} and Al^{3+}, and vanadium cations with unpaired *d*-electrons in a 1:2 ratio. The unpaired electrons are better stabilised in an octahedral ligand field than a tetrahedral one, hence the *B*-site should be fully occupied by vanadium cations and the *A*-site fully-occupied by the closed-shell species.

Transition metal oxides adopting the spinel structure display a host of interesting behaviours.[30] Metallic systems are relatively rare, but two notable examples are

$LiTi_2O_4$, which is a superconductor with a critical temperature of 13 K,[31] and LiV_2O_4, in which heavy-fermion correlations are established below 28 K.[32] Significantly, both of these materials retain the cubic spinel structure in their ground states, and it is thought that these exotic correlated-electron states can form because more conventional spin and charge orders are inhibited by geometric frustration. The effects of frustration are also apparent in insulating spinels such as $ZnCr_2O_4$. On the pyrochlore lattice long-range antiferromagnetic ordering of the Cr^{3+} spins is frustrated, but a spin-liquid state with short-range correlations is established below 30 K. This state is particularly unusual because the spin-liquid fluctuations are not between individual spins, but rather hexagonal six-spin clusters (Figure 1.3(a)).[33] The ground state of $ZnCr_2O_4$, in which long-range antiferromagnetic order does form, is subsequently established below a separate transition at 12.5 K. At this transition, a tetragonal distortion of the cubic structure that relieves the frustration is induced by the spin-Peierls mechanism, which couples the spin degree of freedom to the lattice to reduce the energy of the system.[34]

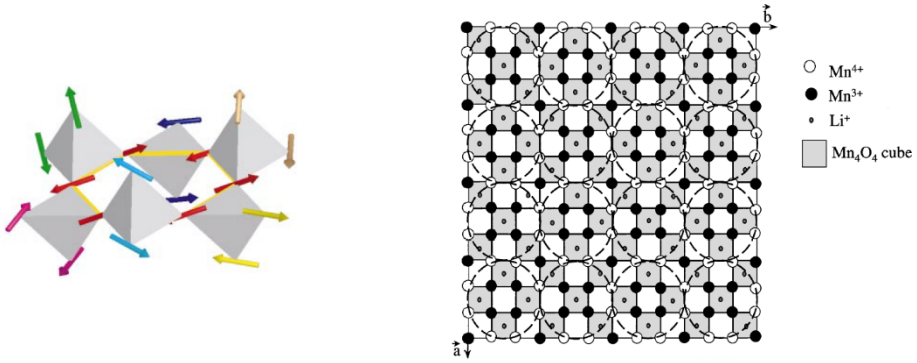

Figure 1.3: (a) In $ZnCr_2O_4$, the spins of groups of six Cr^{3+} cations self-organise into hexagonal antiferromagnetic clusters (red arrows). Figure reproduced from Ref. 33. **(b)** In the charge-ordered phase of $LiMn_2O_4$, Mn^{4+} sites wrap columns of Mn^{3+}-rich sites that run along the *c*-axis. Figure reproduced from Ref. 35.

In $ZnCr_2O_4$ only a spin degree of freedom is available to determine the ground state, but in other spinels charge and orbital ordering are influential. $LiMn_2O_4$ undergoes a coupled charge- and orbital-ordering transition at 290 K, at which

the uniform $Mn^{3.5+}$ *B*-site in the high-temperature cubic phase is segregated into two Mn^{4+} ($t_{2g}^3 e_g^0$) sites and three near-Mn^{3+} ($t_{2g}^3 e_g^1$) sites in an orthorhombic structure (Figure 1.3(b)).[35] This is accompanied by a cooperative Jahn-Teller distortion that lifts the e_g-degeneracy of the Mn^{3+} sites through a distortion of the coordination octahedra. Spinels with a t_{2g}-orbital degree of freedom, such as ZnV_2O_4, are also known; in this material, t_{2g}-orbital order and antiferromagnetic spin order are established below separate transitions, at 51 K and 40 K respectively.[36] Moreover, as the t_{2g} orbitals of neighbouring *B*-site cations interact directly t_{2g}-orbital ordering can result in the formation of orbital molecules, and several examples of spinels in which orbital molecules are found will be detailed in the next Section.

1.4: Orbital molecules

1.4.1: In VO_2

Orbital molecules are covalently-bonded clusters of transition metal cations, formed when *d*-electrons are ordered into directly-interacting orbitals. The materials in which these clusters are found adopt different structure types and demonstrate metal-metal bonding between a range of elements, and whilst they have only recently been classified together as 'orbital molecule' materials[27] the notion of covalent bonding between the cations in oxides with extended structures has a rich history that dates back to early studies of VO_2 and related metal dioxides.[37]

At 340 K VO_2 undergoes a first-order metal-insulator transition.[14] A substantial reduction of conductivity, by four orders of magnitude in high-quality samples, occurs in conjunction with a change from a paramagnetic to a spin-singlet state on a sub-picosecond timescale.[26,38] The changes to the electronic structure of VO_2 that occur at this transition are accompanied by a distortion of the crystal structure.[39,40] The high-temperature, metallic phase of this material has the rutile structure, in which the cations are octahedrally coordinated. The VO_6 octahedra share edges with two neighbours, forming one-dimensional chains that run along

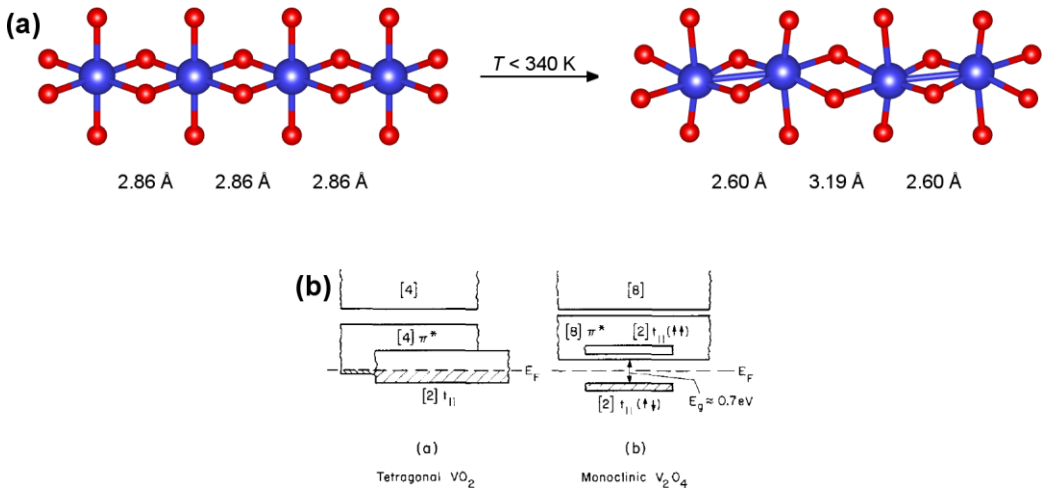

Figure 1.4: (a) The structure of VO_2 consists of one-dimensional chains of edge-sharing VO_6 octahedra. Homopolar V-V bonding below the metal-insulator transition at 340 K causes the uniform separations of neighbouring cations along each chain to become alternatingly short and long. V-V distances taken from Ref. 40. **(b)** The band structures of the two phases of VO_2 in the model proposed by Goodenough. Figure reproduced from Ref. 20.

the ⟨001⟩ direction of the structure, and share corners with the octahedra in adjacent chains. As such, the nearest V-V separations in this structure are between the neighbouring cations in each edge-sharing chain, and these separations are uniform along a chain. However, when the transition to the insulating phase occurs the structure distorts from tetragonal $P4_2/mnm$ to monoclinic $P2_1/c$ symmetry and the vanadium cations displace from the centre of their octahedra, such that the V-V separations along each chain become alternatingly short and long (Figure 1.4(a)). As neighbouring cations have t_{2g} orbitals that can interact directly it was recognised that this distortion can be understood as the formation of covalent 'homopolar bonds' between the pairs of cations with short V-V separations, with the spin-paired localisation of the itinerant *d*-electrons into these bonds accounting for the accompanying change in properties.[26]

A phenomenological model proposed by Goodenough[20] provides the basis for the description of this transition (Figure 1.4(b)). The one-dimensional character of the rutile structure splits the t_{2g} orbitals into two subsets: an a_{1g} singlet for the orbitals that interact along an edge-sharing chain, which form a narrow cation-sublattice band labelled $d_{//}$; and an e_g doublet of *d*-orbitals that hybridise with the

2*p* orbitals of the coordinating oxygens to form bonding π and antibonding π^* bands. In the high-temperature phase the $d_{//}$ and π^* bands overlap and are partially filled, hence this phase is metallic. Furthermore, as each cation has an unpaired *d*-electron, this phase has paramagnetic susceptibility. However, the antiferroelectric displacements of the cations at the phase transition change the V-V and V-O distances, splitting the $d_{//}$ band into bonding and antibonding components and raising the energy of the π^* band. This causes a bandgap of 0.7 eV to open, and the valence *d*-electrons fill the bonding $d_{//}$ band. Thus, the material becomes insulating, and as filling the band requires the electrons to be paired this phase has spin-singlet susceptibility.

This model describes the changes that occur in VO_2 during the metal-insulator transition, but it does not explain why the transition occurs. Broadly, two scenarios have been considered: a Peierls transition, in which the distortion is driven by electron-lattice coupling; and a Mott transition, in which it is driven by electron-electron correlations. The Goodenough model is reminiscent of the former: the $d_{//}$ band is one-dimensional, the structural distortion doubles the lattice periodicity, and the localisation of electrons into V-V bonds forms a charge density wave. However, the lattice distortion alone cannot account for all features of the transition. For example, dimerisation still occurs in VO_2 films just three octahedra thick – a length-scale at which an electronic band description is no longer meaningful – implying that local electronic interactions are involved.[41]

In practice, the phase transition in VO_2 has characteristics of both Peierls and Mott transitions but neither fully captures the behaviour of this material. Hybrid 'Mott-Peierls' descriptions have been developed in an attempt to incorporate the desirable features of each scenario.[42,43] In either case the transition is driven by an electronic instability, but more recently it has been suggested that the transition in VO_2 is actually the result of a structural instability, driven by the energetic gain of forming metal-metal bonds.[44] This is well-illustrated by a comparison of VO_2 and NbO_2: the two materials are isoelectronic and isostructural, and NbO_2 undergoes a similar dimerisation transition to that described for VO_2 but with a transition temperature of 1080 K.[45] The stabilisation

of the dimerised state in NbO_2 simply reflects the increased strength of metal-metal bonds formed by more spatially-extended 4*d* orbitals. In other words, the homopolar bonds in these metal dioxides are covalent σ-bonds formed by the unpaired electrons in directly-interacting t_{2g} orbitals. Accordingly, each pair of cations connected by such a bond may be thought of as an M_2^{8+} dimer – an orbital molecule.

1.4.2: In other vanadium oxides

For cations to form orbital molecules, they must have an electron configuration that allows their valence electrons to order into bonding orbitals. This requirement is fulfilled by octahedrally-coordinated V^{4+} (t_{2g}^1), hence V_2^{8+} dimers can form in VO_2. It is also fulfilled by V^{3+} (t_{2g}^2), and orbital molecules appear to be formed by the V^{3+} cations in $LiVO_2$.

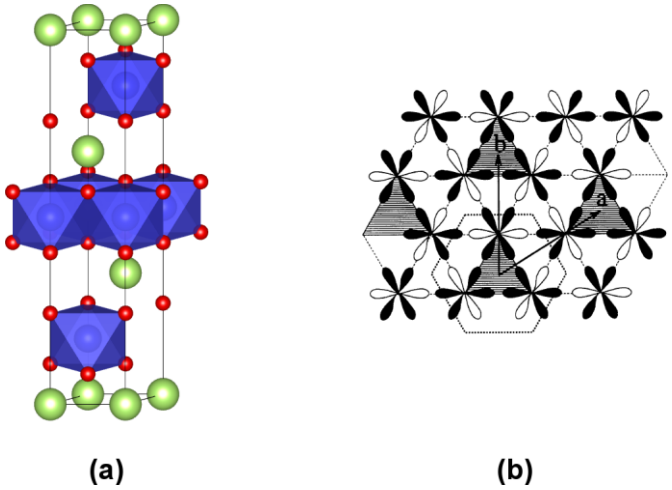

Figure 1.5: (a) The unit cell of $LiVO_2$, showing Li (green), V (blue) and O (red). In the layers of VO_6 octahedra, each shares edges with two neighbours. **(b)** A schematic view of the t_{2g} orbitals in a single VO_6 layer, illustrating the ordering of the two *d*-electrons available to each cation that occurs to form V_3^{9+} trimers (shaded triangles). Figure reproduced from Ref. 48.

The structure of $LiVO_2$ comprises alternating layers of octahedrally-coordinated Li^+ and V^{3+}, and within each layer VO_6 octahedra share edges with two neighbours (Figure 1.5(a)). This material undergoes a phase transition at ~460 K that involves a dramatic reduction of conductivity and a change from paramagnetic to

spin-singlet susceptibility, and is accompanied by a structural distortion that increases the periodicity of the lattice. This is indicative of a Peierls-like distortion akin to that in VO_2, but as each V^{3+} cation in $LiVO_2$ has two valence electrons and two nearest neighbours, the orbital molecules suggested to form are not dimers but triangular V_3^{9+} trimers.[25] Due to a lack of high-quality samples the formation of these trimers has not been confirmed crystallographically, but the requisite structure has been inferred from electron diffraction patterns,[46] and ^{51}V-NMR measurements confirm the spin-singlet nature of the ground state.[47] In addition, theoretical work has suggested that the most stable orbital ordering scheme for d^2 cations on a triangular lattice is the one that forms these orbital trimers (Figure 1.5(b)).[48]

The vanadium cations in both VO_2 and $LiVO_2$ have an integer valence, but there are many related compounds in which mixed-valence vanadium is found. In these, both orbital and charge degrees of freedom are available. Orbital and charge ordering tends to occur concurrently, but as different cations have different orbital degrees of freedom more complex orbital molecule states can arise, as illustrated by the ground states of the Magnéli phases. These phases have the general composition V_nO_{2n-1} and are structurally related to VO_2, being comprised of rutile-like slabs n octahedra thick that are separated by shear planes. Magnéli phases undergo metal-insulator transitions, and the similarity of their structures to that of VO_2 suggests a mechanism involving similar V-V bonding. For example, in the metallic phase of V_4O_7 all of the cations have the same averaged valence of +3.5, but in the insulating phase that forms below the 250 K charge-ordering transition the cations in each four-octahedron chain are either all V^{3+} or all V^{4+}. Orbital ordering occurs simultaneously, and the vanadium sites displace such that all of the V^{3+} cations and half of the V^{4+} cations are paired through short V-V bonds.[49] Electronic structure calculations suggest that the V^{4+}-V^{4+} dimers are spin singlets whilst the V^{3+}-V^{3+} dimers are not, so that the V^{3+} cations and the non-bonding V^{4+} cations also become magnetically ordered.[50]

Na_xVO_2 ($0.5 \leq x \leq 1$) phases are isostructural with $LiVO_2$. Stoichiometric $NaVO_2$ has the same orbital degrees of freedom as $LiVO_2$, but as the V-V nearest-

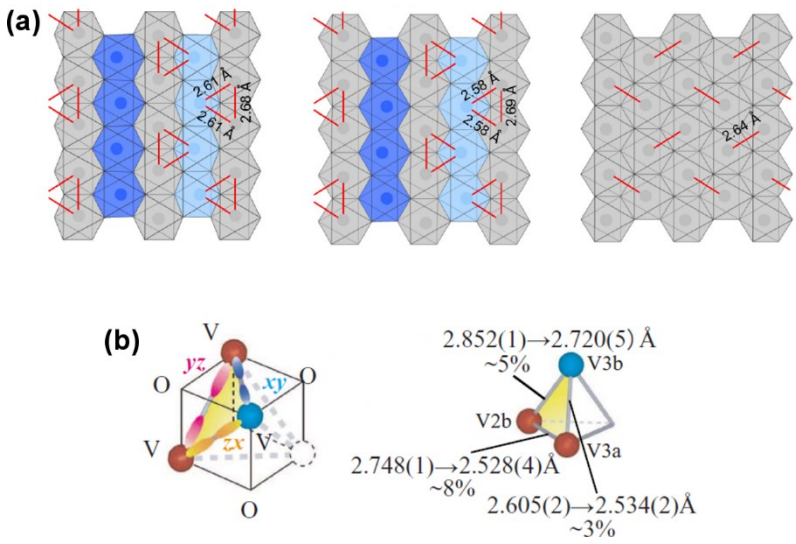

Figure 1.6: (a) Different polymorphs of $Na_{0.5}VO_2$ (left to right: P'3, P2 and O'3) have different orbital molecule ground states. The short V-V distances in each are shown as red lines. Figure reproduced from Ref. 54. **(b)** V_3^{9+} clusters form in $BaV_{10}O_{15}$. Shown are the t_{2g} orbital interactions required for trimer bonding, and the shortening of V-V distances that accompanies the orbital ordering transition. Figure reproduced from Ref. 55.

neighbour separation is increased by the larger ionic radius of the Na^+ cation its ground state has a different orbital order that does not involve V-V bonding.[51] However, when Na^+ cations are removed, the lattice contracts and orbital molecules can form.[52,53] Various polymorphs of $Na_{0.5}VO_2$, in which the Na-site vacancies have different orderings, have been synthesised, and interestingly these can have very different ground states – both dimerised and trimerised systems have been found (Figure 1.6(a)).[54] The layers of edge-sharing VO_6 octahedra that allow orbital molecules to form in these materials are also found in vanadium oxides that adopt different structure types. In $BaV_{10}O_{15}$ the average vanadium oxidation state is +2.8 and this material becomes charge-ordered below 130 K, with V^{3+} and V^{2+} cations in a 4:1 ratio.[55] Three-quarters of the V^{3+} cations in this phase form V_3^{9+} trimers through orbital ordering that allows certain V-V bonds to shorten (Figure 1.6(b)), whilst the remaining cations, half of which are V^{3+} and half of which are V^{2+}, are non-bonding and become antiferromagnetically ordered below a separate transition at 46 K.

1.4.3: In spinels

The vanadium oxides discussed above have structures in which VO_6 octahedra share edges in one and two dimensions. An analogous three-dimensional network is realised by the BX_6 octahedra in the spinel structure, so if the *B*-site cations have a t_{2g} orbital degree of freedom they too can form orbital molecules. Different *B*-*B* bonding arrangements are illustrated by the ground states of three well-known examples – $MgTi_2O_4$, $CuIr_2S_4$, and Fe_3O_4.

As in the vanadium oxides, the formation of metal-metal bonds in a spinel should be associated with both a structural distortion – specifically, one that breaks the uniformity of the six *B*-*B* nearest-neighbour distances – and a change to the electronic properties of the material. $MgTi_2O_4$ undergoes such an ordering transition at 260 K. And like V^{4+}, Ti^{3+} has a single *d*-electron, so Ti^{3+} cations can form spin-singlet dimers. The shortening of particular Ti-Ti separations reveals that such dimers are present in the ground state of $MgTi_2O_4$, and that they have a remarkable chiral arrangement (Figure 1.7(a)); the dimers, defined by short (2.85 Å) Ti-Ti bonds, are arranged into helical chains along which they are separated by much longer (3.16 Å) distances.[56]

Spin-singlet dimers can also be formed by low-spin d^5 cations. In $CuIr_2S_4$, the metal-insulator transition at 340 K is associated with charge ordering that segregates Ir^{3+} and Ir^{4+}. The two charge states organise into eight-membered rings (Figure 1.7(b)). Ir^{3+} cations (t_{2g}^6) lack an orbital degree of freedom, and the Ir-Ir separations around each Ir^{3+} ring are reasonably uniform (3.47 Å – 3.60 Å), but Ir^{4+} cations (t_{2g}^5) can dimerise, and the separations around each Ir^{4+} ring are alternatingly short (2.96 Å – 3.01 Å) and long (3.46 Å – 3.58 Å).[57]

In magnetite, Fe_3O_4, the spins of the *A*-site and *B*-site cations interact through superexchange and establish ferrimagnetic order below 858 K. This aligns the spins of the *B*-site cations – which, as Fe_3O_4 is an inverse spinel, have an average valence of +2.5 – in parallel. Both the Fe^{2+} and Fe^{3+} cations occupying the *B*-site have high-spin electron configurations so the former ($t_{2g}^4 e_g^2$) have one more t_{2g} electron than the latter ($t_{2g}^3 e_g^2$), and the ferrimagnetic ordering forces this

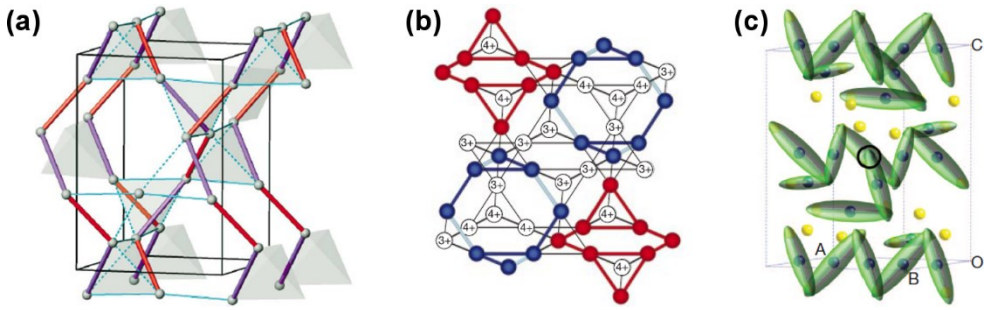

Figure 1.7: Orbital molecule states in spinels. **(a)** Ti_2^{6+} dimers in $MgTi_2O_4$, which self-organise into helical chains. Along each chain Ti-Ti distances are alternatingly short (red) and long (purple). Figure reproduced from Ref. 56. **(b)** Ir_2^{8+} dimers in $CuIr_2S_4$. Charge ordering forms rings of Ir^{3+} (red) and Ir^{4+} (blue); Ir-Ir distances alternate in the latter. Figure reproduced from Ref. 57. **(c)** Fe_3^{8+} trimerons in Fe_3O_4, formed by the delocalisation of the minority-spin electron of each Fe^{2+} (blue atoms) over two neighbouring Fe^{3+} sites (yellow atoms). Figure reproduced from Ref. 59.

electron to have a spin that opposes those of the other t_{2g} electrons. As the t_{2g} orbitals interact directly this minority-spin electron can hop between neighbouring *B*-site cations, so ferrimagnetic Fe_3O_4 is an electrical conductor. However, the conductivity decreases dramatically at 120 K.[58] To a first approximation this change in properties is the result of charge ordering, which localises the minority-spin electron such that the averaged $Fe^{3+}[(Fe^{2.5+})_2]O_4$ charge distribution of the metallic phase becomes ordered $Fe^{3+}[Fe^{2+}Fe^{3+}]O_4$, but there is an additional distortion of the cubic spinel structure that shortens the Fe-Fe distances within linear three-atom units by up to 0.16 Å below the average value. This shortening is the result of the partial delocalisation of the minority-spin electron of each Fe^{2+} over two neighbouring Fe^{3+} sites, forming three-atom orbital molecules termed 'trimerons' (Figure (1.7(c)).[59] A notable feature of these orbital molecules is that, as their bonding involves a single electron rather than a spin-singlet pair, each trimeron retains a net spin.

1.4.4: Order and disorder

The examples detailed above illustrate the range of materials in which orbital molecule states have been found. The orbital molecules themselves show considerable variation – they can be formed by 3*d*, 4*d* and 5*d* valence electrons;

they have different sizes and bonding geometries; and their bonds may involve paired or unpaired electrons – but the transitions by which the orbital molecule states form in these different materials all share common characteristics. Firstly, there is a crystallographic distortion – orbital molecules with long-range structural order emerge from a structure with uniform or near-uniform metal-metal distances by displacive distortions that shorten some of those distances; and secondly, this distortion is accompanied by dramatic changes of electrical conductivity and magnetic susceptibility. These similarities suggest that the orbital molecules in these different materials are formed through a common mechanism. In both VO_2 and $LiVO_2$, substantial orbital polarisations that increase the one-dimensional character of each system have been experimentally identified.[43,47] One-dimensionality is characteristic of a Peierls distortion, and although strong electron correlations are required to actually achieve this polarisation, a Peierls-like description provides the basis for a common mechanism of orbital molecule formation. For $MgTi_2O_4$ and $CuIr_2S_4$, a Peierls transition induced by orbital ordering along the intersecting edge-sharing chains of the spinel structure can account for the dimerisations that occur in these materials.[60] In any system a Peierls-like mechanism establishes long-range orbital order from an orbitally-disordered state, so this mechanism accounts for the crystallographic distortions and changes of properties that occur at the phase transitions where orbital molecules form.

However, there are two orbital molecule systems that show very different behaviour. $LiRh_2O_4$, a spinel, and Li_2RuO_3, which has a honeycomb-lattice structure, both have ground states in which 4*d* orbital dimers establish long-range order. As in the orbital molecule systems described previously, the formation of such a state is evidenced by the shortening of metal-metal bonds through a crystallographic distortion. These materials are unusual, though, because studies of their local structures through atomic pair distribution function (PDF) analysis have revealed that the shortened dimer bonds exist as local distortions well above the temperatures at which their long-range order is lost. In $LiRh_2O_4$ the dimers are ordered below 170 K but persist to 350 K,[61] whilst in

Li_2RuO_3 they are ordered below 540 K but persist to at least 920 K.[62] In other words, the dimers in $LiRh_2O_4$ and Li_2RuO_3 persist from structurally-ordered low-temperature phases into structurally-disordered high-temperatures phases; the transitions in these materials are not the result of long-range order emerging from a uniform, disordered state, but of short-range order becoming established on a long-range scale.

The stability of local metal-metal bonding interactions in $LiRh_2O_4$ and Li_2RuO_3 suggests that the dimers in these materials form through a very different mechanism to the Peierls-type description used for other orbital molecule systems, and PDF studies of VO_2,[63] $Na_{0.5}VO_2$[64] and $CuIr_2S_4$[65] have confirmed that orbital molecules do not exist on any length-scale in the high-temperature phases of these materials. By the Peierls-type mechanism metal-metal σ-bonds form as the result of an electronic instability in the band structure, and it is a measure of the sensitivity of this mechanism to perturbations of the electronic structure that the different polymorphs of $Na_{0.5}VO_2$, which differ only in the positions of the Na-site vacancies, can have radically different orbital molecule ground states. In $LiRh_2O_4$ and Li_2RuO_3 the structural rearrangements at the transition must perturb the electronic structure, but the metal-metal bonding is clearly unaffected. In fact, the behaviour of the dimers in these materials is more like that of conventional molecules – when a crystal of ice melts, its constituent water molecules lose long-range order but the molecules themselves are not decomposed.

1.5: Orbital molecules in vanadium oxide spinels

Although orbital molecules have been identified in numerous systems, the mechanisms by which they form and the extent to which they can be manipulated are not yet well-understood. To develop this understanding, a system in which orbital molecules can be readily formed and manipulated is required. As several stable vanadium cations have an electron configuration suitable for V-V bonding, and the spinel structure provides a suitable template upon which they can do so,

the family of AV_2O_4 spinels was expected to be a good system with which to study orbital molecule phenomenology.

AV_2O_4 spinels with monovalent, divalent and trivalent *A*-site cations are known. An orbital molecule state has only previously been reported in one of these materials, AlV_2O_4, but it is spectacular – each vanadium 'heptamer' is comprised of not two or three cations, but seven (Figure 1.8).[66] Other AV_2O_4 systems, such as ZnV_2O_4 and LiV_2O_4, have complex correlated-electron ground states, and although ordered orbital molecules have not been identified in these materials it has been proposed that local V-V bonding interactions are important in determining their electronic behaviour.

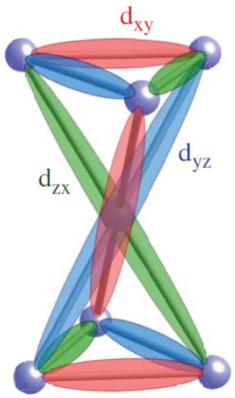

Figure 1.8: Bonding in a V_7 'heptamer'. These orbital molecules have been reported to form in the ground state of the spinel AlV_2O_4. Figure reproduced from Ref. 66.

The aim of this Thesis is therefore to investigate the behaviour of a range of AV_2O_4 systems with regard to orbital molecule formation. Structural studies, both crystallographic and local, and measurements of magnetic and transport properties are used to characterise the orbital states of both known and newly-synthesised materials and identify orbital molecules. Furthermore, the manipulation of the orbital states in these materials through structural and electronic perturbations is explored.

Chapter 2: Experimental methods

2.1: Synthesis

All of the materials studied in this Thesis were prepared by the ceramic method of solid-state synthesis. This method uses high temperatures and long heating times to overcome the large energetic barriers to the diffusion of charged ions that is necessary for a chemical reaction between solid reagents to occur.[67]

By the ceramic method, bulk powder samples are synthesised from mixtures of powdered metals, metal oxides, and/or metal oxy-acid salts, such as metal carbonates. So that the constituent species are in the appropriate ratio the use of dry, high-purity reagents is essential. To overcome the rate-limiting diffusion of chemical species between particles of the different reagents they are normally ground together to give a fine, homogenous mixture, and then pressed into pellets so that inter-grain contact is maximised. Reactions are carried out by heating these pellets in a furnace; for completion to be reached both high temperatures, of 700 °C or more, and long heating times, of hours or days, are typically required. It can be necessary to heat a sample several times, with intermediate regrinding and pellet-pressing, to form a homogenous product.

In the use of high temperatures, several practical considerations must be accounted for. Reactions carried out under such conditions are likely to be under thermodynamic control, so the maximum temperature reached influences the phase, or mixture of phases, that is formed. The reaction can also be influenced by heating the sample under a flowing gas: O_2 and H_2 are oxidising and reducing agents, respectively, whilst Ar can be used to maintain an inert atmosphere. Particularly sensitive reactions can be carried out under closed-system conditions by sealing the sample inside an evacuated quartz ampoule prior to heating. For any reaction, care must be taken to avoid the melting or evaporation

of any component of the reaction mixture. Reagents can also be susceptible to a reaction with the sample container – for example, vanadium reacts with alumina crucibles, and lithium with quartz ampoules. Any such reactions must also be avoided, and can be countered by separating the sample and container with an inert material such as gold foil.

2.2: Diffraction and scattering

2.2.1: Theoretical basis

(a) Crystals and diffraction

Scattering is the process by which radiation is deflected upon interaction with matter. Individual waves scatter from individual particles, and the scattering process is defined by the changes of direction and energy that the scattered wave experiences. Additional effects arise from the interference of different waves scattered simultaneously by different particles. If the wavelength of the radiation is of a similar magnitude to the separations of atoms within the scattering material, the scattering and interference are related to the atomic structure of the material.

Crystals are materials in which the arrangement of atoms has periodic translational symmetry. This symmetry is defined by the crystal lattice, which is an infinite array of points whose positions in space $\mathbf{l}$ relative to an origin are defined by integer multiples of the three basis vectors $\mathbf{a}$, $\mathbf{b}$ and $\mathbf{c}$

$$\mathbf{l} = n_1\mathbf{a} + n_2\mathbf{b} + n_3\mathbf{c} \qquad \textbf{(2.1)}$$

The volume of space associated with each lattice point is called the unit cell. A unit cell is a parallelepiped with a lattice point at each vertex, and its shape it defined by six lattice parameters – three edge lengths a, b and c; and three angles α, β and γ – which are determined by the magnitudes of the basis vectors and the angles between them. The unit cells of every lattice point pack together according to the lattice symmetry and fill space completely, and as such the arrangement of

atoms in each is repeated periodically in space to build the crystal structure. This arrangement is described by a basis set of atoms that is assigned to each lattice point. The position **R** of an atom within the unit cell is defined with respect to the origin of the unit cell by fractions of the basis vectors, with the fractional coordinates *x*, *y* and *z* each taking a value between 0 and 1

$$\mathbf{R} = x\mathbf{a} + y\mathbf{b} + z\mathbf{c} \qquad \textbf{(2.2)}$$

The shape, symmetry and contents of a unit cell, and hence the structure of a crystalline material, can be determined by the diffraction of radiation. Bragg diffraction is a scattering process particular to crystals,[68] first observed in the early 20th century and rationalised by considering that the periodic structure of these materials comprises planes of atoms that act as diffraction gratings. Sets of parallel planes are labelled by the Miller indices *hkl* that denote how many planes of a given set intersect each axis of the unit cell. Within each set of planes, neighbouring planes are equally spaced by a distance d_{hkl}. Incident radiation is reflected by the atomic planes; as depicted in Figure 2.1, incident waves reflect from parallel planes in the same direction and so remain parallel, but will have travelled a different distance through the crystal. The interference between the reflected waves is therefore destructive, and the net intensity of the reflected radiation is zero, unless the difference of the path-lengths travelled by different waves exactly equals an integer multiple *n* of the wavelength *λ*. When this condition is met the waves interfere constructively, and the intensity of the

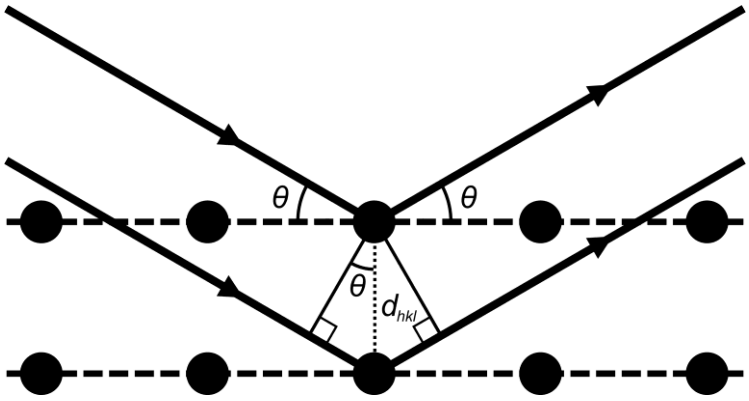

Figure 2.1: The reflection of waves from parallel lattice planes, by which Bragg's law can be derived.

reflected radiation is the sum of the intensities of the individual reflected waves. For this constructive interference to occur the radiation must be reflected by a particular angle 2θ that is determined by the inter-plane separation d_{hkl} according to Bragg's law

$$n\lambda = 2d_{hkl}\sin\theta \qquad \textbf{(2.3)}$$

The diffraction pattern of radiation scattered by a perfectly crystalline material therefore comprises sharp intensity maxima, referred to as Bragg peaks, at the particular 2θ angles defined by the separations between the different sets of planes within the crystal, with no intensity at any other values of 2θ. As such, the lattice parameters and symmetry of the unit cell can be determined from the values of 2θ at which the different Bragg peaks are observed.

However, Bragg's law does not describe the relative intensities of the different reflections, which are dependent on the arrangement of the atoms within the unit cell. To deduce this arrangement the process of diffraction must be considered not as the result of radiation being reflected by planes of atoms, but rather as the result of the scattering of radiation by the periodic arrangement of atoms that comprises a crystal. As this arrangement is static, diffraction is an elastic scattering process – that is, the energy of the radiation is not changed upon scattering. As diffraction is the result of the interference between waves scattered by different atoms, that scattering must also be coherent – different atoms of the same type scatter the same radiation in the same way.

A beam of radiation can be described by the wave equation

$$\psi = Ae^{i\mathbf{k}.\mathbf{x}} \qquad \textbf{(2.4)}$$

where A is the amplitude of the wave, $\mathbf{k}$ is the wavevector, which defines the direction of the propagation and has magnitude $|\mathbf{k}| = 2\pi/\lambda$, and $\mathbf{x}$ is a position in space. When a wave interacts with an atom and is scattered its wavevector is changed from $\mathbf{k}_i$ to $\mathbf{k}_f$, defining the scattering vector $\mathbf{Q}$

$$\mathbf{Q} = \mathbf{k}_i - \mathbf{k}_f \qquad \textbf{(2.5)}$$

and the momentum transfer $\hbar\mathbf{Q}$. For elastic scattering $|\mathbf{k}_i| = |\mathbf{k}_f|$, hence

$$|\mathbf{Q}| = Q = \frac{4\pi \sin\theta}{\lambda} \quad \textbf{(2.6)}$$

Thus, Bragg's law can be expressed in terms of Q

$$d_{hkl} = \frac{2\pi}{Q} \quad \textbf{(2.7)}$$

All of the waves in an incident beam of radiation are parallel and in phase. After scattering the waves may still be parallel, but their phase relationship will depend on the different distances that they have travelled through the sample. In a simple case, of a beam of two waves scattered by two atoms separated by a distance **r**, the phase difference between the scattered waves is **Q**.**r**, thus the scattering process modifies the net amplitude of the beam by a factor of $\left(1 + e^{i\mathbf{Q}.\mathbf{r}}\right)$. For the scattering of a beam of many waves by an assembly of a large number of particles, this becomes

$$F(\mathbf{Q}) = \sum_j f_j e^{i\mathbf{Q}.\mathbf{r}_j} \quad \textbf{(2.8)}$$

The form factor f_j accounts for atoms of different types scattering radiation – specifically X-rays – by different amounts. An analogous parameter, the scattering length b_j, describes the strength of scattering of neutrons by different nuclei. The factors that determine f_j and b_j will be discussed further in the next Section.

The intensity of a wave is proportional to the square of its amplitude. Therefore, the net intensity of radiation scattered from an assembly of particles will only be non-zero when $F(\mathbf{Q})$ is non-zero. If the assembly is crystalline the positions of the atoms are defined by Equations 2.1 and 2.2, such that $\mathbf{r} = \mathbf{l} + \mathbf{R}$, and $F(\mathbf{Q})$ is only non-zero when **Q** is one of a particular set of vectors $\mathbf{d}^*_{hkl}$

$$\mathbf{d}^*_{hkl} = h\mathbf{a}^* + k\mathbf{b}^* + l\mathbf{c}^* \quad \textbf{(2.9)}$$

These are known as the reciprocal lattice vectors. They are the vectors normal to the *hkl* planes of the crystal lattice and each defines a point in the reciprocal lattice, so called because, with $|\mathbf{d}^*_{hkl}| = 2\pi/d_{hkl}$, its dimensions are the inverse of those of the crystal lattice. The reciprocal lattice can also be obtained as the Fourier transform of the crystal lattice. The reciprocal vectors are defined such

that $\mathbf{a}^*.\mathbf{a} = 2\pi$ but $\mathbf{a}^*.\mathbf{b} = \mathbf{a}^*.\mathbf{c} = 0$; hence, when $\mathbf{Q} = \mathbf{d}^*_{hkl}$, $F(\mathbf{Q})$ (Equation 2.8) becomes the structure factor F_{hkl}

$$F_{hkl} = \sum_j f_j e^{2\pi i(hx_j + ky_j + lz_j)} \qquad \textbf{(2.10)}$$

Radiation diffracted by a crystal therefore forms a pattern of Bragg peaks positioned at the reciprocal lattice points defined by the different values of h, k and l, each with an intensity proportional to the corresponding $|F_{hkl}|^2$. As such, a diffraction pattern is the representation of a crystal structure in reciprocal space, and is related to the real-space distribution of atoms in the crystal by the Fourier transform of F_{hkl}.

(b) X-rays and neutrons

Both electromagnetic radiation in the X-ray spectrum and neutrons of thermal energies have wavelengths of approximately 1 Å which, being similar to the interatomic distances in solids, makes them suitable for diffraction. Although the same formalisms describe the scattering of both X-rays and neutrons, the two types of radiation scatter from atoms through very different mechanisms. As such the X-ray form factor f_j (Figure 2.2(a)) and the neutron scattering length b_j (Figure 2.2(b)) show different dependencies on both the atomic number Z of the scattering atoms and on the scattering vector Q.

Being electromagnetic radiation, X-rays are scattered by the electron density surrounding each atom. As such, atoms with larger numbers of electrons scatter X-rays more strongly, and f_j increases systematically with Z. In contrast, neutrons are scattered by the nuclei of atoms. The strength of the scattering interaction, given by b_j, varies between elements but is not correlated with Z. It can also vary significantly between different isotopes of the same element, and between different spin states of nuclei of the same composition.

The size of the scattering particle relative to the wavelength of the radiation also has an important effect on the scattering. As the cloud of electrons around each atom has a size of the same magnitude as the X-ray wavelength, X-rays scattered

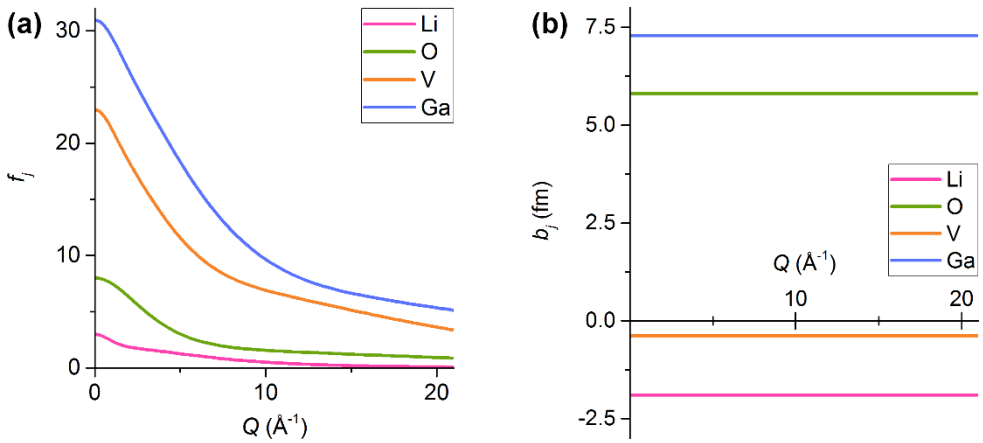

Figure 2.2: (a) The X-ray form factors f_j of selected elements, calculated according to Ref. 69. The dependence of f_j on the atomic number Z and scattering vector Q is evident. **(b)** The coherent neutron scattering lengths b_j of the same elements at natural abundance, taken from Ref. 70. These do not have a Z-dependent variation, and they are constant in Q.

by electrons at different positions around the same atom can lose their phase relationship. This becomes more likely as Q increases, so f_j decreases correspondingly. By comparison, nuclei are several orders of magnitude smaller than neutron wavelengths so act as a point scatterer, and b_j does not vary with Q.

The different mechanisms by which X-rays and neutrons are scattered means that X-ray and neutron diffraction experiments can provide complementary information, and have advantages and disadvantages over one another. The dependence of f_j on Z means that it can be difficult to distinguish species with similar numbers of electrons with X-rays, or to accurately determine the positions of light atoms such as oxygen in the presence of heavier atoms. The decay of f_j with Q also limits the scattering intensity at high Q, with implications for the use of X-rays in the total scattering method that will be discussed in later Sections. Neutrons can offer a better scattering contrast between elements with similar atomic numbers, and are scattered strongly by light elements like Li and O, though some elements – notably vanadium – scatter neutrons very weakly. Furthermore, as neutrons have an intrinsic magnetic moment, they are also scattered by the moments of magnetic atoms. Neutron diffraction can therefore be used to determine the magnetic structures of spin-ordered materials.

(c) Powder diffraction and the Rietveld method

The aim of a diffraction experiment is to measure the scattering angles and intensities of all the Bragg reflections from a sample, such that they can be used to determine its crystal structure. This can be done using a single crystal, giving a diffraction pattern of Bragg peaks at positions determined by the different reciprocal lattice vectors, or a powder sample.[68,71] In principle, a powder comprises a very large number of very small crystallites that are randomly oriented with respect to one another, such that for every set of lattice planes a proportion of the crystallites has the correct orientation with respect to the incident beam for the diffraction from those planes to occur. However, a powder is an isotropic material; crystallites that have the same orientation with respect to the beam may have different orientations with respect to one another, so although they diffract the incident radiation by the same angle they do so in different directions. The radiation diffracted from a powder thus forms a set of Debye-Scherrer cones, giving a diffraction pattern of concentric rings centred on the incident beam direction (Figure 2.3). Powder diffraction can therefore be used to measure the magnitudes $|\mathbf{d}^*_{hkl}|$ of the scattering vectors, but not their directions. This orientational averaging can limit the use of powder diffraction for

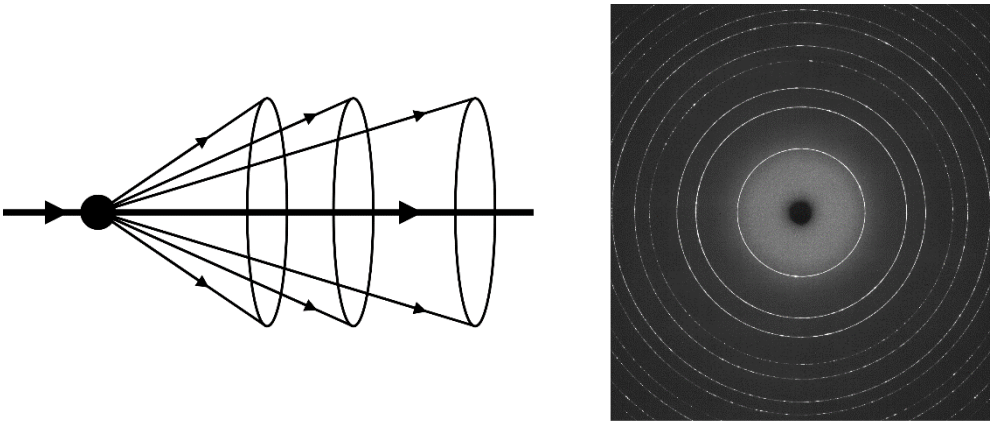

Figure 2.3: (a) Radiation diffracted by a powder sample forms a set of Debye-Scherrer cones. **(b)** The diffraction pattern of Si, collected using a two-dimensional detector at ESRF beamline ID15B, is comprised of concentric circles that each correspond to a Debye-Scherrer cone.

structure-solution in comparison to single crystal techniques, which provide more information about the structure of the scattering material. That said, the refinement of structural models against powder diffraction patterns using the Rietveld method is a powerful tool, and the use of powders has many practical advantages over the use of single crystals: powder samples are generally easier to prepare; powder diffractometers generally have a higher resolution $\Delta Q/Q$; and quantitative phase analysis can be carried out. The orientational averaging of the structure in a powder is also made use of in total scattering experiments, which will be described in the next Section.

To relate a powder diffraction pattern to the structure of the scattering material the positions, intensities and profiles of the measured Bragg peaks must be described. The process of assigning *hkl* values to the observed Bragg peaks is known as indexing, and utilises Bragg's law (Equation 2.3) to relate the scattering angle at which Bragg peaks are observed to the lattice parameters of the unit cell, allowing its shape and symmetry to be determined.

The intensities of the Bragg peaks are primarily dependent on $|F_{hkl}|^2$ (Equation 2.10), but are influenced by many other factors. Some symmetry elements can restrict the values of *hkl* for which $F_{hkl} \neq 0$, causing particular Bragg peaks to be systematically absent; for example, only reflections that have all-odd or all-even values of h, k and l are observed for a face-centred cubic lattice. Measured intensities are also influenced by experimental considerations, such as the flux and polarisation of the incident beam, the absorption of the beam by the sample and the level of background scattering, as well as effects particular to the use of powders. As only $|\mathbf{d}^*_{hkl}|$ is measured, if the symmetry of the unit cell causes several different planes to have the same d_{hkl} their Bragg reflections will overlap and the intensity is correspondingly multiplied. Furthermore, the relative intensities of different reflections will be affected if the diffracting powder sample is not ideal – that is, it does not comprise a large number of randomly oriented crystallites, such that diffraction from all *hkl* planes is not equally probable. If the powder is not ideal – for example, the morphology of the crystallites leads to them having a preferred orientation, or the illuminated sample contains too few

crystallites – diffraction may occur from some sets of planes more than from others, affecting the relative intensities of the Bragg peaks. Spinning or rocking the sample during measurement, to expose different orientations to the incident beam, can help to mitigate these effects.

The measured intensities of the Bragg peaks also have a dependency on Q, due to the Debye-Waller effect. Atoms, and the electrons around them, are always moving, and their time-averaged position can be described by a Gaussian function with mean-squared displacement $\langle u_j^2 \rangle$. This can be described isotropically, in which case $\langle u_j^2 \rangle$ is referred to as the isotropic atomic displacement factor U_{iso}, or anisotropically, using six independent atomic displacement parameters. As $\langle u_j^2 \rangle$ becomes larger it is more likely that two waves scattered from the same atom will lose their phase coherency and so not contribute to the diffracted intensity. The effect of this on the diffraction pattern is accounted for with the Debye-Waller factor

$$I(Q) \propto \exp\left(-\frac{Q^2\langle u_j^2 \rangle}{2}\right) \qquad \textbf{(2.11)}$$

This has the important consequence of limiting the maximum value of Q to which Bragg peaks have measureable intensities.

The Bragg peaks of an ideal diffraction pattern would each be described by a Dirac δ-function, with all of the scattering intensity at precise values of Q in accordance with Equation 2.10. In reality, both the resolution of any diffractometer and the imperfections present in any sample broaden the profiles of the Bragg peaks. A simple description for these profiles is the pseudo-Voigt function, a convolution of Gaussian and Lorentzian peak shapes with a symmetric full-width at half-maximum (FWHM). The Gaussian component primarily accounts for the contribution of the instrumental resolution, which is dependent on factors such as λ-divergence and the resolution of the pixels of a two-dimensional detector, to the measured peak width, and is described by the Caglioti function[72]

$$FWHM = U\tan^2\theta + V\tan\theta + W \qquad \textbf{(2.12)}$$

whilst the Lorentzian component is due to contributions from the sample

$$FWHM = \frac{X}{\cos\theta} + Y\tan\theta \qquad \textbf{(2.13)}$$

The first term in Equation 2.13 accounts for the Scherrer broadening that occurs when the diffracting crystallites are small enough that the assumption of diffraction occurring from an infinite lattice no longer holds, whilst the second term accounts for the broadening caused by crystallite strain. Strain causes the inter-plane spacings d_{hkl} for a set of planes to deviate from the uniform value of an ideal lattice, broadening the resolution $\Delta d/d$ of each Bragg peak; its origin can be both microscopic, the result of faults and defects within the structure, or macroscopic, such as that induced by an applied pressure. In extreme cases strain can cause the peak profiles to broaden asymmetrically, and more complex profile functions have been developed to describe this.[73]

Due to the pulsed nature of the neutron beams generated by spallation sources, the Bragg peaks in time-of-flight diffraction patterns have an unusual asymmetric shape. Their profile can be described with the Ikeda-Carpenter function[74]; the factors that contribute to the resolution of time-of-flight instruments will be discussed in a later Section.

Being a one-dimensional representation of a three-dimensional structure, powder diffraction patterns do not normally contain enough information to be used for absolute structure solution. However, the structure of a material can be deduced by calculating the powder diffraction pattern of a structural model and refining the parameters of the model such that the calculated intensities best fit those measured experimentally. The most commonly-used method for such refinement was developed by Rietveld.[75] A potential limitation of powder diffraction is that different Bragg peaks can diffract with the same, or very similar, values of 2θ and thus be overlapping in the measured diffraction pattern, making it difficult to determine all of the individual structure factors F_{hkl}. The Rietveld method overcomes this by dividing the whole measured range of 2θ into a number of equal steps i, and defining the intensity y_i at each step to be the sum of the intensities $y_{i,hkl}$ of any Bragg peaks that happen to diffract with that value of 2θ, plus a background intensity $y_{i,b}$

$$y_i = y_{i,b} + \sum_{hkl} y_{i,hkl} \qquad \textbf{(2.14)}$$

The refinement of the structural model is carried out by minimising the difference M_y between the calculated intensity $y_{i,calc}$ and the measured intensity $y_{i,obs}$ at each i, using a least-squares method

$$M_y = \sum_i w_i \left(y_{i,obs} - y_{i,calc}\right)^2 \qquad \textbf{(2.15)}$$

where w_i is a weighting factor generally equal to $1/y_{i,obs}$. Structural, instrumental and profile parameters can all be refined, as can a background function. The quality of the fit of the calculated diffraction pattern to the experimental one can be evaluated using three parameters – the profile factor R_p, the weighted profile factor R_{wp}, and the goodness-of-fit parameter χ^2

$$R_p = \frac{\sum_i \left|y_{i,obs} - y_{i,calc}\right|}{\sum_i y_{i,obs}} \qquad \textbf{(2.16)}$$

$$R_{wp} = \left(\frac{\sum_i w_i \left(y_{i,obs} - y_{i,calc}\right)^2}{\sum_i w_i \left(y_{i,obs}\right)^2}\right)^{½} = \left(\frac{M_y}{\sum_i w_i \left(y_{i,obs}\right)^2}\right)^{½} \qquad \textbf{(2.17)}$$

$$\chi^2 = \frac{M_y}{N - P + C} \qquad \textbf{(2.18)}$$

where N is the total number of 2θ steps, P is the number of refined parameters, and C is the number of constraints applied. As the fit improves, R_p and R_{wp} tend towards a value of 0 whilst χ^2 tends to a value of 1.

A modified fitting method, by which the intensities of reflections can be estimated without a structural model, was developed by Le Bail.[76] The contributions of different Bragg peaks to the total observed intensity of a reflection is partitioned following the Rietveld method but the starting F_{hkl} values, instead of being calculated from a model, are all set to an equal arbitrary value. The lattice parameters of the unit cell and the profile parameters of the Bragg peaks can then be refined, allowing the best-possible fit to the measured intensities to be determined.

All Rietveld and Le Bail fits in this Thesis were carried out using the General Structure Analysis System (GSAS) and EXPGUI interface.[77,78]

(d) Total scattering

A beam of radiation scattered coherently by a collection of particles has an amplitude $F(\mathbf{Q})$ (Equation 2.8). The intensity of the scattered beam $I(\mathbf{Q}) = |F(\mathbf{Q})|^2$ is

$$I(\mathbf{Q}) = \sum_{i,j} f_i f_j e^{i\mathbf{Q}.(\mathbf{r}_i - \mathbf{r}_j)} \qquad \textbf{(2.19)}$$

which clearly shows that the intensity of coherent scattering is dependent on the separations of pairs of scattering particles. The structure factor F_{hkl} (Equation 2.10), which determines the intensities of Bragg reflections, is derived from $F(\mathbf{Q})$ when these separations are periodic, such that the correlations between the positions of different atomic pairs extend over a long-range scale. However, this assumption is not implicit in the general description of $I(\mathbf{Q})$ in Equation 2.19. Coherent scattering can also occur from non-periodic structures, in which structural correlations may only exist over a short spatial range, giving rise to measurable intensities known as diffuse scattering.

Just as Bragg scattering encodes information about the periodic structure of materials, diffuse scattering encodes information about structure on the local scale. Scattering from amorphous materials, which have structures lacking any long-range correlations, is entirely diffuse. For crystalline materials, diffuse scattering arises when the atomic positions deviate from their ideal sites – for example, when thermal motion blurs the periodic atomic positions, reducing the intensity of the Bragg peaks according to the Debye-Waller factor and redistributing it as diffuse scattering. Diffuse scattering can also arise from local perturbations to the periodic structure, such as those caused by crystallographic defects and faults, and from static short-range order in a crystal with a disordered average structure.[79] The periodic structure of a disordered crystal is the average

of all possible configurations, so the scattering that gives the Bragg peaks may not be truly representative of the local structural environment.

Short-range structural perturbations are likely to be less uniform than a periodic lattice, so unlike Bragg peaks, which are intense and observed at precise values of Q, diffuse scattering is weak and spread broadly in Q. It is therefore challenging to isolate the diffuse scattering in a scattering measurement. The technique of total scattering[80,81] aims to treat Bragg and diffuse scattering on an equal basis, so that information describing both the average and local structures of a crystalline material can be extracted from a single measurement of the coherent scattering intensity $I(\mathbf{Q})$ (Equation 2.19). For a powder, which is an isotropic material with neither a special origin nor a special orientation, the intensity variation is dependent only on the magnitude of Q and not its direction. Equation 2.19 thus becomes

$$I(Q) = \sum_{i,j} f_i f_j \frac{\sin Q r_{ij}}{Q r_{ij}} \qquad \textbf{(2.20)}$$

where $r_{ij} = |r_i - r_j|$. $I(Q)$ describes all the coherent scattering from all pairs of scattering particles. To obtain $I(Q)$ from a powder diffraction measurement any background contributions that are not scattering from the sample must be corrected for, and the measured intensity normalised by the incident flux. Subsequently $I(Q)$ itself can be normalised to the structure function $S(Q)$, which describes the scattering in absolute units of scattering-per-atom and has an average value $\langle S(Q) \rangle = 1$. For a single-component system of N scattering centres that have an average scattering cross-section $\langle f_j \rangle^2$

$$S(Q) = \frac{I(Q)}{N \langle f_j \rangle^2} \qquad \textbf{(2.21)}$$

As f_j becomes small at high Q, this normalisation has important consequence of amplifying the scattering intensity at high Q relative to that at low Q.

$I(Q)$ (Figure 2.4(a)) and $S(Q)$ are reciprocal-space representations of the structure from which the scattering is occurring and are related to its real-space distribution of atoms, which cannot be measured directly by a scattering

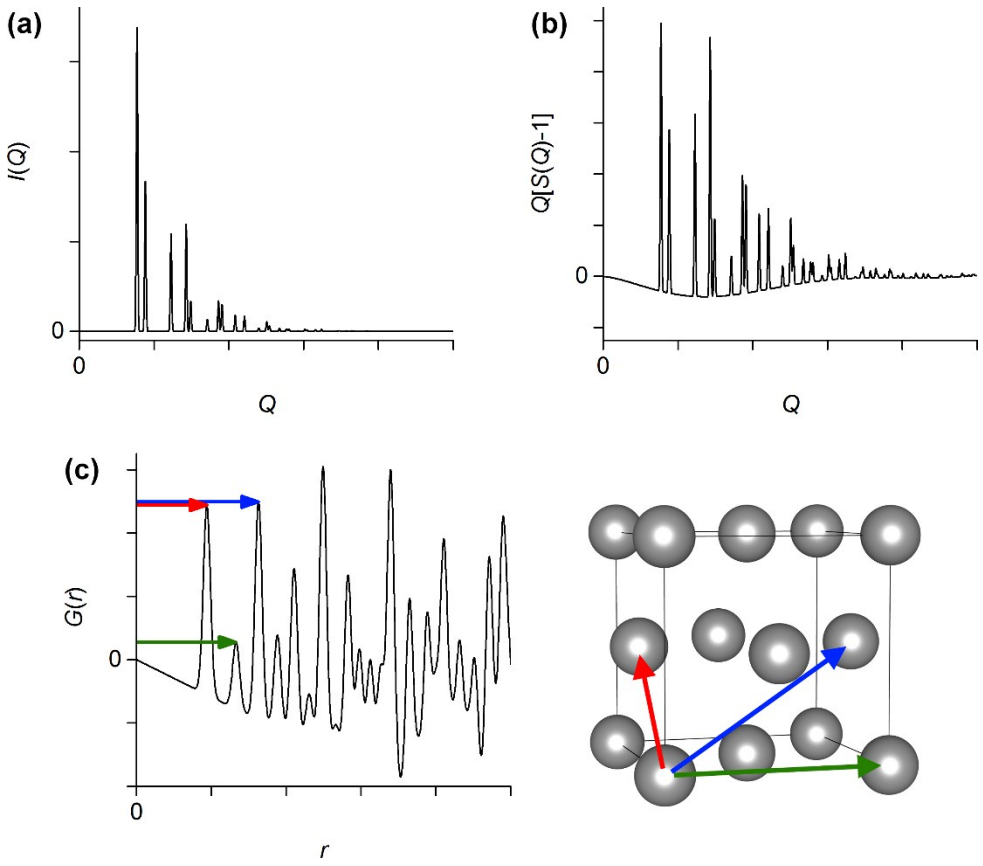

Figure 2.4: Structural functions for a simulated face-centred cubic lattice. The coherent scattering intensity $I(Q)$, in **(a)**, can be calculated using Equation 2.19 and is the function measured during a scattering experiment. $I(Q)$ is normalised to the structure function $S(Q)$ according to Equation 2.21, and the reduced structure function $Q[S(Q)\text{-}1]$, in **(b)**, is Fourier-transformed to the atomic pair distribution function $G(r)$, in **(c)**, according to Equation 2.22. Coloured arrows relate the first three peaks in $G(r)$ to the corresponding structural correlations in the lattice.

experiment, by a Fourier transform. For the scattering from a powder, the orientational averaging defines the structure not through the absolute positons of the atoms but their positions relative to one another, and the Fourier transform of the reduced structure function $Q[S(Q)\text{-}1]$ (Figure 2.4(b)) gives a one-dimensional function $G(r)$ (Figure 2.4(c))

$$G(r) = \frac{2}{\pi}\int_0^\infty Q[S(Q) - 1]\sin(Qr)\,dQ \qquad \textbf{(2.22)}$$

$G(r)$ is an atomic pair distribution function (PDF), a histogram of the separations of all the atomic pairs within a material. The purpose of a total scattering

experiment is to generate $G(r)$ from $I(Q)$; if $I(Q)$ includes both Bragg and diffuse scattering, $G(r)$ includes separations that are correlated on both long-range and short-range scales.

$G(r)$ describes the structure of the scattering material in real space. Physically, this derives from its relationship to the radial distribution function $R(r)$, where $R(r)\mathrm{d}r$ is the number of atoms in a spherical shell of thickness dr a distance r from a reference atom. The two distribution functions are related as

$$G(r) = \frac{R(r)}{r} - 4\pi r \rho_0 \qquad \textbf{(2.23)}$$

where ρ_0 is the average atomic number density of the material. As such, $G(r)$ is a description of the deviation of the actual atomic density of a structure, due to the correlations of different pairs of atoms, from its average value.

$R(r)$ can also be used to calculate the PDF of a structural model. In an ideal structure the separation r_{ij} of each atomic pair can be represented by a Dirac δ-function, such that

$$R(r) = \frac{1}{N}\sum_i \sum_j \delta(r - r_{ij}) \qquad \textbf{(2.24)}$$

$R(r)$, and hence $G(r)$, describe the atomic structure of a material on the local scale. The position of a peak corresponds to a particular atomic separation, whilst its integrated intensity gives the number of bonds with that separation. In practice the δ-functions are broadened by the thermal motion of the atoms in a material and the finite resolution of a measurement, so the peaks in $G(r)$ are modelled using Gaussian profiles.

The functions expressed in Equations 2.21-2.24 strictly only apply to single-component systems. Extensions of these expressions can be made for multi-component systems, with the different scattering cross-sections of different atoms accounted for in the normalisation of $I(Q)$ to $S(Q)$ and the calculation of $R(r)$, and a partial PDF $G_{\alpha\beta}(r)$ for each combination of different atoms is obtained by the Fourier transform of the corresponding partial structure function $S_{\alpha\beta}(Q)$. These are weighted such that, as for $S(Q)$ in a single-component system, each

$S_{\alpha\beta}(Q)$ = 1 at infinite Q. The total functions $S(Q)$ and $G(r)$ for a multi-component system are then the weighted sums of all the partial functions.

(e) PDF analysis

The quality of an experimentally-determined $G(r)$ is dependent on the quality of the measureable $S(Q)$ from which it is calculated. In principle $S(Q)$ can be measured using any powder diffractometer, but as the collection of high-quality total scattering data requires some particular considerations, the rapid-acquisition (RA-PDF) method was developed.[82] This method was used to collect the X-ray total scattering data in this Thesis.

As the Fourier transform of $S(Q)$ to $G(r)$ (Equation 2.22) is over an infinite range of Q, the measurement of $S(Q)$ to a high upper-limit Q_{max} is of principal importance. High-Q scattering data encodes low-r structural information, and $G(r)$ has a resolution $\Delta r \approx 2\pi/Q_{max}$, so the detail of the local structure described in $G(r)$ is improved as the Q-range over which $S(Q)$ is measured is widened. This can be challenging for X-ray scattering, as the Q-dependence of the X-ray form factor causes the scattered intensity to become increasingly weak as Q increases, so the RA-PDF method utilises high-energy, high-intensity synchrotron radiation and a two-dimensional area detector to measure high-Q scattering, with $Q_{max} \approx 25$ Å^{-1} typically accessible. Using this method, measurements with good counting statistics over the whole accessible range of Q can be made in seconds, and the collection and averaging of a number of identical measurements can be done to improve the counting statistics further. The two-dimensional detectors used in the RA-PDF method have a coarser resolution than 'standard' powder diffractometers, which are optimised to minimise $\Delta Q/Q$ so that overlapping Bragg peaks can be resolved, and this manifests as a damping of $G(r)$ with increasing r after the Fourier transform is applied. However, this effect is generally not significant in the low-r region of interest for a description of the local structure, and measuring a wide Q-range using a conventional detector takes much longer than with a two-dimensional detector, with which scattering over a wide Q-range can be captured in a single exposure.

To generate $S(Q)$, and hence $G(r)$, from $I(Q)$, any background scattering must be subtracted from the measured intensity. A high-quality background measurement, for example of an empty capillary, must therefore be made as part of a total scattering experiment. For the same reason, it is important that the experimental setup and incident intensity are stable over the course of an experiment, so that the background subtraction and normalisation of $I(Q)$ to $S(Q)$ are consistent between all measurements.

All of the measured total scattering data in this Thesis were background-corrected, converted to $S(Q)$ and transformed to $G(r)$ using PDFgetX3,[83] which performs the necessary mathematical operations using parameters, such as Q_{max}, chosen by the user. Using a high Q_{max} is desirable, but as both the form factor and Debye-Waller factor reduce the intensity of X-ray scattering at high Q, there is a practical limit to Q_{max} above which scattering cannot be distinguished from statistical noise. This parameter must therefore be chosen such that the physical information to be included in the Fourier transform is maximised but unphysical contributions are not introduced. PDFgetX3 also offers a parameter r_{poly} that allows for the correction of termination ripples by introducing a polynomial contribution to $G(r)$ at low r. Termination ripples are spurious features superimposed on the structural PDF that arise because it is impossible to measure the infinite Q_{max} of Equation 2.22, hence the Fourier transform of $S(Q)$ to $G(r)$ is imperfect.

Structural models were refined against $G(r)$ using PDFgui.[84] This software uses a Rietveld-like least-squares fitting procedure, with the structure modelled using a small 'unit cell' of atoms without periodic symmetry constraints needing to be applied. The lattice parameters, atomic coordinates and thermal factors of the local structure of a material can therefore be determined from its real-space depiction. The shapes of the PDF peaks are described using a Gaussian profile, though r-dependent deviations from this that arise from the Q-resolution of the instrument and the correlations between the positions of nearest-neighbour atomic pairs can also be incorporated. Simulated termination ripples can also be applied to the PDF of the structural model.

(f) Quasi-elastic neutron scattering

The scattering that gives Bragg and diffuse intensities is both elastic and coherent. However, inelastic and incoherent scattering can also occur, and the scattering of neutrons by such processes is of particularly utility.[85] Neutrons that have wavelengths of a magnitude suitable for diffraction also have an energies on the scale of structural excitations, so neutron scattering can probe both the static structure of the lattice and dynamic processes such as diffusion and phonon vibrations. Furthermore, significant incoherent scattering can arise when an element has different isotopes or nuclear spin states that have different neutron scattering lengths.

The intensity of a scattered neutron beam I as a fraction of the incident flux I_0 is dependent on the scattering cross-section σ of the material

$$I = \sigma I_0 \qquad \textbf{(2.25)}$$

Neutrons scatter from the nuclei of atoms, which are much smaller than the wavelength of the neutrons used for scattering experiments. A neutron scattered by a nucleus can therefore be described by a spherical wave, for which the scattered intensity is isotropic. As such

$$\sigma = 4\pi {b_j}^2 \qquad \textbf{(2.26)}$$

The nuclear scattering length b_j is the effective range of the neutron-nucleus interaction. It is dependent on both the nuclear composition, for both different elements and different isotopes of the same element, and the spin state of the scattering nucleus. Thus, for the scattering from a collection of nuclei, the scattering lengths of all the nuclei must be accounted for. The average of the scattering lengths over all isotopes and spin states in the collection gives the coherent scattering length b_{coh}, whilst their root-mean-square deviation gives the incoherent scattering length b_{incoh}

$$b_{coh} = \langle b_j \rangle \qquad \textbf{(2.27)}$$

$$b_{incoh} = \sqrt{\langle {b_j}^2 \rangle - \langle b_j \rangle^2} \quad \textbf{(2.28)}$$

Consequently, a collection of nuclei has both a coherent scattering cross-section σ_{coh} and an incoherent scattering cross-section σ_{incoh}. The total scattering cross-section of the collection is the sum of these two components

$$\sigma = \sigma_{coh} + \sigma_{incoh} \quad \textbf{(2.29)}$$

When a neutron is scattered its wavevector changes and it experiences a momentum transfer $\hbar\mathbf{Q}$ (Equation 2.5). If the scattering process is inelastic the energy of the neutron also changes, and it experiences an energy transfer E

$$E = \hbar\omega = E_i - E_f \quad \textbf{(2.30)}$$

To characterise a scattering process both $\mathbf{Q}$ and E must be determined. The scattering intensity measured during an experiment is dependent on the double-differential scattering cross-section $\left(\mathrm{d}^2\sigma/\mathrm{d}\mathbf{\Omega}\mathrm{d}E_f\right)$, which is the probability that a neutron with incident energy E_i leaves the sample in the solid-angle element $\mathrm{d}\mathbf{\Omega}$ about the direction $\mathbf{\Omega}$ with a final energy between E_f and $\mathrm{d}E_f$. Following Equation 2.29 the total cross-section is the sum of coherent and incoherent scattering contributions

$$\frac{\mathrm{d}^2\sigma}{\mathrm{d}\mathbf{\Omega}\mathrm{d}E_f} = \left(\frac{\mathrm{d}^2\sigma}{\mathrm{d}\mathbf{\Omega}\mathrm{d}E_f}\right)_{coh} + \left(\frac{\mathrm{d}^2\sigma}{\mathrm{d}\mathbf{\Omega}\mathrm{d}E_f}\right)_{incoh} \quad \textbf{(2.31)}$$

each of which contributes to the scattering function $S(\mathbf{Q},E)$ of the scattering material

$$\left(\frac{\mathrm{d}^2\sigma}{\mathrm{d}\mathbf{\Omega}\mathrm{d}E_f}\right)_{coh} \propto S(\mathbf{Q},E)_{coh} \quad \textbf{(2.32)}$$

$$\left(\frac{\mathrm{d}^2\sigma}{\mathrm{d}\mathbf{\Omega}\mathrm{d}E_f}\right)_{incoh} \propto S(\mathbf{Q},E)_{incoh} \quad \textbf{(2.33)}$$

This is directly analogous to the relationship between the scattering intensity $I(Q)$ and the structure function $S(Q)$ given in Equation 2.21. $S(Q)$ describes the elastic, coherent scattering from a sample which, being determined by interference effects, is dependent on the correlations between the positions of different nuclei

and, following Equation 2.22, is the spatial Fourier transform of the pair correlation function $G(r)$, which describes the probability of finding a particle at a position r if there is simultaneously a particle at r = 0. Inelastic coherent scattering is also dependent on the correlations between different nuclei but with an additional time-dependence, such that it is dependent on both the structure and collective dynamics of the scattering particles. The Fourier transform of $S(\mathbf{Q},E)_{coh}$ in space and time gives the time-dependent pair correlation function $G(\mathbf{r},t)$, which describes the probability of finding a particle at position r at time t if there was a particle at r = 0 at t = 0

$$G(\mathbf{r},t) = \frac{1}{(2\pi)^3}\int S(\mathbf{Q},E)_{coh}e^{-i(\mathbf{Q}.\mathbf{r}-Et)}d\mathbf{Q}dE \qquad \textbf{(2.34)}$$

If the scattering is incoherent, interference effects are not possible and information about the correlation between scattering particles is lost. Instead, incoherent inelastic scattering is dependent on the dynamics of individual scattering particles. The Fourier transform of $S(\mathbf{Q},E)_{incoh}$ gives the self-correlation function $G_s(\mathbf{r},t)$, which describes the probability of finding a particle at position r at time t if the same particle was at r = 0 at t = 0

$$G_s(\mathbf{r},t) = \frac{1}{(2\pi)^3}\int S(\mathbf{Q},E)_{incoh}e^{-i(\mathbf{Q}.\mathbf{r}-Et)}d\mathbf{Q}dE \qquad \textbf{(2.35)}$$

Incoherent scattering can therefore be used to study translational and rotational processes such as molecular dynamics and diffusion. The scattering from processes such as these is often described as 'quasi-elastic' because the energy transfers involved are small, typically up to 2 meV, and span a distribution of values around E = 0 so cannot be resolved from the elastic scattering line (Figure 2.5).[86] By comparison, the inelastic scattering from processes such as phonon vibrations involves much larger energy transfers and occurs at discrete energy steps.

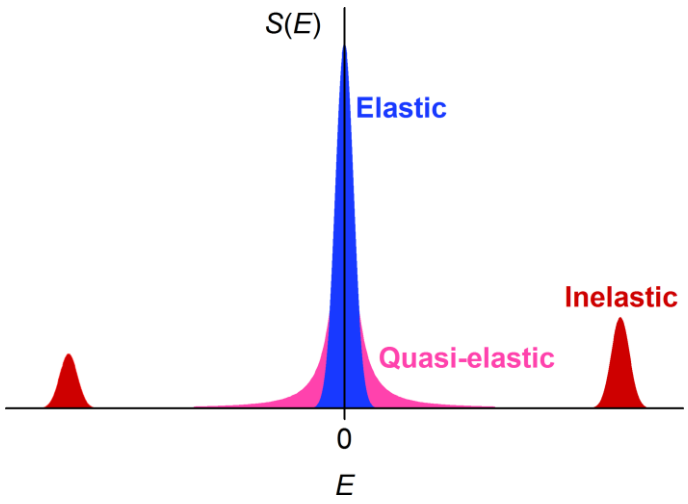

Figure 2.5: Different neutron scattering processes are classified by the energy transfer E they involve. For elastic scattering $E = 0$, though this scattering has a non-zero linewidth determined by the instrumental resolution. Quasi-elastic scattering involves a distribution of energy transfers between 0 and 2 meV, whilst inelastic scattering can occur with much higher values of E. When $E \neq 0$ both energy-gain and energy-loss scattering are possible.

2.2.2: Sources and instrumentation

(a) Laboratory X-rays

Routine diffraction experiments utilise X-rays generated by sealed-tube sources, which are sufficiently small and inexpensive to be suitable for laboratory use. These sources consist of a vacuum tube within which electrons are accelerated by a potential difference and bombard a metal anode target. X-ray radiation is generated by this bombardment through two different mechanisms. *Bremsstrahlung* radiation, which is relatively weak and spans a broad distribution of energies, is generated by the rapid deceleration of the electrons when they pass into the target, whilst characteristic radiation, which has discrete wavelengths and is far more intense, is the result of the bombardment ionising the target atoms. If an inner-shell electron is removed one from a higher-energy shell will lower its energy to fill the vacancy, and in doing so releases a photon of the corresponding quantised energy. The transitions of electrons between different shells therefore release photons of different energies – Kα for $1s \leftarrow 2p$, Kβ for

$1s \leftarrow 3p$, and Lα for $2p \leftarrow 3d$. As the energies of these transitions vary between elements, the wavelengths of the emitted X-rays are characteristic of the metal used for the target. Furthermore, fine-splitting of the electronic energy levels by spin-orbit coupling means that many transitions are actually multiplets – for example, distinct Kα_1 and Kα_2 transitions occur from the different levels of the $2p$ shell.

The high intensities and precise wavelengths of characteristic radiation, particularly from the Kα transition, are utilised for diffraction experiments. Absorbing filters and crystal monochromators within the diffractometer are used to select a specific wavelength from the range produced by the source. Cu, which emits Kα_1 and Kα_2 radiation with wavelengths of 1.54051 Å and 1.54433 Å respectively, is the metal most commonly used for the target anode, though others can be used when a different wavelength would be preferable.

Powder X-ray diffraction measurements were made in the laboratory using a Bruker D2 Phaser diffractometer with a Cu anode emitting Kα_1 and Kα_2 radiation. The diffractometer was operated at room temperature in Bragg-Brentano geometry, with the sample distributed as a thin layer on a spinning silica plate.

(b) Synchrotron sources

Whilst sealed-tube sources are readily accessible, they suffer from two major limitations. Firstly, the maximum intensity of the X-rays that they can produce is limited by the generation of heat within the target; and secondly, the useable wavelengths are limited to the precise values of characteristic radiation. Synchrotron sources provide an alternative method for generating X-rays that overcomes these limitations.

When charged particles travelling at relativistic speeds undergo an acceleration they lose energy by emitting photons. For example, if the particles are accelerating by following a curved path they emit radiation in the direction tangential to the path. This emission is known as synchrotron radiation, and synchrotron light sources exploit this phenomenon by circulating electrons

around a large storage ring. A storage ring is typically not a perfect circle but a series of straight sections interspersed with bending magnets. At each of these the electrons change direction and emit synchrotron radiation that passes out of the ring and along beamlines for use in experiments. Further arrays of magnets can be positioned within the straight sections of the ring and along the beamlines; these insertions devices, known as wigglers and undulators, cause further emission and can be used to tailor the radiation for different applications.

The use of synchrotron sources to generate X-rays offers many advantages over standard laboratory sources. Synchrotron radiation is incredibly bright, highly polarised and collimated, and emitted in a distribution of energies, such that a highly tuneable wavelength can be used for experiments. These properties make synchrotron radiation a powerful probe for the study of the structure of materials *in situ* under non-ambient or variable conditions – high-energy synchrotron X-rays can penetrate through the sample environments used to control temperature and pressure, whilst their high intensity facilitates rapid data collection.

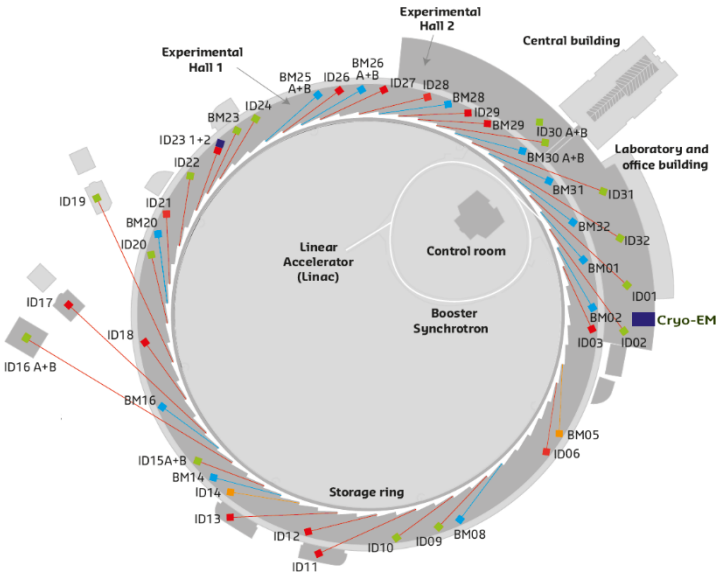

Figure 2.6: Floorplan of the European Synchrotron Radiation Facility, showing the main components of the synchrotron source and the beamlines available in 2017. Figure reproduced from Ref. 87.

The European Synchrotron Radiation Facility (ESRF) in Grenoble, France, is a third-generation synchrotron source (Figure 2.6). Upon production, electrons are

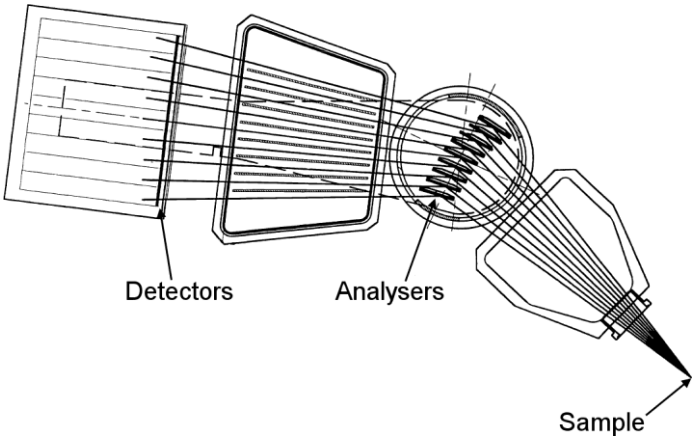

Figure 2.7: The multianalyser stage detector used at ESRF beamline ID22. Diffracted radiation strikes one of nine analyser crystals before entering a corresponding detector. Figure reproduced from Ref. 88.

accelerated in a linear accelerator and a booster synchrotron to an energy of 6 GeV, upon which they pass into the storage ring, which is comprised of 32 sections and is 844 m in diameter. The X-rays produced by these electrons as they circulate the storage ring are directed to 42 beamlines, of which beamline ID22 is dedicated to powder diffraction studies. At ID22 radiation from the storage ring passes through an undulator and then a channel-cut Si monochromator, which is used to select the energy desired for the experiment from a 6-80 keV accessible range. In its standard mode of operation the ID22 diffractometer measures intensity as a function of 2θ using a multianalyser stage detector (Figure 2.7). This comprises a bank of nine individual detectors spaced 2° apart from one another. Each detector is preceded by a Si analyser crystal that stringently defines the angle of diffraction, improving the resolution of the collected diffraction pattern. The use of multiple detectors, which operate simultaneously, offsets the reduction of detected intensity caused by the selectivity of the analyser crystals. All nine detectors are mounted on a single stage so move in unison around the sample being measured, which is mounted in a spinning capillary at the centre of the diffractometer. ID22 can also be configured with a Perkin Elmer XRD1611 two-dimensional detector which, in combination with the high-energy radiation provided by the synchrotron source, allows the high Q_{max} required for total scattering measurements to be accessed.

(c) The diamond anvil cell

The most versatile tool for *in situ* diffraction studies of materials under high pressures is the diamond anvil cell (DAC).[89] The mechanical hardness of diamonds, and their transparency to electromagnetic radiation, make them ideal anvil materials, whilst high-energy, highly-focused beams of synchrotron X-rays are an ideal probe.

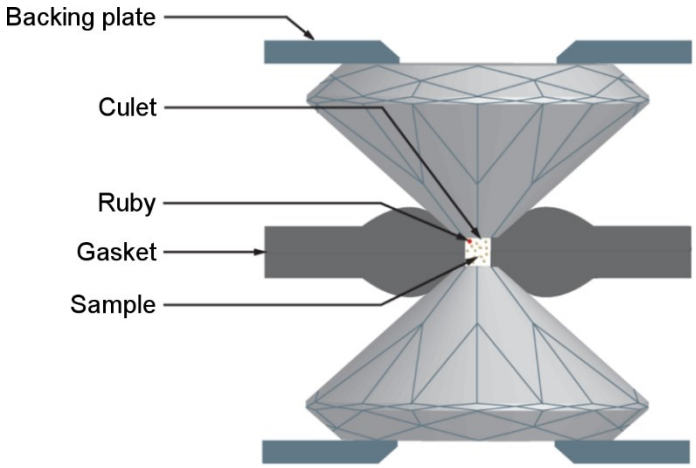

Figure 2.8: Schematic diagram of a typical diamond anvil cell. Force applied to the backing plates is transmitted through the diamonds to deform the gasket and compress the sample.

A typical DAC apparatus is shown in Figure 2.8. Two diamonds are each fixed to a backing plate and mounted in opposition within the cell. Each diamond is cut with a flat tip, called the culet, which is typically less than 0.5 mm in diameter. A thin sheet of metal called the gasket, pre-drilled with a hole into which the sample, pressure-transmitting medium and calibrant are loaded, is placed between the diamonds. Applying a force to the diamonds such that they are pushed together causes the gasket to deform, reducing the volume of the sample hole and applying pressure to its contents. Different DAC designs apply the force to the diamonds through different means. Most commonly the backing plates are connected by screws so can be tightened together; alternative membrane-type designs[90] use a pressurised gas to push the backing plate of one diamond towards the other.

The increase in pressure caused by the deformation of the gasket is applied to the sample through a transmission medium. Ideally this pressure should be applied

non-directionally, necessitating the use of liquid or gaseous mediums. He and other inert gases are commonly used; even when they freeze at sufficiently high pressures, they have a low shear strength so maintain a quasi-hydrostatic pressure distribution. They are also unlikely to react with the material under investigation.

The *in situ* pressure within the DAC can be determined by enclosing a calibrant substance with the sample. The most widely-used calibrant is ruby, which exhibits an optical fluorescence that is strong enough to be easily detected by a spectrometer. The frequency of the fluorescent emission is pressure-dependent, so its measurement from a ruby enclosed in the DAC allows the *in situ* pressure to be determined.[91]

Synchrotron X-rays are the optimal probe for the collection of diffraction patterns from a sample held in a DAC. Their high energies allow them to penetrate the diamonds without being significantly absorbed and, as the components of the cell limit the maximum 2θ to which scattering can be measured, also allow high-Q scattering to be accessed. Furthermore, as the volume of sample within the cell is small, highly-focused synchrotron beams allow the sample to be targeted. This can result in a different problem – that the illuminated sample is too small to realise a good powder average – but this can be minimised by using a two-dimensional detector to measure complete diffraction rings. Dedicated synchrotron beamlines, such as ID15B at the ESRF, have beam and detector configurations optimised for the collection of diffraction data using DACs.

(d) Neutron sources

Neutrons are produced for research use at two different types of sources.

Reactor sources make use of the neutrons that are released by the fission of uranium fuel. These neutrons can have energies that are too high to be useful, so they are passed through a moderator; the final distribution of energies is determined by the moderator material and its temperature. The instruments at

reactor sources are equipped with crystal monochromators that allow a single wavelength of neutrons to be selected from the polychromatic beam.

The Institut Laue Langevin (ILL) in Grenoble, France, is a reactor neutron source with a thermal power of 58 MW. Neutrons are produced with a raw flux of 1.5×10^{15} $s^{-1}cm^{-2}$ and are distributed to 49 instruments. One of these is IN6 (Figure 2.9), a time-of-flight spectrometer optimised for quasi-elastic scattering studies. An assembly of three pyrolytic graphite monochromators selects low-energy neutrons, of a particular incident wavelength between 4 Å and 6 Å, that are sensitive to the small energy transfers to be investigated. A Fermi chopper breaks the continuous incident beam into pulses, and the neutrons in each pulse are scattered by the sample towards a bank of ^{3}He detectors. By measuring the scattering angle and the time taken for the neutrons in each pulse to reach the detectors, $S(\mathbf{Q}, E)$ can be determined.

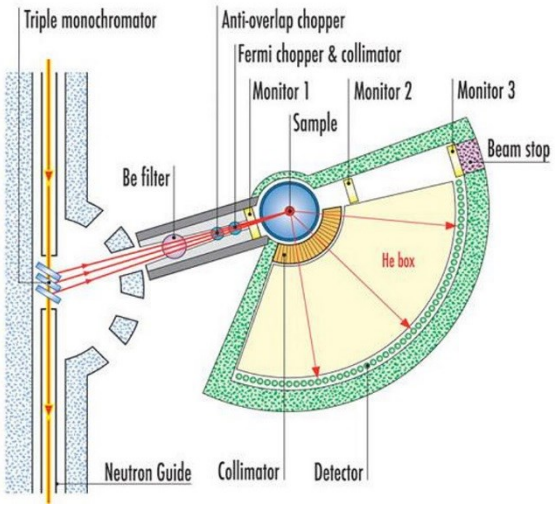

Figure 2.9: Schematic diagram of the neutron spectrometer IN6 at the ILL. Figure reproduced from Ref. 92.

The broad spectrum of neutron wavelengths available at a reactor source makes them highly versatile. However, they suffer from a significant limitation – the maximum flux of neutrons that they can produce is limited by the generation of heat in the reactor. To overcome this limitation, spallation sources utilise a very different process to produce neutrons. At such a source, a beam of high-energy protons strikes a heavy-metal target, causing the nuclei in the target to lose

neutrons as spall. Moderators are again used to control the energies of the neutrons after their production. However, rather than producing neutrons continuously as reactor sources do, spallation sources utilise a pulsed beam of protons to produce pulses of neutrons. The instruments at spallation sources then exploit this pulsed, polychromatic neutron beam. Different neutrons within each pulse have different energies, so take different lengths of time to travel from the source to the detector. As both the time-of-flight t and the path-length L between the target and detector can be measured to a high accuracy, the velocity of the different neutrons in a pulse can be determined. The de Broglie equation relates a particle's velocity to its wavelength, and Bragg's law relates the wavelength to the d-spacing of crystallographic planes, hence

$$d_{hkl} = \frac{ht}{2mL\sin\theta} \qquad \textbf{(2.36)}$$

and a diffraction pattern of intensity as a function of time-of-flight can be collected using a detector at a fixed scattering angle 2θ. The resolution $\Delta d/d$ of the diffraction pattern is dependent on the uncertainties in t, L and θ

$$\frac{\Delta d}{d} = \left[\left(\frac{\Delta t}{t}\right)^2 + \left(\frac{\Delta L}{L}\right)^2 + (\Delta\theta\cot\theta)^2\right]^{½} \qquad \textbf{(2.37)}$$

As such, the finest resolution is obtained when the path-length is long and the detector is placed at a backscattering position with 2θ close to 180°.

The ISIS neutron and muon source at the Rutherford Appleton Laboratory, UK, is a spallation source. Protons are accelerated to 800 MeV and released in 50 Hz pulses, which collide with tungsten blocks in two separate target stations to produce neutrons. The High Resolution Powder Diffractometer (HRPD), which uses neutrons moderated by liquid methane cooled to 90 K, is positioned at the end of a 96 m flight-path. ZnS-scintillator detectors are positioned at 2θ = 168°. The exceptionally long flight-path and high-angle backscattering detectors combine to give a very fine $\Delta d/d \approx 6 \times 10^{-4}$ that allows subtle structural distortions to be identified.

2.3: Magnetism

2.3.1: Principles of magnetism

All electrons have a magnetic moment μ that arises from the orbital angular momentum L and spin angular momentum S that they possess. The value of L depends on the orbital that the electron is occupying, and is analogous to the magnetic field generated by an electrical current moving in a circular coil, whilst S is an intrinsic property that has the same magnitude for all electrons. If an atom has an electron configuration with unpaired electrons, the atom itself has a magnetic moment – this can be considered as the sum of the orbital and spin angular momenta for all the unpaired electrons, which combine through spin-orbit coupling to give a total angular momentum J. The total magnetic moment μ for an atom with unpaired electrons is

$$\mu = g\sqrt{J(J+1)}\mu_{\mathrm{B}} \qquad \textbf{(2.38)}$$

where μ_{B} is the Bohr magneton and g is the Landé g-factor

$$g = \frac{3}{2} + \frac{S(S+1) - L(L+1)}{2J(J+1)} \qquad \textbf{(2.39)}$$

In oxides, particularly those of the first-row transition metals, strong ligand-field effects can quench the orbital angular momentum of the d-electrons such that $L = 0$. Accordingly, Equations 2.38 and 2.39 can be simplified to give the spin-only moment

$$\mu = 2\sqrt{S(S+1)}\mu_{\mathrm{B}} \qquad \textbf{(2.40)}$$

To characterise the behaviour of magnetic materials, the magnitude of the atomic moments and the nature of their interactions must be determined. When an external magnetic field **H** is applied to a material it develops a magnetisation **M**, such that

$$\mathbf{M} = \chi\mathbf{H} \qquad \textbf{(2.41)}$$

where χ is the magnetic susceptibility of the material. DC magnetometry measures the magnetic moment of a sample in a constant field, allowing the

equilibrium magnetisation – and hence χ – to be determined. If the mass of the measured sample and the molar mass of its composition are known, the molar susceptibility can be calculated. The magnitude and sign of χ, and how it varies with temperature, characterise different magnetic behaviours.

All materials, even those without unpaired electrons, exhibit diamagnetism. When a magnetic field is applied to a material its electrons precess around the field, inducing currents that generate a magnetic moment in opposition to the applied field. Consequently, diamagnetic susceptibilities are negative and temperature-independent; however, as their magnitudes are on the order of 10^{-6} emu mol^{-1}, they are normally negligibly small in comparison to the susceptibilities arising from unpaired electrons.

Paramagnetic behaviour is found when unpaired electrons give atoms a magnetic moment but the moments of different atoms do not interact with one another. In the absence of an applied field thermal motion randomises the orientations of the different moments. However, if a field is applied the moments will align with it, resulting in a positive susceptibility that is inversely proportional to temperature

$$\chi = \frac{C}{T} \qquad \textbf{(2.42)}$$

This relationship is known as the Curie law. In practice, few materials are perfect paramagnets with completely non-interacting spins. Interactions can be accounted for by generalising Equation 2.42 to the Curie-Weiss law

$$\chi = \frac{C}{T - \theta} \qquad \textbf{(2.43)}$$

If the spins interact ferromagnetically the Weiss temperature θ is positive, and if they interact antiferromagnetically θ is negative. The Curie constant C is determined by the effective moment μ_{eff} of the material

$$C = N\frac{N_A {\mu_B}^2 {\mu_{eff}}^2}{3k_B} \qquad \textbf{(2.44)}$$

where N_A is Avogadro's constant, k_B is Boltzmann's constant, and N is the number of magnetic atoms *per* formula unit. If the spin-only approximation holds, the

measured μ_{eff} can be used with Equation 2.40 to determine the number of unpaired electrons in the configuration of the magnetic atom. However, if a system has thermally-accessible excited magnetic states its susceptibility may deviate from Curie-Weiss behaviour. Temperature-independent Van Vleck paramagnetism arises when Zeeman splitting, caused by the applied magnetic field, or spin-orbit coupling, caused by unquenched orbital angular momentum, generate thermally-accessible excited states that mix into the ground state and contribute to the total susceptibility.

Thermal disordering causes the spins of atoms with unpaired electrons to behave paramagnetically at high temperatures. However, spins interacting ferro- or antiferro-magnetically should establish long-range ferro- or antiferro-magnetic order when the temperature is sufficiently low. The critical temperature for such ordering is known as the Curie temperature T_C for ferromagnetic order and the Néel temperature T_N for antiferromagnetic order, and in an ideal Curie-Weiss system is given by the magnitude of θ. Dramatic changes of susceptibility accompany such transitions. In a ferromagnet, the spins in domains of the material align in parallel and develop a spontaneous magnetisation below T_C. If the material is cooled through T_C in an applied magnetic field, the magnetisations of different domains will all align with the field and the susceptibility will increase up to the saturation value of all moments being aligned. This increase is less if the sample is cooled in the absence of an applied field, as the magnetisations of different domains will be randomly orientated and can cancel one another out. In an antiferromagnet the antiparallel alignments of the spins means there is no net magnetisation, so the susceptibility will decrease to zero below T_N whether or not a field is applied.

In a geometrically frustrated system it is impossible to satisfy the ordering interactions between all of the different moments. In some such systems long-range order can be established but with significant hindrance, often evidenced by the ordering temperature being much smaller than the magnitude of the Weiss temperature. In other frustrated systems, the inability to establish conventional long-range order can result in more exotic magnetic ground states being

established. One such state is the spin glass, which requires magnetic exchange interactions to be both frustrated and disordered. A spin-glass state is established below a transition temperature at which the spins freeze with their orientations randomly aligned. Below the freezing temperature the susceptibility of a spin glass shows little temperature-dependence if cooled in an applied field but decreases if cooled in the absence of a field, resulting in a cusp at the freezing temperature. Neutron diffraction can help distinguish antiferromagnetic and spin-glass states; the evolution of magnetic Bragg peaks at temperatures below T_N evidences the periodic ordering of spins in the former, whereas in the latter the spins are randomly oriented and diffraction is purely nuclear.

When a paramagnet transitions to a ferromagnetic, antiferromagnetic or spin-glass state, each magnetic atom retains its local moment. However, when magnetic cations form orbital molecules, the unpaired electrons that give rise to each local moment become paired in a covalent bond. The magnetic susceptibility of an orbital molecule state cannot, therefore, be described in terms of localised moments. Instead, each orbital molecule is a magnetic cluster, with the susceptibility of the system described in terms of the spin S of the whole cluster rather than spins of the constituent atoms.[93] In a simple dimer of two spin-½ atoms, the interaction between the spins is described by the spin coupling constant J. When $J < 0$ the coupling is antiferromagnetic, so the cluster has a spin-singlet ($S = 0$) ground state and a spin-triplet ($S = 1$) excited state. Alternatively, when $J > 0$ the coupling is ferromagnetic and the relative energies of the two states are reversed. The magnitude of J is proportional to the strength of the interactions, which also determine the energy gap between the singlet and triplet states of the dimer. The magnetic susceptibility of a system comprised of such dimers is therefore temperature-dependent, varying according to the thermal population of the two states, and is described by the Bleaney-Bowers equation

$$\chi = \frac{2N_A g^2 {\mu_B}^2}{3k_B T}\left[\frac{1}{1+\frac{1}{3}\exp\left(\frac{-2J}{k_B T}\right)}\right] \qquad \textbf{(2.45)}$$

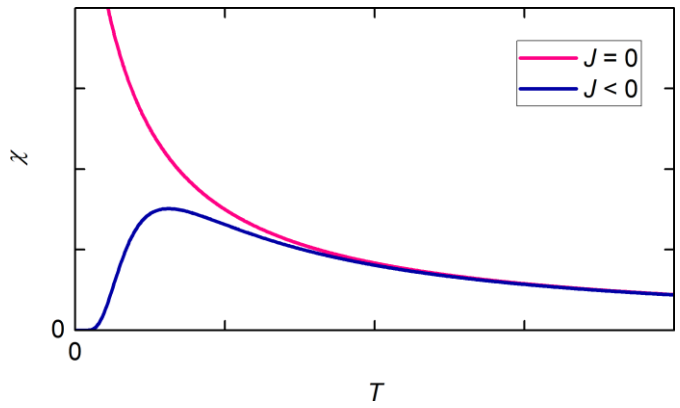

Figure 2.10: Magnetic susceptibilities calculated for a spin-½ dimer system using Equation 2.45. If the spins are uncoupled (J = 0) the susceptibility follows the Curie-Weiss law of Equation 2.43, but when dimers form through antiferromagnetic coupling (J < 0) the susceptibility is 0 at 0 K, increases as the ferromagnetic excited state becomes thermally populated, and tends to Curie-Weiss behaviour in the high-temperature limit.

This description is specific to spin-½ dimers but provides a basis for a general understanding the magnetic susceptibility of orbital molecule systems. Just as the electrons paired in the bonding orbitals of covalent molecules do, the paired electrons in orbital molecule bonds have antiparallel spins.[25] Orbital molecules therefore have a spin-singlet ground state, so a system of many orbital molecules has χ = 0 at 0 K in accordance with Equation 2.45 (Figure 2.10). As the temperature is raised an increasing proportion of these singlet clusters are excited to their triplet state, and χ increases correspondingly. In the triplet state the electrons cannot be paired in a bonding orbital, so this excitation corresponds to the thermal decomposition of the orbital molecules. For a system of orbital molecules than consist of more than two atoms, several increasingly excited states that correspond to molecules with an increasing number of broken bonds can be populated. Finally, in the high-temperature limit, Equation 2.45 becomes the Curie-Weiss law (Equation 2.43) with C = ¾ and $\theta = J/2k_B$. In other words, this limit corresponds to the breaking of all orbital molecule bonds such that their constituent cations behave paramagnetically.

2.3.2: SQUID magnetometry

The most sensitive method for measuring the magnetisation of a sample utilises a Superconducting Quantum Interference Device (SQUID).[94] A SQUID comprises two superconducting components connected by thin insulating layers to form a ring. When the Cooper pairs on each side of these layers, which are known as Josephson junctions, have phase coherence the superconducting current can tunnel through them. SQUIDs are used for magnetometry because a superconducting current flowing through a ring encloses a magnetic field with a quantised magnetic flux. A change to this flux induces a current that opposes the change, giving rise to a phase difference and hence a voltage across the junctions. Measurement of this voltage allows the amount of flux passing through the SQUID to be deduced.

In a SQUID magnetometer the sample is positioned inside a superconducting magnet, away from the SQUID itself. This magnet is used to generate a uniform applied field within a set of superconducting pickup coils. During a measurement the sample is moved through these pickup coils, within which the magnetisation of the sample induces a current. Superconducting circuitry connects the pickup coils to a second set of coils, so the current induced in the former generates a magnetic field passing through the latter. The second set of coils are aligned with the SQUID, so the generated field affects the flux passing through the SQUID and hence the measured voltage across the Josephson junctions.

A Quantum Design SQUID MPMS-XL was used to make all of the magnetometry measurements in this Thesis.

Chapter 3: Orbital molecules in AlV_2O_4 and GaV_2O_4

3.1: Introduction

Numerous vanadium oxides have electronic ground states in which orbital molecules are formed.[27] Dimers, such as the V_2^{8+} species found in VO_2, are most common, and trimers, like the V_3^{9+} clusters in $LiVO_2$, form in several systems. Larger orbital molecules, however, have only been reported in one material. AlV_2O_4 is a spinel that adopts the normal cubic structure at high temperatures, but becomes rhombohedrally distorted below 700 K.[95] The average vanadium valence in this material is +2.5 and the structural distortion was originally attributed to charge ordering, hence the transition temperature is labelled T_{CO}. However, as this valence corresponds to an average electron configuration of $t_{2g}^{2.5}$ orbital ordering is also important, and V_7 'heptamer' orbital molecules (Figure 3.1) have been reported to form in rhombohedral AlV_2O_4.[66]

The ground state structure of AlV_2O_4 has $R\bar{3}m$ symmetry and is formed by the distortion of a 2 × 2 × 2 cubic supercell. In the unit cell there are three vanadium crystallographic sites: V1, with fractional coordinates (0, 0, 0); V2, at (0, 0, ½); and V3, at (*x*, -*x*, *z*). The displacement of the V3 site in this structure forms an ordered array of heptamers as shown in Figure 3.1, with short (2.61 and 2.81 Å) V-V bonds within each heptamer and much longer separations (3.04 and 3.14 Å) between them. The heptamers form an ordered array such that each comprises a central V2-site atom that is between two equidistant triangles of V3-site atoms, whilst the V1 site is occupied by a non-bonding cation.

The magnetic susceptibility of AlV_2O_4 has both spin-singlet and paramagnetic contributions below T_{CO}, which corroborates the structural description of the ground state and allows the charge distribution to be assigned as

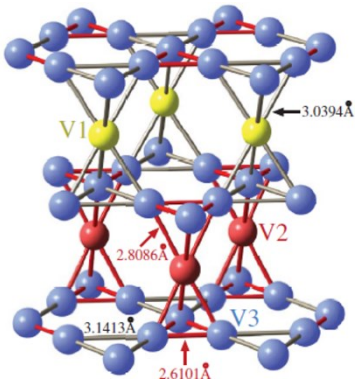

Figure 3.1: The vanadium sublattice of rhombohedral AlV_2O_4, with V_7 orbital molecules indicated by red bonds. Figure reproduced from Ref. 66.

$Al_4[V_7^{17+}V^{3+}]O_{16}$.[66] Each heptamer is a spin-singlet, formed by the pairing of 18 *d*-electrons in nine bonding orbitals. Six of these bonds span two vanadium centres and are electron-precise, and three span three centres and are electron-deficient, hence there are two different V-V bond distances within each heptamer. This spin-singlet character has been confirmed by ^{51}V-NMR measurements.[96] For every heptamer there is also a non-bonding, paramagnetic V^{3+} cation.

Some previous studies have attempted to understand the nature of the V-V interactions in AlV_2O_4, and why such large orbital molecules form in this material. Although theoretical work has highlighted the importance of strong t_{2g} σ-bonding interactions to the formation of the heptamers in rhombohedral AlV_2O_4,[97] experiments have shown that the bonding is easily perturbed: the long-range charge- and orbital-ordering that forms the heptamer state is supressed by substituting 5% V for Cr,[98] or by applying pressures over 21 GPa.[99] Furthermore, although discontinuities are seen in the susceptibility and resistivity of AlV_2O_4 upon crossing the 700 K transition temperature, their magnitude is small – the resistivity changes by a factor of 1.5,[95] in comparison to the order-of-magnitude changes seen in VO_2 and $LiVO_2$. Since the ground state properties are determined by the pairing of *d*-electrons in V-V bonds, the lack of a significant change with the structural distortion suggests that some bonding may still be present in the high-temperature phase. As the atomic pair distribution function (PDF) should clearly reveal the short V-V distances characteristic of orbital molecule bonding whether

or not they have long-range order, X-ray total scattering has been used to study the structure of AlV_2O_4 for the first time.

An additional limitation to the study of the formation and behaviour of large orbital molecules is the lack of any other materials in which they are found. This motivated the synthesis of GaV_2O_4 which, being isoelectronic with AlV_2O_4, was anticipated to have the same heptamer orbital molecules and therefore provide a second system in which they could be studied.

3.2: Experimental

3.2.1: Synthesis

Powder samples of AlV_2O_4 and GaV_2O_4 were synthesised by high-temperature solid-state reactions. Powdered starting materials in the stoichiometric ratio were ground together, pressed into pellets, and sealed in evacuated quartz ampoules for heating. A 1 g sample of AlV_2O_4 was prepared from Al (Alfa Aesar, 99.5%), V_2O_5 (Alfa Aesar, 99.6%) and V_2O_3, made in advance by reducing V_2O_5 under flowing H_2 at 900 °C. In order to make a high purity sample, three successive heatings were required: 48 hours at 900 °C, 24 hours at 1000 °C, and 24 hours at 1150 °C, with intermediate regrinding and pelleting. A 3 g sample of GaV_2O_4 was synthesised from Ga_2O_3 (Sigma Aldrich, 99.99%), V (Alfa Aesar, 99.5%) and V_2O_5 by a single heating of 48 hours at 1000 °C.

3.2.2: Structural characterisation

Lab X-ray diffraction patterns were collected using a Bruker D2 Phaser diffractometer to confirm that the syntheses of AlV_2O_4 and GaV_2O_4 had reached completion. Subsequently, high-energy X-ray total scattering data were collected for both materials using the beamline ID22 at the ESRF. Samples were loaded into quartz capillaries of 0.7 mm diameter and heated from 300 K to 1100 K using a hot air blower. Data were collected using 60 keV radiation (λ = 0.206547 Å) and the two-dimensional detector. 201 exposures were collected and averaged to give

a total scattering pattern for each temperature step. Rietveld analysis of these patterns was carried out using GSAS.[77] Additionally, after suitable background corrections had been made, the data were converted into structure functions $S(Q)$ and hence transformed to PDFs $G(r)$ using PDFgetX3,[83] for momentum transfers $0.5 \leq Q$ (Å^{-1}) ≤ 25.8. Structural models were refined against $G(r)$ over the interatomic distance range $1.5 \leq r$ (Å) ≤ 12 using PDFgui,[84] including simulation of termination ripples.

Further diffraction experiments were employed to accurately characterise the crystallographic structure of GaV_2O_4. High-resolution powder X-ray diffraction data were also collected at ID22, using the multianalyser stage detector and 27.5 keV radiation (λ = 0.450842 Å). Measurements were made on warming, with the sample loaded in a 0.5 mm diameter borosilicate capillary and heated from room temperature to 500 K using a nitrogen cryostream. Powder neutron diffraction data were collected using the HRPD beamline at ISIS. 2.7 g of the sample was loaded into a vanadium can in a furnace and, after heating to 550 K, data were collected on cooling to room temperature using the 168° detectors. All diffraction data were analysed by the Rietveld method using GSAS.

3.2.3: Property measurements

The magnetic behaviour of AlV_2O_4 and GaV_2O_4 was measured using a Quantum Design SQUID MPMS-XL. DC magnetisation measurements were made for both materials over the temperature range 2-300 K in an applied field of 100 Oe, under zero-field cooled and field cooled conditions. Additionally, the magnetisation of GaV_2O_4 was measured on warming from 300 to 600 K in an applied field of 5000 Oe.

The electrical resistance of a sintered pellet of GaV_2O_4 was measured over the temperature range 300-800 K by the four-probe technique, using in-house apparatus to maintain an evacuated sample environment during heating.

3.2.4: Quasi-elastic neutron scattering

Quasi-elastic neutron scattering (QENS) spectra were collected for GaV_2O_4 using the time-of-flight spectrometer IN6 at the ILL. The same sample as used for the neutron diffraction experiment was loaded in a niobium can, and a furnace was used to heat the sample from 400 K to 1100 K. The incident neutrons had wavelength λ = 5.12 Å. Eight spectra were collected at each temperature step and averaged scattering functions $S(Q,E)$, where E is the energy transfer, were generated with vanadium normalisation and empty-can background corrections.

3.3: Results and discussion

3.3.1: Ground state structure of AlV_2O_4

Initial characterisation showed the synthesised sample of AlV_2O_4 to be consistent with the reported description. The Bragg peaks in the lab X-ray diffraction pattern could be indexed with a unit cell of the correct $R\bar{3}m$ symmetry and Rietveld refinements gave hexagonal lattice parameters a_H = 5.7536(3) Å and c_H = 28.8460(16) Å, which are comparable to the literature values a_H = 5.75148(3) Å and c_H = 28.85407(14) Å. A minor impurity phase of Al_2O_3, with weight fraction 4.1%, was also identified. The magnetic susceptibility (discussed in detail in Section 3.3.4) also shows the expected behaviour, with paramagnetic and spin-singlet contributions. However, the heptamer model – deduced by Rietveld analysis,[66] and thus a description of the average structure of the ground state – does not give a good fit to the 300 K PDF (Figure 3.2(a)), which describes structural correlations on the local scale. V-V nearest-neighbour distances contribute to the PDF in the region of r from 2.5 to 3.2 Å (the shaded region in Figure 3.2(a)), so the particularly poor fit of the heptamer model to this region of the PDF indicates that the heptamer description of local V-V bonding interactions is incorrect.

Modifications to the heptamer structural model were therefore explored, and it was found that the fit to the PDF could be brought into good agreement by

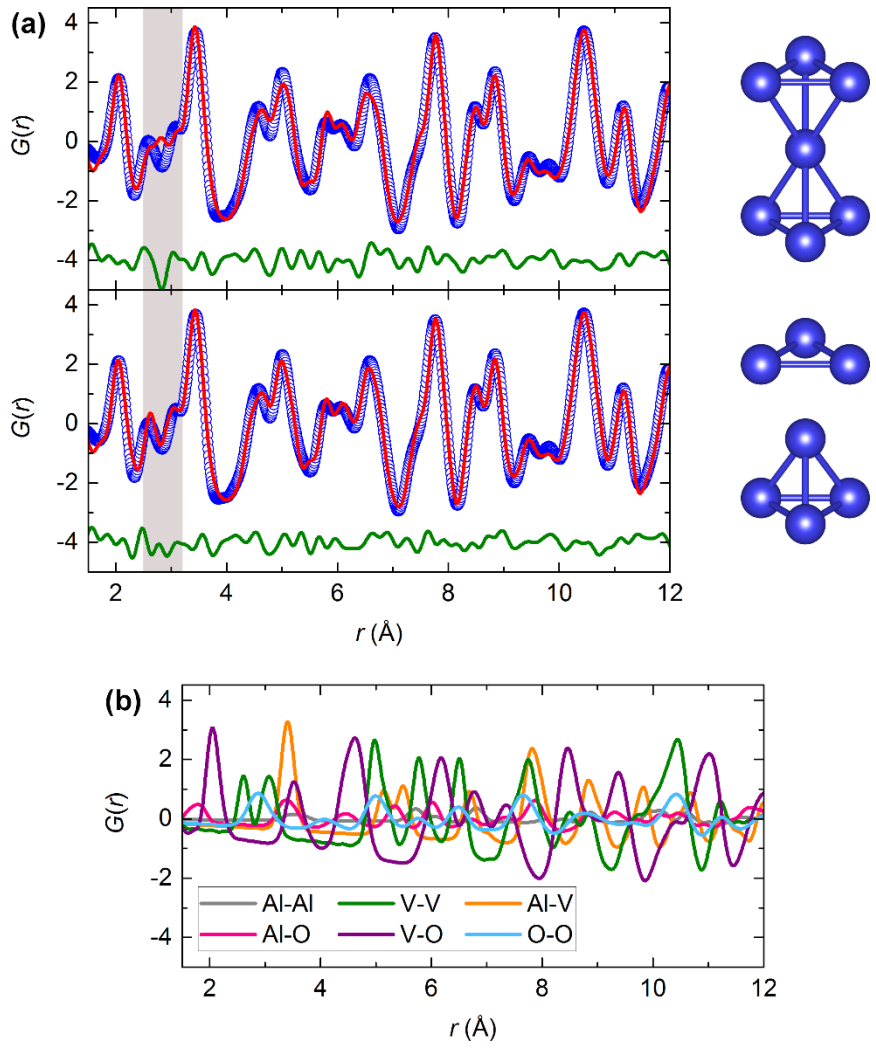

Figure 3.2: (a) Fits of the reported $R\bar{3}m$ heptamer model (upper, R_w = 16.3%) and the $R3m$ model with a displaced V2 site (lower, R_w = 13.6%) to the 300 K PDF of AlV_2O_4. This displacement greatly improves the fit to the first V-V coordination shell (the shaded region from 2.5 to 3.2 Å), and the species formed by V-V nearest-neighbour interactions in each model are shown. **(b)** The partial PDFs that comprise the fitted $R3m$ model.

displacing the V2 site along *z*. This displacement moves the central atom of each heptamer towards one of the triangular end-faces and changes the V-V nearest-neighbour distances such that the short separations (< 2.70 Å) characteristic of orbital molecule bonding define triangular V_3 clusters and tetrahedral V_4 clusters. Much longer separations (> 2.90 Å) are found between these smaller clusters. The improved fit to the 300 K PDF by making this structural modification is also shown in Figure 3.2(a). The partial PDFs in Figure 3.2(b), which reveal the contributions of different correlations to the total PDF, show that V-V correlations

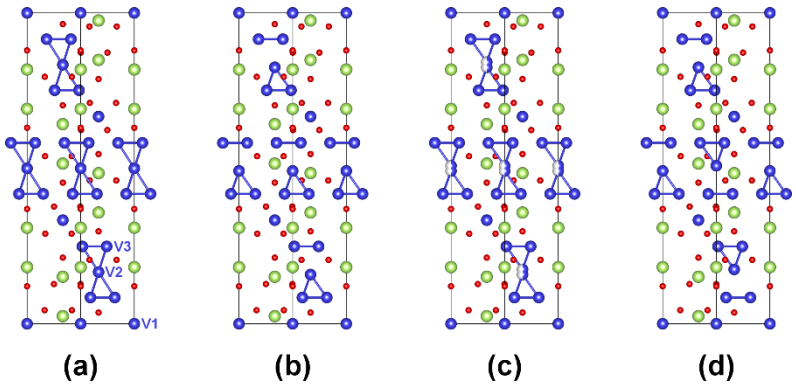

Figure 3.3: Structural models for the ground state of AlV_2O_4. In each the unit cell is projected on the (110) plane with the *c*-axis vertical; Al (green), V (blue) and O (red) atoms are shown, as are short (< 2.90 Å) V-V distances. **(a)** The previously reported model, which has $R\bar{3}m$ symmetry and features ordered V_7 clusters. The three symmetry-independent V sites are labelled. **(b)** The $R3m$ model used for PDF fitting, in which ferroelectric displacements of the V2 site atoms result in V_3 and V_4 clusters with long-range order. **(c)** The $R\bar{3}m$ model with a split V2 site, representing disordered antiferroelectric displacements, that best describes the average ground state structure. **(d)** One possible local arrangement corresponding to this disordered average.

dominate in the 2.5-3.2 Å region, with a clear distinction between short intra-cluster and long inter-cluster distances.

That each 'heptamer' in the average structure of rhombohedral AlV_2O_4 comprises a trimer-tetramer orbital molecule pair can also be seen through Rietveld analysis of the total scattering data. The unit cell of the reported heptamer structure is shown in Figure 3.3(a). Previous structural refinements using this model have identified that the V2 site has highly anisotropic thermal parameters,[66] indicative of a displacement of this site along *z* from its reported position at (0, 0, ½). Fits of different structural models to the 300 K diffraction pattern are shown in Figure 3.4, and although the heptamer $R\bar{3}m$ model (Figure 3.3(a)) gives a reasonable fit (Figure 3.4(a)), improvements are made by displacing the V2 site such that ordered heptamers in rhombohedral AlV_2O_4 become ordered trimer-tetramer pairs. There are, however, two different configurations that the orbital molecules within each pair can adopt, according to whether the V2 atom displaces to $z < 0.5$ or $z > 0.5$. There are therefore different possible ground state structures, in which

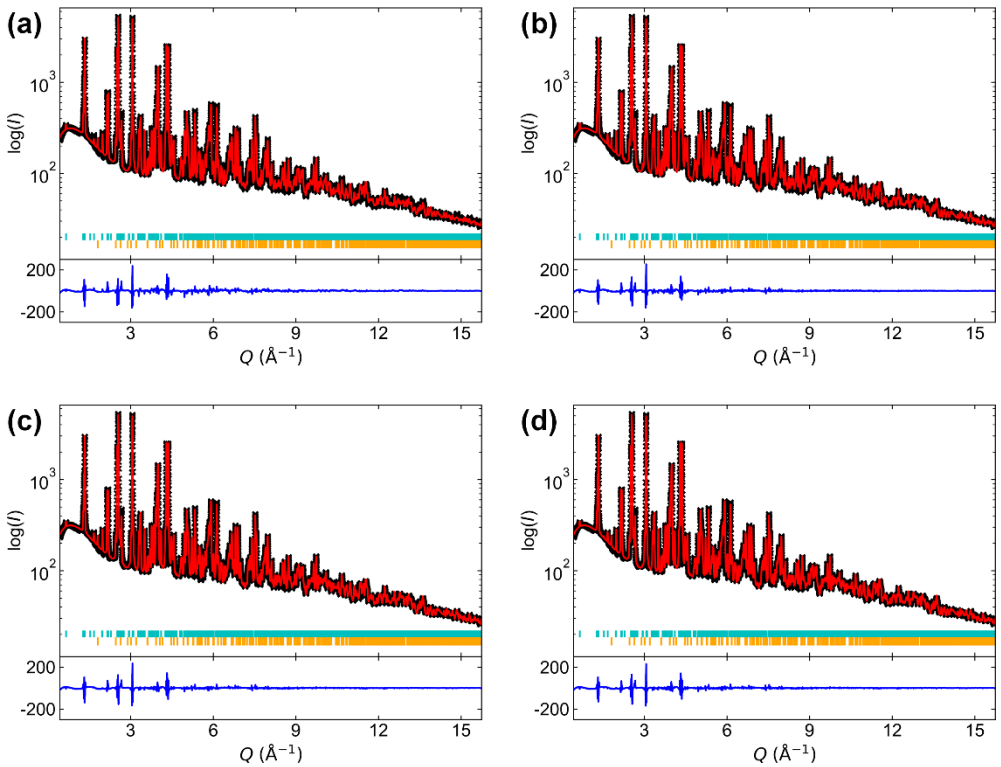

Figure 3.4: Rietveld fits of different rhombohedral structural models to the 300 K total scattering pattern of AlV_2O_4. Tick marks correspond to AlV_2O_4 (blue) and an Al_2O_3 impurity phase (orange). **(a)** The previously reported $R\bar{3}m$ model with V_7 orbital molecules (R_w = 5.53%). **(b)** The $R3m$ model used for PDF fits, with ordered V_3 and V_4 orbital molecules (R_w = 4.33%). **(c)** The $R\bar{3}m$ model with a split V2 site, corresponding to ordered V_3-V_4 pairs (R_w = 4.16%). **(d)** The split-site $R3m$ model, in which the occupancies of the split V2 sites can be refined (R_w = 4.11%).

different proportions of the trimer-tetramer pairs adopt each configuration, and as these correspond to different average structures they can be distinguished by Rietveld analysis. To aid refinement stability all models were fitted using a single isotropic thermal factor U_{iso} for the crystallographic sites occupied by atoms of each of the three elements present.

One possibility is for all trimer-tetramer pairs to adopt the same configuration, giving the structure shown in Figure 3.3(b) in which the trimers and tetramers have long-range order. As this is achieved by the V2 atoms of every pair displacing in parallel in the same direction it is a ferroelectric structure, which requires the space group symmetry be lowered to $R3m$. As both $R3m$ and $R\bar{3}m$ diffraction patterns have the same systematic absences this does not change which

reflections are observed, but as the different symmetries allow different atomic displacements they can be distinguished by refinement against the intensities of those reflections. The Rietveld fit using this $R3m$ model is shown in Figure 3.4(b).

A structural model with antiparallel V2 site displacements, such that half of the trimer-tetramer pairs adopt one configuration and half the other, was also considered, and gives the fit in Figure 3.4(c). As the V2 site atoms occupy a triangular lattice long-range antiferroelectric ordering is inhibited by frustration, so these displacements are modelled by maintaining $R\bar{3}m$ symmetry and splitting the V2 site. This gives the average structure shown in Figure 3.3(c), in which pairs of V_3 and V_4 orbital molecules have long-range order but the configurations adopted by different pairs are disordered. One possible set of local configurations corresponding to this average structure is shown in Figure 3.3(d).

Both the $R3m$ (R_w = 4.33%) and split-site $R\bar{3}m$ (R_w = 4.16%) models give a better fit to the Bragg intensities of rhombohedral AlV_2O_4 than the original heptamer model (R_w = 5.53%). Finally, a split-site $R3m$ model was also tested (Figure 3.4(d)). The lower symmetry allows the occupancies of the two components of the V2 site to be refined, but as the 0.57(2):0.43(2) occupancy ratio obtained is very close to the 0.5:0.5 ratio of the split-site $R\bar{3}m$ model and the fit is not much improved (R_w = 4.11%), the split-site $R\bar{3}m$ model is taken as the best representation of the ground state structure of AlV_2O_4. That said, the model used to fit the PDFs is the $R3m$ model in which the V2 site displaces with full occupancy (though for the PDF fits, constraints consistent with $R\bar{3}m$ symmetry were applied to all crystallographic sites split by the lowering of symmetry to $R3m$ so that the number of refined parameters was reduced). Both the $R3m$ and split-site $R\bar{3}m$ models feature trimer-tetramer pairs, so the local structural correlations in each are the same; the $R3m$ model was used for PDF fitting as the half-occupied split-site used to model the configurational disorder in the $R\bar{3}m$ model, whilst suitable for describing the average atomic distribution, does not meaningfully represent the local structure.

Previous measurements[66,96] have shown that the orbital molecules in AlV_2O_4 have a spin-singlet ground state. The V_3 trimers and V_4 tetramers that have been

identified must, therefore, be spin singlets. This can be achieved by a charge ordering that allows these smaller orbital molecules to be formed by uniform two-centre two-electron bonding: V^{3+} cations, each with a t_{2g}^2 electron configuration, can form two bonds each to make V_3^{9+} triangles, whilst V^{2+} cations, each with a t_{2g}^3 electron configuration, can bond with three others to form V_4^{8+} tetrahedra. This revises the charge distribution in the ground state of AlV_2O_4 from $Al_4[V_7^{17+}V^{3+}]O_{16}$ to $Al_4[V_4^{8+}V_3^{9+}V^{3+}]O_{16}$.

3.3.2: High-temperature structure of AlV_2O_4

Above T_{CO} = 700 K AlV_2O_4 adopts the normal spinel crystal structure, which has the cubic space group $Fd\bar{3}m$. The Rietveld fit of this model to the 1100 K diffraction pattern is shown in Figure 3.5(a), and it describes an average structure in which mixed-valence $V^{2.5+}$ is represented by a single vanadium crystallographic site and all V-V nearest-neighbour distances are equal. The rhombohedral to cubic structural transition at T_{CO} therefore corresponds to the loss of long-range orbital molecule ordering. This refinement does, however, give an unfeasibly large value of U_{iso} for the vanadium site. An improved fit (Figure 3.5(b)), with an acceptable U_{iso} for the vanadium site, is achieved by letting seven-eighths of the vanadium intensity – representing the proportion of vanadium cations involved in orbital

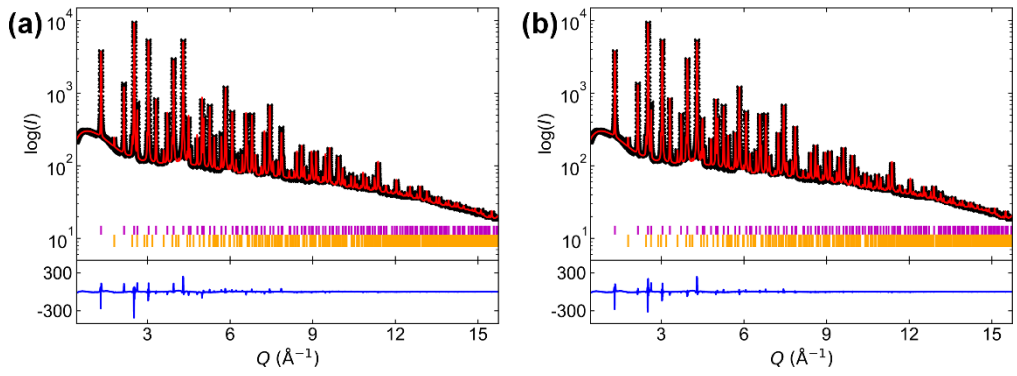

Figure 3.5: Rietveld fits of a cubic average structure to the 1100 K total scattering pattern of AlV_2O_4. Ticks marks correspond to AlV_2O_4 (pink) and Al_2O_3 (orange). **(a)** The normal $Fd\bar{3}m$ spinel structure, which has a single V crystallographic site (R_w = 4.92%). **(b)** A disordered $Fd\bar{3}m$ structure with seven-eighths of the vanadium displaced as a split site away from its ideal position (R_w = 4.24%).

molecule bonding – displace as a split site away from the ideal position that holds the remaining one-eighth. This is indicative of some positional disorder of the vanadium cations in this cubic phase.

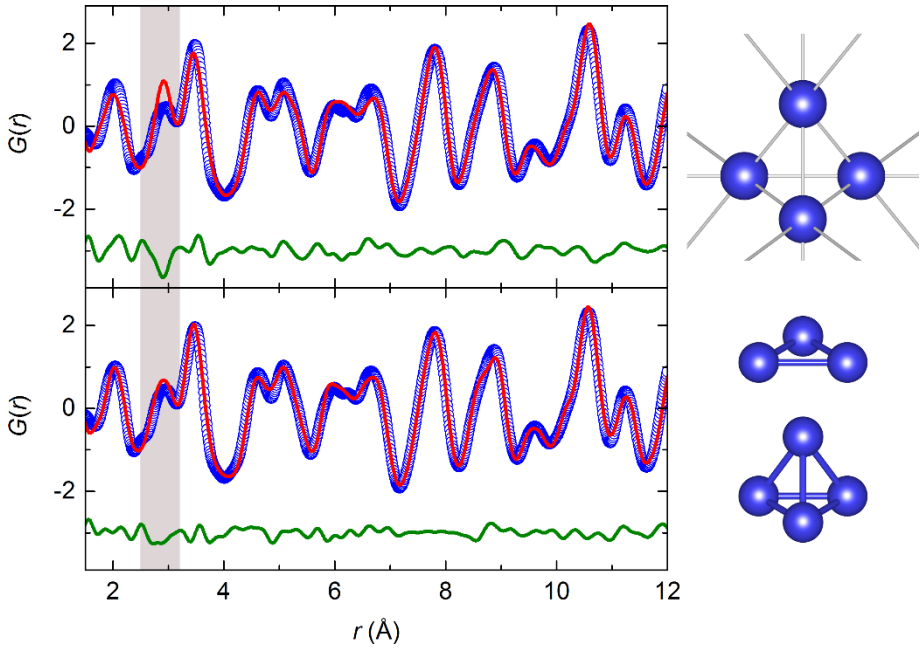

Figure 3.6: Fits of the normal $Fd\bar{3}m$ spinel structure (upper, R_w = 16.6%) and the $R3m$ model used to fit the PDFs below T_{CO} (lower, R_w = 11.6%) to the 1100 K PDF of AlV_2O_4. In the former all V-V nearest-neighbour distances are equal, whilst in the latter orbital molecules are defined. The local vanadium structure in each model is shown.

The PDFs generated from the high temperature scattering data reveal the nature of the local V displacements (Figure 3.6). The uniform spinel structure with a single V-V nearest-neighbour distance gives a poor fit to the 1100 K PDF, particularly in the 2.5-3.2 Å region of the first V-V coordination shell. Instead, a much better fit is given by the $R3m$ model used to describe the ground state structure, implying that local V-V bonding persists into the high-temperature cubic phase even though the structural order of the orbital molecules is lost. The $R3m$ model was subsequently fit to all of the PDFs collected over the 300-1100 K measured temperature range. For the fits to the PDFs collected above T_{CO} the lattice parameters a_H and c_H were constrained in the metrically cubic ratio, where $c_H/a_H = \sqrt{24}$, to be consistent with the lattice of the average structure. Furthermore the displacements of the V2 and V3 sites away from their ideal

spinel positions were constrained to be equal, which was needed for refinement stability. This results in the V2-V3 and V3-V3 bonding distances also being equal. These fits reveal that the V-V nearest-neighbour distances evolve continuously through T_{CO} (Figure 3.7). Even at 1100 K the orbital molecules are well-defined, with a V-V bond distance of 2.78 Å much shorter than the 2.93-3.06 Å inter-cluster distances, even though Rietveld analysis gives a single V-V distance of 2.92 Å in the cubic average structure. The displacement of the V2 and V3 sites that gives this range of V-V distances in the local structure of AlV_2O_4 is 0.09 Å at 1100 K, comparable to the 0.12 Å displacement of the vanadium split-site in the $Fd\bar{3}m$ Rietveld refinement at the same temperature; the displacements decrease smoothly as the temperature increases (Figure 3.8) and their extrapolation

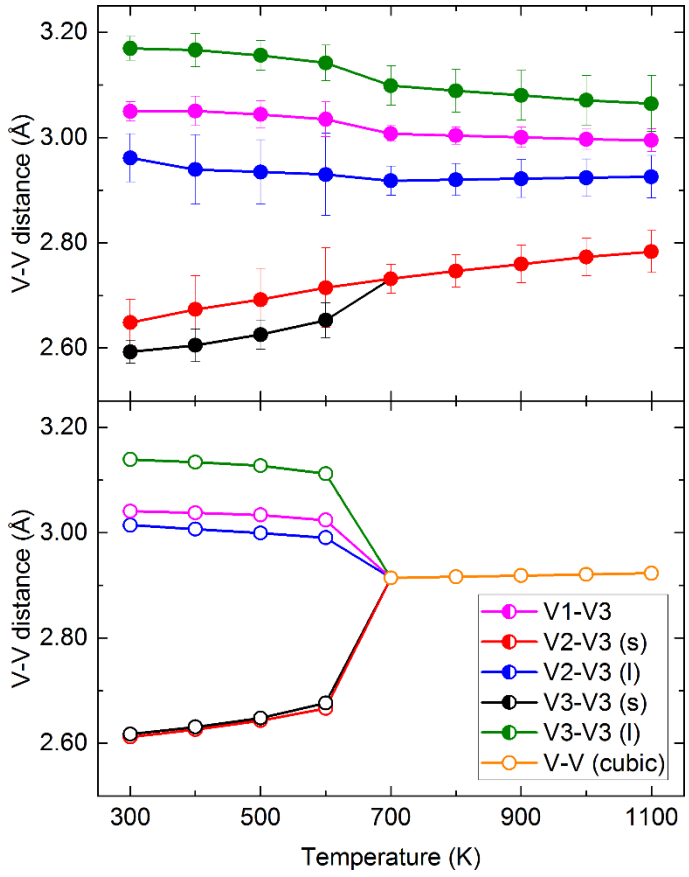

Figure 3.7: Comparison of the V-V nearest-neighbour distances in AlV_2O_4, from PDF (upper) and Rietveld (lower) fits. The distribution of short and long distances determined by the PDF fits evidences the persistence of orbital molecules to 1100 K, but as these are disordered above T_{CO} Rietveld fits of this structure only give the single average V-V distance.

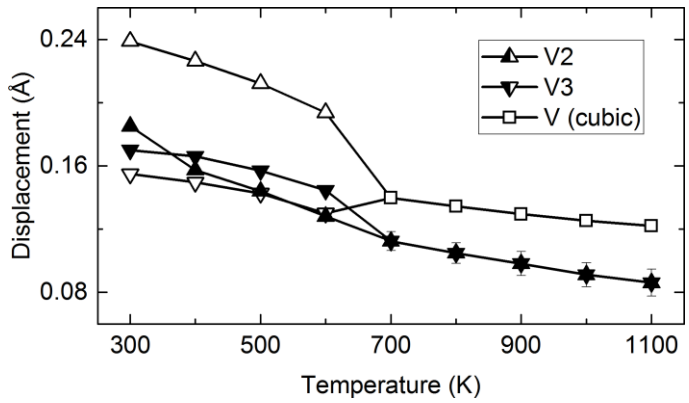

Figure 3.8: Displacements of V atoms away from the positions they would occupy in an ideal spinel structure due to V-V bonding. The smooth decrease through T_{CO} is consistent with the orbital molecules transitioning from an ordered to a disordered state, rather than breaking up. Filled symbols are values from PDF fits using the $R3m$ structural model over the whole temperature range, with the V2 and V3 site displacements constrained to be equal above T_{CO} to aid refinement stability. Open symbols are values from Rietveld fits, which used the split-site $R\bar{3}m$ model below T_{CO} and the split-site $Fd\bar{3}m$ model above T_{CO}.

suggests that zero displacement, corresponding to a uniform spinel structure, would not be reached until well above the ~1400 K synthesis temperature of the material.

The determination of the local structure of AlV_2O_4 by X-ray total scatting and PDF analysis substantially revises the description of the orbital molecules found in this material. The rhombohedral to cubic structural transition at T_{CO} = 700 K does not correspond to the formation and breakup of V_7^{17+} heptamers, but rather the pairwise-order to disorder transition of V_3^{9+} and V_4^{8+} clusters. The details of all refined structural models, for both the low-temperature and high-temperature phases, are provided in Appendix A.

3.3.3: Structural characterisation of GaV_2O_4

GaV_2O_4 is a newly synthesised material. Initial lab powder X-ray diffraction (Figure 3.9(a)) revealed that at room temperature, GaV_2O_4 has a rhombohedral structure like that of AlV_2O_4, with lattice parameters a_H = 5.8519(4) Å and c_H = 29.0467(22) Å. Subsequently, high-resolution X-ray powder diffraction data were

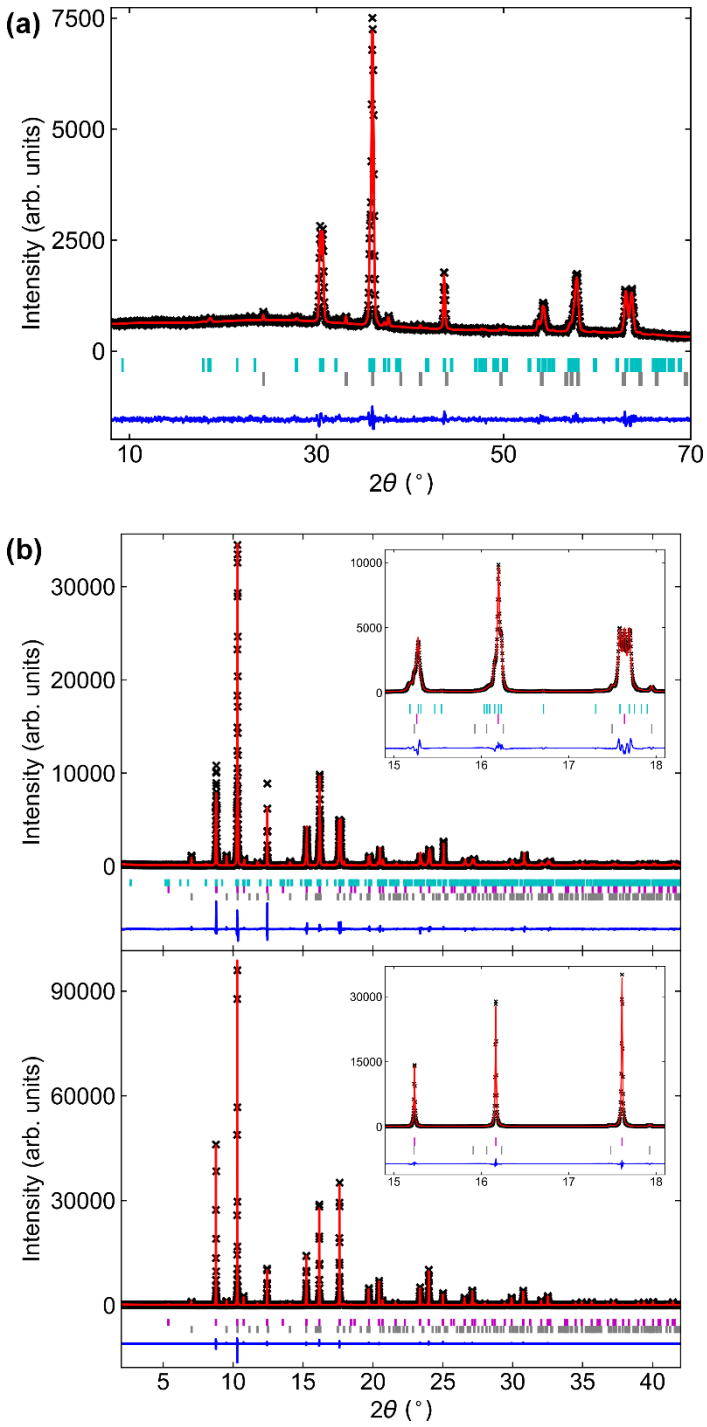

Figure 3.9: Rietveld analysis of GaV_2O_4. Tick marks correspond to rhombohedral GaV_2O_4 (blue), cubic GaV_2O_4 (pink), and V_2O_3 (grey). **(a)** Lab X-ray diffraction, with λ = 1.54051 Å and 1.54433 Å (R_w = 4.7%). **(b)** High-resolution X-ray diffraction patterns, with λ = 0.450842 Å, at room temperature (upper, R_w = 12.3%) and 500 K (lower, R_w = 9.0%). The peak splitting caused by the rhombohedral distortion is evident in the expanded region shown in the insets.

Table 3.1: Structural parameters of rhombohedral GaV_2O_4, from Rietveld refinement against the room temperature powder X-ray diffraction data in Figure 3.9(b). The space group is $R\bar{3}m$, with lattice parameters a_H = 5.86207(4) Å and c_H = 28.98268(37) Å.

Atom	**Site**	***x***	***y***	***z***	**Occ.**	U_{iso} **(Å²)**
Ga1	6*c*	0	0	0.18489(10)	1.0	0.0069(1)
Ga2	6*c*	0	0	0.31051(9)	1.0	
V1	3*a*	0	0	0	1.0	
V2	3*b*	0	0	0.49537(32)	0.5	0.0059(2)
V3	18*h*	0.83981(19)	0.16019(19)	0.41668(9)	1.0	
O1	6*c*	0	0	0.12467(45)	1.0	
O2	6*c*	0	0	0.37487(40)	1.0	0.0103(4)
O3	18*h*	0.83613(70)	0.16387(70)	0.54151(29)	1.0	
O4	18*h*	0.82758(70)	0.17242(70)	0.28884(28)	1.0	

Table 3.2: Structural parameters of cubic GaV_2O_4, from Rietveld refinement against the 500 K powder X-ray diffraction data in Figure 3.9(b). The space group is $Fd\bar{3}m$, with lattice parameter a_C = 8.330016(5) Å.

Atom	**Site**	***x***	***y***	***z***	**Occ.**	U_{iso} **(Å²)**
Ga1	8*a*	0.125	0.125	0.125	1.0	0.0078(1)
V1a	16*d*	0.5	0.5	0.5	0.125	0.0061(1)
V1b	32*e*	0.49086(9)	0.49086(9)	0.49086(9)	0.4375	
O1	32*e*	0.25324(10)	0.25324(10)	0.25324(10)	1.0	0.0110(2)

collected between room temperature and 500 K and reveal the same change of crystal structure as occurs in AlV_2O_4, with the rhombohedral structure converting to the cubic spinel structure upon heating. The split-site $R\bar{3}m$ and split-site $Fd\bar{3}m$ structural models used to describe the average structure of AlV_2O_4 give good Rietveld fits to these data (Figure 3.9(b)), and short V-V distances of ~2.80 Å define ordered pairs of V_3 and V_4 orbital molecules in the rhombohedral phase. A V_2O_3 impurity phase of weight fraction 5.3% was also identified. The refined

structural parameters for rhombohedral GaV_2O_4 at room temperature and cubic GaV_2O_4 at 500 K are given in Table 3.1 and Table 3.2 respectively, and the metal-oxygen bond distances and angles and V-V nearest-neighbour distances in the two phases are given in Appendix B.

The crystallographic transitions in AlV_2O_4 and GaV_2O_4 can be described through the deviation of the lattice parameters a_H and c_H of the rhombohedral unit cell from their metrically cubic values $a_H = a_C/\sqrt{2}$ and $c_H = \sqrt{12}a_C$, where a_C is the lattice parameter of the cubic unit cell. This is observed experimentally as the splitting of cubic Bragg peaks (Figure 3.9(b), insets). Previous characterisation of AlV_2O_4 has determined this transition to be first-order in nature.[95] In magnetite orbital-molecule ordering also occurs below a first-order transition, and below the transition temperature (labelled T_{CO} for consistency with the notation in this Chapter) order parameter-like structural quantities X such as the lattice parameters and root-mean-square displacements vary according to the critical equation

$$X = X_{CO} + (X_0 - X_{CO}) \tanh(W_X t^{½}) \,/\, \tanh(W_X) \qquad \textbf{(3.1)}$$

where X takes values X_0 and X_{CO} at T = 0 and T = T_{CO} respectively, the reduced temperature $t = (T_{CO} - T)/T_{CO}$, and $W_X \approx 2$ is a fitting parameter.[100] The reduced lattice parameters $\sqrt{2}a_H$ and $c_H/\sqrt{12}$ of GaV_2O_4 have been determined from Rietveld refinements against the high-resolution X-ray diffraction patterns and their thermal variation is well-described by Equation 3.1, which establishes T_{CO} = 415 K (Figure 3.10(a)).

The diffraction data also reveal that a proportion of GaV_2O_4 remains cubic below T_{CO}. In polycrystalline magnetite microstructural strain suppresses the Verwey transition in some crystallites,[100] and it is likely that similar strains suppress T_{CO} in some crystallites of GaV_2O_4 – the diffraction peak profiles of rhombohedral GaV_2O_4 were found to be highly asymmetric and were refined using the Stephens model for strain-induced anisotropic broadening,[73] whilst those of the cubic phase have symmetrical profiles. The structural parameters and phase fraction of the residual cubic phase were refined using the split-site $Fd\bar{3}m$ model used for

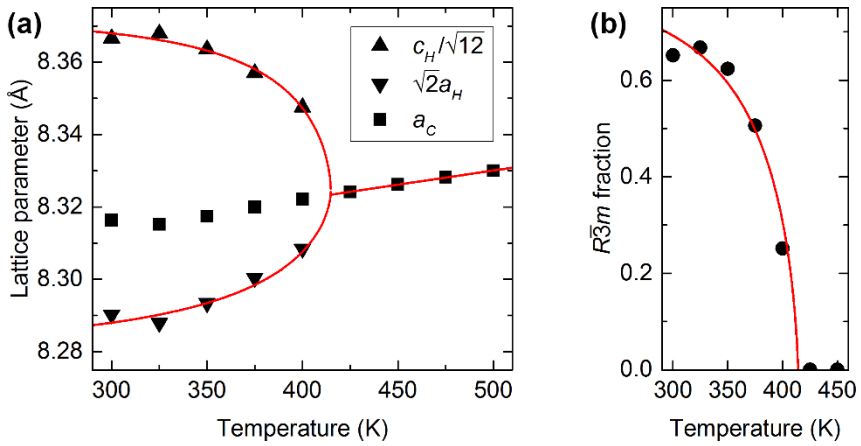

Figure 3.10: (a) The lattice parameters of the two phases of GaV_2O_4, and **(b)** the rhombohedral phase fraction, determined from Rietveld refinements against the high-resolution X-ray diffraction data. Fits of Equation 3.1 with T_{CO} = 415 K are shown.

cubic GaV_2O_4 above T_{CO}, and the decreasing fraction of rhombohedral GaV_2O_4 on warming is also well-described by Equation 3.1 with T_{CO} = 415 K (Figure 3.10(b)).

Powder neutron diffraction data collected for GaV_2O_4 (Figure 3.11(a)) corroborate the above structural characterisation, though due to poor thermal equilibration of the large sample used the structural transition appears at 465 K. Rietveld refinements with these data did not include any site splitting, as the weak diffraction of neutrons by vanadium prevented a sensible refinement of the positions of the vanadium sites, though the high neutron scattering contrast of Ga and V was used to confirm that no antisite disorder (V on the spinel *A* site, and Ga on the *B* site) occurs. Furthermore, the residual cubic phase and asymmetric peak profiles of the rhombohedral-phase seen in the powder X-ray diffraction data below T_{CO} are also seen with neutrons.

The lattice parameters a_H, c_H and a_C determined from Rietveld analysis of the neutron diffraction data were used to calculate the spontaneous strains s_a and s_c of rhombohedral GaV_2O_4

$$s_a = \frac{\sqrt{2}a_H - a_C}{a_C} \qquad \textbf{(3.2)}$$

$$s_c = \frac{c_H/\sqrt{12} - a_C}{a_C} \tag{3.3}$$

Spontaneous strain is an order parameter. The linear variation of s_a^2 and s_c^2 against T/T_{CO} in the critical region (Figure 3.11(b)) is consistent with the variation

$$s^2 = s_0^2\left(1 - \frac{T}{T_{CO}}\right) \tag{3.4}$$

that is characteristic of a quasi-continuous first-order transition.

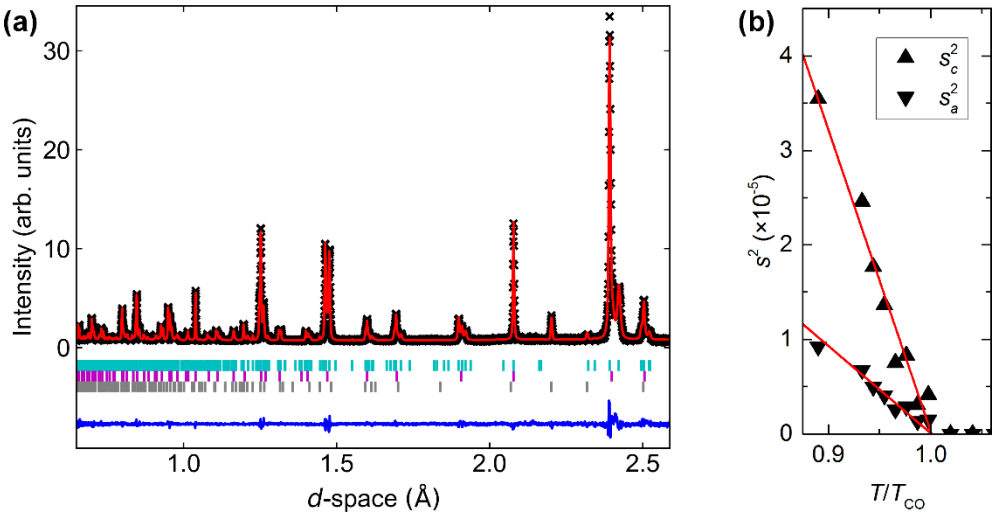

Figure 3.11: (a) Rietveld fit to the room temperature powder neutron diffraction pattern of GaV_2O_4 (R_w = 5.7%). Tick mark colours are consistent with those in Figure 3.9. **(b)** The squared spontaneous lattice strains of rhombohedral GaV_2O_4, determined from the powder neutron diffraction data, decrease linearly to zero at $T = T_{CO}$ in keeping with Equation 3.4 for a quasi-continuous first-order transition.

The long-range and local structural correlations in GaV_2O_4 have been explored using X-ray total scattering, in the same manner as described for AlV_2O_4, and reveal the same order-disorder transition of the V_3 and V_4 orbital molecules at T_{CO}. Rietveld analyses of these data, using the split-site $R\bar{3}m$ model and the split-site $Fd\bar{3}m$ model as appropriate, are consistent with those using the high-resolution diffraction data and confirm that T_{CO} is the temperature below which the orbital molecules have long-range pairwise order. By comparison, over the whole 300-1100 K measured temperature range PDFs generated from the total

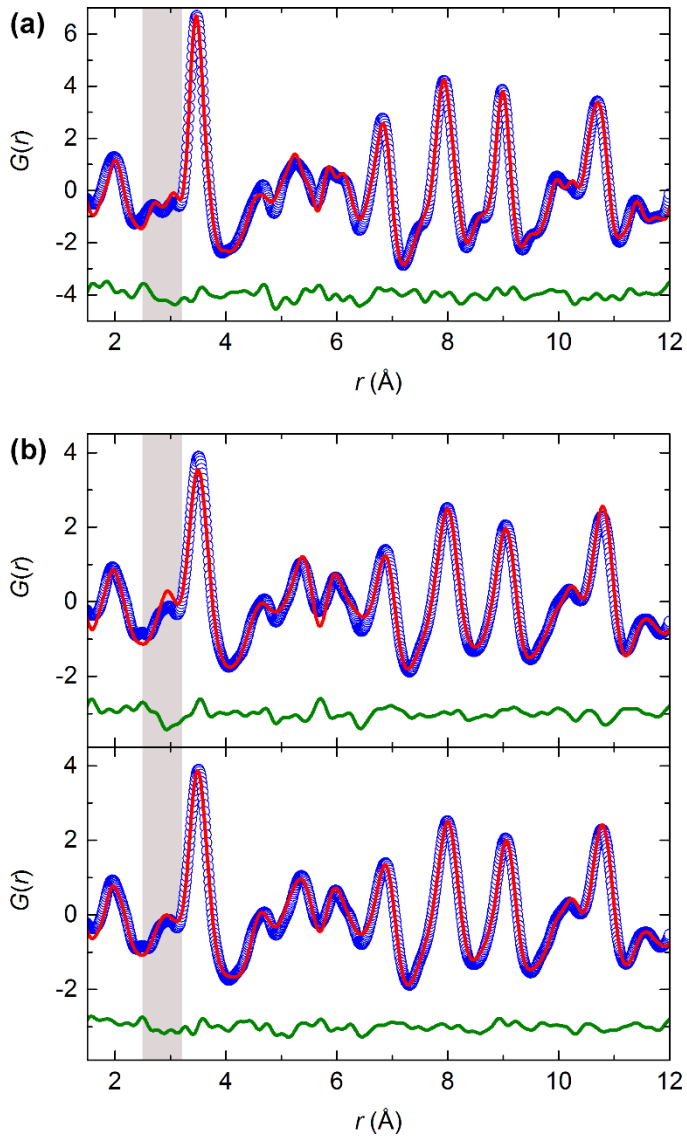

Figure 3.12: (a) Fit of the $R3m$ model, featuring V_3 and V_4 orbital molecules, to the 300 K PDF of GaV_2O_4 (R_w = 11.9%). **(b)** In comparison to the $Fd\bar{3}m$ average-structure model (upper, R_w = 13.5%) the $R3m$ model (lower, R_w = 10.3%) gives an improved fit to the 1100 K PDF of GaV_2O_4, particularly in the V-V nearest-neighbour region from 2.5 to 3.2 Å.

scattering data are best-fit using the $R3m$ model used to fit the PDFs of AlV_2O_4 (Figure 3.12). The V2 and V3 site displacements, constrained to be equal above T_{CO}, determined from these fits are comparable to those found in the split-site Rietveld refinements (Figure 3.13(a)) and result in short V-V distances that correspond to orbital molecules persisting into a disordered state above T_{CO} (Figure 3.13(b)). The residual cubic phase of GaV_2O_4 found below T_{CO} was not included in the analysis of the total scattering data; the relatively coarse

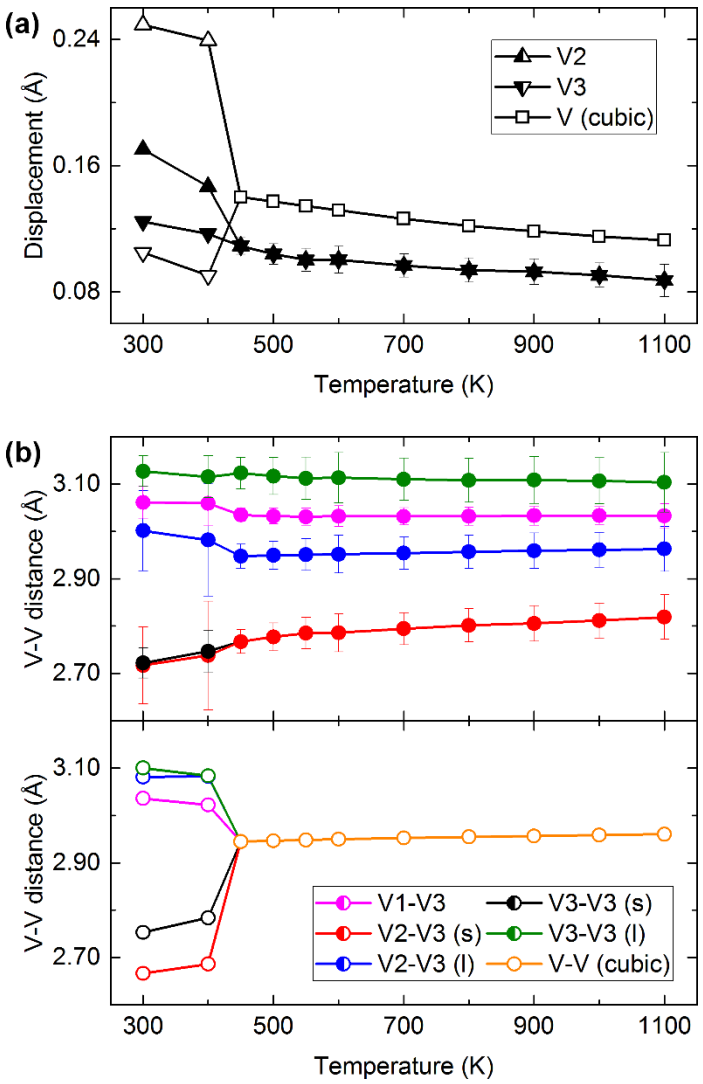

Figure 3.13: (a) V site displacements, and **(b)** V-V nearest-neighbour distances, determined from PDF (filled symbols) and Rietveld (open symbols) analysis of the X-ray total scattering data collected for GaV_2O_4. The continuous evolution of these structural parameters demonstrates that the orbital molecules in GaV_2O_4 persist through the crystallographic distortion at T_{CO} = 415 K and into a high-temperature disordered state.

resolution of the diffraction patterns meant that it could not be distinguished from the profiles of the rhombohedral phase in Rietveld fits, and as both phases of GaV_2O_4 have the same local structure a separate contribution of the cubic phase to the PDF fits is not required.

The structural characterisation of AlV_2O_4 and GaV_2O_4 shows that these materials have the same electronic states, with V_3 and V_4 orbital molecules that have long-range pairwise order in the rhombohedral phase below T_{CO} persisting into a

disordered state in the high-temperature cubic phase. This similarity should be expected; as the average number of electrons *per* vanadium cation is not affected by the change of *A*-site cation from Al^{3+} and Ga^{3+}, the charge distribution $A_4[V_4^{8+}V_3^{9+}V^{3+}]O_{16}$ can be achieved for both materials. The change of *A*-site cation does, however, cause T_{CO} to decrease substantially, from 700 K in AlV_2O_4 to 415 K in GaV_2O_4. This is the result of Ga^{3+} having a larger ionic radius (0.47 Å) than Al^{3+} (0.39 Å).[101] The average V-V separation is therefore also larger – 2.96 Å in GaV_2O_4 at 1100 K, compared to 2.92 Å in AlV_2O_4. Orbital molecule ordering is the result of direct t_{2g}-t_{2g} interactions, which are weakened when the V-V separation increases, hence the ordered state is destabilised. Increasing the average V-V separation also weakens the local bonding interactions within the orbital molecules. Not only are the V-V bond distances in GaV_2O_4 (both 2.72 Å at 300 K) longer than those in AlV_2O_4 (2.59 and 2.65 Å), but the difference between the bonding and non-bonding distances (2.72-3.13 Å in GaV_2O_4, 2.59-3.17 Å in AlV_2O_4) is less, as the weaker bonding reduces the displacements of the vanadium sites. Weaker bonding is also evidenced by GaV_2O_4 having a smaller spin-gap energy and semiconductor activation energy than AlV_2O_4, as will be discussed in the next Section. However, as total scattering data were collected to 1100 K for both materials, the lower T_{CO} of GaV_2O_4 allows this material to define a greater temperature range over which V-V bonding interactions can be found. 1100 K is $1.6T_{CO}$ for AlV_2O_4 and $2.7T_{CO}$ for GaV_2O_4, so these results demonstrate that the local electronic interactions that form orbital molecules in these materials, particularly GaV_2O_4, are stable well above the temperatures at which the long-range ordering of the orbital molecules is lost.

3.3.4: Magnetic and transport properties

From the structural characterisation detailed above, and the previously reported characterisation of AlV_2O_4, the charge distribution in AlV_2O_4 and GaV_2O_4 has been deduced as $A_4[V_4^{8+}V_3^{9+}V^{3+}]O_{16}$, with orbital molecules formed by two-centre two-electron bonding and non-bonding cations retaining two unpaired electrons. The magnetic susceptibilities of these materials should therefore reflect this

allocation of the vanadium *d*-electrons. The magnetic susceptibility of the ground state of AlV_2O_4 was previously described as

$$\chi = \frac{C}{T-\theta} + \frac{D}{T[1+\frac{1}{3}\exp\left(\frac{E_g}{k_B T}\right)]} \qquad \textbf{(3.5)}$$

where the total susceptibility is the sum of a Curie-Weiss term and a Bleaney-Bowers -like spin-gap term.[66] These two terms account respectively for the contributions of the non-bonding V^{3+} cations, which are paramagnetic, and orbital molecules, which are spin singlets. Equation 3.5 can be fit to the measured susceptibilities of AlV_2O_4 and GaV_2O_4 (Figure 3.14). This assumes an average value of E_g for the V_3^{9+} and V_4^{8+} clusters as two spin-gap terms could not be fitted independently, though this is a reasonable approximation as both clusters are formed by two-centre two-electron bonding. The parameters obtained from these fits are given in Table 3.3, and those for AlV_2O_4 are in good agreement with literature values. For both materials the paramagnetic moment μ_{eff} is close to the spin-only value of 2.83 μ_B expected for a d^2 cation. Following the Bleaney-Bowers description of the susceptibility of a spin-½ dimer system, the spin-gap energy

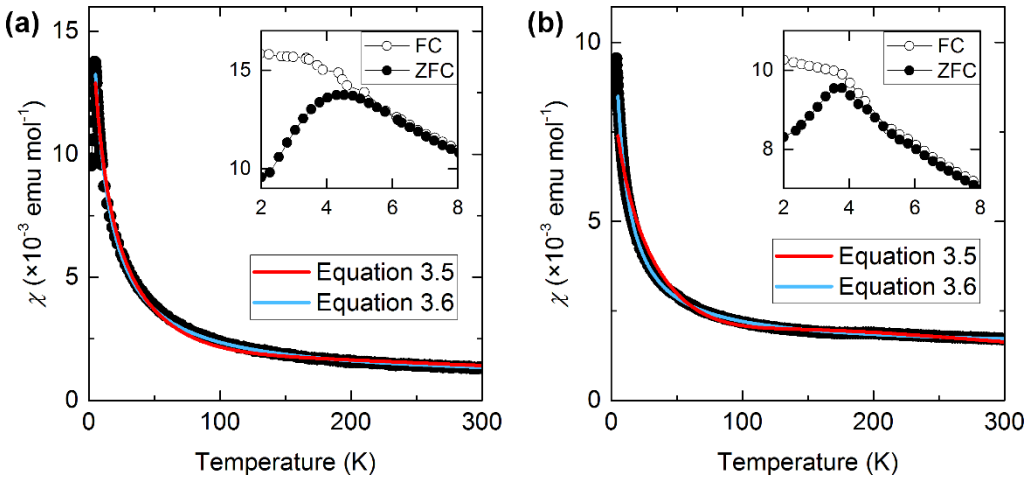

Figure 3.14: The zero-field cooled magnetic susceptibilities of **(a)** AlV_2O_4 and **(b)** GaV_2O_4. Fits of Equations 3.5 and 3.6, which use a spin-gap term and a constant, respectively, to account for the contributions of the spin-singlet V_3^{9+} and V_4^{8+} orbital molecules to the total susceptibilities, are shown over the range 5-300 K and give the parameters listed in Table 3.3. Insets show the cusp, below which the zero-field cooled (ZFC) and field cooled (FC) susceptibilities diverge, found for both materials, which is attributed to the non-bonding V^{3+} spins forming a spin-glass state.

Table 3.3: Magnetic susceptibility parameters for AlV_2O_4 and GaV_2O_4, determined from the fits of Equations 3.5 and 3.6 shown in Figure 3.14.

	C (emu K mol^{-1})	μ_{eff} (μ_B)	θ (K)	D (emu K mol^{-1})	E_g/k_B (K)	A ($\times 10^{-3}$ emu mol^{-1})
AlV_2O_4 (Ref. 66)	0.250	2.83	-22.6	0.616	844	-
AlV_2O_4 (Eq. 3.5)	0.233	2.73	-13.0	0.550	495	-
GaV_2O_4 (Eq. 3.5)	0.225	2.68	-25.4	0.662	416	-
AlV_2O_4 (Eq. 3.6)	0.170	2.33	-8.7	-	-	0.80
GaV_2O_4 (Eq. 3.6)	0.079	1.59	-6.2	-	-	1.46

E_g/k_B is the energy required to excite the singlet ground state of the orbital molecules, in which 18 electrons are paired in nine V-V bonds, to a triplet state in which two electrons are unpaired. The smaller value of E_g/k_B for GaV_2O_4 is consistent with it having weaker V-V bonds than AlV_2O_4.

The fits of Equation 3.5 deviate from the measured susceptibilities of both materials at very low temperatures. Improved fits are achieved by using a temperature-independent constant A to account for the contribution to the susceptibility of the triplet excited state of the orbital molecules mixing into the singlet ground state, such that

$$\chi = \frac{C}{T - \theta} + A \qquad \textbf{(3.6)}$$

The parameters obtained from fits of Equation 3.6 to the susceptibilities of both materials are also given in Table 3.3. These still give a negative value of θ, consistent with the V^{3+} spins having antiferromagnetic correlations, though the moments μ_{eff} obtained are smaller than expected for an $S = 1$ paramagnet. A larger value of A is obtained for GaV_2O_4 as the weaker V-V bonding allows the triplet excited state to mix with the singlet ground state to a greater degree.

At very low temperatures the susceptibilities of both materials have a cusp, below which the zero-field cooled and field cooled susceptibilities diverge (Figure 3.14, insets). Previous characterisation of AlV_2O_4 has attributed this transition to the paramagnetic V^{3+} spins freezing and forming a spin-glass state.[95] The transition temperature is slightly lower in GaV_2O_4 (3.8 K) than AlV_2O_4 (4.4 K), in line with the larger V^{3+}-V^{3+} separation in the former material weakening the interaction of the spins.

Previous measurements of AlV_2O_4 have shown that the magnetic susceptibility and resistivity of this material change very little through the structural transition at T_{CO}.[95] Equivalent measurements have been made for GaV_2O_4 and, similarly to the behaviour found in AlV_2O_4, show little change at T_{CO} = 415 K (Figure 3.15). This behaviour is unlike that of VO_2 and other vanadium oxides, in which the structural transitions at which ordered orbital molecule states form are accompanied by dramatic changes of the electronic properties. In any of these materials, the properties of the ground state are the result of electrons being paired in V-V bonds. In VO_2 these bonds break at the transition temperature,[63] and the release of the bonding electrons accounts for the change of properties. The absence of such a change in AlV_2O_4 and GaV_2O_4 is therefore consistent with the structural characterisation, with the transition at T_{CO} being between ordered and disordered orbital molecule states rather than one at which the V-V bonding is

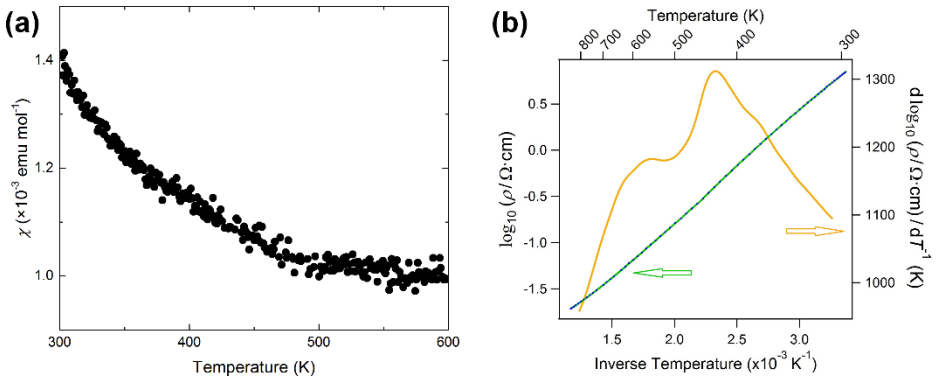

Figure 3.15: (a) The high-temperature magnetic susceptibility of GaV_2O_4, measured on warming, does not show a pronounced anomaly at T_{CO} = 415 K. **(b)** Logarithmic plot of the high-temperature resistivity of GaV_2O_4 against T^{-1}, which is also continuous through T_{CO}, though a change of slope at T_{CO} is evident in the derivative.

modified. The breakdown of the trimers and tetramers into smaller species would increase the susceptibility, as C increases up to 2.88 emu K mol^{-1} for paramagnetic AV^{2+}V^{3+}O$_4$. Similarly, the resistivity should be reduced as the bonding electrons become delocalised, but GaV$_2$O$_4$ is a semiconductor over the whole measured temperature range and using the Arrhenius relationship

$$\rho = \rho_0 \exp\left(\frac{E_a}{k_B T}\right) \qquad \textbf{(3.7)}$$

an activation energy E_a = 0.24 eV is determined. This is smaller than the 0.4 eV activation energy of AlV$_2$O$_4$[95] which, like the smaller spin-gap energy, is consistent with GaV$_2$O$_4$ having weaker V-V bonds.

3.3.5: Quasi-elastic neutron scattering

The structural analysis and property measurements described above demonstrate the persistence of disordered orbital molecules into the high-temperature phases of AlV$_2$O$_4$ and GaV$_2$O$_4$. However, with these techniques is it not possible to distinguish between glass-like static disorder and liquid-like dynamic disorder. QENS is a spectroscopic technique that can probe the dynamic behaviour of molecules,[86] so has been used to investigate the nature of the disorder in GaV$_2$O$_4$.

The scattering of neutrons by vanadium is almost solely incoherent (b_{coh} = -0.38 fm, b_{incoh} = 6.35 fm).[70] This limits the use of neutrons in determining vanadium pair-correlations, but does allow the vanadium self-correlation function to be extracted. This function describes the behaviour of individual nuclei, so any dynamic motion or interchange of vanadium cations in a liquid-like high-temperature state should have associated excitations that scatter neutrons incoherently. The excitations associated with molecular dynamics typically have energies on the quasi-elastic scale (E < 2 meV), so any scattering should appear as a broadening of the elastic scattering line. The timescale of dynamic behaviour τ is related to the full-width at half-maximum (FWHM) of the scattering function,[102] as

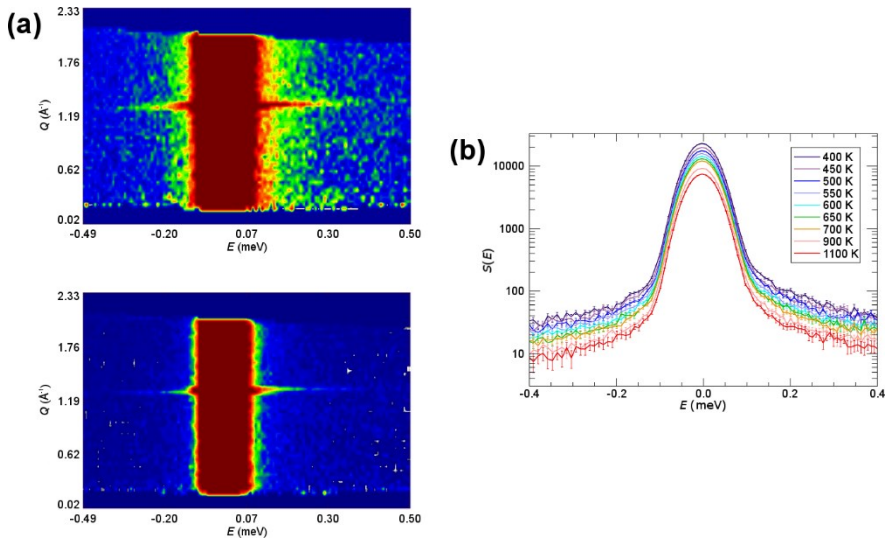

Figure 3.16: (a) QENS scattering functions $S(Q,E)$ of GaV_2O_4, collected at 400 K (upper) and 1100 K (lower). The full measured range of Q is shown, and the intensity scale is the same for both spectra. The feature at Q = 1.30 Å^{-1} is Bragg scattering (the 111 reflection in the cubic phase). **(b)** Integrated scattering functions $S(E)$ for all temperatures measured. Quasi-elastic scattering from orbital molecule dynamics, which would broaden the elastic line, is not seen, suggesting that the orbital molecules have static disorder between T_{CO} and 1100 K.

$$\tau(\text{ns}) = \frac{1.317}{\text{FWHM}(\mu\text{eV})} \qquad \textbf{(3.8)}$$

QENS data were collected between 400 K, at which temperature the orbital molecules in GaV_2O_4 have long-range pairwise order and so should be static, and 1100 K. The scattering functions $S(Q,E)$, of which those collected at 400 and 1100 K are shown in Figure 3.16(a), were integrated over the whole measured Q-range to give the scattering as a function of energy transfer $S(E)$, shown for all measured temperatures in Figure 3.16(b). The intensity of the elastic line decreases on heating due to the Debye-Waller effect, but no broadening of the elastic line due to quasi-elastic scattering is observed up to 1100 K. The observed FWHM of 80 μeV therefore provides a limiting value of τ: any dynamic behaviour must be slower than 1.6×10^{-11} s, indicating that even well above T_{CO} the trimers and tetramers in GaV_2O_4 are both well-defined and statically disordered.

3.4: Conclusions

By studying the structure of AlV_2O_4 on the local scale, the reported description of ordered V_7^{17+} 'heptamer' orbital molecules emerging from a uniform spinel structure has been substantially revised. Each 'heptamer' in the ground state, which is formed below the long-range ordering transition at T_{CO} = 700 K, is actually a pair of orbital molecules – a V_3^{9+} trimer and a V_4^{8+} tetramer. Rietveld analysis of the average ground state structure has revealed that the trimer-tetramer pairs have long-range order, but that each pair adopts one of two configurations in a disordered manner. This analysis reduces the upper size-limit of known orbital molecules, from seven- to four-atom species, though the distribution of known sizes is now more consistent, with these tetramers complementing the dimers and trimers known to form in other vanadium oxides. It also provides the first example of a system in which different orbital molecule species each comprised of more than two atoms coexist.

Above T_{CO} AlV_2O_4 appears to have the normal cubic spinel structure, but there are significant local distortions from this uniform average that are the result of the V_3^{9+} and V_4^{8+} orbital molecules persisting into a fully-disordered state. The same V_3^{9+} and V_4^{8+} orbital molecules have also been identified in GaV_2O_4, a newly synthesised material, and the replacement of Al^{3+} with Ga^{3+} suppresses their order-disorder transition at T_{CO} to 415 K. Together, the orbital molecules in these materials provide the first example of those formed by 3*d*-orbital interactions, and of those comprised of more than two atoms, having a disordered high-temperature state.

This behaviour sets AlV_2O_4 and GaV_2O_4 apart from other vanadium oxides with orbital molecule ground states. Previous PDF studies have shown that the dimers in VO_2 and the trimers in $Na_{0.5}VO_2$ do not persist on any length-scale above their respective long-range ordering temperatures,[63,64] whereas in AlV_2O_4 and GaV_2O_4 local V-V bonding is stable well-above the critical regime – to $2.7T_{CO}$ in the latter case. This implies that different mechanisms drive the V-V bonding in different vanadium oxides. A conventional Peierls-like transition, by which orbital

molecules emerge through displacive distortions of a uniform structure below the transition temperature, appears to account for the behaviour of VO_2 and most other systems. In this regime the temperature scales of orbital molecule formation and ordering are the same, but a mechanism that allows them to be very different is required for AlV_2O_4 and GaV_2O_4. In these materials the cubic spinel structure is unstable at all temperatures, at least at ambient pressure, with respect to the local orbital- and charge-ordering that forms V-V bonds. The structural distortion at T_{CO} then shows where the temperature is sufficiently low for the orbital molecules to establish long-range order.

Chapter 4: Ordering in ZnV_2O_4, $Zn_xGa_{1-x}V_2O_4$, and related systems

4.1: Introduction

AV_2O_4 spinels exhibit a diverse range of electronic ground states. These are determined primarily by the behaviour of the vanadium *d*-electrons but the choice of *A*-site cation is important, because its charge and size influence the number of *d*-electrons available and the degree of interaction between the orbitals of neighbouring vanadium cations. A comparison of the ground states of different AV_2O_4 spinels illustrates this importance: whilst orbital molecules are formed in GaV_2O_4, as described in Chapter 3, antiferromagnetic order is established in ZnV_2O_4,[36] and heavy-fermion correlations dominate in LiV_2O_4.[32]

The ground state of ZnV_2O_4 has notable spin and orbital ordering. Two transitions occur at low temperature: a tetragonal distortion of the high-temperature cubic spinel structure, below T_S = 51 K; and long-range antiferromagnetic ordering, below T_N = 40 K.[36] The magnetic structure has been determined by powder neutron diffraction and comprises an unusual combination of *up-down-up-down* spins along the chains of edge-sharing VO_6 octahedra that lie in the *xy* plane and *up-up-down-down* spins along the chains in the *xz* and *yz* planes. This spin ordering is related to the orbital ordering of the two V^{3+} *d*-electrons caused by the tetragonal distortion (Figure 4.1). In the cubic structure adopted at high temperatures each V^{3+} cation has an orbitally degenerate t_{2g}^2 electron configuration. A Jahn-Teller distortion that lifts this degeneracy might, therefore, be expected. However, the tetragonal distortion that ZnV_2O_4 undergoes below T_S compresses the cubic *c*-axis and the degeneracy is only partially lifted. The singly-occupied d_{xy} orbitals of each V^{3+} interact to give the *up-down-up-down* spin chains,

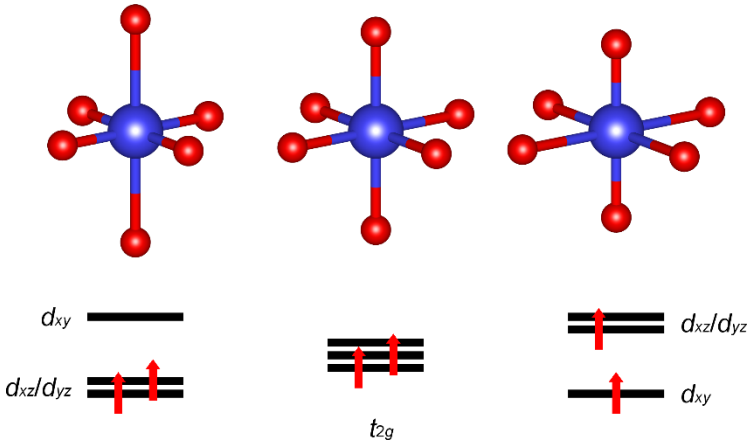

Figure 4.1: Orbital ordering for octahedrally-coordinated V^{3+}. In a regular octahedral environment the two *d*-electrons occupy three degenerate t_{2g} orbitals (centre). A conventional Jahn-Teller distortion would lift the orbital degeneracy by extending the octahedron along one axis (left). In ZnV_2O_4 and MgV_2O_4 the VO_6 octahedra are compressed by the tetragonal distortion and partial degeneracy is retained (right).

whilst the *up-up-down-down* chains are formed by the interactions of d_{xz} and d_{yz} orbitals, which remain degenerate and share the second electron.

Various theoretical models for the occupation of the d_{xz} and d_{yz} orbitals in tetragonal ZnV_2O_4 have been put forward (Figure 4.2), but no one model appears to be consistent with the experimentally-determined behaviour of this material. ZnV_2O_4 is a Mott insulator, and both antiferro- and ferro-orbital ordering schemes for localised *d*-electrons have been proposed.[103,104] Antiferro-orbital ordering was used to explain the one-dimensional character of the magnetic interactions below T_S that was identified by inelastic neutron scattering[105] but has $I4_1/a$ symmetry, lower than the $I4_1/amd$ symmetry determined by diffraction[36] and infrared phonon spectroscopy[106] that is consistent with ferro-orbital ordering.

Subsequent studies have gone on to suggest that a localised-electron description may not even be valid. MgV_2O_4, with T_N = 40 K and T_S = 62 K,[107] and CdV_2O_4, with T_N = 35 K and T_S = 97 K,[108] are isoelectronic with ZnV_2O_4 and undergo the same sequence of ordering transitions. The V-V nearest-neighbour distance in each of these materials is close to the 2.94 Å critical separation predicted by Goodenough for itinerant behaviour[25] and varies according to the ionic radius of *A*-site cation, being larger in CdV_2O_4 than in ZnV_2O_4 and MgV_2O_4. The behaviour of these

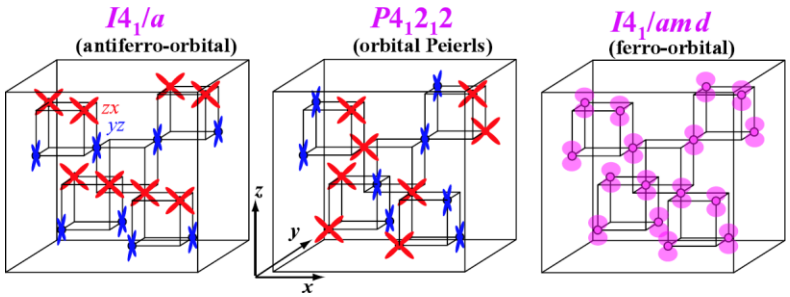

Figure 4.2: Orbital ordering schemes proposed for tetragonal ZnV_2O_4. Antiferro-orbital order, with the d_{xz} and d_{yz} orbitals alternatingly occupied along the *c*-axis, and ferro-orbital order, with a complex $d_{yz} \pm id_{xz}$ orbital occupied at every site, have been proposed for localised *d*-electrons. A partial delocalisation that forms V-V dimers, similar to the orbital Peierls transition in $MgTi_2O_4$, has also been suggested. Figure reproduced from Ref. 113.

materials, both at ambient pressure and in response to applied pressure, demonstrates that CdV_2O_4 is an insulator but that ZnV_2O_4 and MgV_2O_4 are in proximity to an insulator-metal transition and may have partially delocalised *d*-electrons.[109,110] It has been suggested that this delocalisation occurs through the formation of V-V homopolar bonds between ferromagnetic pairs of spins – in other words, orbital molecule dimerisation – and electronic structure calculations give an alternating V-V separation of 2.92 Å and 3.01 Å between ferromagnetic and antiferromagnetic pairs along the *up-up-down-down* spin chains.[111] This corresponds to a tetragonal structure with $P4_12_12$ symmetry, like that of the ground state of $MgTi_2O_4$ in which an orbital Peierls distortion forms helices of Ti-Ti dimers.[60] Analogous V-V dimers have not been identified in previous crystallographic studies of ZnV_2O_4 or MgV_2O_4, though inelastic neutron scattering has identified phonon anomalies in MgV_2O_4 that appear to be similar to those coupled to charge fluctuations in other Peierls systems.[112] This again suggests that MgV_2O_4 is in proximity to a dimerisation transition.

In the first section of this Chapter, X-ray total scattering is used to help resolve the nature of the orbital order in the ground states of ZnV_2O_4 and MgV_2O_4. Long-range order must have a symmetry consistent with that of the average tetragonal structure, which can be deduced from the observed Bragg reflections.

Additionally, probing the local structure should allow any distortions arising from short-range ordering or local V-V homopolar bonding to be identified.

Subsequently, the crossover from the orbital molecule ground state of GaV_2O_4 to the antiferromagnetic ground state of ZnV_2O_4 is studied in the $Zn_xGa_{1-x}V_2O_4$ system. Although the ground state is determined by the interactions of the vanadium *d*-electrons, two properties of the *A*-site cation influence the nature of these interactions: its charge determines the vanadium oxidation state, and hence the number of *d*-electrons that are available, whilst its size affects the V-V nearest-neighbour distance and thus the extent of t_{2g}-t_{2g} orbital overlap. Substitution of the spinel *A*-site cation, through the preparation of $A_xA'_{1-x}V_2O_4$ solid solutions, allows these properties – and hence the behaviour of the spinel – to be tuned. As described in the previous Chapter, the V_3 and V_4 orbital molecules in GaV_2O_4 undergo an order-disorder transition at 415 K but are stable to at least 1100 K. As Zn^{2+} has both a lower charge than Ga^{3+}, so reduces the number of *d*-electrons available for V-V bonding, and a larger ionic radius that stretches V-V bonds, Zn-substitution allows the stability of the ordered and disordered orbital molecule states in GaV_2O_4 to be tested further.

The presence of multiple *A*-site cations also introduces new structural effects (Figure 4.3). If the substituting cation occupies sites randomly, structural disorder is introduced. As this disrupts the interactions between *B*-site nearest neighbours it can destabilise long-range order – in $Li_xZn_{1-x}V_2O_4$, the introduction of 10% Li is sufficient to suppress the orbital and spin ordering that develops in unsubstituted ZnV_2O_4 and a spin-glass ground state is formed instead.[114] Alternatively, the *A*-site cations can have structural order. The spinels $Li_{0.5}A'_{0.5}Cr_2O_4$ (*A*' = Ga^{3+}, In^{3+}) are cubic at room temperature but the *A*-site cations have a zinc-blende -like ordered distribution that lowers the cubic symmetry to $F\bar{4}3m$. This allows the Cr^{3+} ions to displace and form a 'breathing' pyrochlore lattice of alternating small and large Cr_4 tetrahedra.[115] Although these are not orbital molecules, as Cr^{3+} (t_{2g}^3) lacks an orbital degree of freedom, some similarities can be seen. Between $Li_{0.5}Ga_{0.5}Cr_2O_4$ and $Li_{0.5}In_{0.5}Cr_2O_4$ the breathing distortion is increased and this is accompanied

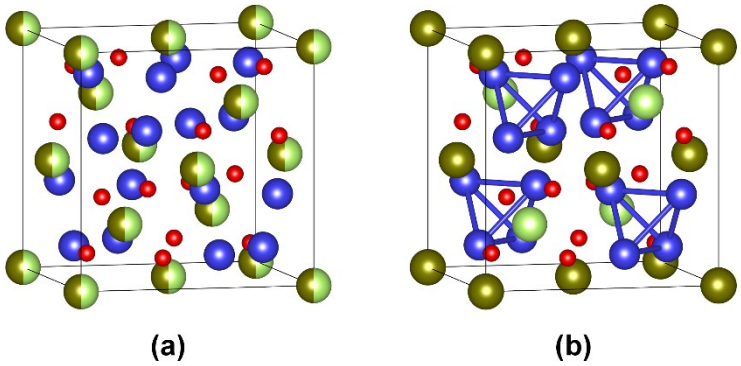

Figure 4.3: Two structural arrangements for the *A*-site cations, shown in green and gold, in a cubic $A_{0.5}A'_{0.5}B_2O_4$ spinel. **(a)** A disordered distribution maintains $Fd\bar{3}m$ symmetry and all *B*-*B* nearest-neighbour distances are equivalent. **(b)** A zinc-blende -like ordering lowers the symmetry to $F\bar{4}3m$, allowing the *B*-site cations to displace and form a breathing pyrochlore lattice. Short *B*-*B* distances are shown.

by a change of magnetic behaviour, from antiferromagnetic spin-liquid correlations to a spin-gapped state.

$Li_{0.5}Ga_{0.5}V_2O_4$ has also been synthesised, and its characterisation is discussed in the final section of this Chapter. With a t_{2g}^2 electron configuration orbital degrees of freedom are available, so a structure with *A*-site cation ordering like that found in $Li_{0.5}Ga_{0.5}Cr_2O_4$ could offer a template for orbital molecule formation. Furthermore, as a candidate orbital molecule system it offers comparisons to both ZnV_2O_4, with which it is isoelectronic, and Zn-substituted GaV_2O_4.

4.2: Experimental

4.2.1: ZnV_2O_4, MgV_2O_4, and $Zn_xGa_{1-x}V_2O_4$

High-temperature solid-state reactions were used to synthesise 1 g $Zn_xGa_{1-x}V_2O_4$ powder samples with x = 0.02, 0.04, 0.06, 0.125, 0.25, 0.375, 0.5, 0.625, 0.75, 0.875 and 1. For each composition suitable quantities of ZnO (Aldrich, 99.999%), Ga_2O_3 (Sigma Aldrich, 99.99%), V (Alfa Aesar, 99.5%) and V_2O_3, prepared in advance by reducing V_2O_5 (Alfa Aesar, 99.6%) under flowing H_2 at 900 °C, in the stoichiometric ratio were ground together and pressed into a pellet, which was

sealed in an evacuated quartz ampoule. Reactions were carried out by heating for 48 hours at 1000 °C for x = 0.02, 0.04 and 0.06, and for 48 hours at 900 °C for $x \geq 0.125$. The sample of GaV_2O_4 used for the experiments in Chapter 3 provided the x = 0 phase.

A 1 g powder sample of MgV_2O_4 was also prepared. Suitable quantities of MgO (Sigma Aldrich, 99%) and V_2O_5 in the stoichiometric ratio were ground together and pressed into a pellet. A first heating was carried out under flowing H_2 at 600 °C for two hours, to reduce V_2O_5 to V_2O_3, and then at 1080 °C for a further 12 hours. As this yielded a mixture of phases the pellet was reground and pressed again, and sealed in an evacuated quartz ampoule that was heated at 1100 °C for 48 hours.

Lab X-ray diffraction, using a Bruker D2 Phaser powder diffractometer, was used to confirm that all reactions had reached completion. A minor impurity phase of V_2O_3 was found in all samples except ZnV_2O_4 and MgV_2O_4, in which no impurities could be identified. DC magnetisation measurements in an applied field of 5000 Oe were made for all samples using a Quantum Design SQUID MPMS-XL.

Two X-ray total scattering experiments were carried out at ESRF beamline ID22. During the first experiment, a He cryostat was used for temperature control. Data were collected for GaV_2O_4 (over the temperature range 5-280 K), $Zn_{0.125}Ga_{0.875}V_2O_4$ (5-280 K), $Zn_{0.875}Ga_{0.125}V_2O_4$ (5-280 K), ZnV_2O_4 (10-280 K), and MgV_2O_4 (10-100 K). During the second experiment, a N_2 cryostream was used and data were collected at room temperature and 90 K for all $Zn_xGa_{1-x}V_2O_4$ phases. Additional data were collected at temperature steps up to 500 K for GaV_2O_4, $Zn_{0.02}Ga_{0.98}V_2O_4$ and $Zn_{0.04}Ga_{0.96}V_2O_4$, and at temperature steps between 90 K and room temperature for $Zn_{0.06}Ga_{0.94}V_2O_4$.

Experimental parameters and data processing were kept as consistent as possible between the two experiments. 70 keV radiation was used for both, with calibrated wavelengths of 0.177022 Å for the first and 0.176938 Å for the second. Samples were always held in 0.5 mm-diameter borosilicate capillaries, and the total scattering pattern at each temperature step was the average of 201 1 s exposures. Rietveld analysis was done using GSAS.[77] PDFgetX3 was used to make background

corrections, generate structure functions $S(Q)$ and transform these to atomic pair distribution functions $G(r)$.[83] For patterns collected during the first experiment these transforms were done for momentum transfers $1.0 \leq Q$ (Å^{-1}) ≤ 19.2, whilst $0.5 \leq Q$ (Å^{-1}) ≤ 20.0 was used for patterns collected during the second experiment. The reduced range in the former case was needed to avoid background anomalies from the cryostat that could not be properly corrected for. Subsequent fitting that included simulation of termination ripples was done using PDFgui,[84] over the interatomic distance range $1.5 \leq r$ (Å) ≤ 12 for all PDFs.

4.2.2: $Li_{0.5}Ga_{0.5}V_2O_4$

$Li_{0.5}Ga_{0.5}V_2O_4$ was synthesised by the solid-state reaction of $LiGaO_2$ and V_2O_3. $LiGaO_2$ was prepared from Li_2CO_3 (Sigma-Aldrich, 98%, with a 5% molar excess used to account for Li evaporation) and Ga_2O_3, ground together and pressed into a pellet that was heated for 12 hours in air at 900 °C. V_2O_3 was prepared by the reduction of V_2O_5 as detailed in the previous section. Suitable quantities of these precursors were ground together in the stoichiometric ratio, with an appropriate amount of additional Li_2CO_3 to provide a 10% excess of Li. The ground powder was held in a gold capsule that was sealed in an evacuated quartz ampoule; this was heated at 850 °C for 72 hours then quenched to room temperature. Lab X-ray diffraction was used to confirm a complete synthesis. Two 1 g samples and two 0.5 g samples were prepared and combined, and each sample only had a minor V_2O_3 impurity. Other synthesis conditions were explored but resulted in significant V_2O_3 and $LiVO_2$ impurities; quenching minimised the formation of impurity phases, and Rietveld analysis of the lab X-ray data collected for samples prepared under these and other conditions indicated that the distribution of the *A*-site cations within the main spinel phase was not affected by quenching.

The DC magnetisation of the sample was measured in a 1000 Oe applied field using a Quantum Design SQUID MPMS-XL. Powder neutron diffraction data were collected at ISIS beamline HRPD. 2.6 g of the sample was held in a slab-geometry vanadium can and cooled to 4.2 K with a standard orange cryostat, and diffraction patterns were collected at temperature steps on warming to 300 K. GSAS was

used to refine structural models against the diffraction patterns collected by the 168° detectors.

4.3: Results and discussion

4.3.1: ZnV_2O_4 and MgV_2O_4

The orbital order in the ground states of ZnV_2O_4 and MgV_2O_4 is inherently related to the tetragonal distortion that these materials undergo at low temperature. X-ray total scattering has been used to determine the tetragonal symmetry of their ground state crystal structures, with which any long-range order must be consistent, and to search for local-structure distortions that might arise from short-range ordering.

ZnV_2O_4 undergoes two ordering transitions at low temperatures, and magnetic susceptibility measurements reveal that these occur at T_N = 39 K and T_S = 50 K in the synthesised sample (Figure 4.4(a)). These are consistent with literature values of 40 K and 51 K.[36] Previous structural characterisation by powder neutron diffraction has identified a transition from $Fd\bar{3}m$ cubic symmetry to $I4_1/amd$ tetragonal symmetry at T_S,[36] and Rietveld fits to the collected total scattering patterns using these structural models (Figure 4.4(b)) confirm that the expected tetragonal distortion, which compresses the c-axis of the unit cell such that $c_T/\sqrt{2}a_T < 1$, occurs below T_S. These fits used a single isotropic thermal parameter for all crystallographic sites, and the oxygen site in each phase was fixed at the position determined by neutron diffraction. Rietveld analysis also determines that there is only 1% antisite disorder. Other, lower-symmetry tetragonal space groups ($I4_1/a$ and $P4_12_12$) have been proposed for the ground state structure of ZnV_2O_4, but the additional reflections that would be allowed if one of these was adopted are not seen (Figure 4.4(b), inset). The ground state structure of this material therefore appears to be consistent with long-range ferro-orbital ordering.

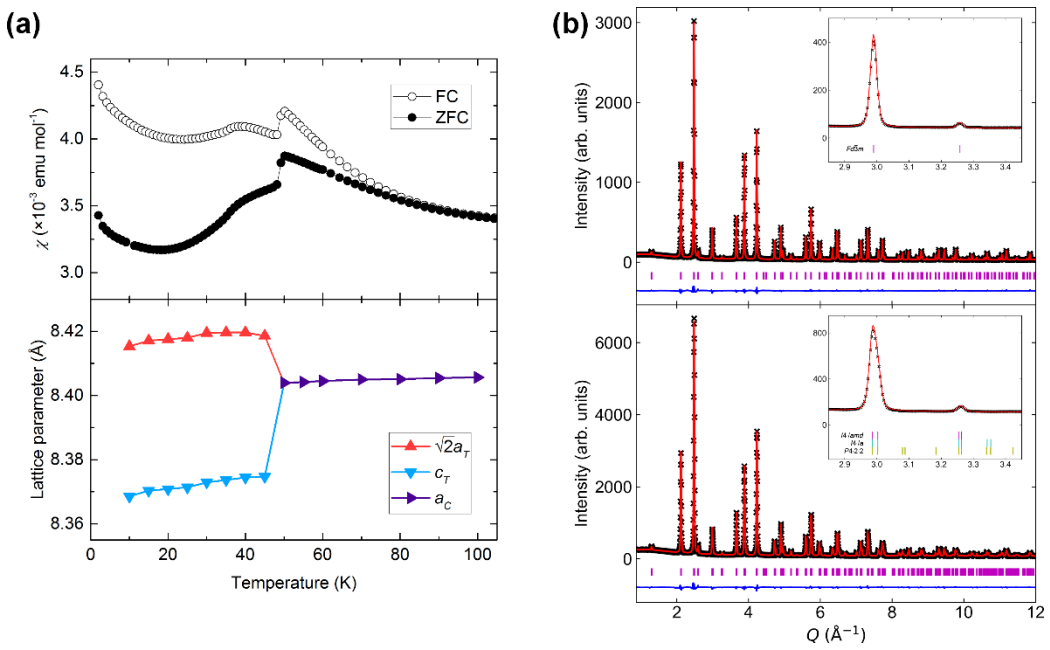

Figure 4.4: Characterisation of ZnV_2O_4. **(a)** Discontinuities in the magnetic susceptibility identify the transition temperatures T_N = 39 K and T_S = 50 K, and the refined lattice parameters show a tetragonal distortion below T_S. **(b)** Rietveld fits to the total scattering patterns collected at 100 K (upper, $Fd\bar{3}m$, R_w = 2.08%) and 10 K (lower, $I4_1/amd$, R_w = 1.96%). In the expanded region shown in the insets, broadening of the cubic 400 (Q = 2.99 Å^{-1}) and 331 (Q = 3.26 Å^{-1}) reflections by the tetragonal distortion is evident but the additional reflections of a lower-symmetry tetragonal structure are not seen.

The synthesised sample of MgV_2O_4 was measured and analysed in the same way. Magnetic susceptibility measurements determine T_N = 34 K and T_S = 57 K, similar to literature values of 40 K and 62 K,[107] and a tetragonal distortion that compresses the c-axis below T_S is evident through Rietveld refinements against the total scattering patterns (Figure 4.5(a)). A previous synchrotron single-crystal diffraction study has suggested $I4_1/a$ symmetry for the ground state structure of MgV_2O_4, although the additional reflections that distinguish this from $I4_1/amd$ symmetry were not seen in synchrotron powder diffraction patterns reported concurrently.[107] The reflections in the total scattering patterns collected for MgV_2O_4 below T_S are consistent with $I4_1/amd$ symmetry, and as was the case for ZnV_2O_4 the additional reflections for $I4_1/a$ or $P4_12_12$ symmetry are not seen (Figure 4.5(b)).

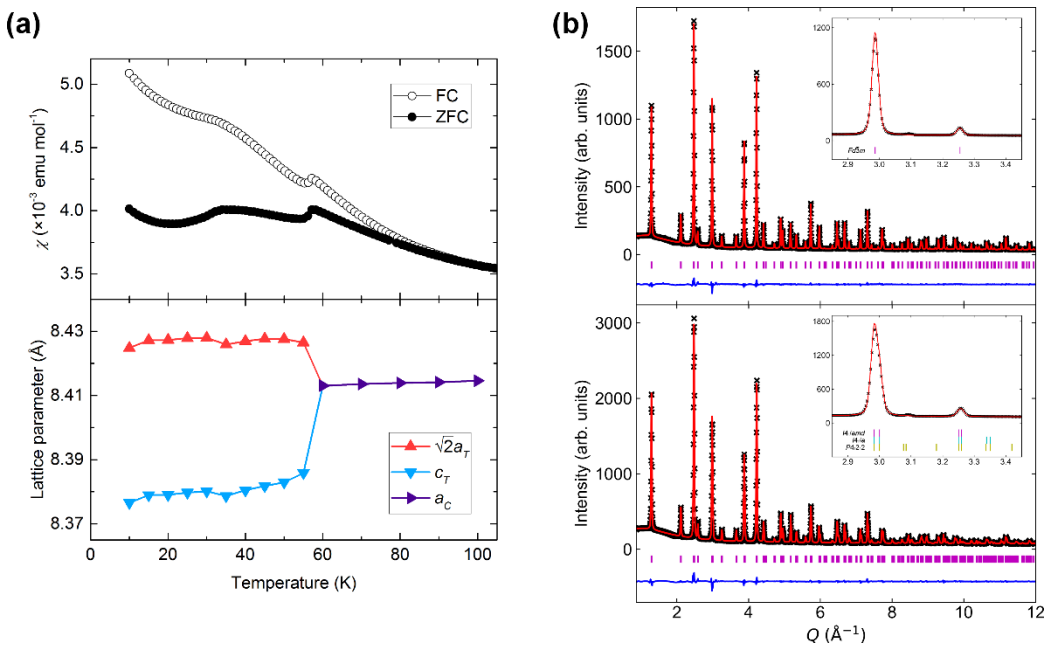

Figure 4.5: Characterisation of MgV_2O_4. **(a)** Magnetic susceptibility measurements reveal the transitions at T_N = 34 K and T_S = 57 K, the latter of which is associated with a tetragonal distortion. **(b)** Rietveld fits to the total scattering patterns collected at 100 K (upper, $Fd\bar{3}m$, R_w = 2.69%) and 10 K (lower, $I4_1/amd$, R_w = 3.10%). Below T_S only the reflections corresponding to $I4_1/amd$ symmetry are seen.

The proximity of ZnV_2O_4 and MgV_2O_4 to an insulator-metal transition,[109] and the identification of short-range charge fluctuations in MgV_2O_4,[112] have led to suggestions that the *d*-electrons in these materials are partially delocalised, to form V-V homopolar bonds. In such a regime the delocalisation should be accompanied by displacements of the vanadium sites such that vanadium dimers are defined; chains of alternating short (2.92 Å) and long (3.01 Å) V-V separations have been predicted for a dimer state in ZnV_2O_4.[111] However, for these displacements to be possible the tetragonal symmetry must be lower than the $I4_1/amd$ average determined by Rietveld analysis. The tetragonal distortion inherently breaks the equivalence of all V-V nearest-neighbour distances found in the high-temperature cubic structure, but for both $I4_1/amd$ and $I4_1/a$ symmetries the *A*-site and vanadium site are at fixed positions and cannot displace further. These two symmetries can only be distinguished by refining the position of the oxygen site, which is $(0, y, z)$ for $I4_1/amd$ and (x, y, z) for $I4_1/a$. However, under $P4_12_12$ symmetry the *A*-site, vanadium and two independent

oxygen sites can all displace from their ideal spinel positions, so the bond-shortening required for V-V dimerisation can occur. Therefore, whilst the Rietveld analysis described above demonstrates that structurally ordered vanadium dimers are not present in the ground states of ZnV_2O_4 and MgV_2O_4, a disordered dimer state could exist if the local symmetry was lower than the $I4_1/amd$ average.

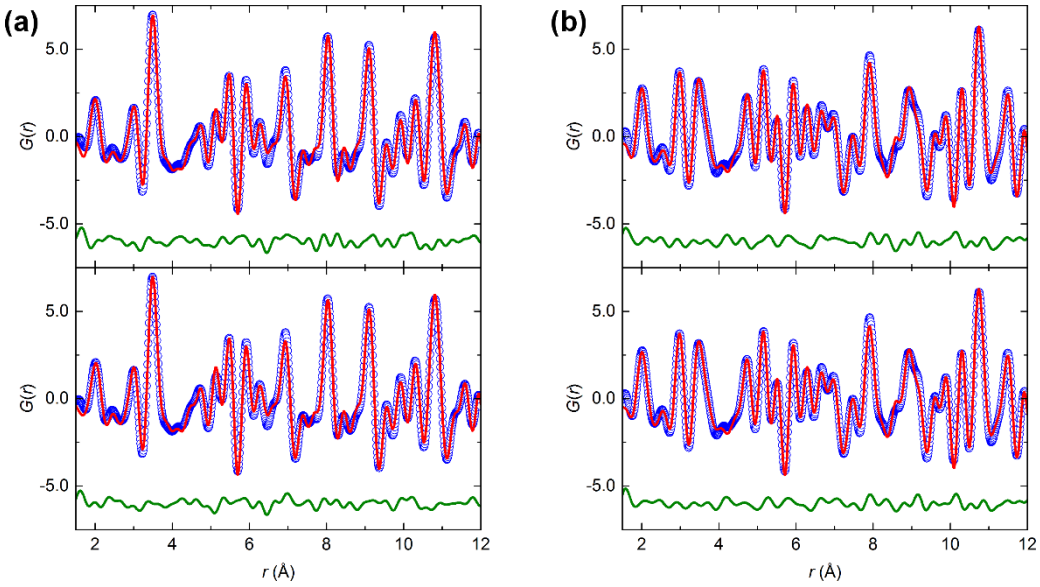

Figure 4.6: Fits to the 10 K PDFs of **(a)** ZnV_2O_4, and **(b)** MgV_2O_4. For both, the upper fit is of an $I4_1/amd$ model in which the vanadium site is fixed (R_w = 12.0% for ZnV_2O_4, 12.4% for MgV_2O_4) and the lower is of a $P4_12_12$ model in which it can displace (R_w = 10.9% for ZnV_2O_4, 11.8% for MgV_2O_4).

To determine whether there are local vanadium displacements in the ground states of ZnV_2O_4 and MgV_2O_4, fits of the three tetragonal structures were made to their 10 K PDFs. The tetragonal lattice parameters, all allowed site displacements, and independent isotropic thermal parameters for the A-site, vanadium and oxygen sites were refined. The fits of the $I4_1/amd$ and $P4_12_12$ models for both materials are shown in Figure 4.6, and the results of all fits are summarised in Table 4.1 for ZnV_2O_4 and Table 4.2 for MgV_2O_4. For both ZnV_2O_4 and MgV_2O_4 the fit of the $P4_12_12$ model is better than those of the $I4_1/amd$ and $I4_1/a$ models, which are themselves very similar. Greater distortions of the AO_4 tetrahedra and VO_6 octahedra, evident in the distribution of A-O and V-O bond distances, are found with $P4_12_12$ symmetry because more structural degrees of freedom are

Table 4.1: Comparison of the fits of different tetragonal structures and the refined nearest-neighbour bond distances to the 10 K PDF of ZnV_2O_4.

Space group	R_w (%)	V-V (Å)	Zn-O (Å)	V-O (Å)
$I4_1/amd$	12.0	2.966(4) 2.978(3)	1.98(5)	1.99(4) 2.02(2)
$I4_1/a$	12.1	2.966(5) 2.977(3)	1.99(5)	1.99(5) 2.02(2) 2.02(2)
$P4_12_12$	10.9	2.95(7) 2.97(7) 2.98(7) 2.98(4)	1.95(7) 2.06(5)	1.83(5) 1.95(8) 2.03(7) 2.04(12) 2.05(12) 2.12(8)

Table 4.2: Comparison of the fits of different tetragonal structures and the refined nearest-neighbour bond distances to the 10 K PDF of MgV_2O_4.

Space group	R_w (%)	V-V (Å)	Mg-O (Å)	V-O (Å)
$I4_1/amd$	12.4	2.967(2) 2.984(1)	1.96(2)	1.98(2) 2.05(1)
$I4_1/a$	12.6	2.967(2) 2.985(2)	1.96(3)	1.98(2) 2.04(2) 2.04(2)
$P4_12_12$	11.8	2.95(9) 2.97(9) 2.98(4) 2.99(9)	1.87(11) 2.08(8)	1.89(6) 2.00(13) 2.03(13) 2.03(14) 2.05(7) 2.10(14)

available, but the displacements refined using this model do not significantly shorten any V-V nearest-neighbour distances. Shortened distances that define V-V dimers would distinguish local $P4_12_12$ symmetry from the other models, particularly as X-rays are scattered more strongly by vanadium than oxygen. However, as short V-V distances cannot be identified it is not apparent that the

improved fits obtained with the $P4_12_12$ model are not just the result of overfitting by the greater number of refinable parameters that are available to this model, and therefore that the local symmetry is actually lower than the $I4_1/amd$ average.

That said, theoretical work has suggested that in a partially-delocalised regime charge fluctuations could give rise to the antiferromagnetic ground state established in ZnV_2O_4 and MgV_2O_4 through the dimerisation of ferromagnetic V-V pairs but with very little bond-length alternation.[116] To clarify whether there is a local lowering of symmetry, neutron total scattering may provide a useful comparison. Neutrons scatter weakly from vanadium but scatter far more strongly from oxygen than X-rays do, so where X-ray total scattering cannot definitively distinguish local $P4_12_12$ symmetry in ZnV_2O_4 and MgV_2O_4 on the basis of vanadium site displacements, an equivalent neutron scattering study might identify a low local symmetry through the distortions of the AO_4 tetrahedra and VO_6 octahedra that are suggested by the fits of the $P4_12_12$ model to the X-ray PDFs. Neutron PDFs of ZnV_2O_4 have previously been obtained,[117] but structural refinements were not performed and only $I4_1/a$ symmetry was considered in their interpretation.

4.3.2: $Zn_xGa_{1-x}V_2O_4$

Whilst ZnV_2O_4 has an antiferromagnetic ground state with near-uniform V-V nearest-neighbour distances, GaV_2O_4 has a ground state in which V_3 and V_4 orbital molecules are formed by large displacements of the vanadium sites. $Zn_xGa_{1-x}V_2O_4$ solid solutions of these two spinels were prepared over the complete range of x ($0 \leq x \leq 1$), allowing the crossover from the orbital molecule ground state of one end-member to the antiferromagnetic ground state of the other to be studied.

As described in Chapter 3, the V-V bonding in GaV_2O_4 results in the charge distribution $Ga_4[V_4^{8+}V_3^{9+}V^{3+}]O_{16}$. The V_4^{8+} and V_3^{9+} orbital molecules only have long-range order below T_{CO} = 415 K, but as the local V-V bonding interactions are very stable with respect to temperature these orbital molecules persist in a disordered state to at least 1100 K. This stability can therefore be tested further through the substitution of Ga^{3+} for Zn^{2+} in $Zn_xGa_{1-x}V_2O_4$. Increasing x by 0.25

oxidises one V^{2+} to V^{3+}, so bonding *d*-electrons are removed, and as the ionic radius[101] of the *A*-site cation is increased from 0.47 Å for Ga^{3+} to 0.60 Å for Zn^{2+} the V-V nearest-neighbour distance is stretched upon this substitution. As the stability of both ordered and disordered orbital molecule states must be considered X-ray total scattering was again employed for structural characterisation. For both Rietveld and PDF fits the distribution of the *A*-site cations was treated as being disordered, and independent isotropic thermal parameters were used for the *A*-site, vanadium and oxygen sites in all cases except the Rietveld fits to the patterns collected for GaV_2O_4, $Zn_{0.125}Ga_{0.875}V_2O_4$and $Zn_{0.875}Ga_{0.125}V_2O_4$ using the He cryostat, for which a single isotropic thermal parameter was used for all sites.

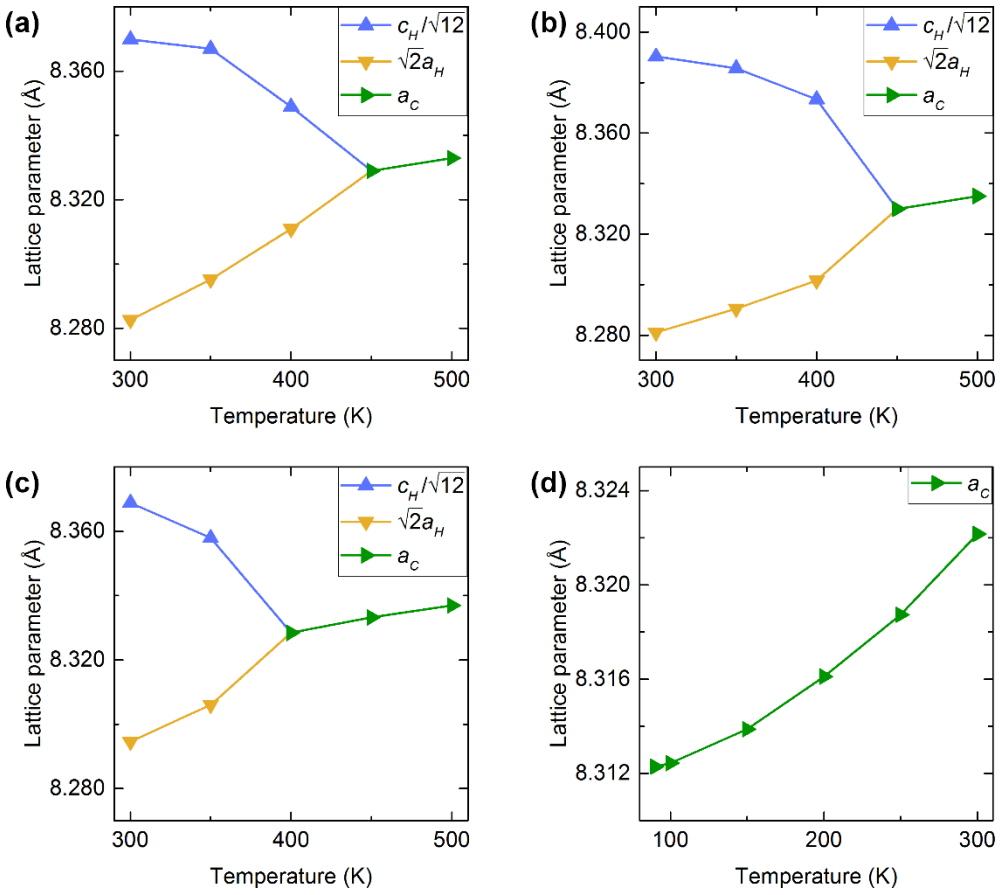

Figure 4.7: Thermal variation of the lattice parameters in **(a)** GaV_2O_4, **(b)** $Zn_{0.02}Ga_{0.98}V_2O_4$, **(c)** $Zn_{0.04}Ga_{0.96}V_2O_4$, and **(d)** $Zn_{0.06}Ga_{0.94}V_2O_4$, from Rietveld refinements against the X-ray total scattering data. Long-range orbital molecule ordering, which causes the $Fd\bar{3}m$-$R\bar{3}m$ structural distortion, is rapidly destabilised by Zn-substitution.

The formation of long-range orbital molecule order in GaV_2O_4 below T_{CO} results in a rhombohedral distortion of the cubic spinel structure. The same distortion is seen in $Zn_xGa_{1-x}V_2O_4$ phases with small amounts of substitution, though T_{CO} is rapidly suppresed as x increases (Figure 4.7). For $Zn_{0.02}Ga_{0.98}V_2O_4$ $T_{CO} \approx 400$ K and for $Zn_{0.04}Ga_{0.96}V_2O_4$ $T_{CO} \approx 350$ K, and no distortion is observed for $Zn_{0.06}Ga_{0.94}V_2O_4$ above 90 K. $Zn_{0.125}Ga_{0.875}V_2O_4$ remains cubic at 5 K (Figure 4.8(a)). The discontinuity in the lattice parameter of this material at 5 K is likely to be the result of a weak spin-lattice coupling as a magnetic transition occurs at the same temperature; the magnetic behaviour of these materials will be discussed fully later in this Section.

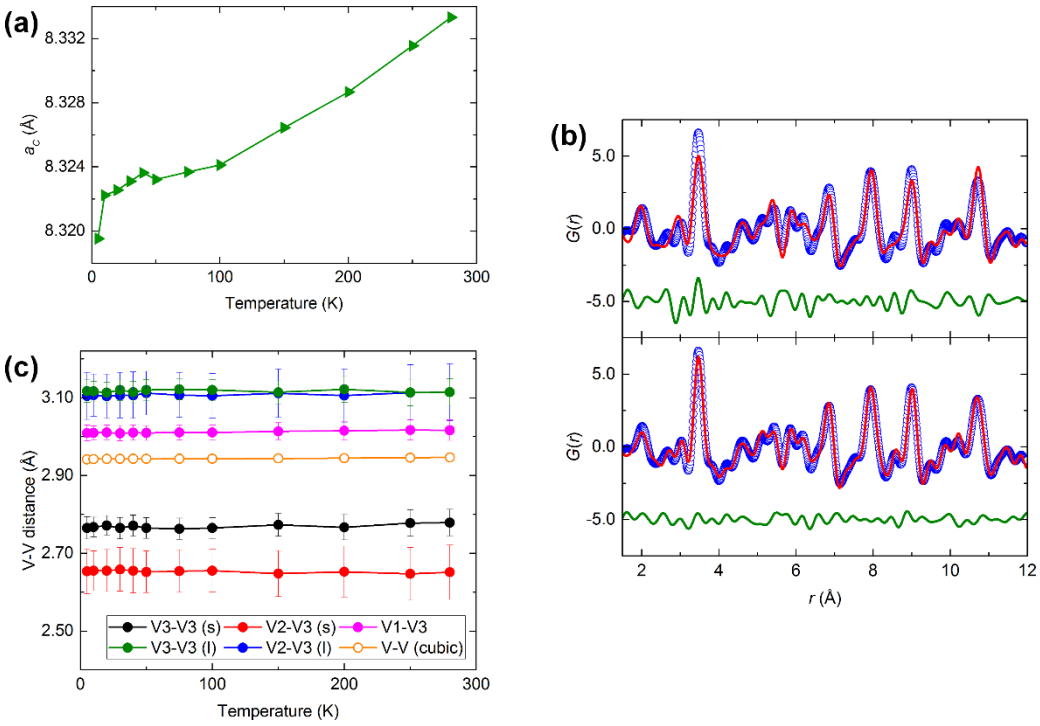

Figure 4.8: Characterisation of $Zn_{0.125}Ga_{0.875}V_2O_4$. **(a)** Thermal variation of the lattice parameter of the cubic average structure. **(b)** Fits to the 5 K PDF using an $Fd\bar{3}m$ model (upper, R_w = 28.9%) and an $R3m$ model (lower, R_w = 15.9%). **(c)** Thermal variation of the V-V nearest-neighbour distances determined from the $R3m$ local structure (filled symbols) and $Fd\bar{3}m$ average structure (open symbols).

This rapid suppression of the rhombohedral distortion with increasing x suggests that the interactions between orbital molecules, which are required for them to establish long-range order, are highly sensitive to the disruption induced by the

disordered distribution of *A*-site cations. However, as demonstrated by the high-temperature phase of GaV_2O_4, the loss of long-range orbital molecule order does not necessarily mean that local V-V bonds are broken. $Zn_{0.125}Ga_{0.875}V_2O_4$ has a cubic average structure at 5 K, but the corresponding PDF is much better fit by the $R3m$ model of V_3-V_4 cluster pairs that was used to describe the local structure of GaV_2O_4 (Figure 4.8(b)). Substantial local displacements of the vanadium sites are evidenced through the distribution of bonding (< 2.80 Å) and non-bonding (> 3.00 Å) V-V nearest-neighbour distances that are very different to the single 2.94 Å separation found in the cubic average structure, and these show very little variation with temperature (Figure 4.8(c)).

So that the structural variation, and in particular the V-site displacements that result from V-V bonding, could be studied in the $Zn_xGa_{1-x}V_2O_4$ system with respect to *x*, X-ray total scattering data were collected for all synthesised phases at both 90 K and room temperature and analysed through Rietveld and PDF fitting. In both types of fit the displacements of the vanadium sites can correlate with the thermal parameter used for those sites. As the thermal parameter is smaller at 90 K than at room temperature the effects of this correlation are less so the 90 K data are presented and discussed herein, though the same trends are also seen at room temperature.

The variation of crystal structure and average V-site displacement has been determined by Rietveld analysis (Figure 4.9). Below T_{CO} GaV_2O_4 has a rhombohedrally distorted lattice and, as previously shown in Figure 4.7, the same distortion is seen in $Zn_{0.02}Ga_{0.98}V_2O_4$ and $Zn_{0.04}Ga_{0.96}V_2O_4$. This distortion corresponds to an ordered orbital molecule phase, evidenced by the large (> 0.1 Å) refined displacements of the V2 and V3 sites from the positions they would occupy in a uniform spinel. For $x \geq 0.06$ the lattice is cubic, and the lattice parameter increases linearly with *x* in accordance with Vegard's law. Allowing seven-eighths of the vanadium intensity to displace away from the ideal spinel position, as was done for the high-temperature phase of GaV_2O_4 in Chapter 3, allows the vanadium disorder in the average structure to be described. This displacement decreases gradually, by ~0.05 Å, between $x = 0.06$ and $x = 0.625$,

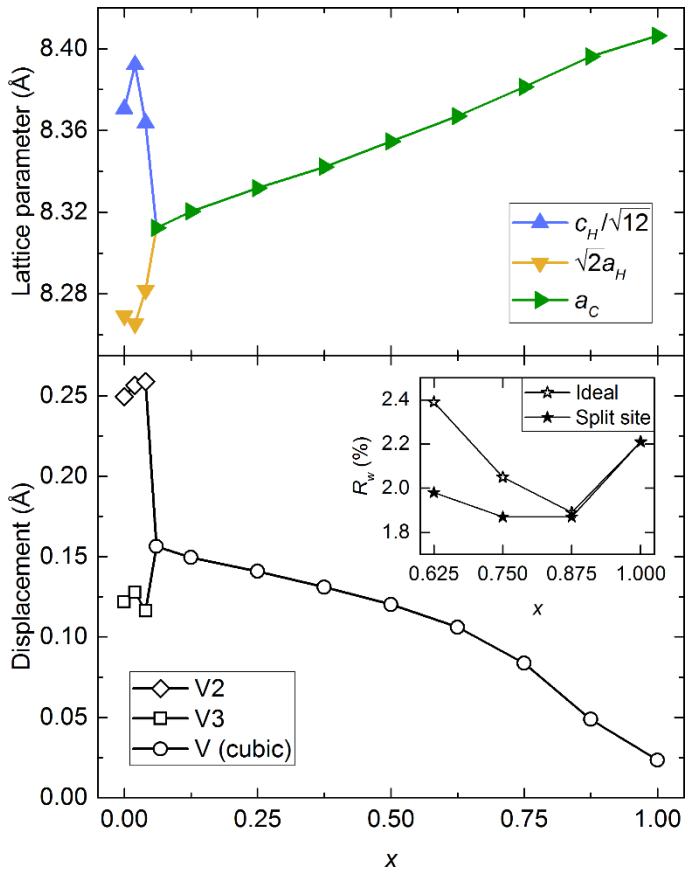

Figure 4.9: Structural parameters of $Zn_xGa_{1-x}V_2O_4$ phases at 90 K, from Rietveld refinements. For $x \leq 0.04$ the crystal structure is rhombohedrally distorted and V_3-V_4 cluster pairs have long-range structural order. In the cubic structure adopted when $x \geq 0.06$ significant displacement of vanadium intensity from the ideal spinel position indicates disorder in the average structure, as seen for GaV_2O_4 above T_{CO}. R_w values for Rietveld fits with the vanadium intensity fixed at its ideal position or allowed to refine as a split site are shown in the inset.

then decreases more rapidly as x increases further. As described in the previous Section ZnV_2O_4 has an ideal cubic structure above T_S = 50 K, in which the V-site displacement is zero, though a refined value of 0.02344(4) Å is actually obtained. This is likely due to the correlation between the displacement and the thermal parameter of the V site; a comparison of the R_w-factors for Rietveld fits in which the thermal parameter is refined and the vanadium is either fixed at the ideal site or allowed to refine as a split-site shows that for ZnV_2O_4, no improvement to the quality of the fit is made by allowing the site to split, but an increasing improvement is found at smaller x (Figure 4.9, inset).

The changing nature of the V-V bonding has been assessed on the local scale by PDF analysis (Figure 4.10). Fits, using the $R3m$ model of ordered V_3-V_4 pairs as used to describe the local structure of GaV_2O_4, were made to the PDFs of all $Zn_xGa_{1-x}V_2O_4$ phases. The hexagonal lattice parameters were constrained to be metrically cubic where appropriate, though the displacements of the V2 and V3 sites could be refined independently in all cases. For the phases with $x \leq 0.04$ the displacements of these two sites are comparable to those determined by Rietveld refinement, and they vary continuously through the rhombohedral-cubic distortion that occurs between $x = 0.04$ and $x = 0.06$. This implies that the orbital molecules undergo a substitution-induced order-disorder transition equivalent

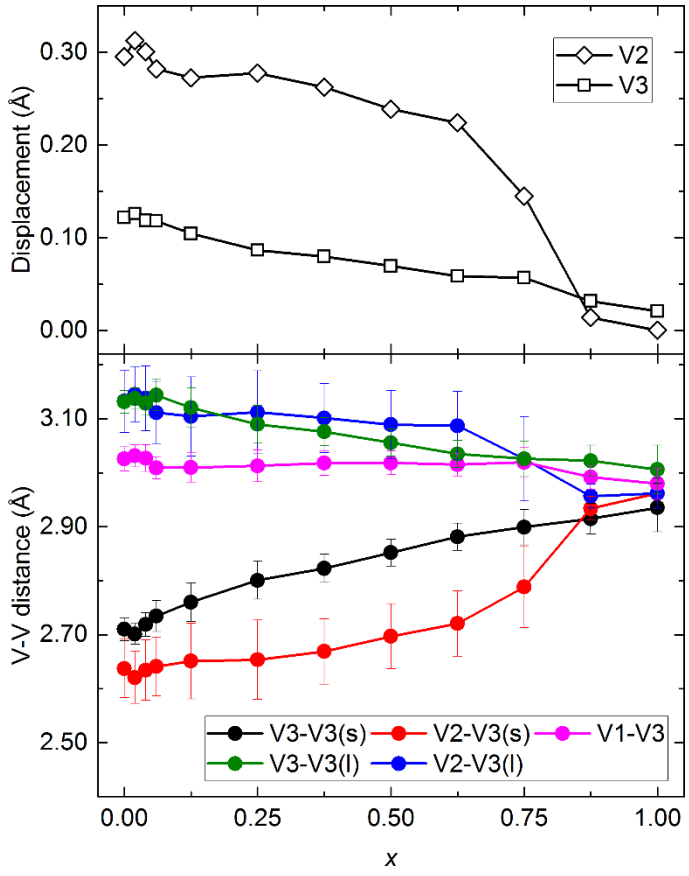

Figure 4.10: Structural parameters of $Zn_xGa_{1-x}V_2O_4$ phases at 90 K from PDF refinements, using an $R3m$ model for all x. The vanadium site displacements and V-V bond distances evolve continuously through the crystallographic distortion at low x, demonstrating an order-disorder transition of the orbital molecules. The rapid decrease of the V2-site displacement when $x > 0.625$, and corresponding convergence of V-V nearest-neighbour distances, evidences the decomposition of orbital molecules.

to the thermally-induced transition that occurs at T_{CO} in phases with $x \leq 0.04$. The displacements of both sites show a gradual decrease of ~0.05 Å between $x = 0$ and $x = 0.625$. The displacement of the V2 site shows critical behaviour, decreasing to zero when x is between 0.875 and 1. The displacement of the V3 site is smaller and decreases more steadily, reaching a value of 0.02 Å at $x = 1$. As with the corresponding Rietveld fit there is likely to be some correlation between this displacement and the thermal parameter of the vanadium sites such that it is non-zero.

The vanadium site displacements determined from the Rietveld and PDF analyses of the $Zn_xGa_{1-x}V_2O_4$ solid solutions indicate that the orbital molecules present in GaV_2O_4 remain stable upon substitution up to $x = 0.625$, but then break apart and are not present in ZnV_2O_4. This is demonstrated further by the distribution of V-V nearest-neighbour distances extracted from the PDF fits, also shown in Figure 4.10. Short and long distances, indicative of V-V bonding, remain distinct for $x \leq 0.625$ but converge at larger values of x, so that even with the non-zero displacement of the V3 site given by the Rietveld and PDF fits there is no significant difference between the shortest and longest V-V nearest-neighbour distances at $x = 1$.

Interestingly, in $Zn_{0.875}Ga_{0.125}V_2O_4$ the V3-V3 bond distance is significantly shorter than the average but the V2-V3 bond distance is not. This can also be seen in the V-V distances determined from fits to PDFs of this material collected between 5 K and 280 K. Like $Zn_{0.125}Ga_{0.875}V_2O_4$, $Zn_{0.875}Ga_{0.125}V_2O_4$ has a cubic average structure over this temperature range (Figure 4.11(a)), and like the discontinuity that can be seen in the lattice parameter of the former at 5 K, a discontinuity in the lattice parameter of the latter at 20 K coincides with a magnetic transition. Over the whole measured temperature range the PDFs of $Zn_{0.875}Ga_{0.125}V_2O_4$ are always better-fit by an $R3m$ model than an $Fd\bar{3}m$ one (Figure 4.11(b)), though only the two V3-V3 distances (2.91 Å and 3.02 Å) are significantly different from the 2.97 Å average separation (Figure 4.11(c)). In GaV_2O_4 the V3-site cations form V_3^{9+} trimers, so the retention of short V3-V3 distances suggests that these orbital molecules are still present at $x = 0.875$. Conversely, V2-V3 bonds are exclusively

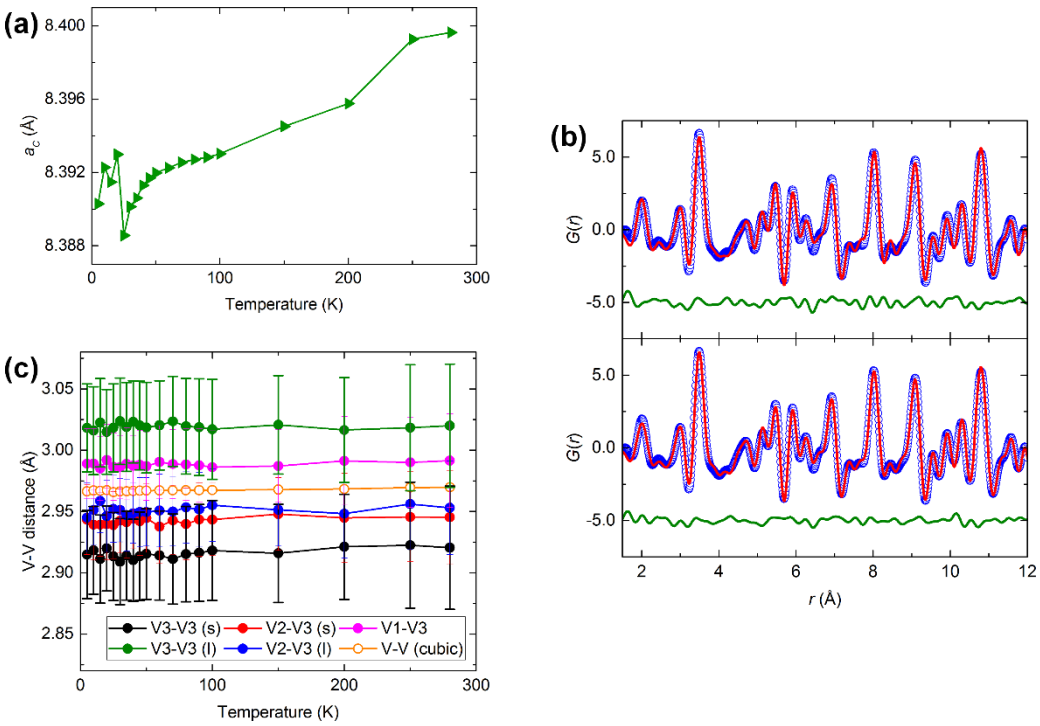

Figure 4.11: Characterisation of $Zn_{0.875}Ga_{0.125}V_2O_4$. **(a)** The refined lattice parameter of the cubic average structure. **(b)** Fits to the 5 K PDF using an $Fd\bar{3}m$ model (upper, R_w = 12.4%) and an $R3m$ model (lower, R_w = 10.0%). **(c)** Of the V-V nearest-neighbour distances in the local structure (filled symbols), only the two V3-V3 distances (error bars boldened for clarity) are significantly different from the average V-V separation (open symbols).

within V_4^{8+} tetramers, so the loss of significant V2-V3 bond-shortening implies that tetramers are not present in this phase. This can be rationalised by considering that the loss of bonding electrons that occurs as x increases is more likely to affect the bonds within orbital molecules formed of V^{2+} cations than those formed of V^{3+} cations.

This analysis of the X-ray total scattering data allows a phase diagram for the $Zn_xGa_{1-x}V_2O_4$ system to be constructed (Figure 4.12). The ground state of GaV_2O_4, which has a distorted $R\bar{3}m$ crystal structure with ordered V_3-V_4 orbital molecule pairs, is only stable at low T and low x. But, whilst the long-range order of orbital molecules is rapidly destabilised by Zn-substitution of the spinel A-site, the orbital molecules themselves are remarkably resilient and are present in $Zn_xGa_{1-x}V_2O_4$ phases to at least x = 0.875. The variable-temperature data collected for $Zn_{0.125}Ga_{0.875}V_2O_4$ and $Zn_{0.875}Ga_{0.125}V_2O_4$ demonstrate that if V-V bonding is

present in a material it shows little thermal variation, at least up to room temperature. The boundary for disordered orbital molecule stability is estimated at $x = 0.9$. The boundary for the suppression of the tetragonal distortion in ZnV_2O_4 is also estimated. 10% Li-substitution is sufficient to suppress this distortion,[114] so provides a reasonable estimate for the level of Ga-substitution that would have the same effect. Nonetheless, additional $Zn_xGa_{1-x}V_2O_4$ phases with $x \geq 0.875$ should be prepared so that these two estimated phase boundaries can be determined precisely.

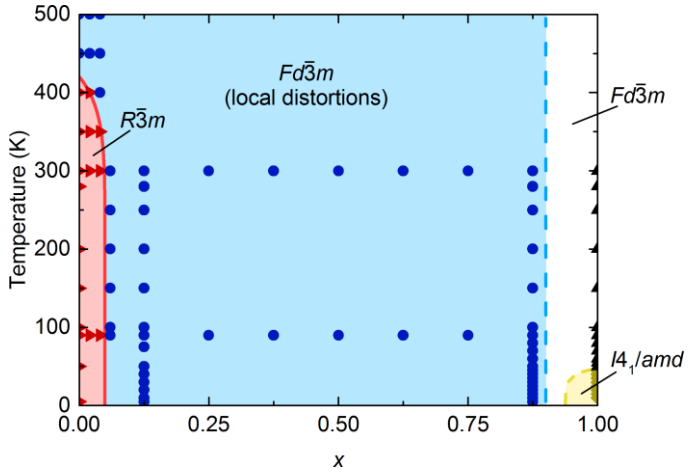

Figure 4.12: Structural phase diagram for the $Zn_xGa_{1-x}V_2O_4$ system, constructed from the X-ray total scattering analysis. V-V bonding that distorts the local structure is found in most compositions, though long-range orbital molecule order is only established in the $R\bar{3}m$ region at low x and low T. The undistorted $Fd\bar{3}m$ spinel structure is only adopted when x and T are large, though ZnV_2O_4 undergoes a tetragonal distortion at low T.

To accompany the structural analysis described above, magnetisation measurements were made for all the synthesised $Zn_xGa_{1-x}V_2O_4$ phases. In Chapter 3 the susceptibility of GaV_2O_4 was described as the sum of Curie-Weiss and temperature-independent terms, which account for the contributions to the total susceptibility of the non-bonding cations and the orbital molecules, respectively

$$\chi = \frac{C}{T - \theta} + A \qquad \textbf{(4.1)}$$

This description arises from the pairing of some d-electrons in V-V bonds and is not dependent on the orbital molecules formed by those bonds have long-range

order. It can, therefore, be used to describe the susceptibilities of systems in which the orbital molecules undergo an order-disorder transition and those in which long-range order is not observed.

Previous characterisation of ZnV_2O_4, in which orbital molecules do not form, has revealed very different magnetic behaviour in this material, with $S = 1$ paramagnetism at high temperatures evolving below 100 K into complex behaviour related to the spin- and orbital-ordering transitions. Nonetheless the paramagnetic susceptibility can also be described by Equation 4.1 as the small temperature-independent orbital component arising from the t_{2g}^2 electron configuration must also be accounted for, though very large values of C (≈ 3 emu K mol^{-1}) and θ (≈ -1000 K) have been reported.[118]

The susceptibilities of the $Zn_xGa_{1-x}V_2O_4$ phases show only gradual variation with x as it is increased (Figure 4.13). Fits of Equation 4.1 were made to all susceptibilities over the temperature range 100-300 K, and these are provided in Appendix C. The three parameters C, θ and A were fit independently to all susceptibilities except that of ZnV_2O_4, for which $A = 2.2 \times 10^{-4}$ emu mol^{-1} was fixed at the value determined by previous high-temperature measurements.[108] A cusp, indicating a magnetic transition at temperature T_{spin}, is also seen in the susceptibilities of all the $Zn_xGa_{1-x}V_2O_4$ phases. In GaV_2O_4 this transition is the spin-glass freezing of the non-bonding V^{3+} spins, whilst in ZnV_2O_4 it is the antiferromagnetic ordering of all the V^{3+} spins.

The variation of C, θ, A and T_{spin} with x is shown in Figure 4.14. In GaV_2O_4 A is the only one of these four parameters that arises from the contribution of the orbital molecules to the overall susceptibility; the others are related to the interactions between the non-bonding cations. For $0 \leq x \leq 0.375$ C, θ and T_{spin} show little variation, implying that in this range of x the interactions between the non-bonding cations are unaffected by the removal of d-electrons caused by increasing x. By extension, this indicates that the ratio of one non-bonding V^{3+} to seven bonding cations is maintained. The removal of d-electrons instead appears to weaken the V-V bonds without breaking up the orbital molecules. A is dependent on the mixing of a triplet excited state into the singlet ground state; removing d-

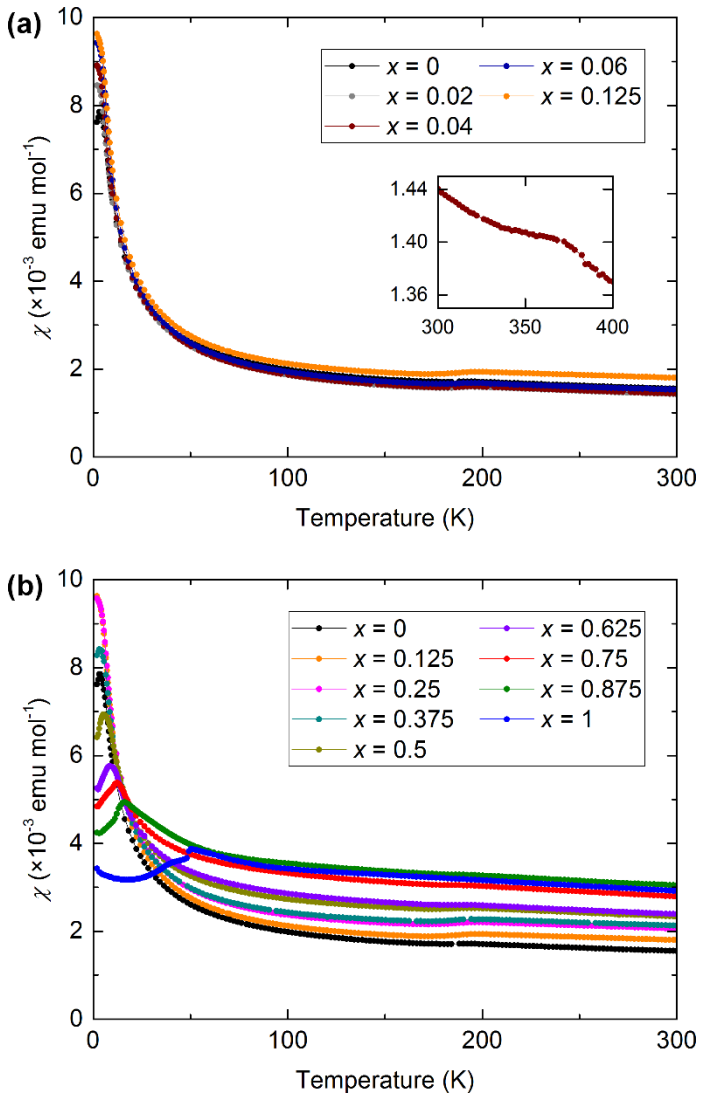

Figure 4.13: The magnetic susceptibilities of all synthesised $Zn_xGa_{1-x}V_2O_4$ phases. **(a)** Very little change to the susceptibilities is seen between $x = 0$ and $x = 0.125$ though a discontinuity, shown in the inset, is seen in the $x = 0.04$ susceptibility at T_{CO}. **(b)** The gradual variation of the susceptibilities over the whole range of x is consistent with the gradual structural changes seen in the total scattering data.

electrons weakens the V-V bonds so the energy gap between the ground and excited states is reduced, more mixing can occur and A becomes larger. The value of A determined from fits of Equation 4.1 increases from 1.34 $\times 10^{-3}$ emu mol^{-1} for GaV_2O_4 to 2.06 $\times 10^{-3}$ emu mol^{-1} for $Zn_{0.375}Ga_{0.625}V_2O_4$.

For $x \geq 0.5$, C and θ become increasingly large and A simultaneously becomes smaller. An increasing paramagnetic contribution, and corresponding decrease of

the temperature-independent contribution, to the overall susceptibility is consistent with the breakup of orbital molecules into non-bonding species, which would be expected as the *d*-electrons that form V-V bonds are removed. This breakup is also evident in the increase of T_{spin}, from 4 K in $Zn_{0.375}Ga_{0.625}V_2O_4$ to 16 K in $Zn_{0.875}Ga_{0.125}V_2O_4$; as more non-bonding cations become available, a greater number of interactions are possible and the spin-glass state is stabilised. Finally, A, C, θ, and T_{spin} all show a dramatic change between $x = 0.875$ and $x = 1$, which corresponds to the complete decomposition of the orbital molecules and the establishment of the paramagnetic state of ZnV_2O_4.

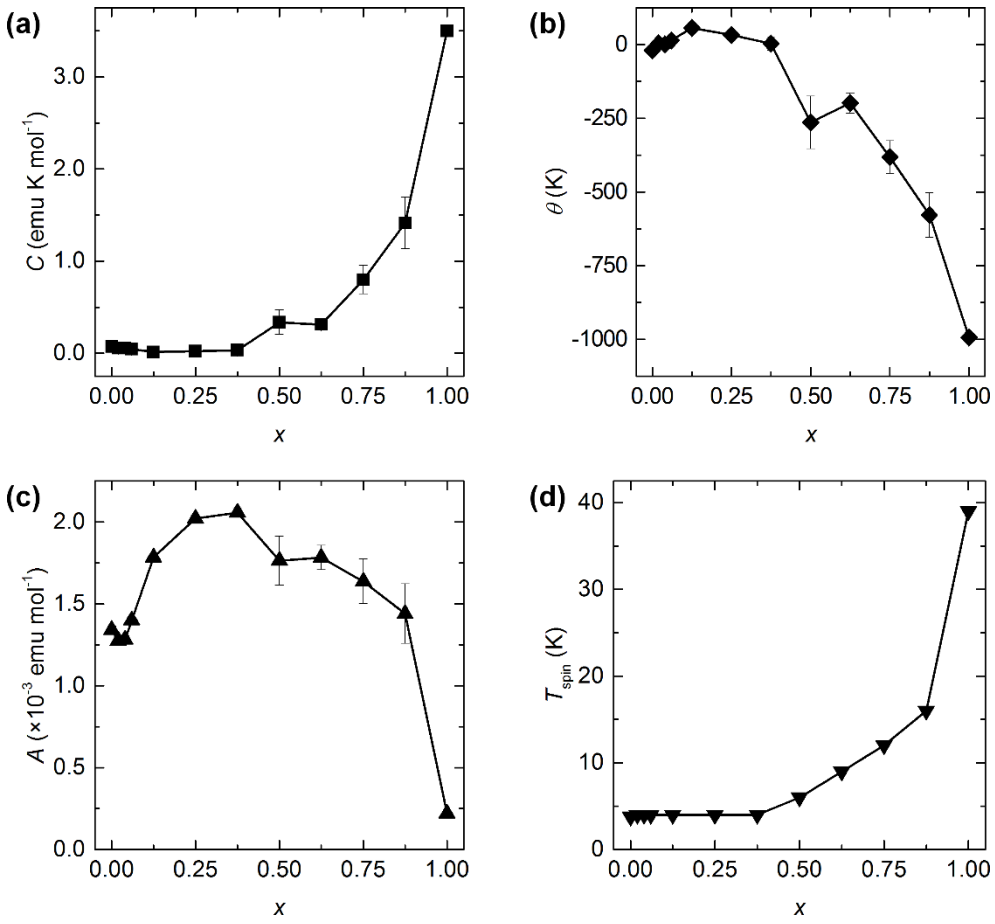

Figure 4.14: The three parameters obtained from fits of Equation 4.1 to the susceptibilities in Figure 4.13 are plotted in **(a)**, **(b)** and **(c)** Their variation is consistent with V-V bonds being weakened, and then decomposing, as x increases. **(d)** All susceptibilities show a low-temperature magnetic transition at temperature T_{spin}. Except for $x = 1$, where it is due to antiferromagnetic ordering, this transition arises from the formation of a spin-glass state by the V^{3+} cations not involved in V-V bonding.

The magnetic behaviour of the $Zn_xGa_{1-x}V_2O_4$ phases is therefore consistent with the structural behaviour deduced from the X-ray total scattering data. The orbital molecules found in GaV_2O_4 are initially persistent as x increases, but gradually decompose as x is increased above 0.5 and are absent when x = 1. The total scattering data also showed that when orbital molecules are present they are thermally stable to at least room temperature, and the absence of any discontinuities or deviations in the measured susceptibilities corroborates this description. The only discontinuity is seen in the susceptibility of $Zn_{0.04}Ga_{0.96}V_2O_4$ at 370 K (Figure 4.13(a), inset) and corresponds to the order-disorder transition that was identified at ~350 K by Rietveld analysis. Similar discontinuities are not seen in the more heavily-substituted phases, in agreement with the structural data that showed the rapid suppression of long-range orbital molecule ordering upon *A*-site substitution.

4.3.3: $Li_{0.5}Ga_{0.5}V_2O_4$

To explore the effects of substituting other cations on the orbital- and charge-ordering in GaV_2O_4, $Li_{0.5}Ga_{0.5}V_2O_4$ was also synthesised. For a given concentration x, substitution of Li^+ into GaV_2O_4 removes twice as many *d*-electrons as does substitution of Zn^{2+}; hence, $Li_{0.5}Ga_{0.5}V_2O_4$ is isoelectronic with ZnV_2O_4, with each vanadium having a t_{2g}^2 electron configuration. Furthermore, given the large charge difference between Li^+ and Ga^{3+} it may be expected that the *A*-site cations in $Li_{0.5}Ga_{0.5}V_2O_4$ have structural order, as is found in $Li_{0.5}Ga_{0.5}Cr_2O_4$.[115]

Variable-temperature powder neutron diffraction was used to study the crystal structure of $Li_{0.5}Ga_{0.5}V_2O_4$ and reveals that this material adopts the $Fd\bar{3}m$ cubic spinel structure at all temperatures down to 4.2 K (Figure 4.15). The additional reflections that would arise if $Li_{0.5}Ga_{0.5}V_2O_4$ adopted the $F\bar{4}3m$ symmetry of $Li_{0.5}Ga_{0.5}Cr_2O_4$ are not seen, implying that in this material Li^+ and Ga^{3+} have a disordered distribution over the *A*-site. Li and Ga have a high neutron scattering contrast, with coherent scattering lengths of -1.90 fm and 7.29 fm respectively,[70] and a refined *A*-site occupancy of 0.470(2) Li:0.530(2) Ga was obtained. Furthermore, the lack of a structural distortion in $Li_{0.5}Ga_{0.5}V_2O_4$ implies that the

ordered ground state of ZnV_2O_4 does not form in an isoelectronic but structurally disordered system. This again demonstrates that the long-range ordering found in ZnV_2O_4 is sensitive to structural perturbations.

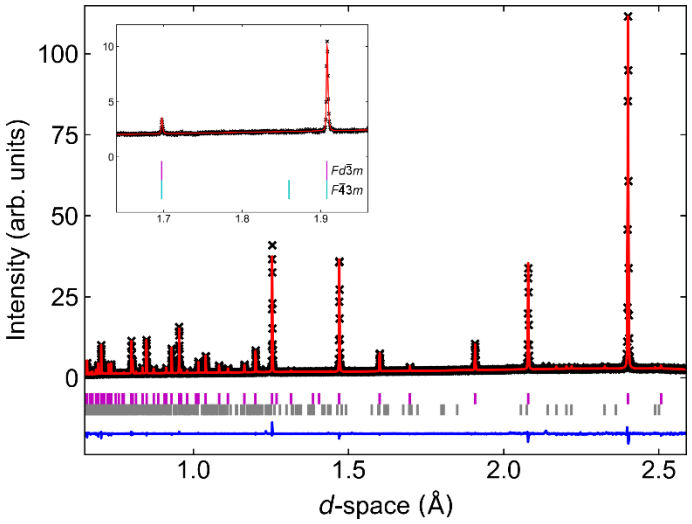

Figure 4.15: Rietveld fit to the powder neutron diffraction pattern of $Li_{0.5}Ga_{0.5}V_2O_4$ collected at 4.2 K (R_w = 3.71%). Tickmarks correspond to the spinel phase (pink), which has $Fd\bar{3}m$ symmetry, and a V_2O_3 impurity with 2.2% weight fraction (grey). In the expanded region shown in the inset the additional reflection of a lower-symmetry structure, in which the *A*-site cations are ordered, is not seen.

The low-temperature structural and magnetic behaviours of $Li_{0.5}Ga_{0.5}V_2O_4$ are compared in Figure 4.16. The cubic lattice parameter a_C was obtained from Rietveld refinements against the neutron diffraction data; a value of 8.31532(3) Å is obtained at 4.2 K and a_C shows little temperature-dependence below 60 K, though it increases to a value of 8.32376(1) Å at 300 K. Moreover, although a structural distortion is not observed in $Li_{0.5}Ga_{0.5}V_2O_4$ its magnetic susceptibility exhibits a transition at 16 K below which the zero-field cooled and field cooled susceptibilities diverge. This behaviour is similar to that of the $Zn_xGa_{1-x}V_2O_4$ phases in which orbital molecules are present, which have a magnetic transition at T_{spin} arising from the formation of a spin-glass state by the non-bonding V^{3+} cations. As done for the $Zn_xGa_{1-x}V_2O_4$ susceptibilities Equation 4.1 was fit to the susceptibility of $Li_{0.5}Ga_{0.5}V_2O_4$ between 100 K and 300 K, giving C = 0.75(2) emu K mol^{-1}, θ = -251(7) K, and A = 1.28(3) ×10^{-3} emu mol^{-1}. From comparison to Figure 4.14 these values are similar to those of $Zn_{0.75}Ga_{0.25}V_2O_4$,

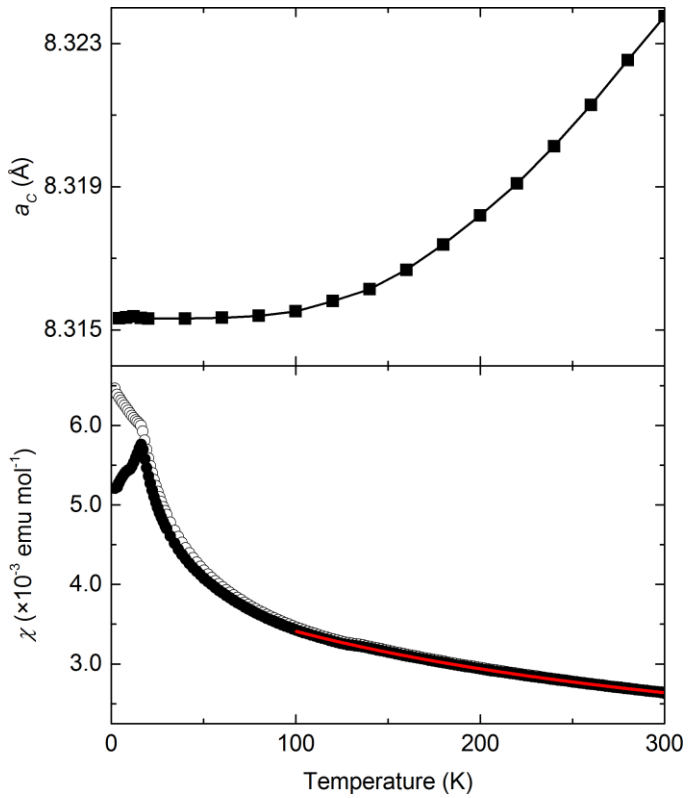

Figure 4.16: The cubic lattice parameter a_C of $Li_{0.5}Ga_{0.5}V_2O_4$ varies monotonically between 4.2 K and 300 K. The lack of a structural distortion demonstrates that long-range orbital ordering is not established. However, its magnetic behaviour is comparable to $Zn_xGa_{1-x}V_2O_4$ phases with disordered orbital molecules. A magnetic transition can be seen at T_{spin} = 16 K, and the fit of Equation 4.1 between 100 K and 300 K is shown.

and the analysis of the total scattering data collected for that material, discussed in the previous Section, clearly reveals the presence of disordered orbital molecules. This would suggest that disordered orbital molecules are also present in $Li_{0.5}Ga_{0.5}V_2O_4$. Due to the weak diffraction of neutrons by vanadium the Rietveld analysis of the obtained data was not sensitive to a site splitting that could be used to infer the presence of disordered orbital molecules in the average structure of $Li_{0.5}Ga_{0.5}V_2O_4$, so an X-ray total scattering study should be conducted to confirm the nature of its local structure.

Nonetheless, orbital molecules do seem to be present in $Li_{0.5}Ga_{0.5}V_2O_4$. This material is isoelectronic with ZnV_2O_4, with two *d*-electrons *per* vanadium cation. Orbital molecules are not found in ZnV_2O_4, so $Li_{0.5}Ga_{0.5}V_2O_4$ is electron-deficient with respect to the $Zn_xGa_{1-x}V_2O_4$ phases with $x \leq 0.875$ in which disordered orbital

molecules have been identified. A comparison of the lattice parameters in Figure 4.16 and Figure 4.9 shows that of $Li_{0.5}Ga_{0.5}V_2O_4$ to be similar to that of $Zn_{0.06}Ga_{0.94}V_2O_4$, and about 0.1 Å smaller than that of ZnV_2O_4. Therefore, the relative lack of *d*-electrons with which V-V bonds can form in $Li_{0.5}Ga_{0.5}V_2O_4$ appears to be compensated for by the relatively short V-V nearest-neighbour distance, which allows the strength of the direct V-V orbital interactions to be increased sufficiently for an orbital molecule state to be stabilised.

The formation of disordered orbital molecules may also explain why the *A*-site cations in $Li_{0.5}Ga_{0.5}V_2O_4$ do not order as they do in $Li_{0.5}Ga_{0.5}Cr_2O_4$. The order in $Li_{0.5}Ga_{0.5}Cr_2O_4$ has been suggested to arise as a means of minimising the electrostatic repulsions between monovalent and trivalent *A*-site cations,[115] and though this ordering lowers the cubic symmetry and allows the *B*-*B* nearest-neighbour distances to shorten, the breathing pyrochlore lattice thus formed restricts the geometry of possible orbital molecules to a template of B_4 tetrahedral units. Cr^{3+} does not have an orbital degree of freedom, so an ordering transition to form orbital molecules is not possible in $Li_{0.5}Ga_{0.5}Cr_2O_4$. In $Li_{0.5}Ga_{0.5}V_2O_4$ such a transition is possible, and appears to occur, so the adoption of the disordered high-symmetry structure by this material must indicate that the orbital molecules are better-stabilised in this structure than the cation-ordered low-symmetry one. This could be due to the geometric restrictions of the breathing pyrochlore lattice; two *d*-electrons are available to each V^{3+} so the bonding within each V_4 unit could give a V_4^{12+} tetramer that would be electron-deficient, two V_2^{6+} dimers that would be electron-rich, or electron-precise V_3^{9+} trimers with a non-bonding cation left out. Conversely, as the disordered structure does not restrict which neighbouring V^{3+} cations can form V-V bonds the system can freely establish the most stable orbital molecule state, and a total scattering study would reveal its nature.

4.4: Conclusions

The ground states of ZnV_2O_4 and MgV_2O_4 arise from a complex interplay of electronic correlations, spin-orbit coupling and cooperative Jahn-Teller distortions.[119] It has been suggested that the electrons occupying the degenerate d_{xz} and d_{yz} orbitals are partially delocalised, forming homopolar bonds between neighbouring V^{3+} cations that have ferromagnetically-oriented spins.[111] However, the bond-alternation predicted to accompany such delocalisation is not evident in either the periodic or local structures of these materials. This could be because delocalisation is simply not occurring, and long-range ferro-orbital order of localised electrons consistent with the crystal symmetry is established,[104] or because the weak bond-alternation that has also been suggested for a delocalised regime is realised.[116] Further investigations are required to understand the complex electronic interactions in ZnV_2O_4 and MgV_2O_4, though their local structures have now been quantitatively analysed for the first time.

That said, V-V dimerisation may be important to other properties of the $A^{2+}V_2O_4$ spinels. Electric polarisation measurements have demonstrated that CdV_2O_4 is a ferroelectric whilst ZnV_2O_4 and MgV_2O_4 are not, and electronic structure calculations have suggested that this arises from variations of the V-O bond distances caused by V-V dimerisation.[120] This has not been confirmed by structural experiments, so a total scattering study of CdV_2O_4 that can be compared to that of ZnV_2O_4 and MgV_2O_4 detailed in this Chapter would be of value. Furthermore, the role of dimerisation in the behaviour of these materials under high pressures should be considered. Several $A^{2+}V_2O_4$ spinels approach an insulator-metal transition as the lattice is compressed and the V-V distance is shortened towards the critical separation required for itinerant behaviour.[121,122] X-ray diffraction has revealed that at room temperature ZnV_2O_4 undergoes structural transitions at 10 GPa and 21 GPa,[110] but how these are related to the transition to itinerant behaviour, and whether the partial or full delocalisation of the *d*-electrons results in V-V bonds being formed, remains to be resolved.

Orbital molecules are present in the ground state of GaV_2O_4. The substitution of Ga^{3+} with Zn^{2+} or Li^{+} reveals that, whilst their long-range order is rapidly supressed, the orbital molecules themselves are highly resilient to the structural and electronic perturbations induced by the substitution. It appears that both the vanadium oxidation state and the V-V nearest-neighbour separation are important in determining whether V-V bonds are formed, and these parameters can be controlled by both the choice of Zn^{2+} or Li^{+} as the substituting cation and their concentration. In the $Zn_xGa_{1-x}V_2O_4$ system the average charge and size of the *A*-site is varied simultaneously, so a greater insight into the control of V-V bonding could be gained by investigating the effects of varying them separately. This would require systems in which the *A*-site cations have the same size but different valences, such as $Zn_xIn_{1-x}V_2O_4$, and systems in which the *A*-site cations that have the same valence but different sizes, such as $Li_{0.5}A'_{0.5}V_2O_4$ with *A*' = Ga^{3+}, Al^{3+} or In^{3+}. Varying the radius of the *A*-site cation uses chemical pressure to tune the V-V nearest-neighbour separation. Similarly, applying external pressure should also offer a route to controlling the formation and ordering of orbital molecules in vanadium oxide spinels.

Chapter 5: Structural studies of LiV_2O_4

5.1: Introduction

The ground states of vanadium oxide spinels vary according to the charge, spin and orbital degrees of freedom that are available. Perhaps the most unusual is that of LiV_2O_4, in which the first example of a *d*-electron heavy-fermion state was discovered.[32] In heavy-fermion systems, strong correlations cause the effective mass of the electrons to increase by several orders of magnitude. This behaviour had previously only been found for the *f*-electrons of some lanthanide and actinide intermetallics, such as $CeAl_3$, $CePd_2Si_2$ and UPt_3, in which heavy fermions are related to unusual phenomena such as unconventional superconductivity and quantum criticality.[123,124] The discovery of similar behaviour in LiV_2O_4 has thus drawn considerable attention to this material.

LiV_2O_4 is a cubic spinel with the normal cation distribution. At high temperatures it is a metal, though a relatively poor one due to the electron correlations, and has a Curie-Weiss magnetic susceptibility of localised S = ½ spins.[125] The heavy-fermion state forms below 28 K.[32] This is most clearly seen in the electronic heat capacity coefficient $\gamma(T) = C(T)/T$, which increases to 0.42 J mol^{-1} K^{-2} as the heavy fermion correlations emerge. This is an exceptionally large value for a transition metal oxide – $\gamma(T)$ is 0.018 J mol^{-1} K^{-2} in $LiTi_2O_4$[126] and 0.07 J mol^{-1} K^{-2} in V_2O_3[127] – but is comparable to the values found for *f*-electron heavy-fermion systems, such as 0.42 J mol^{-1} K^{-2} in UPt_3 and 1.62 J mol^{-1} K^{-2} in $CeAl_3$.[123] The crossover from localised-moment to heavy-fermion behaviour can also be seen in magnetic susceptibility and resistivity measurements,[32,125] and in changes to the electronic structure, which has been probed through photoemission spectroscopy and optical reflectivity measurements.[128,129]

Despite intense experimental and theoretical interest, the mechanism by which heavy fermions are formed in LiV_2O_4 remains unknown. The vanadium oxidation state is +3.5, giving an average of 1.5 *d*-electrons *per* vanadium cation, so spin, charge and orbital degrees of freedom must all be considered. Importantly, the crystal structure of LiV_2O_4 remains cubic in the heavy-fermion phase.[130] The pyrochlore lattice of vanadium cations therefore has no periodic distortion, so geometric frustration inhibits long-range order – neither magnetic ordering nor spin-glass freezing occurs above 2 K.[32] However, short-range interactions are likely to be important. Antiferromagnetic fluctuations that become enhanced in the heavy-fermion state have been identified through inelastic neutron scattering and NMR experiments.[131,132] The excitations seen in neutron scattering spectra have been attributed to antiferromagnetic interactions along the V-V chains that make up the pyrochlore lattice, and also reveal that the spin of each V cation is partially delocalised, with the delocalised component occupying a sufficiently large volume that those of neighbouring cations overlap.[133] Furthermore, theoretical work incorporating orbital interactions has demonstrated that the ground state of LiV_2O_4 can be represented by simple molecular orbitals on V_4 tetrahedra, that the dominant interactions are exchange processes between neighbouring V_4 tetrahedra, and that the overall properties of this material are determined by local spin and orbital degrees of freedom.[134] These results are suggestive of an orbital-molecule -like state, with V-V bonds formed within the tetrahedra of the pyrochlore lattice. The lack of a crystallographic distortion shows that structurally-ordered orbital molecules are not present in the heavy fermion phase of LiV_2O_4 but as its local atomic structure has not previously been studied it is not known whether disordered orbital molecules, perhaps related to the short-range fluctuations thought to be responsible for the effective-mass enhancement, are present.

A second reason to consider that orbital molecules may be found in LiV_2O_4 arises from its behaviour under pressure. Whilst this material is metallic at ambient pressure, resistivity measurements have revealed a transition to an insulating state when the pressure is increased above 6.8 GPa at low temperatures.[135] A

thorough exploration of the *p*-*T* phase diagram of LiV_2O_4 was made using optical reflectivity measurements, and identified three distinct phases (Figure 5.1).[136] Two phases with markedly different conductivities, corresponding to metallic and insulating behaviour, were found at low pressures and high pressures respectively. The measured conductivities of these phases show little pressure-dependence, but they are separated by an intermediate phase in which the change from metallic to insulating conductivity gradually occurs.

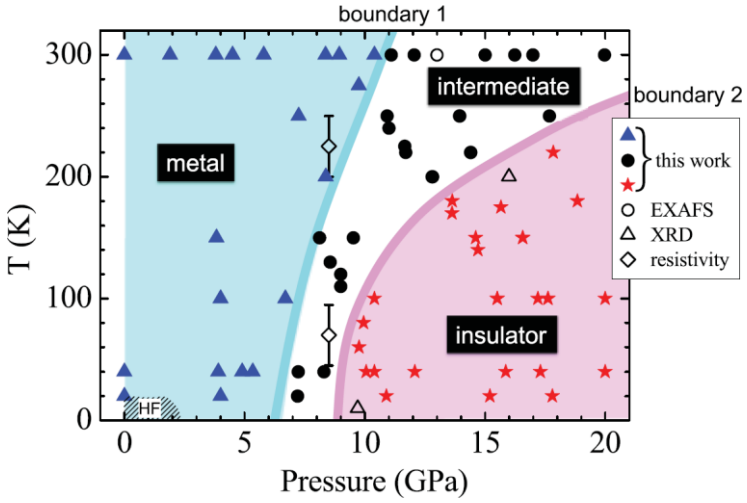

Figure 5.1: *p*-*T* phase diagram of LiV_2O_4 determined from optical reflectivity measurements. Figure reproduced from Ref. 136.

That LiV_2O_4 undergoes a metal-insulator transition is reminiscent of the behaviour of VO_2 and other vanadium oxides, in which such behaviour is the result of an orbital molecule state being formed. A band gap of 0.4 eV, similar in magnitude to that found in AlV_2O_4 and GaV_2O_4 (Chapter 3) has been determined from the optical spectra of LiV_2O_4 in the insulating phase. In addition, ^{7}Li- and ^{51}V-NMR experiments have revealed a partial transition from local-moment to spin-singlet magnetic behaviour concurrent with the transition between the metallic and intermediate phases shown in Figure 5.1.[137] To rationalise this observation, it was suggested that the change of properties occurring at this phase boundary is the result of the pairing of electrons into V-V bonds to form tetrahedral V_4 clusters.

Theoretical work[134] has suggested that LiV_2O_4 has several near-degenerate low-energy states; as compression shortens the V-V nearest-neighbour distances and improves t_{2g}-t_{2g} orbital overlap, a state in which the electrons are stabilised by forming V-V bonds should become favoured at high pressures. However, the structure of the high-pressure phase of LiV_2O_4 have not been determined. The only reported diffraction study has revealed that the Bragg peaks of the cubic metallic phase split above 12.8 GPa at 10 K, and are recovered upon warming above 200 K at 16 GPa.[135] Based on which peaks split the distorted structure was suggested to have rhombohedral symmetry, though no indexing or structural refinement was reported. EXAFS, a local structure probe, has also found a distortion above 12 GPa at room temperature.[138] Analysis of the first two coordination shells suggested that the distortion gave a structure similar to the heptamer structure of AlV_2O_4, with V-V nearest-neighbour distances ranging from 2.66 Å to 3.09 Å. Nonetheless, the relationship between the structure and properties of LiV_2O_4 under pressure is not fully understood.

To investigate the possibility of orbital molecules contributing to the unusual electronic behaviour of LiV_2O_4, two structural studies have been undertaken. Firstly, X-ray total scattering has been used to identify any local-structure distortions that accompany the formation of heavy fermions in the ambient-pressure ground state. Secondly, powder X-ray diffraction has been used to study how the structure of this material changes under pressure at the phase boundaries previously determined by property measurements.

5.2: Experimental

A 0.5 g powder sample of LiV_2O_4 was synthesised by a high-temperature solid-state reaction similar to a previously reported method.[114] Two precursors were prepared in advance: V_2O_3 by reducing V_2O_5 (Alfa Aesar, 99.6%) under flowing H_2 at 900 °C, and Li_3VO_4 by the reaction of Li_2CO_3 (Sigma-Aldrich, 98%, with a 5% molar excess used to account for Li evaporation) and V_2O_5 in air at 800 °C for 36 hours. To synthesise LiV_2O_4 suitable quantities of Li_3VO_4, V_2O_3 and V_2O_5 in the

stoichiometric ratio were ground together and pressed into a pellet. This was held in a closed gold capsule within a quartz ampoule that was evacuated and sealed, and heated at 900 °C for 48 hours. Lab X-ray diffraction, using a Bruker D2 Phaser powder diffractometer, was used to confirm that the reaction had reached completion. The zero-field cooled DC magnetisation of the sample was measured with a Quantum Design SQUID MPMS-XL in a 1000 Oe applied field.

X-ray total scattering data were collected using the two-dimensional detector configuration of ESRF beamline ID22. A portion of the sample was loaded into a borosilicate capillary 0.7 mm in diameter. A He cryostat was used for temperature control and data were collected at temperature steps from 5 K to room temperature using 60 keV radiation (λ = 0.206547 Å). 201 exposures were collected at each temperature step and averaged to give a total scattering pattern. Rietveld analysis of these patterns was carried out using GSAS.[77] Additionally, after suitable background corrections had been made, the data were converted into structure functions $S(Q)$ and hence transformed to atomic pair distribution functions $G(r)$ using PDFgetX3,[83] for momentum transfers $0.5 \leq Q$ (Å^{-1}) ≤ 20.2. Structural models were refined against $G(r)$ over the interatomic distance range $1.5 \leq r$ (Å) ≤ 10 using PDFgui,[84] including simulation of termination ripples.

High-pressure powder X-ray diffraction data were collected at ESRF beamline ID15B using membrane-type diamond anvil cells (DACs). Two identical DACs were prepared. In each, a portion of the sample was loaded into a stainless steel gasket between anvils with culets 0.3 mm in diameter. He was used as the pressure transmitting medium, and the ruby fluorescence method[91] was used for pressure determination. One DAC was used for measurements at room temperature, with the pressure systematically increased until the gasket failed above 21 GPa. The second DAC was cooled using a He cryostat, and a first set of measurements were made at 20 K on compression to approximately 15 GPa. The DAC was then warmed to 100 K whilst maintaining this pressure, and a further set of measurements were made on decompression at 100 K. Diffraction patterns were collected using 30 keV radiation (λ = 0.411536 Å) and a Marresearch mar555 two-dimensional detector, and processed using DIOPTAS.[139] A 1 s

exposure was collected at each pressure step, with the DAC rocked by ±3° during the exposure to improve powder averaging. Nonetheless the measured Bragg intensities and profiles were strongly affected by texturing and strain effects. This prevented meaningful Rietveld refinements from being carried out, though Le Bail refinements could be performed and were done using GSAS.

5.3: Results and discussion

5.3.1: Total scattering at ambient pressure

Short-range spin and orbital ordering is thought to be important in the formation of the heavy-fermion ground state of LiV_2O_4, so X-ray total scattering was used to determine whether these degrees of freedom are coupled to any local-scale structural distortions. Powder neutron diffraction has shown that the average structure of LiV_2O_4 remains cubic in the ground state.[130] Rietveld analysis of the collected total scattering data confirm that the synthesised sample has the expected $Fd\bar{3}m$ cubic spinel structure at all temperatures between 5 K and 290 K (Figure 5.2). The refined lattice parameter a_C is 8.22846(4) Å at 5 K and 8.24445(1) Å at 290 K, comparable to values of 8.22672(3) Å at 4 K and 8.24039(3) Å at 295 K determined by neutron diffraction.[130] No antisite disorder could be identified, and although two impurity phases, V_2O_3 and V_3O_5, are present both are minor, with weight fractions 0.9% and 0.4% respectively.

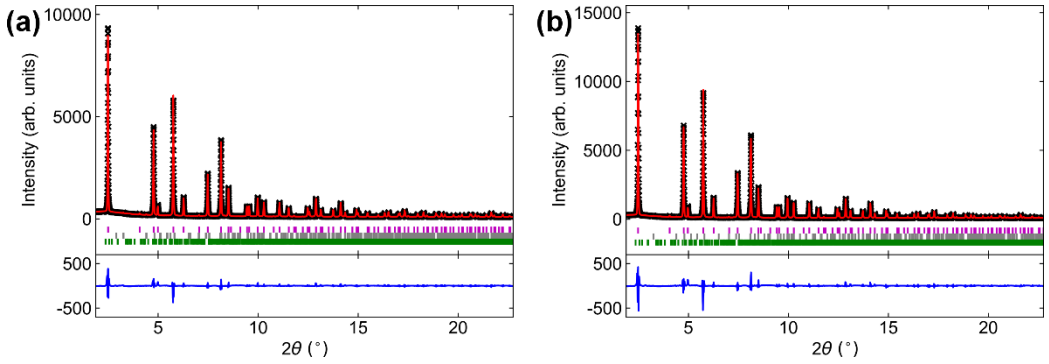

Figure 5.2: Rietveld fits to the total scattering patterns of LiV_2O_4 at **(a)** 5 K (R_w = 4.0%) and **(b)** 290 K (R_w = 4.7%), demonstrating that the average structure of LiV_2O_4 adopts $Fd\bar{3}m$ symmetry at all temperatures. Tick marks correspond to LiV_2O_4 (pink), V_2O_3 (grey) and V_3O_5 (green).

Whilst no crystallographic changes accompany the onset of heavy-fermion behaviour in LiV_2O_4, it is evident in measurements of the magnetic susceptibility (Figure 5.3). At high temperatures the spins of the vanadium cations are localised and Curie-Weiss behaviour is followed; a linear fit to the inverse susceptibility gives C = 0.962 emu K mol^{-1} and θ = -46.3 K. These are in line with reported values of $C \approx$ 0.9 emu K mol^{-1} and $\theta \approx$ -40 K, which show some variation according to the method of sample preparation.[140] The discontinuity seen in the susceptibility at 25 K corresponds to the crossover from local-moment to heavy-fermion behaviour. The susceptibility in the heavy-fermion state is nearly temperature-independent, though paramagnetic impurities in the spinel structure are commonly found in LiV_2O_4 samples and are the cause of the susceptibility increase seen below 10 K. Such impurities typically have concentrations of less than 1% and do not affect the heavy-fermion behaviour.[140]

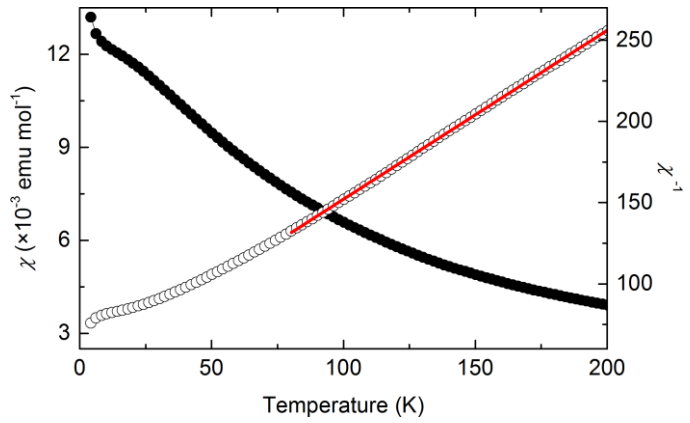

Figure 5.3: The magnetic susceptibility of LiV_2O_4 (filled symbols), and its inverse (open symbols). A linear Curie-Weiss fit to the inverse susceptibility between 80 K and 200 K is shown. The discontinuity seen at 25 K is due to the onset of heavy-fermion correlations, whilst the increase seen below 10 K is due to paramagnetic impurities.

The formation of heavy fermions changes the properties of LiV_2O_4 without distorting its crystal structure. PDFs generated from the total scattering data were used to establish whether any local structural distortions accompany this change of properties (Figure 5.4). As would be expected the 290 K PDF is well fit by an $Fd\bar{3}m$ cubic model consistent with the average structure, with a V-V nearest-neighbour distance of 2.915(1) Å. The 5 K PDF is also well fit by this model, with

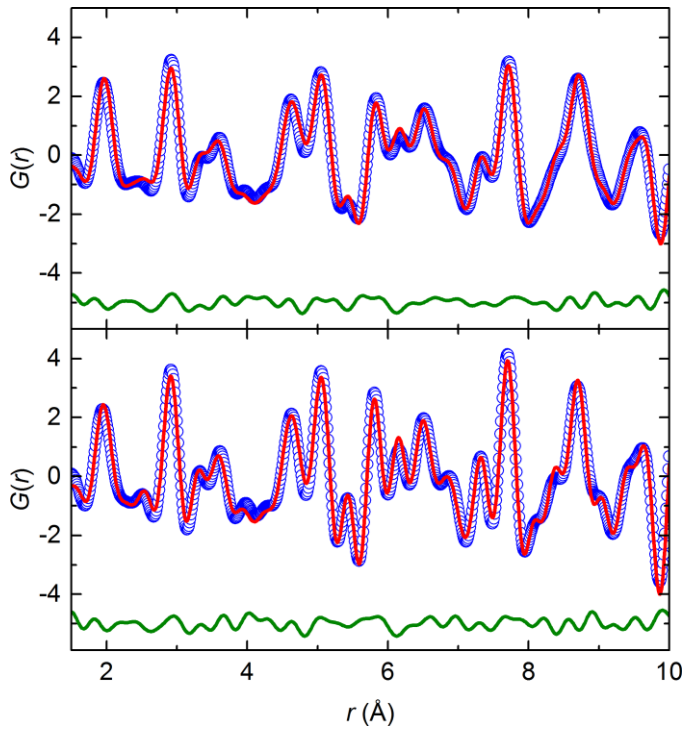

Figure 5.4: The PDFs of LiV_2O_4 at 290 K (upper) and 5 K (lower). Both are well fit by an $Fd\bar{3}m$ model consistent with the cubic average structure, with R_w = 11.6% and 12.3% respectively.

a V-V nearest-neighbour distance of 2.908(1) Å. $Fd\bar{3}m$ symmetry results in all V-V nearest-neighbour distances being equal, so fits of lower-symmetry structural models were made to the 5 K PDF to try and identify subtle distortions. A cubic $F\bar{4}3m$ model like that used to describe the structure of $Li_{0.5}Ga_{0.5}Cr_2O_4$,[115] in which V_4 tetrahedra could form on a breathing pyrochlore lattice, gave V-V nearest-neighbour distances of 2.908(99) Å and 2.909(99) Å, whilst a rhombohedral $R3m$ model following the proposed high-pressure distortion[135] gave distances of 2.90(41) Å, 2.90(45) Å, 2.91(45) Å and 2.92(41) Å. Large errors, particularly for the $R3m$ model, arise because the PDF refinements become unstable when the atomic coordinates are close to the positions they would adopt in a higher-symmetry structure. As such, these fits to the 5 K PDF show that the V-V nearest-neighbour distances do not vary significantly from a uniform value when the symmetry of the structural model is lowered from $Fd\bar{3}m$. As a check to these fits, Rietveld refinements were done with the vanadium displaced away from its ideal position as a split site. In the cubic phases of AlV_2O_4 and GaV_2O_4 similar

refinements allowed the vanadium disorder in the average structure to be described (Chapter 3), but no such displacement is found for LiV_2O_4. The total scattering results therefore demonstrate that the cubic spinel structure does not distort on either the average or local scale in the heavy-fermion ground state.

5.3.2: Powder diffraction at high pressures

Whilst the structure of LiV_2O_4 is cubic at all temperatures at ambient pressure, pressure-induced distortions have been identified in both diffraction and EXAFS experiments.[135,138] The nature of this distortion, and its relationship to the changes of conductivity and magnetic behaviour also identified at high pressures,[136,137] has not been properly determined. To better understand the behaviour of LiV_2O_4 under pressure isothermal powder X-ray diffraction data have been collected at 20 K, 100 K and room temperature, to maximum pressures of 15.3 GPa, 15.5 GPa and 21.0 GPa respectively. The profiles and relative intensities of the measured reflections were affected by pressure-induced strain and poor powder averaging from the small samples used so full structural refinements using the Rietveld method could not be done, though Le Bail refinements were used to determine the symmetry and lattice parameters of the LiV_2O_4 unit cell. The minor impurity phases identified in the total scattering patterns could not be seen against the high background of the DAC so were not included in the fits, and the region of 2θ from 6.0-7.8° – in which no Bragg peaks are found – was excluded from all refinements to mask a broad background feature that could not be properly fit.

The volume of a unit cell is determined by its lattice parameters. These vary with pressure, and the relationship between the volume of the unit cell of a material and the pressure to which it is subjected can be described by the third-order Birch-Murnaghan equation of states:

$$p(V) = \frac{3B_0}{2}\left[\left(\frac{V_0}{V}\right)^{\frac{7}{3}} - \left(\frac{V_0}{V}\right)^{\frac{5}{3}}\right]\left\{1 + \frac{3}{4}(B_0' - 4)\left[\left(\frac{V_0}{V}\right)^{\frac{2}{3}} - 1\right]\right\} \qquad \textbf{(5.1)}$$

where V_0 is the volume at zero pressure, B_0 is the bulk modulus at zero pressure and B_0' is the derivative of B_0 with respect to pressure:

$$B_0 = -V\left(\frac{\partial p}{\partial V}\right)_{p=0} \quad \textbf{(5.2)}$$

$$B_0' = \left(\frac{\partial B}{\partial p}\right)_{p=0} \quad \textbf{(5.3)}$$

At all three measured temperatures the structure of LiV_2O_4 has $Fd\bar{3}m$ symmetry at low pressures. At room temperature, no distortion of this structure is seen over the whole measured pressure range (Figure 5.5). The volume of the cubic unit cell decreases steadily with increasing pressure, and a fit of Equation 5.1 (Figure 5.6) with B_0' = 4 fixed gives V_0 = 560.2(2) Å^3 and B_0 = 123.2(6) GPa. The value of V_0 corresponds to a lattice parameter of 8.244 Å, similar to the value determined from the room temperature total scattering data, whilst the value of B_0 is smaller than the 160-180 GPa values determined for vanadium oxide spinels with divalent *A*-site cations[122] due to the relative softness of monovalent Li^+.

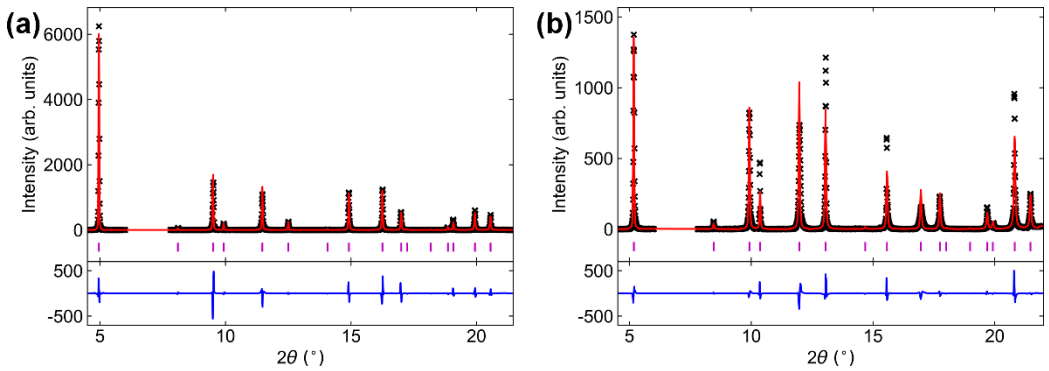

Figure 5.5: Le Bail fits of an $Fd\bar{3}m$ unit cell to the room temperature diffraction patterns of LiV_2O_4 at **(a)** 0.2 GPa (R_w = 26.3%) and **(b)** 21.0 GPa (R_w = 35.6%). Although strain and texture effects limit the quality of the fits, no peak splitting that would indicate of a distortion of the ambient-pressure structure is seen.

The only previous high-pressure diffraction study of LiV_2O_4 reported a splitting of Bragg peaks, indicating a distortion of the cubic spinel structure, at pressures above 12.8 GPa at 10 K.[135] In the diffraction patterns collected at both 20 K and 100 K, peak splitting is also seen at high pressures. However, the proposed

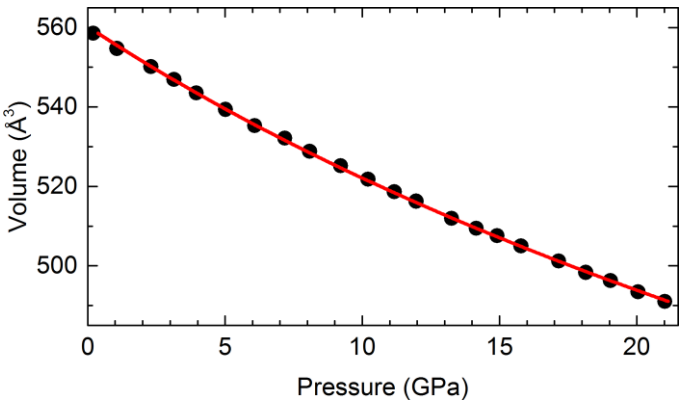

Figure 5.6: The volume of the cubic unit cell decreases smoothly upon compression at room temperature and is well-fit by the third-order Birch-Murnaghan equation of states (Equation 5.1).

rhombohedral ($R\bar{3}m$) distortion does not account for all of the reflections that result from the observed splitting. For example, the 111-type reflections of the cubic structure would split into two separate reflections upon an $R\bar{3}m$ distortion, but three reflections are actually observed (Figure 5.7). Different distortions were therefore considered, and a monoclinic distortion of the ambient-pressure $Fd\bar{3}m$ structure – in effect, a slight extra distortion of the proposed rhombohedral one – can account for all of the observed reflections (Figure 5.8). Such a distortion gives a unit cell of symmetry $C2/m$ with lattice parameters that deviate from metrically

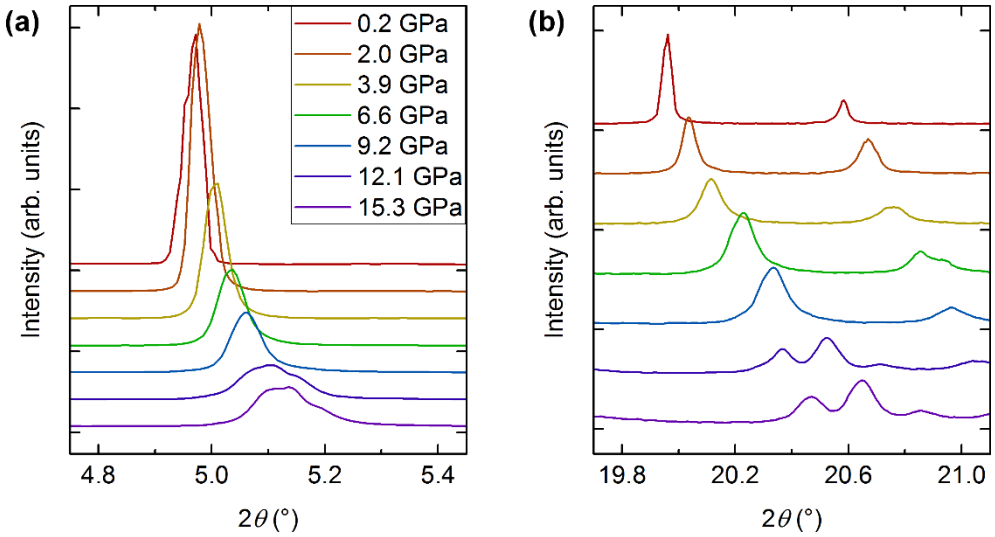

Figure 5.7: Diffraction patterns collected at 20 K reveal that the 111 reflection (2θ = 4.97° at 0.2 GPa) shown in **(a)** and the 444 reflection (2θ = 19.96° at 0.2 GPa) shown in **(b)** of cubic LiV_2O_4 split into three distinct reflections at high pressures.

cubic values $a_M = \sqrt{1.5}a_C$, $b_M = c_M = a_C/\sqrt{2}$ and $\beta = 125.26°$. Refined lattice parameters of a_M = 9.8552(8) Å, b_M = 5.6128(5) Å, c_M = 5.6004(7) Å and β = 125.844(6)° are obtained at 20 K and 15.3 GPa. Other possible distortions were considered, and a comparison of the fits of different structural models to a particular diffraction pattern is shown in Figure 5.9. Spinels are more commonly found to undergo tetragonal ($I4_1/amd$) or orthorhombic ($Fddd$) distortions,[141] but neither account for the observed peak splitting. An $R\bar{3}m$ supercell like that used to describe the ground state structures of AlV_2O_4 and GaV_2O_4 in Chapter 3, and suggested by EXAFS for the distortion in LiV_2O_4,[138] is also inadequate. Furthermore, whilst a rhombohedral distortion alone does not account for all of the observed reflections, the additional reflections could arise because the low-pressure phase only partially distorts. However, fits of a two-phase model with different ratios of $R\bar{3}m$ and $Fd\bar{3}m$ phases are always poorer than a fit with a single monoclinic phase.

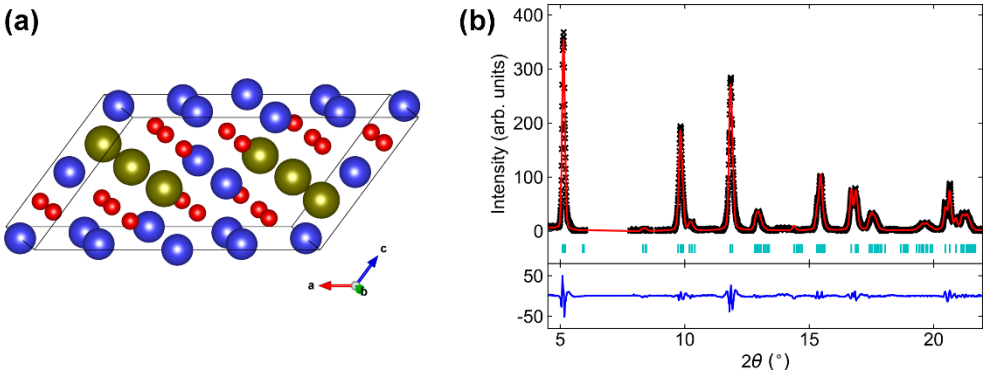

Figure 5.8: At low temperatures and high pressures the structure of LiV_2O_4 becomes monoclinic. **(a)** The $C2/m$ monoclinic unit cell, showing Li (gold), V (blue) and O (red) atoms. Alternating kagome and triangular lattices of V cations stack in the *ab* plane. **(b)** The Le Bail fit of this structure to the diffraction pattern of LiV_2O_4 collected at 20 K and 15.3 GPa (R_w = 22.0%).

The pressure-induced phase transition in LiV_2O_4 is therefore associated with a monoclinic distortion of the ambient-pressure cubic structure. The pressure at which this transition occurs can be determined from the change in unit cell volume that accompanies the distortion. At both 20 K and 100 K the volume of the cubic unit cell changes steadily at low pressures, similarly to the behaviour

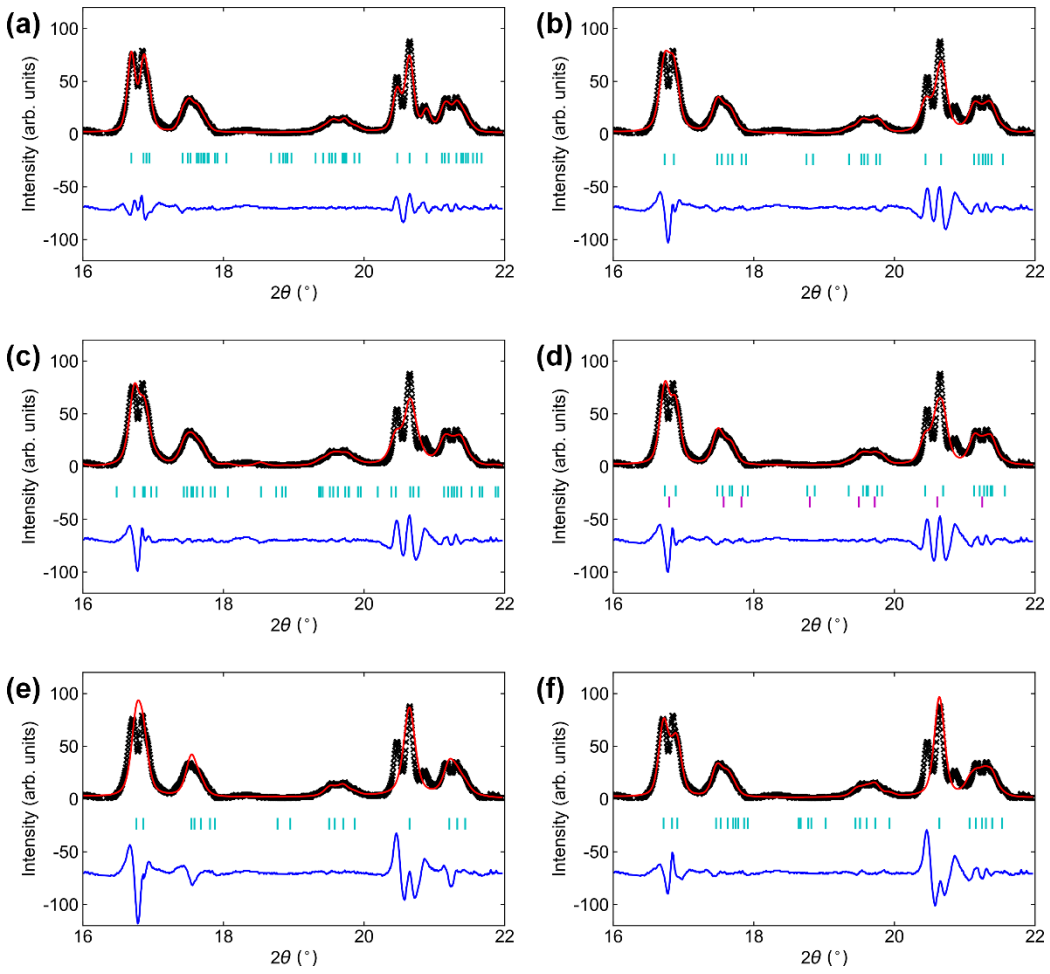

Figure 5.9: Fits of different structural models to the diffraction pattern in Figure 5.8(b), showing only the high-angle region for clarity. **(a)** $C2/m$ (R_w = 22.0%). **(b)** $R\bar{3}m$ (R_w = 27.6%). **(c)** $R\bar{3}m$ supercell (R_w = 26.1%). **(d)** Two-phase $R\bar{3}m$ and $Fd\bar{3}m$ (R_w = 25.9%). **(e)** $I4_1/amd$ (R_w = 35.5%). **(f)** $Fddd$ (R_w = 26.4%).

seen upon compression at room temperature. The volume of an undistorted $C2/m$ unit cell, V_M, is half that of its parent $Fd\bar{3}m$ unit cell, V_C; however, the distortion allows the lattice parameters of the monoclinic unit cell to deviate from their metrically cubic values, which allows the volume of the unit cell to shrink further. There is therefore a discontinuity in the variation of unit cell volume with pressure at the pressure where the phase transition occurs. At 20 K this is at approximately 11 GPa (Figure 5.10(a)), whilst at 100 K it is at approximately 12 GPa (Figure 5.10(b)).

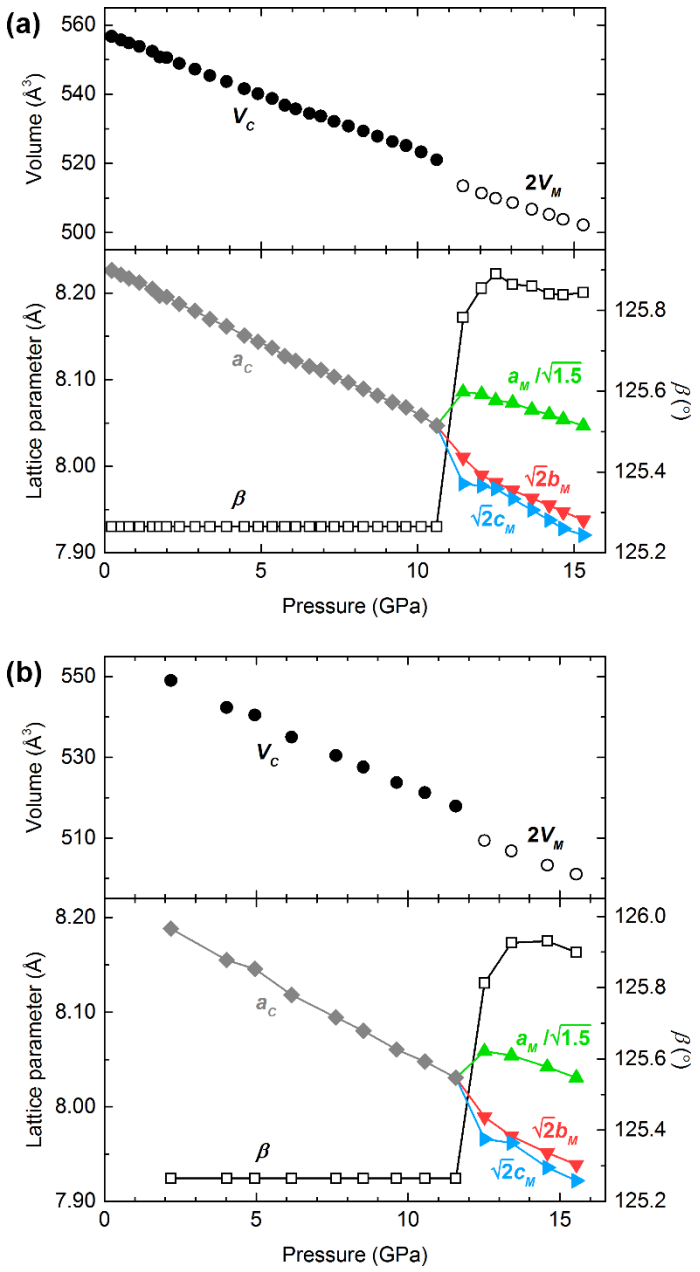

Figure 5.10: The refined unit cell volume and lattice parameters of LiV_2O_4 at **(a)** 20 K and **(b)** 100 K. The cubic-monoclinic phase transition occurs at 11 GPa and 12 GPa, respectively.

These pressures are comparable to the 12.8 GPa value reported previously,[135] and a comparison to the phase diagram determined by optical reflectivity (Figure 5.1) suggests that this distortion accompanies the transition between the intermediate and insulating phases.

The properties of LiV_2O_4 also change with the application of pressure, and these changes – from metallic to insulating conductivity, and from localised-moment to spin-singlet magnetism – are suggestive of orbital molecule formation. As in other orbital molecule systems this would require a structural distortion that shortens some V-V nearest-neighbour distances, but as Rietveld analysis could not be performed the atomic positions – and hence the V-V distances – in the monoclinic phase of LiV_2O_4 cannot be determined from the collected data. In breaking the cubic symmetry the monoclinic distortion does itself affect the V-V distances, and a Le Bail refinement with the vanadium sites at their ideal spinel positions (Figure 5.8(b)) gives V-V nearest neighbour distances of 2.7929(3) Å, 2.8002(4) Å, 2.8064(2) Å and 2.8354(2) Å at 20 K and 15.3 GPa. In the monoclinic unit cell (Figure 5.8(a)) kagome- and triangular-lattice layers of V cations stack in the *ab* plane and interestingly, the two shorter V-V distances are those that connect the cations in adjacent layers whilst the two longer distances are those within each kagome layer. This may be indicative of an arrangement of V-V bonds within the monoclinic structure, though these distances span a much smaller range than the 2.66-3.09 Å values determined by EXAFS analysis that included displacements of the V sites away from their ideal spinel positions.[138]

A further restriction of being limited to Le Bail analysis is that the precise space group of the monoclinic structure cannot be determined. The refinements were carried out using a unit cell with $C2/m$ symmetry but the diffraction patterns of unit cells with the same lattice parameters and $C2$ or Cm symmetry have the same reflections and systematic absences, so give identical Le Bail fits. As the different symmetries allow different displacements of the crystallographic sites they could be distinguished by Rietveld refinements against the measured intensities, so higher-quality diffraction data should be collected to fully-determine the crystal structure of monoclinic LiV_2O_4 and identify any short V-V distances that define orbital molecules.

Nevertheless, these results can be integrated with the previous studies of LiV_2O_4 under high pressures. The cubic-monoclinic crystallographic distortion appears to coincide with Boundary 2 in Figure 5.1, between the intermediate and

insulating phases. However, the properties start to change at Boundary 1, between the metallic and intermediate phases, and the reported local-structure distortion also appears to coincide with this boundary. It has been suggested that there are two separate phase boundaries because the structural distortion occurs gradually, through the development of insulating grains, hence an intermediate region exists between the metallic and insulating phases.[136] However, if the ordering that gives rise to insulating behaviour requires a crystallographic distortion such gradual conversion should be evidenced through the coexistence of cubic and monoclinic phases in that intermediate region. The collected diffraction patterns do not show such coexistence, but that complete cubic-monoclinic conversion occurs abruptly at the identified pressures.

Instead, the presence of two distinct phase boundaries may be the result of short-range and long-range order being established at different pressures. Ordering that forms orbital molecules would change the properties of LiV_2O_4 whether it was over a short-range or a long-range scale, and would distort the structure locally in either case, but long-range order can only be realised through a distortion of the cubic average structure. In AlV_2O_4 and GaV_2O_4 orbital molecules are present at all temperatures at ambient pressure but only establish long-range order when the temperature is sufficiently low. LiV_2O_4 may behave similarly but, as it has fewer valence *d*-electrons, with high pressures required to improve t_{2g}-t_{2g} overlap and stabilise V-V bonding. Hence, Boundary 1 in Figure 5.1 may define the pressure at which orbital molecules form through local interactions at a given temperature, whilst Boundary 2 may define the region of sufficiently high pressures and low temperatures in which long-range order can be established.

5.4: Conclusions

Two studies have been conducted to better understand the relationship between the structure of LiV_2O_4 and its electronic behaviour.

Firstly, at ambient pressure, LiV_2O_4 has a remarkable heavy-fermion ground state. This is very unusual for a *d*-electron system, and the mechanism by which this

state forms remains the subject of investigation. Conventional long-range magnetic ordering is inhibited by geometric frustration, as the cubic average structure does not distort in the heavy-fermion state. However, short-range antiferromagnetic fluctuations in this state had been detected experimentally, and theoretical work had suggested that local spin and orbital interactions determine the properties of this material. Complementary studies of the average and local structures of LiV_2O_4 through X-ray total scattering have revealed that in the heavy-fermion state, the electronic degrees of freedom are not coupled to a structural distortion on any length scale.

Secondly, under high pressure, LiV_2O_4 undergoes a metal-insulator transition. It had been suggested that this transition was the result of vanadium orbital molecules being formed, though two distinct phase boundaries had been reported. A monoclinic distortion of the ambient-pressure cubic structure has been identified through powder diffraction under low-temperature high-pressure conditions and appears to coincide with the higher-pressure reported phase boundary, though the atomic arrangement in this phase could not be determined. Further structural studies are therefore required, particularly as changes to the properties and local structure of LiV_2O_4 appear to occur at the lower-pressure phase boundary. This may be the result of short-range and long-range orbital molecule ordering, with accompanying local- and average-structure distortions, being established at different pressures. EXAFS had revealed a local-structure distortion at room temperature, and could be used at low temperatures to determine whether that distortion occurs at a lower pressure than the crystallographic distortion observed with diffraction. Higher-quality diffraction data is also needed to determine the atomic structure in the monoclinic phase. Given that powder diffraction has been of limited use single crystal diffraction may be preferable, and could also provide information about local distortions through diffuse scattering.

Chapter 6: Concluding remarks

Orbital molecules are clusters of transition metal cations formed when their valence *d*-electrons order into metal-metal bonds. They are commonly found in both vanadium oxides that have structures with edge-sharing octahedra, and transition metal oxides adopting the spinel structure-type, making the AV_2O_4 family of vanadium oxide spinels a good candidate for a system in which the formation and behaviour of orbital molecules can be studied. The work in this Thesis was therefore undertaken to explore the electronic states of a range of AV_2O_4 spinels, identify orbital molecules, and determine their relationship to the electronic and magnetic properties that these materials display.

AlV_2O_4 was the only AV_2O_4 system in which orbital molecules had previously been found but the reinvestigation of its structure, using X-ray total scattering to give both average and local descriptions, has both revised the nature the orbital molecules in the ordered ground state and revealed that they persist into a disordered high-temperature state. Analogous orbital molecule states have also been identified in GaV_2O_4, a newly-synthesised material that provides a second example of this behaviour. Changing the *A*-site cation from Al^{3+} to the larger Ga^{3+} suppresses the order-disorder transition temperature T_{CO} from 700 K to 415 K, though in both materials disordered orbital molecules are stable to at least 1100 K. Subsequently, through the substitution of Ga^{3+} for Zn^{2+} in the $Zn_xGa_{1-x}V_2O_4$ system the stability of local V-V bonding with respect to both the removal of valence *d*-electrons and the increase of the V-V nearest-neighbour distance has been demonstrated. In ZnV_2O_4 itself orbital molecules do not appear to be present on any length-scale at ambient pressure, though it has been suggested that V-V bonding evolves under high-pressure conditions[110] so a structural study of this material under such conditions would be an important future experiment. Moreover, the changes induced in the structure of a different spinel, LiV_2O_4, by the application of pressure have been explored. Orbital

molecules do not appear to contribute to the ambient-pressure ground state of this material, which is distinguished by exotic heavy-fermion correlations, but a monoclinic structural distortion has been identified above 11 GPa at low temperatures. In combination with previously reported high-pressure structural and property measurements this suggests that orbital molecules do form in LiV_2O_4 as the pressure is increased, firstly on the local scale and then with long-range order, though a full solution of the high-pressure structure of this material remains for future work.

The identification of highly-stable local V-V bonding – or, equivalently, highly-stable disordered orbital molecules – in vanadium oxide spinels is perhaps the key result of the work in this Thesis. Disordered 4*d* dimer states had previously been identified in $LiRh_2O_4$ and Li_2RuO_3,[61,62] but the behaviour of the V_3^{9+} and V_4^{8+} clusters in AlV_2O_4 and GaV_2O_4 demonstrates that orbital molecules formed both by 3*d* orbital interactions and of more than two atoms can have a high-temperature disordered state. This is extended further by the $Zn_xGa_{1-x}V_2O_4$ phases in which disordered orbital molecules are present and do not appear to form an ordered state at all. This opens both new questions, about the nature of the metal-metal bonding in vanadium oxides and orbital molecule systems more generally, and new possibilities for research, to identify and exploit this disorder.

Firstly, these results suggest that disordered orbital molecules may be more common than previously thought. For most orbital molecule systems the shortening of metal-metal bonds has only been determined through crystallographic analysis, so whilst ordered states have been identified disordered states may have been overlooked. In magnetite, for example, the anomalously small entropy change at the ordering transition and the diffuse scattering observed above the transition may be the result of trimeron-bonding correlations persisting into a disordered high-temperature phase.[59] In a crystalline system the formation of non-periodic metal-metal bonds is an example of correlated orbital disorder[142]; another example is the orbital-ice state of the pyrochlore $Y_2Mo_2O_7$, in which disordered Mo-Mo dimers are formed.[143] So that such disordered states can be properly identified and described the

characterisation of orbital molecule systems using local-structure probes should be considered routinely in the future.

Secondly, it is not clear why the orbital molecules in some systems, vanadium oxides or otherwise, have a disordered state but those in other systems do not. The orbital molecules found in compositionally- and structurally-related materials often appear to be similar – for example, those in vanadium oxides all seem to follow simple two-centre two-electron bonding rules – but the distinction between species that can become disordered and those that cannot implies that apparently similar orbital molecules can be formed by very different mechanisms. A Peierls-type mechanism, in which metal-metal bonding is the result of an instability in the band structure, has been used to describe the behaviour of many orbital molecule systems but inherently results in long-range order alone.[43,47,60] Conversely, if the bonding is the result of strong local interactions, the formation and long-range ordering of orbital molecules can occur separately – in other words, they behave like conventional covalent systems, in which intra- and inter-molecular bonds have very different energies. To fully understand these different mechanisms, and why one or the other is favoured in a particular system, a combination of further experiments, such as spectroscopic probing of the orbital occupancy as has recently been demonstrated for VO_2,[144] band-structure calculations and theoretical descriptions will be required.

Finally, materials in which orbital molecules can be formed and manipulated might find increasing technological application. Some have already been heavily investigated – for example, applications that utilise the metal-insulator transition in VO_2 are inherently exploiting the formation of orbital dimers in that material. Future applications might make use of both ordered and disordered orbital molecule states. The self-organisation of orbital molecules can induce ordering transitions that lift inversion symmetry, making ferroelectric – and hence multiferroic – behaviour accessible. This would be achieved in the ground states of AlV_2O_4 and GaV_2O_4 if the V_3^{9+}-V_4^{8+} cluster pairs could be organised in a fully-ordered manner. Alternatively, in analogy to spintronic technology that utilises coupled spin- and charge-transport for applications such as data-storage,[145]

'orbitronic' technology based on orbital angular-momentum currents has been proposed.[146,147] Although QENS has suggested that the disordered orbital molecules in GaV_2O_4 are static, if their transport could be demonstrated the orbital anisotropy associated with their formation could make orbital molecules useful for future orbitronics.

References

1 P. A. Cox, *Transition Metal Oxides: An introduction to their electronic structure and properties*, Oxford University Press, Oxford, 2010.

2 C. N. R. Rao, *Annu. Rev. Phys. Chem.*, 1989, **40**, 291–326.

3 E. Dagotto, *Rev. Mod. Phys.*, 1994, **66**, 763–840.

4 S. Jin, T. H. Tiefel, M. McCormack, R. A. Fastnacht, R. Ramesh and L. H. Chen, *Science*, 1994, **264**, 413–415.

5 M. Imada, A. Fujimori and Y. Tokura, *Rev. Mod. Phys.*, 1998, **70**, 1039–1263.

6 J. B. Goodenough, *Chem. Mater.*, 2014, **26**, 820–829.

7 M. Fiebig, T. Lottermoser, D. Meier and M. Trassin, *Nat. Rev. Mater.*, 2016, **1**, 16046.

8 R. E. Peierls, *Quantum Theory of Solids*, Oxford University Press, Oxford, 1955.

9 A. R. Armstrong, C. Lyness, P. M. Panchmatia, M. S. Islam and P. G. Bruce, *Nat. Mater.*, 2011, **10**, 223–229.

10 Y. Wang and G. Cao, *Adv. Mater.*, 2008, **20**, 2251–2269.

11 F. K. Butt, M. Tahir, C. Cao, F. Idrees, R. Ahmed, W. S. Khan, Z. Ali, N. Mahmood, M. Tanveer, A. Mahmood and I. Aslam, *Appl. Mater. Interfaces*, 2014, **6**, 13635–13641.

12 N. M. Sammes, G. A. Tompsett, H. Näfe and F. Aldinger, *J. Eur. Ceram. Soc.*, 1999, **19**, 1801–1826.

13 I. E. Wachs, *Dalt. Trans.*, 2013, **42**, 11762–11769.

14 F. J. Morin, *Phys. Rev. Lett.*, 1959, **3**, 34–36.

15 Z. Yang, C. Ko and S. Ramanathan, *Annu. Rev. Mater. Res.*, 2011, **41**, 337–367.

16 E. Janod, J. Tranchant, B. Corraze, M. Querré, P. Stoliar, M. Rozenberg, T. Cren, D. Roditchev, V. T. Phuoc, M. P. Besland and L. Cario, *Adv. Funct. Mater.*, 2015, **25**, 6287–6305.

17 S. Wang, M. Liu, L. Kong, Y. Long, X. Jiang and A. Yu, *Prog. Mater. Sci.*, 2016, **81**, 1–54.

18 D. B. McWhan, A. Menth, J. P. Remeika, W. F. Brinkman and T. M. Rice, *Phys. Rev. B*, 1973, **7**, 1920–1931.

19 J.-H. Park, L. Tjeng, A. Tanaka, J. W. Allen, C. Chen, P. Metcalf, J. Honig, F. de Groot and G. A. Sawatzky, *Phys. Rev. B*, 2000, **61**, 11506–11509.

20 J. B. Goodenough, *J. Solid State Chem.*, 1971, **3**, 490–500.

21 Y. Tokura and N. Nagaosa, *Science*, 2000, **288**, 462–468.

22 S. Mori, C. H. Chen and S.-W. Cheong, *Nature*, 1998, **392**, 473–476.

23 P. M. M. Thygesen, C. A. Young, E. O. R. Beake, F. D. Romero, L. D. Connor, T. E. Proffen, A. E. Phillips, M. G. Tucker, M. A. Hayward, D. A. Keen and A. L. Goodwin, *Phys. Rev. B*, 2017, **95**, 174107.

24 A. P. Ramirez, *Annu. Rev. Mater. Sci.*, 1994, **24**, 453–480.

25 J. B. Goodenough, *Magnetism and the Chemical Bond*, Wiley-Interscience, New York, 1963.

26 J. B. Goodenough, *Phys. Rev.*, 1960, **117**, 1442–1451.

27 J. P. Attfield, *APL Mater.*, 2015, **3**, 041510.

28 K. E. Sickafus, J. M. Wills and N. W. Grimes, *J. Am. Ceram. Soc.*, 1999, **82**, 3279–3292.

29 K. Momma and F. Izumi, *J. Appl. Crystallogr.*, 2011, **44**, 1272–1276.

30 H. Takagi and S. Niitaka, in *Introduction to Frustrated Magnetism: Materials, Experiments, Theory*, Springer-Verlag, Berlin Heidelberg, 2011, pp. 155–175.

31 D. C. Johnston, H. Prakash, W. H. Zachariasen and R. Viswanathan, *Mater. Res. Bull.*, 1973, **8**, 777–784.

32 S. Kondo, D. C. Johnston, C. A. Swenson, F. Borsa, A. V. Mahajan, L. L. Miller, T. Gu, A. I. Goldman, M. B. Maple, D. A. Gajewski, E. J. Freeman, N. R. Dilley, R. P. Dickey, J. Merrin, K. Kojima, G. M. Luke, Y. J. Uemura, O. Chmaissem and J. D. Jorgensen, *Phys. Rev. Lett.*, 1997, **78**, 3729–3732.

33 S.-H. Lee, C. Broholm, W. Ratcliff, G. Gasparovic, Q. Huang, T. H. Kim and S.-W. Cheong, *Nature*, 2002, **418**, 856–858.

34 S.-H. Lee, C. Broholm, T. H. Kim, W. Ratcliff II and S.-W. Cheong, *Phys. Rev. Lett.*, 2000, **84**, 3718–3721.

35 J. Rodríguez-Carvajal, G. Rousse, C. Masquelier and M. Hervieu, *Phys. Rev. Lett.*, 1998, **81**, 4660–4663.

36 M. Reehuis, A. Krimmel, N. Buttgen, A. Loidl and A. Prokofiev, *Eur. Phys. J. B - Condens. Matter*, 2003, **35**, 311–316.

37 B.-O. Marinder and A. Magnéli, *Acta Chem. Scand*, 1957, **11**, 1635–1640.

38 A. Cavalleri, C. Tóth, C. W. Siders, J. A. Squier, F. Ráksi, P. Forget and J. C. Kieffer, *Phys. Rev. Lett.*, 2001, **87**, 237401.

39 A. Magnéli and G. Andersson, *Acta Chem. Scand.*, 1955, **9**, 1378–1381.

40 K. D. Rogers, *Powder Diffr.*, 1993, **8**, 240–244.

41 K. Shibuya, M. Kawasaki and Y. Tokura, *Phys. Rev. B*, 2010, **82**, 205118.

42 S. Biermann, A. Poteryaev, A. I. Lichtenstein and A. Georges, *Phys. Rev. Lett.*, 2005, **94**, 026404.

43 M. W. Haverkort, Z. Hu, A. Tanaka, W. Reichelt, S. V. Streltsov, M. A. Korotin, V. I. Anisimov, H. H. Hsieh, H. J. Lin, C. T. Chen, D. I. Khomskii and L. H. Tjeng, *Phys. Rev. Lett.*, 2005, **95**, 196404.

44 Z. Hiroi, *Prog. Solid State Chem.*, 2015, **43**, 47–69.

45 T. Sakata, K. Sakata and I. Nishida, *Phys. Status Solidi B*, 1967, **20**, K155–K157.

46 W. Tian, M. F. Chisholm, P. G. Khalifah, R. Jin, B. C. Sales, S. E. Nagler and D. Mandrus, *Mater. Res. Bull.*, 2004, **39**, 1319–1328.

47 T. Jin-no, Y. Shimizu, M. Itoh, S. Niitaka and H. Takagi, *Phys. Rev. B*, 2013, **87**, 075135.

48 H. F. Pen, J. van den Brink, D. I. Khomskii and G. A. Sawatzky, *Phys. Rev. Lett.*, 1997, **78**, 1323–1326.

49 M. Marezio, D. B. McWhan, P. D. Dernier and J. P. Remeika, *J. Solid State Chem.*, 1973, **6**, 419–429.

50 A. S. Botana, V. Pardo, D. Baldomir, A. V. Ushakov and D. I. Khomskii, *Phys. Rev. B*, 2011, **84**, 115138.

51 T. M. McQueen, P. W. Stephens, Q. Huang, T. Klimczuk, F. Ronning and R. J. Cava, *Phys. Rev. Lett.*, 2008, **101**, 166402.

52 C. Didier, M. Guignard, J. Darriet and C. Delmas, *Inorg. Chem.*, 2012, **51**, 11007–11016.

53 M. Guignard, C. Didier, J. Darriet, P. Bordet, E. Elkaïm and C. Delmas, *Nat. Mater.*, 2013, **12**, 74–80.

54 M. Guignard and C. Delmas, *ChemistrySelect*, 2017, **2**, 5800–5804.

55 T. Kajita, T. Kanzaki, T. Suzuki, J. E. Kim, K. Kato, M. Takata and T. Katsufuji, *Phys. Rev. B*, 2010, **81**, 060405(R).

56 M. Schmidt, W. Ratcliff, P. G. Radaelli, K. Refson, N. M. Harrison and S. W. Cheong, *Phys. Rev. Lett.*, 2004, **92**, 056402.

57 P. G. Radaelli, Y. Horibe, M. J. Gutmann, H. Ishibashi, C. H. Chen, R. M. Ibberson, Y. Koyama, Y.-S. Hor, V. Kiryukhin and S.-W. Cheong, *Nature*, 2002, **416**, 155–158.

58 E. J. W. Verwey, *Nature*, 1939, **144**, 327.

59 M. S. Senn, J. P. Wright and J. P. Attfield, *Nature*, 2012, **481**, 173–176.

60 D. I. Khomskii and T. Mizokawa, *Phys. Rev. Lett.*, 2005, **94**, 156402.

61 K. R. Knox, A. M. M. Abeykoon, H. Zheng, W.-G. Yin, A. M. Tsvelik, J. F. Mitchell, S. J. L. Billinge and E. S. Bozin, *Phys. Rev. B*, 2013, **88**, 174114.

62 S. A. J. Kimber, I. I. Mazin, J. Shen, H. O. Jeschke, V. Sergey, D. N. Argyriou, R. Valent, D. I. Khomskii, S. V. Streltsov and R. Valentí, *Phys. Rev. B*, 2014, **89**, 081408(R).

63 S. A. Corr, D. P. Shoemaker, B. C. Melot and R. Seshadri, *Phys. Rev. Lett.*, 2010, **105**, 056404.

64 M. Guignard, D. Carlier, C. Didier, M. R. Suchomel, E. Elkaïm, P. Bordet, R. Decourt, J. Darriet and C. Delmas, *Chem. Mater.*, 2014, **26**, 1538–1548.

65 E. S. Božin, A. S. Masadeh, Y. S. Hor, J. F. Mitchell and S. J. L. Billinge, *Phys. Rev. Lett.*, 2011, **106**, 045501.

66 Y. Horibe, M. Shingu, K. Kurushima, H. Ishibashi, N. Ikeda, K. Kato, Y. Motome, N. Furukawa, S. Mori and T. Katsufuji, *Phys. Rev. Lett.*, 2006, **96**, 086406.

67 M. Hayward, in *Comprehensive Inorganic Chemistry II (Second Edition): From Elements to Applications*, Elsevier, Oxford, 2013, vol. 2, pp. 417–453.

68 M. T. Dove, *Structure and Dynamics: An atomic view of materials*, Oxford University Press, Oxford, 2003.

69 P. J. Brown, A. G. Fox, E. N. Maslen, M. A. O'Keefe and B. T. M. Willis, in *International Tables for Crystallography, Volume C*, 2006, pp. 554–595.

70 V. Sears, *Neutron News*, 1992, **3**, 26–37.

71 R. E. Dinnebier and S. J. L. Billinge, Eds., *Powder Diffraction: Theory and Practice*, Royal Society of Chemistry, Cambridge, 2008.

72 G. Caglioti, A. Paoletti and F. P. Ricci, *Nucl. Instruments*, 1958, **3**, 223–228.

73 P. W. Stephens, *J. Appl. Crystallogr.*, 1999, **32**, 281–289.

74 S. Ikeda and J. M. Carpenter, *Nucl. Inst. Methods Phys. Res.*, 1985, **A239**, 536–544.

75 H. M. Rietveld, *J. Appl. Crystallogr.*, 1969, **2**, 65–71.

76 A. Le Bail, *Powder Diffr.*, 2005, **20**, 316–326.

77 A. C. Larson and R. B. Von Dreele, *Los Alamos Natl. Lab. Rep. LAUR*, 2004, 86–748.

78 B. H. Toby, *J. Appl. Crystallogr.*, 2001, **34**, 210–213.

79 C. A. Young and A. L. Goodwin, *J. Mater. Chem.*, 2011, **21**, 6464.

80 T. Egami and S. J. L. Billinge, *Underneath the Bragg Peaks: Structural Analysis of Complex Materials*, Elsevier Ltd, Oxford, 2003.

81 S. Billinge, in *Powder Diffraction: Theory and Practice*, Royal Society of Chemistry, Cambridge, 2008, pp. 464–493.

82 P. J. Chupas, X. Qiu, J. C. Hanson, P. L. Lee, C. P. Grey and S. J. L. Billinge, *J. Appl. Crystallogr.*, 2003, **36**, 1342–1347.

83 P. Juhas, T. Davis, C. L. Farrow and S. J. L. Billinge, *J. Appl. Crystallogr.*, 2013, **46**, 560–566.

84 C. L. Farrow, P. Juhas, J. W. Liu, D. Bryndin, E. S. Božin, J. Bloch, T. Proffen and S. J. L. Billinge, *J. Phys. Condens. Matter*, 2007, **19**, 335219.

85 G. L. Squires, *Introduction to the Theory of Thermal Neutron Scattering*, Cambridge University Press, Cambridge, 2012.

86 M. Bée, *Quasielastic Neutron Scattering: Principles and Applications in Solid State Chemistry, Biology and Materials Science*, Adam Hilger, Bristol and Philadelphia, 1988.

87 http://www.esrf.eu/Apache_files/Highlights/HL2017.pdf.

88 J.-L. Hodeau, P. Bordet, M. Anne, A. Prat, A. N. Fitch, E. Dooryhee, G. Vaughan and A. K. Freund, in *SPIE 3448, Crystal and Multilayer Optics*, 1998, pp. 353–361.

89 P. Norby and U. Schwarz, in *Powder Diffraction: Theory and Practice*, Royal Society of Chemistry, Cambridge, 2008, pp. 439–463.

90 R. Letoullec, J. P. Pinceaux and P. Loubeyre, *High Press. Res.*, 1988, **1**, 77–90.

91 H. K. Mao, J. Xu and P. M. Bell, *J. Geophys. Res.*, 1986, **91**, 4673–4676.

92 https://www.ill.eu/users/instruments/instruments-list/in6-sharp/description/instrument-layout/.

93 R. L. Carlin, *Magnetochemistry*, Springer-Verlag, Berlin Heidelberg, 1986.

94 W. G. Jenks, S. S. H. Sadeghi and J. P. Wikswo, *J. Phys. D. Appl. Phys.*, 1997, **30**, 293–323.

95 K. Matsuno, T. Katsufuji, S. Mori, Y. Moritomo, A. Machida, E. Nishibori, M. Takata, M. Sakata, N. Yamamoto and H. Takagi, *J. Phys. Soc. Japan*, 2001, **70**, 1456–1459.

96 Y. Shimizu, M. Tanaka, M. Itoh and T. Katsufuji, *Phys. Rev. B*, 2008, **78**, 144423.

97 K. Matsuda, N. Furukawa and Y. Motome, *J. Phys. Soc. Japan*, 2006, **75**, 124716.

98 K. Matsuno, T. Katsufuji, S. Mori, M. Nohara, A. Machida, Y. Moritomo, K. Kato, E. Nishibori, M. Takata, M. Sakata, K. Kitazawa and H. Takagi, *Phys. Rev. Lett.*, 2003, **90**, 096404.

99 S. Kalavathi, S. Vennila Raju, S. Chandra, Q. Williams and P. C. Sahu, *Solid State Commun.*, 2017, **250**, 23–27.

100 M. S. Senn, J. P. Wright, J. Cumby and J. P. Attfield, *Phys. Rev. B*, 2015, **92**, 024104.

101 R. D. Shannon, *Acta Crystallogr.*, 1976, **A32**, 751–767.

102 G. Ehlers, A. L. Cornelius, T. Fennell, M. Koza, S. T. Bramwell and J. S. Gardner, *J. Phys. Condens. Matter*, 2004, **16**, S635–S642.

103 H. Tsunetsugu and Y. Motome, *Phys. Rev. B*, 2003, **68**, 060405(R).

104 O. Tchernyshyov, *Phys. Rev. Lett.*, 2004, **93**, 157206.

105 S.-H. Lee, D. Louca, H. Ueda, S. Park, T. J. Sato, M. Isobe, Y. Ueda, S. Rosenkranz, P. Zschack, J. Iñiguez, Y. Qiu and R. Osborn, *Phys. Rev. Lett.*, 2004, **93**, 156407.

106 S. Jung, J. Noh, J. Kim, C. L. Zhang, S. W. Cheong and E. J. Choi, *J. Phys. Condens. Matter*, 2008, **20**, 175205.

107 S. Niitaka, H. Ohsumi, K. Sugimoto, S. Lee, Y. Oshima, K. Kato, D. Hashizume, T. Arima, M. Takata and H. Takagi, *Phys. Rev. Lett.*, 2013, **111**, 267201.

108 N. Nishiguchi and M. Onoda, *J. Phys. Condens. Matter*, 2002, **14**, 551–557.

109 S. Blanco-Canosa, F. Rivadulla, V. Pardo, D. Baldomir, J. S. Zhou, M. García-Hernández, M. A. López-Quintela, J. Rivas and J. B. Goodenough, *Phys. Rev. Lett.*, 2007, **99**, 187201.

110 C. Kuntscher, K. Rabia, M. K. Forthaus, M. M. Abd-Elmeguid, F. Rivadulla, Y. Kato and C. D. Batista, *Phys. Rev. B*, 2012, **86**, 020405(R).

111 V. Pardo, S. Blanco-Canosa, F. Rivadulla, D. I. Khomskii, D. Baldomir, H. Wu and J. Rivas, *Phys. Rev. Lett.*, 2008, **101**, 256403.

112 T. Weber, B. Roessli, C. Stock, T. Keller, K. Schmalzl, F. Bourdarot, R. Georgii, R. A. Ewings, R. S. Perry and P. Böni, *Phys. Rev. B*, 2017, **96**, 184301.

113 T. Suzuki, M. Katsumura, K. Taniguchi, T. Arima and T. Katsufuji, *Phys. Rev. Lett.*, 2007, **98**, 127203.

114 Y. Ueda, N. Fujiwara and H. Yasuoka, *J. Phys. Soc. Japan*, 1997, **66**, 778–783.

115 Y. Okamoto, G. J. Nilsen, J. P. Attfield and Z. Hiroi, *Phys. Rev. Lett.*, 2013, **110**, 097203.

116 Y. Kato, G. W. Chern, K. A. Al-Hassanieh, N. B. Perkins and C. D. Batista, *Phys. Rev. Lett.*, 2012, **108**, 247215.

117 Z. Zhang, D. Louca, A. Visinoiu, S.-H. Lee, J. Thompson, T. Proffen, A. Llobet, Y. Qiu, S. Park and Y. Ueda, *Phys. Rev. B*, 2006, **74**, 014108.

118 H. Mamiya and M. Onoda, *Solid State Commun.*, 1995, **95**, 217–221.

119 T. Maitra and R. Valentí, *Phys. Rev. Lett.*, 2007, **99**, 126401.

120 G. Giovannetti, A. Stroppa, S. Picozzi, D. Baldomir, V. Pardo, S. Blanco-Canosa, F. Rivadulla, S. Jodlauk, D. Niermann, J. Rohrkamp, T. Lorenz, S. Streltsov, D. I. Khomskii and J. Hemberger, *Phys. Rev. B*, 2011, **83**, 060402(R).

121 A. Kismarahardja, J. S. Brooks, A. Kiswandhi, K. Matsubayashi, R. Yamanaka, Y. Uwatoko, J. Whalen, T. Siegrist and H. D. Zhou, *Phys. Rev. Lett.*, 2011, **106**, 056602.

122 Z.-Y. Li, X. Li, J.-G. Cheng, L. G. Marshall, X.-Y. Li, A. M. Dos Santos, W.-G. Yang, J. J. Wu, J.-F. Lin, G. Henkelman, T. Okada, Y. Uwatoko, H. B. Cao, H. D. Zhou, J. B. Goodenough and J.-S. Zhou, *Phys. Rev. B*, 2016, **94**, 165159.

123 G. R. Stewart, *Rev. Mod. Phys.*, 1984, **56**, 755–787.

124 S. Wirth and F. Steglich, *Nat. Rev. Mater.*, 2016, **1**, 16051.

125 C. Urano, M. Nohara, S. Kondo, F. Sakai, H. Takagi, T. Shiraki and T. Okubo, *Phys. Rev. Lett.*, 2000, **85**, 1052–1055.

126 D. C. Johnston, C. Swenson and S. Kondo, *Phys. Rev. B*, 1999, **59**, 2627–2641.

127 S. A. Carter, T. F. Rosenbaum, P. Metcalf, J. M. Honig and J. Spalek, *Phys. Rev. B*, 1993, **48**, 16841(R).

128 A. Shimoyamada, S. Tsuda, K. Ishizaka, T. Kiss, T. Shimojima, T. Togashi, S. Watanabe, C. Q. Zhang, C. T. Chen, Y. Matsushita, H. Ueda, Y. Ueda and S. Shin, *Phys. Rev. Lett.*, 2006, **96**, 026403.

129 P. E. Jönsson, K. Takenaka, S. Niitaka, T. Sasagawa, S. Sugai and H. Takagi, *Phys. Rev. Lett.*, 2007, **99**, 167402.

130 O. Chmaissem, J. D. Jorgensen, S. Kondo and D. C. Johnston, *Phys. Rev. Lett.*, 1997, **79**, 4866–4869.

131 S.-H. Lee, Y. Qiu, C. Broholm, Y. Ueda and J. J. Rush, *Phys. Rev. Lett.*, 2001, **86**, 5554–5557.

132 Y. Shimizu, H. Takeda, M. Tanaka, M. Itoh, S. Niitaka and H. Takagi, *Nat. Commun.*, 2012, **3**, 981.

133 K. Tomiyasu, K. Iwasa, H. Ueda, S. Niitaka, H. Takagi, S. Ohira-Kawamura, T. Kikuchi, Y. Inamura, K. Nakajima and K. Yamada, *Phys. Rev. Lett.*, 2014, **113**, 236402.

134 K. Hattori and H. Tsunetsugu, *Phys. Rev. B*, 2009, **79**, 035115.

135 K. Takeda, H. Hidaka, H. Kotegawa, T. C. Kobayashi, K. Shimizu, H. Harima, K. Fujiwara, K. Miyoshi, J. Takeuchi, Y. Ohishi, T. Adachi, M. Takata, E. Nishibori, M. Sakata, T. Watanuki and O. Shimomura, *Phys. B Condens. Matter*, 2005, **359**, 1312–1314.

136 A. Irizawa, S. Suga, G. Isoyama, K. Shimai, K. Sato, K. Iizuka, T. Nanba, A. Higashiya, S. Niitaka and H. Takagi, *Phys. Rev. B*, 2011, **84**, 235116.

137 H. Takeda, Y. Kato, M. Yoshimura, Y. Shimizu, M. Itoh, S. Niitaka and H. Takagi, *Phys. Rev. B*, 2015, **92**, 045103.

138 L. Pinsard-Gaudart, N. Dragoe, P. Lagarde, A. M. Flank, J. P. Itie, A. Congeduti, P. Roy, S. Niitaka and H. Takagi, *Phys. Rev. B*, 2007, **76**, 045119.

139 C. Prescher and V. B. Prakapenka, *High Press. Res.*, 2015, **35**, 223–230.

140 S. Kondo, D. C. Johnston and L. L. Miller, *Phys. Rev. B*, 1999, **59**, 2609–2626.

141 M. C. Kemei, J. K. Harada, R. Seshadri and M. R. Suchomel, *Phys. Rev. B*, 2014, **90**, 064418.

142 D. A. Keen and A. L. Goodwin, *Nature*, 2015, **521**, 303–309.

143 P. M. M. Thygesen, J. A. M. Paddison, R. Zhang, K. A. Beyer, K. W. Chapman, H. Y. Playford, M. G. Tucker, D. A. Keen, M. A. Hayward and A. L. Goodwin, *Phys. Rev. Lett.*, 2017, **118**, 067201.

144 N. B. Aetukuri, A. X. Gray, M. Drouard, M. Cossale, L. Gao, A. H. Reid, R. Kukreja, H. Ohldag, C. A. Jenkins, E. Arenholz, K. P. Roche, H. A. Dürr, M. G. Samant and S. S. P. Parkin, *Nat. Phys.*, 2013, **9**, 661–666.

145 C. Felser, G. H. Fecher and B. Balke, *Angew. Chemie - Int. Ed.*, 2007, **46**, 668–699.

146 B. A. Bernevig, T. L. Hughes and S.-C. Zhang, *Phys. Rev. Lett.*, 2005, **95**, 066601.

147 D. Go, J. P. Hanke, P. M. Buhl, F. Freimuth, G. Bihlmayer, H. W. Lee, Y. Mokrousov and S. Blügel, *Sci. Rep.*, 2017, **7**, 46742.

Appendix A: Structural models for AlV_2O_4

As described in Sections 3.3.1 and 3.3.2, PDF and Rietveld analysis of X-ray total scattering data has been used to revise the description of the structures of both the low- and high-temperature phases of AlV_2O_4. The following Tables provide the details of all of the refined structural models used in this analysis:

- Tables A.1-A.2: Fits to the 300 K PDF, shown in Figure 3.2
- Tables A.3-A.6: Fits to the 300 K diffraction pattern, shown in Figure 3.4
- Tables A.7-A.8: Fits to the 1100 K diffraction pattern, shown in Figure 3.5
- Tables A.9-A.10: Fits to the 1100 K PDF, shown in Figure 3.6

Table A.1: $R\bar{3}m$ heptamer model refined against the 300 K PDF. Lattice parameters a_H = 5.756(5) Å and c_H = 28.839(44) Å. R_w = 16.3%.

Atom	Site	*x*	*y*	*z*	Occ.	U_{iso} (Å²)
Al1	6*c*	0	0	0.1821(13)	1.0	0.0065(15)
Al2	6*c*	0	0	0.3090(14)	1.0	
V1	3*a*	0	0	0	1.0	
V2	3*b*	0	0	0.5	1.0	0.0061(6)
V3	18*h*	0.8506(9)	0.1494(9)	0.4178(4)	1.0	
O1	6*c*	0	0	0.1190(35)	1.0	
O2	6*c*	0	0	0.3749(31)	1.0	0.0141(20)
O3	18*h*	0.8196(32)	0.1804(32)	0.5390(17)	1.0	
O4	18*h*	0.8257(37)	0.1743(37)	0.2879(20)	1.0	

Table A.2: $R3m$ model refined against the 300 K PDF. Lattice parameters a_H = 5.762(5) Å and c_H = 28.859(45) Å. R_w = 13.6%.

Atom	Site	*x*	*y*	*z*	Occ.	U_{iso} (Å²)
Al1a	3*a*	0	0	0.1803(12)	1.0	0.0058(14)
Al1b	3*a*	0	0	0.8197(12)	1.0	
Al2a	3*a*	0	0	0.3100(16)	1.0	
Al2b	3*a*	0	0	0.6900(16)	1.0	
V1	3*a*	0	0	0	1.0	
V2	3*a*	0	0	0.4936(11)	1.0	0.0056(6)
V3a	9*b*	0.8500(9)	0.1500(9)	0.4179(4)	1.0	
V3b	9*b*	0.1500(9)	0.8500(9)	0.5821(4)	1.0	
O1a	3*a*	0	0	0.1235(25)	1.0	0.0123(21)
O1b	3*a*	0	0	0.8765(25)	1.0	
O2a	3*a*	0	0	0.3652(21)	1.0	
O2b	3*a*	0	0	0.6348(21)	1.0	
O3a	9*b*	0.8245(31)	0.1755(31)	0.5417(18)	1.0	
O3b	9*b*	0.1755(31)	0.8245(31)	0.4583(18)	1.0	
O4a	9*b*	0.8239(32)	0.1761(14)	0.2870(15)	1.0	
O4b	9*b*	0.1761(14)	0.8239(32)	0.7130(15)	1.0	

Table A.3: $R\bar{3}m$ heptamer model refined against the 300 K diffraction pattern. Lattice parameters a_H = 5.75626(7) Å and c_H = 28.86439(40) Å. R_w = 5.53%.

Atom	Site	*x*	*y*	*z*	Occ.	U_{iso} (Å²)
Al1	6*c*	0	0	0.18213(7)	1.0	0.00301(19)
Al2	6*c*	0	0	0.30886(7)	1.0	
V1	3*a*	0	0	0	1.0	
V2	3*b*	0	0	0.5	1.0	0.00715(10)
V3	18*h*	0.84869(5)	0.15131(5)	0.41784(3)	1.0	
O1	6*c*	0	0	0.12066(13)	1.0	
O2	6*c*	0	0	0.36938(13)	1.0	0.00600(19)
O3	18*h*	0.83188(15)	0.16812(15)	0.53896(9)	1.0	
O4	18*h*	0.82996(15)	0.17004(15)	0.28967(9)	1.0	

Table A.4: $R3m$ model refined against the 300 K diffraction pattern. Lattice parameters a_H = 5.75628(3) Å and c_H = 28.86488(24) Å. R_w = 4.33%.

Atom	Site	*x*	*y*	*z*	Occ.	U_{iso} (Å²)
Al1a	3*a*	0	0	0.18248(21)	1.0	0.00394(15)
Al1b	3*a*	0	0	0.81660(22)	1.0	
Al2a	3*a*	0	0	0.30883(19)	1.0	
Al2b	3*a*	0	0	0.68961(21)	1.0	
V1	3*a*	0	0	0	1.0	
V2	3*a*	0	0	0.49177(13)	1.0	0.00518(8)
V3a	9*b*	0.84879(18)	0.15121(18)	0.41753(13)	1.0	
V3b	9*b*	0.15242(19)	0.84758(19)	0.58190(13)	1.0	
O1a	3*a*	0	0	0.12222(33)	1.0	
O1b	3*a*	0	0	0.87731(30)	1.0	
O2a	3*a*	0	0	0.37302(28)	1.0	
O2b	3*a*	0	0	0.63139(29)	1.0	0.00469(23)
O3a	9*b*	0.83971(50)	0.16029(50)	0.54040(17)	1.0	
O3b	9*b*	0.17729(52)	0.82271(52)	0.46119(24)	1.0	
O4a	9*b*	0.82622(62)	0.17378(62)	0.29161(24)	1.0	
O4b	9*b*	0.16713(59)	0.83287(59)	0.71058(20)	1.0	

Table A.5: Split site $R\bar{3}m$ model refined against the 300 K diffraction pattern. Lattice parameters a_H = 5.75631(3) Å and c_H = 28.86439(23) Å. R_w = 4.16%.

Atom	Site	*x*	*y*	*z*	Occ.	U_{iso} (Å²)
Al1	6*c*	0	0	0.18287(5)	1.0	0.00375(14)
Al2	6*c*	0	0	0.30959(5)	1.0	
V1	3*a*	0	0	0	1.0	0.00462(7)
V2	6*c*	0	0	0.49173(5)	0.5	
V3	18*h*	0.84844(4)	0.15156(4)	0.41792(2)	1.0	
O1	6*c*	0	0	0.12204(10)	1.0	0.00658(14)
O2	6*c*	0	0	0.37061(10)	1.0	
O3	18*h*	0.83131(11)	0.16869(11)	0.53899(6)	1.0	
O4	18*h*	0.82985(11)	0.17015(11)	0.28996(6)	1.0	

Table A.6: Split site $R3m$ model refined against the 300 K diffraction pattern. Lattice parameters a_H = 5.75630(3) Å and c_H = 28.86444(23) Å. R_w = 4.11%.

Atom	Site	*x*	*y*	*z*	Occ.	U_{iso} (Å²)
Al1a	3*a*	0	0	0.18137(31)	1.0	0.00392(16)
Al1b	3*a*	0	0	0.81556(32)	1.0	
Al2a	3*a*	0	0	0.30975(42)	1.0	
Al2b	3*a*	0	0	0.69069(43)	1.0	
V1	3*a*	0	0	0	1.0	0.00469(7)
V2a	3*a*	0	0	0.49166(7)	0.57(2)	
V2b	3*a*	0	0	0.50835(7)	0.43(2)	
V3a	9*b*	0.84919(22)	0.15081(22)	0.41774(25)	1.0	
V3b	9*b*	0.15262(23)	0.84738(23)	0.58193(25)	1.0	
O1a	3*a*	0	0	0.12395(42)	1.0	0.00424(23)
O1b	3*a*	0	0	0.88006(40)	1.0	
O2a	3*a*	0	0	0.37184(44)	1.0	
O2b	3*a*	0	0	0.63100(45)	1.0	
O3a	9*b*	0.84195(49)	0.15805(49)	0.53956(23)	1.0	
O3b	9*b*	0.17939(51)	0.82061(51)	0.46104(33)	1.0	
O4a	9*b*	0.83069(62)	0.16931(62)	0.29246(29)	1.0	
O4a	9*b*	0.17104(61)	0.82896(61)	0.71207(30)	1.0	

Table A.7: Normal $Fd\bar{3}m$ model refined against the 1100 K diffraction pattern. Lattice parameter a_C = 8.26747(2) Å. R_w = 4.92%.

Atom	Site	*x*	*y*	*z*	Occ.	U_{iso} (Å²)
Al1	8*a*	0.125	0.125	0.125	1.0	0.01223(13)
V1	16*d*	0.5	0.5	0.5	1.0	0.01596(7)
O1	32*e*	0.24981(5)	0.24981(5)	0.24981(5)	1.0	0.01521(15)

Table A.8: Split site $Fd\bar{3}m$ model refined against the 1100 K diffraction pattern. Lattice parameter a_C = 8.26747(2) Å. R_w = 4.24%.

Atom	Site	*x*	*y*	*z*	Occ.	U_{iso} (Å²)
Al1	8*a*	0.125	0.125	0.125	1.0	0.01235(12)
V1a	16*d*	0.5	0.5	0.5	0.125	0.01148(9)
V1b	32*e*	0.49148(7)	0.49148(7)	0.49148(7)	0.4375	
O1	32*e*	0.24946(4)	0.24946(4)	0.24946(4)	1.0	0.01516(13)

Table A.9: $Fd\bar{3}m$ model refined against the 1100 K PDF. Lattice parameter a_C = 8.2670(78) Å. R_w = 16.6%.

Atom	Site	*x*	*y*	*z*	Occ.	U_{iso} (Å²)
Al1	8*a*	0.125	0.125	0.125	1.0	0.0115(28)
V1	16*d*	0.5	0.5	0.5	1.0	0.0156(2)
O1	32*e*	0.2510(21)	0.2510(21)	0.2510(21)	1.0	0.0292(39)

Table A.10: *R*3*m* model refined against the 1100 K PDF. Lattice parameters a_H = 5.848(6) Å and c_H = 28.648(29) Å. R_w = 11.6%.

Atom	**Site**	***x***	***y***	***z***	**Occ.**	U_{iso} **(Å²)**
Al1a	3*a*	0	0	0.1834(52)	1.0	0.0104(59)
Al1b	3*a*	0	0	0.8166(52)	1.0	
Al2a	3*a*	0	0	0.3106(48)	1.0	
Al2b	3*a*	0	0	0.6894(48)	1.0	
V1	3*a*	0	0	0	1.0	0.0126(18)
V2	3*a*	0	0	0.4970(8)	1.0	
V3a	9*b*	0.8413(21)	0.1587(21)	0.4177(3)	1.0	
V3b	9*b*	0.1587(21)	0.8413(21)	0.5823(3)	1.0	
O1a	3*a*	0	0	0.1276(69)	1.0	0.0129(53)
O1b	3*a*	0	0	0.8724(69)	1.0	
O2a	3*a*	0	0	0.3663(59)	1.0	
O2b	3*a*	0	0	0.6337(59)	1.0	
O3a	9*b*	0.8270(84)	0.1730(84)	0.5426(40)	1.0	
O3b	9*b*	0.1730(84)	0.8270(84)	0.4574(40)	1.0	
O4a	9*b*	0.8162(110)	0.1838(110)	0.2835(31)	1.0	
O4b	9*b*	0.1838(110)	0.8162(110)	0.7165(31)	1.0	

Appendix B: Structural characterisation of GaV_2O_4

In Section 3.3.3, the structural characterisation of GaV_2O_4 using high-resolution powder X-ray diffraction data was described. Rietveld analysis was performed using a split-site $R\bar{3}m$ model below T_{CO} = 415 K and a split-site $Fd\bar{3}m$ model above T_{CO}. The fits to the diffraction patterns measured at room temperature and 500 K are shown in Figure 3.9(b); the refined metal-oxygen bond distances from these fits are given in Table B.1, the metal-oxygen bond angles are given in Table B.2, and the V-V nearest-neighbour distances are given in Table B.3.

Table B.1: Refined *M*-O bond distances in GaV_2O_4.

	Room temperature	**500 K**
Ga1-O1	1.745(12) Å	1.8502(14) Å
Ga1-O3	1.848(7) Å	
Ga2-O2	1.865(11) Å	
Ga2-O4	1.860(7) Å	
V1-O4	2.081(8) Å	2.0559(8) Å
V2-O3	1.978(9) Å	
V2-O3	2.135(10) Å	
V3-O1	2.127(8) Å	
V3-O2	2.028(7) Å	
V3-O3	2.043(6) Å	
V3-O4	2.038(5) Å	

Table B.2: Refined O-*M*-O bond angles in GaV_2O_4.

	Room temperature	500 K
O1-Ga1-O3	111.42(26)°	109.471(0)°
O3-Ga1-O3	107.45(28)°	
O2-Ga2-O4	109.74(26)°	
O4-Ga2-O4	109.20(26)°	
O4-V1-O4	85.65(29)°	88.50(5)° 91.50(5)° 180.000(0)°
O4-V1-O4	94.35(29)°	
O4-V1-O4	180.000(0)°	
O3-V2-O3	84.9(4)°	
O3-V2-O3	90.62(31)°	
O3-V2-O3	93.5(4)°	
O3-V2-O3	173.9(4)°	
O1-V3-O2	177.6(4)°	
O1-V3-O3	89.28(27)°	
O1-V3-O4	85.96(25)°	
O2-V3-O3	92.44(24)°	
O2-V3-O4	92.30(27)°	
O3-V3-O3	89.7(4)°	
O3-V3-O4	91.01(31)°	
O3-V3-O4	175.18(22)°	
O4-V3-O4	87.9(4)°	

Table B.3: Refined V-V nearest-neighbour distances in GaV_2O_4.

	Room temperature	500 K
V1-V3	2.988(2) Å	2.94511(1) Å
V2-V3	2.801(8) Å	
V2-V3	3.024(8) Å	
V3-V3	2.817(3) Å	
V3-V3	3.045(3) Å	

Appendix C: $Zn_xGa_{1-x}V_2O_4$ magnetic susceptibilities

The magnetic behaviour of the $Zn_xGa_{1-x}V_2O_4$ system is detailed in Section 4.3.2. The zero-field cooled susceptibilities of all synthesised phases, plotted together in Figure 4.13, are given individually in Figures C.1-C.12, as are the associated field-cooled susceptibilities where measured. Equation 4.1 is fit to each of the zero-field cooled susceptibilities over the range 100-300 K and the parameters C, θ and A obtained from these fits, as well as the magnetic transition temperature T_{spin}, which are plotted in Figure 4.14 are given for each phase.

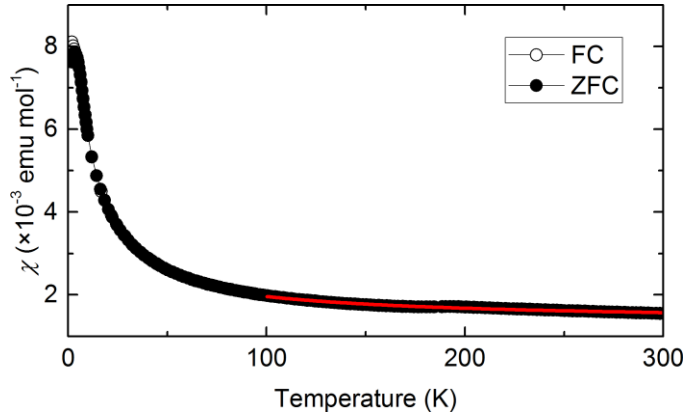

Figure C.1: x = 0. C = 0.074(9) emu K mol^{-1}, θ = -20(11) K, and A = 1.34(2) ×10^{-3} emu mol^{-1}. T_{spin} = 3.8 K.

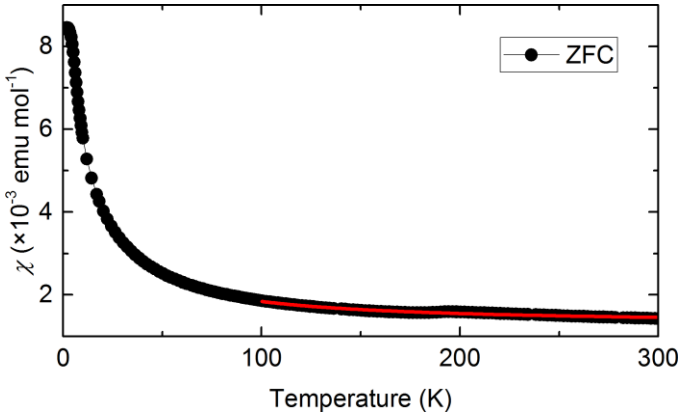

Figure C.2: x = 0.02. C = 0.054(7) emu K mol^{-1}, θ = 5(11) K, and A = 12.8(2) ×10^{-3} emu mol^{-1}. T_{spin} = 4 K.

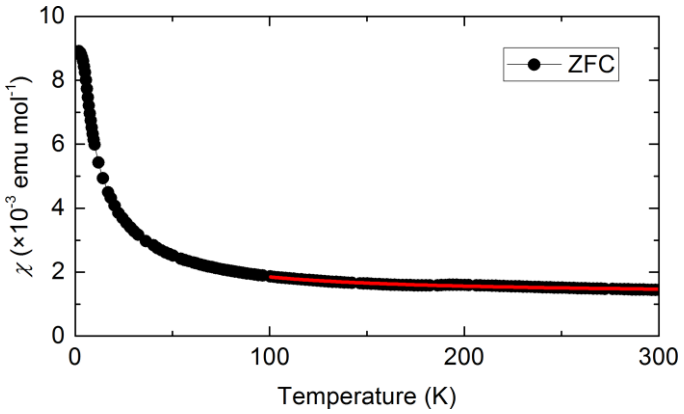

Figure C.3: x = 0.04. C = 0.056(8) emu K mol^{-1}, θ = 1(11) K, and A = 1.28(2) ×10^{-3} emu mol^{-1}. T_{spin} = 4 K.

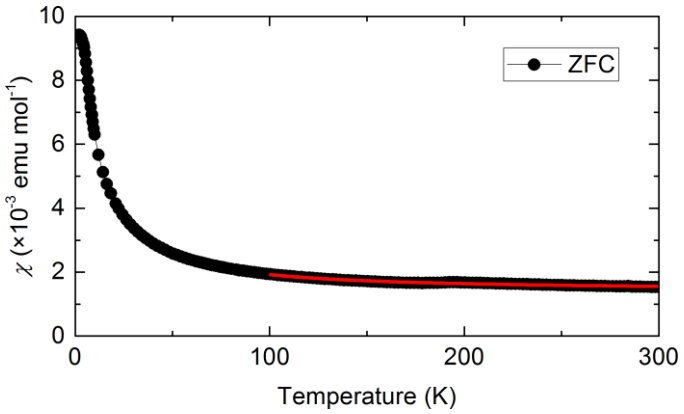

Figure C.4: x = 0.06. C = 0.045(5) emu K mol^{-1}, θ = 14(8) K, and A = 1.40(2) ×10^{-3} emu mol^{-1}. T_{spin} = 4 K.

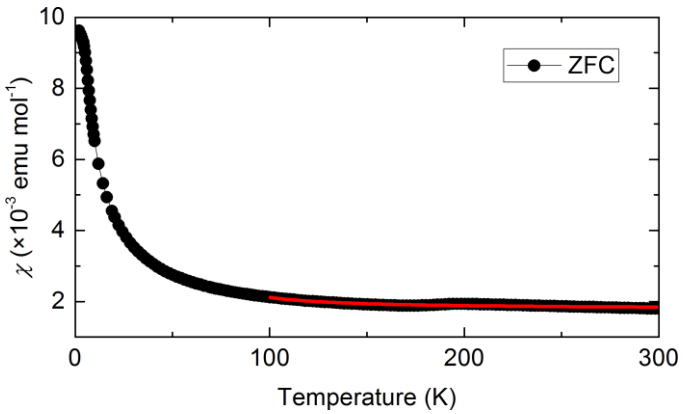

Figure C.5: x = 0.125. C = 0.015(2) emu K mol^{-1}, θ = 56(7) K, and A = 1.78(1) ×10^{-3} emu mol^{-1}. T_{spin} = 4 K.

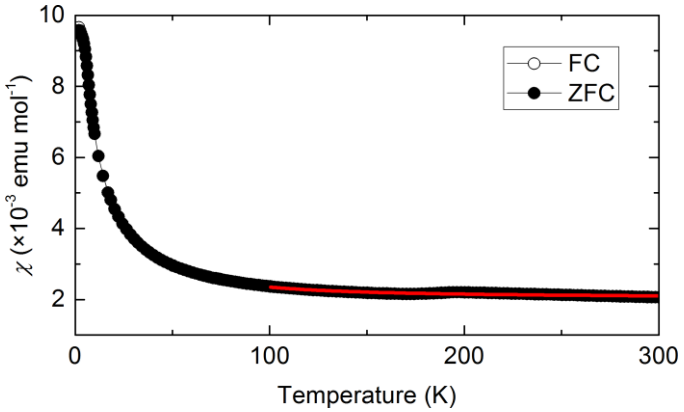

Figure C.6: x = 0.25. C = 0.022(5) emu K mol^{-1}, θ = 33(14) K, and A = 2.02(2) ×10^{-3} emu mol^{-1}. T_{spin} = 4 K.

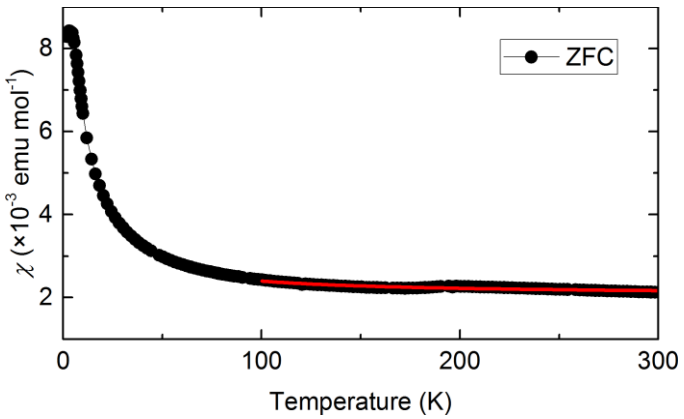

Figure C.7: x = 0.375. C = 0.03(1) emu K mol^{-1}, θ = 3(23) K, and A = 2.06(3) ×10^{-3} emu mol^{-1}. T_{spin} = 4 K.

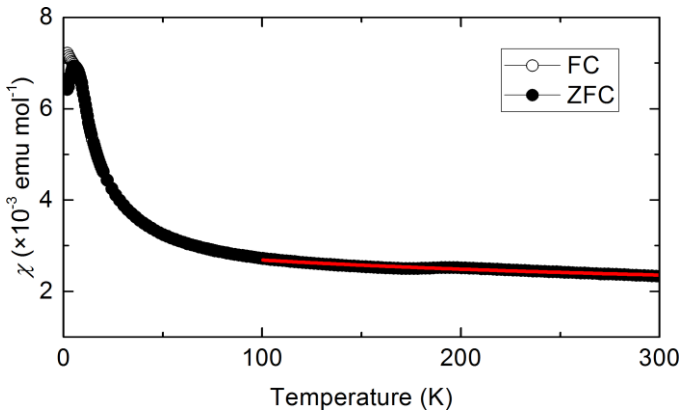

Figure C.8: x = 0.5. C = 0.34(13) emu K mol^{-1}, θ = -264(89) K, and A = 1.76(15) ×10^{-3} emu mol^{-1}. T_{spin} = 6 K.

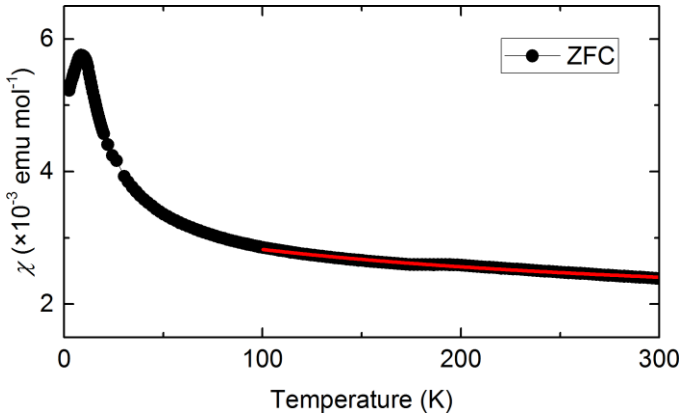

Figure C.9: x = 0.625. C = 0.31(6) emu K mol^{-1}, θ = -198(35) K, and A = 1.78(7) ×10^{-3} emu mol^{-1}. T_{spin} = 9 K.

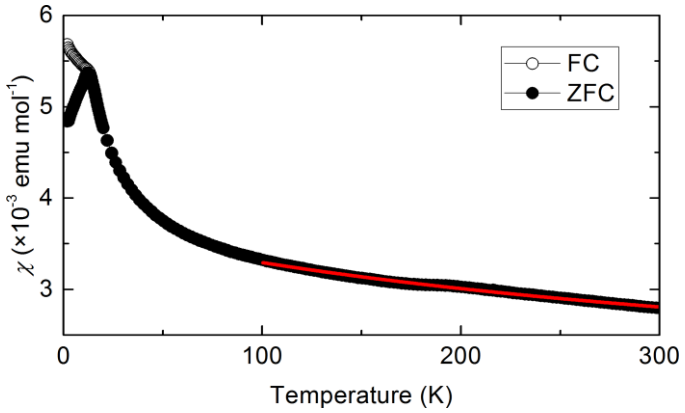

Figure C.10: x = 0.75. C = 0.80(16) emu K mol^{-1}, θ = -382(55) K, and A = 1.64(14) ×10^{-3} emu mol^{-1}. T_{spin} = 12 K.

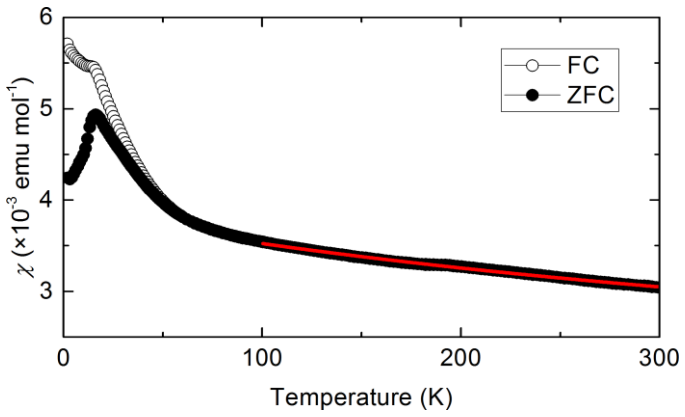

Figure C.11: x = 0.875. C = 1.41(28) emu K mol^{-1}, θ = -578(76) K, and A = 1.44(18) ×10^{-3} emu mol^{-1}. T_{spin} = 16 K.

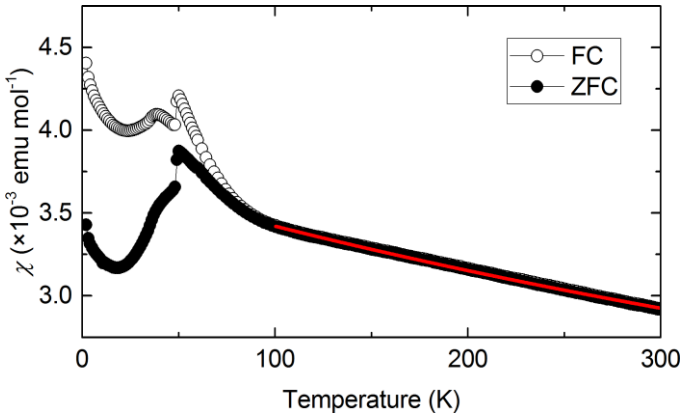

Figure C.12: x = 1. C = 3.50(1) emu K mol^{-1}, θ = -993(4) K, and A = 0.22(0) ×10^{-3} emu mol^{-1}. T_{spin} = 39 K.

Publications

The following publications have resulted from work presented in this Thesis:

- *Persistent three- and four-atom orbital molecules in the spinel AlV_2O_4*
  A. J. Browne, S. A. J. Kimber and J. P. Attfield
  Reprinted with permission from *Phys. Rev. Mater.*, 2017, **1**, 052003(R)

- *Orbital molecules in the new spinel GaV_2O_4*
  A. J. Browne, C. Lithgow, S. A. J. Kimber and J. P. Attfield
  Reprinted with permission from *Inorg. Chem.*, 2018, **57**, 2815-2822

PHYSICAL REVIEW MATERIALS **1**, 052003(R) (2017)

Persistent three- and four-atom orbital molecules in the spinel AlV_2O_4

Alexander J. Browne,[1] Simon A. J. Kimber,[2] and J. Paul Attfield[1,*]

[1]*Centre for Science at Extreme Conditions and School of Chemistry, University of Edinburgh, West Mains Road, Edinburgh EH9 3FD, United Kingdom*

[2]*Chemical and Engineering Materials Division, Oak Ridge National Laboratory, Oak Ridge, Tennessee 37831, USA*

(Received 15 August 2017; published 31 October 2017)

Electronic instabilities in transition-metal compounds may lead to ground states containing orbital molecules when direct metal-metal orbital interactions occur. The spinel AlV_2O_4 was reported to contain V_7^{17+} orbital heptamers that emerge below a 700 K charge ordering transition. Our x-ray total scattering analysis of AlV_2O_4 between 300 and 1100 K reveals a very different picture as the postulated heptamers are found to be pairs of spin-singlet V_3^{9+} trimers and V_4^{8+} tetramers, and these orbital molecules persist to at least 1100 K in a disordered high-temperature cubic phase.

DOI: 10.1103/PhysRevMaterials.1.052003

Notable electronic and magnetic properties arise from the ordering of charge, orbital, and spin degrees of freedom in transition-metal (M) oxides and related compounds [1,2]. When M-M distances are short, for example, through edge or face sharing of MO_6 octahedra, moleculelike clusters of metal cations may be formed if ordering localizes electrons into appropriately oriented d orbitals [3]. Clusters of metal-metal bonded cations formed below an orbital ordering transition have thus been termed "orbital molecules" [4]. A classic exemplar is VO_2, where a metal-insulator transition and accompanying structural (Peierls) distortion at 340 K leads to the formation of $(V^{4+})_2$ dimers within one-dimensional chains from V ions that are uniformly spaced above the transition [5,6]. The importance of moleculelike bonding interactions in driving the dimerization in VO_2, and related materials such as Ti_4O_7, V_4O_7, and NbO_2, has recently been highlighted [7]. More complex arrangements of orbital dimers are found in $CuIr_2S_4$ [8] and $MgTi_2O_4$ [9], and the formation of disordered $(Mo^{4+})_2$ orbital dimers has recently been identified at the spin-glass transition of the pyrochlore $Y_2Mo_2O_7$ [10].

Orbital molecules of more than two M ions are less common. Triangular $(V^{3+})_3$ clusters are found in A_xVO_2 (A = Li,Na) materials and $BaV_{10}O_{15}$ [11–13], while linear Fe_3^{8+} "trimerons" are observed in the complex electronic order of magnetite (Fe_3O_4) below the much-studied Verwey transition [14,15], and coexisting dimers and trimers are reported in the related material Fe_4O_5 [16]. The largest orbital molecules claimed to date are heptameric clusters, reported in AlV_2O_4 below a charge and orbital ordering transition accompanied by a rhombohedral to cubic structural distortion at $T_{CO} = 700$ K [17]. The ground state was reported as having a formal charge distribution $Al_4[V_7^{17+}V^{3+}]O_{16}$, where the V_7^{17+} heptamer has 18 $3d$ electrons occupying nine localized orbitals with an overall spin $S = 0$, while the remaining $S = 1$ V^{3+} cation is paramagnetic. The spin singlet nature of the heptamers was confirmed by ^{51}V NMR measurements [18] and further studies revealed that the long-range charge and orbital ordering is suppressed by replacing V with 5% Cr [19], or by applying pressures over 21 GPa [20].

The conventional picture of orbital molecule formation is that these quantum states emerge by displacive distortions from a structurally uniform high-temperature phase below some electronic and structural transition temperature, ranging from the Peierls transition in VO_2 to an intersecting one-dimensional orbital ordering wave description of the heptamer order in AlV_2O_4 [21]. However, recent studies of local structure through analysis of the pair distribution function (PDF) obtained from total scattering measurements have shown that disordered $4d$ orbital dimers persist above the transition in $LiRh_2O_4$, where $(Rh^{4+})_2$ dimers persist up to 350 K, well above their 170 K ordering temperature [22], and in Li_2RuO_3, where $(Ru^{4+})_2$ dimers order below 540 K but are evident to at least 920 K [23]. However, similar PDF studies of $CuIr_2S_4$ and VO_2 (the only $3d$ transition-metal material investigated in this way) have reported that the orbital dimers disappear from both the long-range and local structure above their transition temperatures [24,25]. To investigate whether large orbital molecules can persist to high temperatures, we have studied the long-range and local structure of AlV_2O_4, and in this Rapid Communication we report a very different picture of the electronic ordering in this material than that previously described.

Polycrystalline AlV_2O_4 was synthesized from powdered Al, V_2O_5, and V_2O_3 ground together in the stoichiometric ratio, pressed into pellets, and sealed in evacuated quartz ampoules for three heatings up to 1150 °C for a total of 96 h, with intermediate regrinding and pelleting. V_2O_3 was prepared by a reduction of V_2O_5 under flowing H_2 at 900 °C. Magnetization measurements shown in the Supplemental Material [30] are similar to those in the literature [17]. High-energy x-ray total scattering data were collected on beamline ID22 at the European Synchrotron Radiation Facility using wavelength $\lambda = 0.206547$ Å. The AlV_2O_4 sample was held in a 0.7-mm-diameter quartz capillary and heated to temperatures between 300 and 1100 K using a hot air blower. Rietveld fits to the x-ray patterns were carried out using the GSAS program [26]. For PDF analysis, background-corrected scattering functions $S(Q)$ were transformed to pair distribution functions $G(r)$, using PDFGETX3 [27], for momentum transfers Q between 0.5 and 25.8 Å^{-1}. Structural models were refined against the PDF data using the PDFGUI program [28], including simulation of termination ripples, over the interatomic distance range $1.5 \leqslant r(\text{Å}) \leqslant 12$. As a further check that orbital molecule features

*j.p.attfield@ed.ac.uk

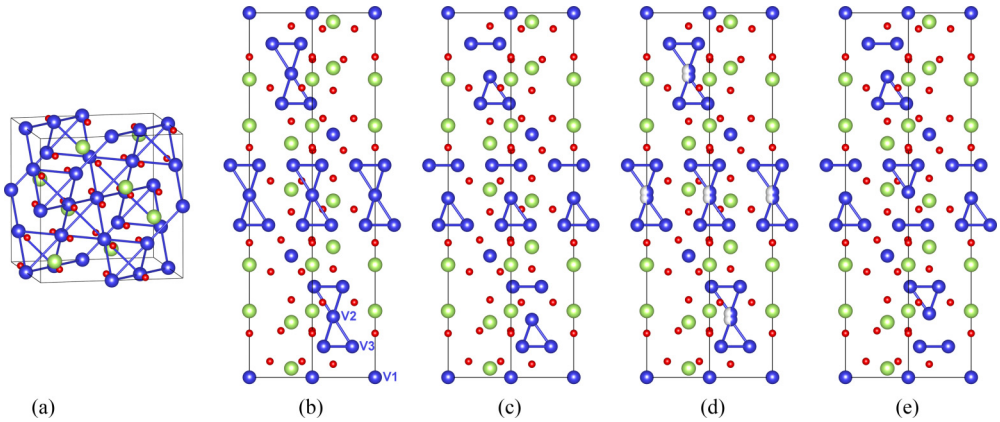

FIG. 1. Structural models for AlV_2O_4 where Al/V/O are green/blue/red atoms. (a) The cubic spinel structure, showing nearest-neighbor V-V connections, which are all equivalent. (b) The previously reported V_7 cluster model with $R\bar{3}m$ symmetry. The three symmetry-independent vanadium sites are labeled: Site V1 is occupied by paramagnetic V^{3+} cations, while each heptamer comprises a central V2 atom between two triangles of V3 atoms. (c) The $R3m$ model used for PDF fitting, in which V_3 and V_4 orbital molecules have long-range ferroelectric order. (d) The split-site $R\bar{3}m$ model used to describe the disordered antiferroelectric average crystal structure in the Rietveld fits. (e) A local configuration showing a statistical distribution of the clusters corresponding to the split-site average in (d). The rhombohedral unit cells in (b)–(e) are projected on the (110) plane with the c axis vertical, and short (<2.90 Å) orbital molecule V-V distances are shown.

extracted from the AlV_2O_4 PDFs are not the result of termination errors or other data artifacts, comparable x-ray data were also collected at 300 K from the cubic spinel LiV_2O_4, which is of interest for heavy fermion behavior [29]. Fits to the LiV_2O_4 PDF do not evidence orbital molecules or other deviations from the cubic spinel structure. These and further structural results for AlV_2O_4 are in the Supplemental Material [30].

AlV_2O_4 is reported to have a cubic spinel structure [Fig. 1(a)] at high temperatures, and a rhombohedral ordered arrangement of V_7 heptamers (space group $R\bar{3}m$) below $T_{CO} = 700$ K [Fig. 1(b)] [17]. However, the $R\bar{3}m$ heptamer model was found to give a poor fit to the PDF derived from 300 K x-ray scattering data, particularly in the 2.4–3.2 Å range where nearest-neighbor V-V distances lie [Fig. 2(a)]. This indicates that the heptamer description of short-range V-V bonding is incorrect. Modifications to the orbital molecule structure were investigated, and a simple change was found to bring the fit into agreement with the PDF in the V-V region. Allowing the central V atom of the heptamers (atom V2 in the structural model) to move in the z direction towards one of the two triangular end faces greatly improves the overall fit [Fig. 2(a)]. This displacement forms separate triangular V_3 and tetrahedral V_4 clusters within which V-V distances are short (<2.7 Å), indicative of bonding, while intercluster V-V distances are much longer (>2.9 Å). Previous measurements indicated that the apparent V_7^{17+} heptamers have a spin singlet ground state [17,18], and the same condition is met by a combination of $S = 0$ V_3^{9+} trimers and $S = 0$ V_4^{8+} tetramers. These result from simple two-center two-electron V-V bonding: Three $3d^2$ V^{3+} ions form two bonds each, giving V_3^{9+} triangles, and four $3d^3$ V^{2+} ions are each bonded to three others in V_4^{8+} tetrahedra. The charge distribution in the ground state of AlV_2O_4 is thus $Al_4[V_4^{8+}V_3^{9+}V^{3+}]O_{16}$, showing an unprecedented coexistence of two large orbital molecules.

The $Al_4[V_4{}^{8+}V_3{}^{9+}V^{3+}]O_{16}$ model was fitted to the low-temperature PDF data by allowing all V2 atoms to displace in the same direction which lowers the space group symmetry to polar $R3m$, although $R\bar{3}m$ symmetry constraints were applied to all other atoms to reduce the number of variables. The long-range ordering of pairs of V_3^{9+} and V_4^{8+} orbital molecules in this $R3m$ model [Fig. 1(c)] is polar and could give rise to ferroelectricity. A simple ordering of antiparallel V2 displacements to give an alternative antiferroelectric order is frustrated in rhombohedral symmetry as the V2 sites are arranged in triangular layers, so the alternative ground state has the disordered structural average shown in Fig. 1(d), where a half-occupied split V2 site models the disorder within each orbital molecule pair. Rietveld fits (shown in the Supplemental Material [30]) of the ferroelectric ordered pair model gave poorer fits than the disordered antiferroelectric average model, hence the latter is taken as our proposed ground-state structure for AlV_2O_4 corresponding to a long-range ordered array of disordered pairs of V_3^{9+} and V_4^{8+} orbital molecules, as shown in Fig. 1(e), equivalent to the split V2 site model of Fig. 1(d) in the crystallographic average.

Above $T_{CO} = 700$ K the structural symmetry of AlV_2O_4 changes from rhombohedral to cubic. The cubic $Fd\bar{3}m$ normal spinel structure [Fig. 1(a)] has one electronically averaged $V^{2.5+}$ site, and all nearest-neighbor V-V distances are equal. However, this model gives a poor fit to the PDF derived from 1100 K x-ray data in the relevant 2.4–3.2 Å region [Fig. 2(b)], suggesting that local V displacements are still present above T_{CO}. To explore whether the V_3^{9+} and V_4^{8+} orbital molecules survive to high temperatures, the $R3m$ model [Fig. 1(c)] was used to fit the PDFs above 700 K. The hexagonal lattice parameters a_H and c_H were constrained to give a metrically cubic lattice ($c_H/a_H = \sqrt{24}$), consistent with the average structure, and all V-V distances within the two orbital molecules were constrained to be equal to improve refinement stability at high temperatures. This model greatly improves the fit to the PDF data [Fig. 2(b)] and the derived V-V distances are found to evolve continuously between the rhombohedral and cubic phases [Fig. 3(a)]. Even at 1100 K, bonding V-V distances within orbital molecules are 2.78 Å and nonbonding

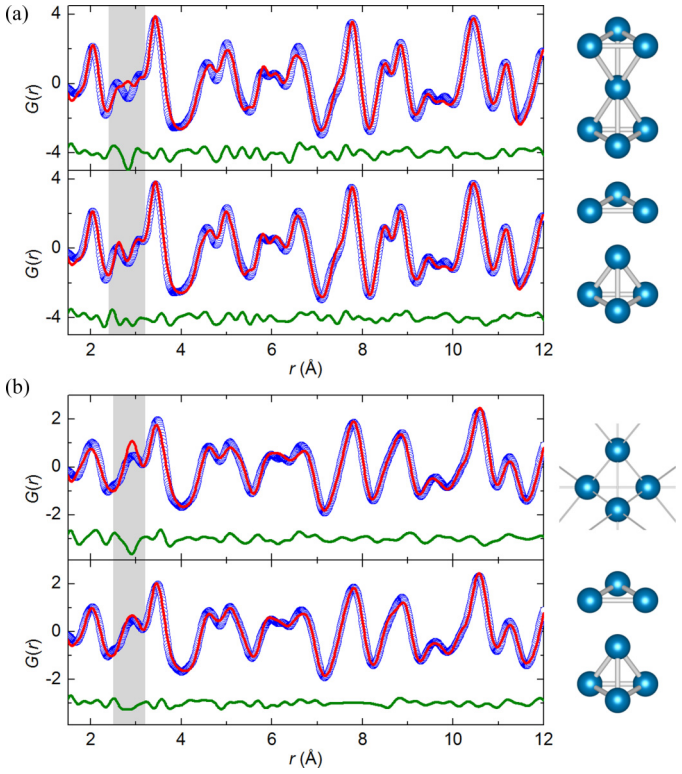

FIG. 2. Comparisons of fits to pair distribution functions (PDFs) of AlV_2O_4 where nearest-neighbor V-V distances lie in the shaded region at $r = 2.4$–3.2 Å. The local vanadium species in each structural model are shown to the right. (a) 300 K PDF, where the upper fit (residual $R_w = 16.3\%$) of the $R\bar{3}m$ V_7 heptamer model [Fig. 1(b)] agrees poorly in the V-V region, but allowing the central V to move off center to form V_3 and V_4 orbital molecules in the $R3m$ model [Fig. 1(c)] gives the improved fit shown below ($R_w = 13.6\%$). (b) 1100 K PDF, where the upper fit of the ideal cubic $Fd\bar{3}m$ spinel model [Fig. 1(a)] gives a poor fit in the shaded region ($R_w = 16.6\%$), but the lower fit of V_3 and V_4 orbital molecules in a $R3m$ model [Fig. 1(c)] constrained by metrically cubic cell parameters greatly improves the agreement ($R_w = 11.6\%$).

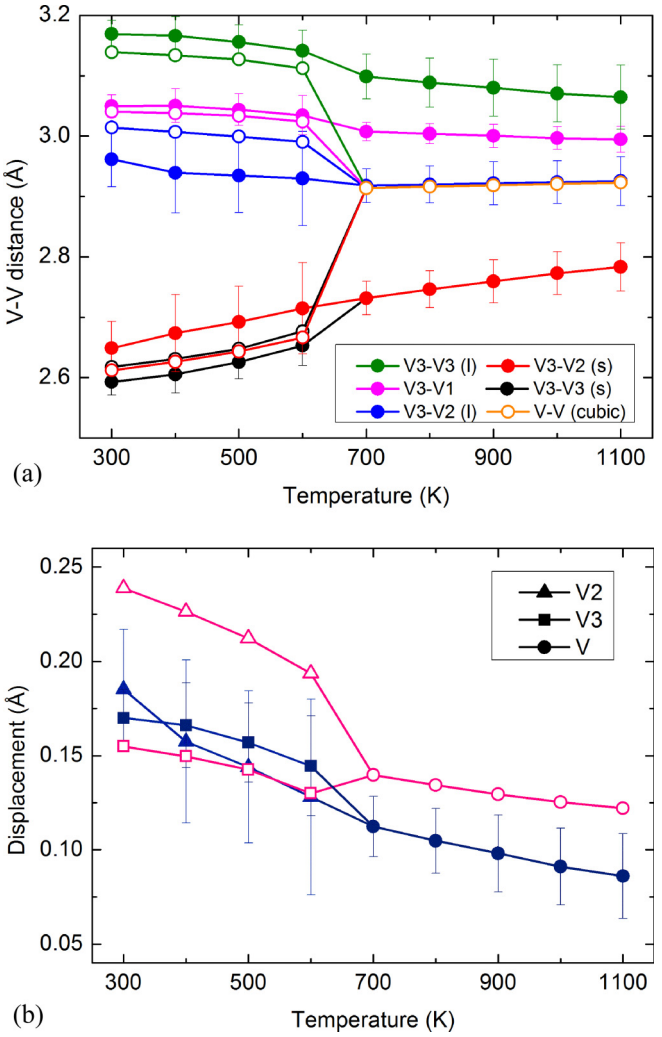

FIG. 3. (a) Comparison of V-V nearest-neighbor distances in AlV_2O_4 from PDF fits (solid symbols) using the $R3m$ structural description, and Rietveld analyses (open symbols) using the split-site $R\bar{3}m$ and cubic $Fd\bar{3}m$ spinel models respectively below and above $T_{CO} = 700$ K. Rietveld V-V distances all converge to a single value above T_{CO} because disordered orbital molecules are not described by a cubic average spinel structure, but PDF fitting shows that they persist above T_{CO}. (The two bonding V-V distances were constrained to be equal in the PDF fits above T_{CO} for refinement stability.) (b) Displacements of V atoms from their ideal sites due to orbital molecule formation, from PDF (solid symbols) and the split-site Rietveld (open symbols) analyses. Both sets of displacements decrease smoothly on heating, but evidence the persistence of orbital molecules to 1100 K.

distances vary between 2.93 and 3.06 Å, whereas the standard cubic spinel description predicts all V-V distances to be 2.92 Å. To describe the disordered orbital molecules within the cubic average structure of $Al_4[V_4^{8+}V_3^{9+}V^{3+}]O_{16}$ in Rietveld fits we used a split-site $Fd\bar{3}m$ model in which 7/8 of the V scattering (representing the proportion of vanadium atoms in orbital molecules) is displaced to two sites either side of the ideal position that holds the remaining 1/8. This leads to an improved fit to all the high-temperature profiles, as shown in the Supplemental Material [30]. Whether the orbital molecules have significant dynamics with motions coupled to the phonon modes at high temperatures is unclear from the present data, and inelastic scattering experiments will be needed to test this possibility.

A comparison of V atom displacements derived from the PDF fits and split-site Rietveld refinements in Fig. 3(b) shows that they agree well, with the V displacement decreasing from ~0.2 Å at 300 K to ~0.1 Å at 1100 K. Extrapolation indicates that zero displacement (i.e., a uniform cubic spinel arrangement) would be reached above ~2000 K, which is far above the ~1400 K synthesis temperature for AlV_2O_4. Previous measurements showed little change in magnetization or conductivity through the transition at $T_{CO} = 700$ K (AlV_2O_4 is a semiconductor with activation energy ~0.4 eV) [31], which corroborates the validity of the $Al_4[V_4^{8+}V_3^{9+}V^{3+}]O_{16}$ description at high temperatures as smaller species derived from the breakdown of the $S = 0$ V_3^{9+} and V_4^{8+} orbital molecules would either lead to large increases in paramagnetic susceptibility from electron-localized states, as the theoretical Curie

constant per V atom changes from $C = 0.125$ emu K mol^{-1} for $Al_4[V_4^{8+}V_3^{9+}V^{3+}]O_{16}$ towards 1.44 emu K mol^{-1} for paramagnetic $AlV^{2+}V^{3+}O_4$, or to increased conductivity through electron delocalization. Hence, AlV_2O_4 has remarkably stable V_3^{9+} and V_4^{8+} orbital molecules that are disordered within the high-temperature cubic spinel phase to at least 1100 K, and form an ordered array of disordered pairs below the apparent charge ordering transition at 700 K.

The structural insights derived from this study demand a substantial revision of theoretical descriptions for the electronic transition in AlV_2O_4 and the physics of large orbital molecule formation. The ground state of AlV_2O_4 is found to contain pairs of spin-singlet V_3^{9+} trimers and V_4^{8+} tetramers, rather than V_7^{17+} heptamers as previously reported. The upper size limit of known orbital molecules is thus reduced from seven- to four-atom clusters. This provides a more consistent size distribution for the known species, with many dimers, a few trimers, and tetrameric V_4^{8+} orbital molecules as the largest example. AlV_2O_4 is thus notable for containing a mixture of the two largest known orbital molecules. The $V_3{}^{9+}/V_4^{8+}$ orbital molecules within each pair in the ground state appear to be disordered, but could lead to a novel ferroelectric state if ordered. High-temperature studies demonstrate that disordered $V_3{}^{9+}$ and V_4^{8+} orbital molecules "hidden" in the crystallographic cubic average structure of AlV_2O_4 persist to at least 1100 K, far above the apparent charge ordering transition at 700 K. The conventional picture of orbital molecules emerging displacively from a structurally uniform phase below the electronic and structural transition is thus incorrect for this spinel. The ideal cubic structure is apparently unstable over all its existence range with respect to local charge and orbital ordering that produces orbital molecules, and their disorder to a pairwise order transition leads to the cubic to rhombohedral structural change observed on cooling below T_{CO}. The temperature scales for the formation and the long-range ordering of orbital molecules are thus very different for AlV_2O_4, unlike in VO_2 in which they are the same [25], showing that orbital molecule phenomena in these apparently similar 3*d*-metal oxides can originate from real-space (molecular) or momentum-space (Fermi surface) electronic instabilities. Reinvestigation of similar materials using local structure methods will thus be important to discover whether "hidden" orbital molecules are present in other apparently uniform average structures.

We thank Mauro Coduri for help with data collection. This work was supported by the ERC and access to ESRF was provided by STFC. Part of this work was supported by the US Department of Energy (DOE), Office of Science, Basic Energy Sciences, at the Oak Ridge National Laboratory.

[1] C. N. R. Rao and B. Raveau, *Transition Metal Oxides* (Wiley-VCH, New York, 1998).
[2] P. A. Cox, *Transition Metal Oxides: An Introduction to Their Electronic Structure and Properties* (Oxford University Press, Oxford, UK, 2010).
[3] J. B. Goodenough, Phys. Rev. **117**, 1442 (1960).
[4] J. P. Attfield, APL Mater. **3**, 041510 (2015).
[5] A. Magnéli, and G. Andersson, Acta Chem. Scand. **9**, 1378 (1955).
[6] F. J. Morin, Phys. Rev. Lett. **3**, 34 (1959).
[7] Z. Hiroi, Prog. Solid State Chem. **43**, 47 (2015).
[8] P. G. Radaelli, Y. Horibe, M. J. Gutmann, H. Ishibashi, C. H. Chen, R. M. Ibberson, Y. Koyama, Y.-S. Hor, V. Kiryukhin, and S. W. Cheong, Nature (London) **416**, 155 (2002).
[9] M. Schmidt, W. Ratcliff II, P. G. Radaelli, K. Refson, N. M. Harrison, and S. W. Cheong, Phys. Rev. Lett. **92**, 056402 (2004).
[10] P. M. M. Thygesen, J. A. M. Paddison, R. Zhang, K. A. Beyer, K. W. Chapman, H. Y. Playford, M. G. Tucker, D. A. Keen, M. A. Hayward, and A. L. Goodwin, Phys. Rev. Lett. **118**, 067201 (2017).
[11] T. Jin-no, Y. Shimizu, M. Itoh, S. Niitaka, and H. Takagi, Phys. Rev. B **87**, 075135 (2013).
[12] M. Guignard, D. Carlier, C. Didier, M. R. Suchomel, E. Elkaïm, P. Bordet, R. Decourt, J. Darriet, and C. Delmas, Chem. Mater. **26**, 1538 (2014).
[13] T. Kajita, T. Kanzaki, T. Suzuki, J. E. Kim, K. Kato, M. Takata, and T. Katsufuji, Phys. Rev. B **81**, 060405(R) (2010).
[14] E. J. W. Verwey, Nature (London) **144**, 327 (1939).
[15] M. S. Senn, J. P. Wright, and J. P. Attfield, Nature (London) **481**, 173 (2012).
[16] S. V. Ovsyannikov *et al.*, Nat. Chem. **8**, 501 (2016).
[17] Y. Horibe, M. Shingu, K. Kurushima, H. Ishibashi, N. Ikeda, K. Kato, Y. Motome, N. Furukawa, S. Mori, and T. Katsufuji, Phys. Rev. Lett. **96**, 086406 (2006).
[18] Y. Shimizu, M. Tanaka, M. Itoh, and T. Katsufuji, Phys. Rev. B **78**, 144423 (2008).
[19] K. Matsuno, T. Katsufuji, S. Mori, M. Nohara, A. Machida, Y. Moritomo, K. Kato, E. Nishibori, M. Takata, M. Sakata, K. Kitazawa, and H. Takagi, Phys. Rev. Lett. **90**, 096404 (2003).
[20] S. Kalavathi, S. Vennila Raju, S. Chandra, Q. Williams, and P. Ch. Sahu, Solid State Commun. **250**, 23 (2017).
[21] M. Croft, V. Kiryukhin, Y. Horibe, and S.-W. Cheong, New J. Phys. **9**, 86 (2007).
[22] K. R. Knox, A. M. M. Abeykoon, H. Zheng, W.-G. Yin, A. M. Tsvelik, J. F. Mitchell, S. J. L. Billinge, and E. S. Bozin, Phys. Rev. B **88**, 174114 (2013).
[23] S. A. J. Kimber, I. I. Mazin, J. Shen, H. O. Jeschke, S. V. Streltsov, D. N. Argyriou, R. Valentí, and D. I. Khomskii, Phys. Rev. B **89**, 081408(R) (2014).
[24] E. S. Božin, A. S. Masadeh, Y. S. Hor, J. F. Mitchell, and S. J. L. Billinge, Phys. Rev. Lett. **106**, 045501 (2011).
[25] S. A. Corr, D. P. Shoemaker, B. C. Melot, and R. Seshadri, Phys. Rev. Lett. **105**, 056404 (2010).
[26] A. C. Larson and R. B. Von Dreele, General Structure Analysis System (GSAS), Los Alamos National Laboratory Report No. LAUR 86-748, 2004 (unpublished).
[27] P. Juhás, T. Davis, C. L. Farrow, and S. J. L. Billinge, J. Appl. Crystallogr. **46**, 560 (2013).

[28] C. L. Farrow, P. Juhas, J. W. Liu, D. Bryndin, E. S. Božin, J. Bloch, Th. Proffen, and S. J. L. Billinge, J. Phys.: Condens. Matter **19**, 335219 (2007).

[29] S. Kondo *et al.*, Phys. Rev. Lett. **78**, 3729 (1997).

[30] See Supplemental Material at http://link.aps.org/supplemental/10.1103/PhysRevMaterials.1.052003 for further details of magnetic susceptibility, PDF, and Rietveld analyses. Open data for this article are at http://datashare.is.ed.ac.uk/handle/10283/838.

[31] K. Matsuno, T. Katsufuji, S. Mori, Y. Moritomo, A. Machida, E. Nishibori, M. Takata, M. Sakata, N. Yamamoto, and H. Takagi, J. Phys. Soc. Jpn. **70**, 1456 (2001).

Inorganic Chemistry
Cite This: Inorg. Chem. 2018, 57, 2815−2822
Article
pubs.acs.org/IC

Orbital Molecules in the New Spinel GaV_2O_4

Alexander J. Browne,[†] Calum Lithgow,[†] Simon A. J. Kimber,[‡] and J. Paul Attfield*[,†]

[†]Centre for Science at Extreme Conditions and School of Chemistry, University of Edinburgh, West Mains Road, Edinburgh EH9 3FD, United Kingdom

[‡]Diffraction Group, Neutron Sciences Division, Oak Ridge National Laboratory, Oak Ridge, Tennessee 37831, United States

Supporting Information

ABSTRACT: The structures and properties of vanadium oxides are often related to the formation of molecule-like clusters of vanadium cations through direct V−V bonding. GaV_2O_4, a new vanadium spinel, was synthesized. Powder diffraction and X-ray total scattering studies, complemented by magnetization and resistivity measurements, reveal that the low-temperature phase of this material is structurally distorted and features ordered pairs of three- and four-atom vanadium clusters. These clusters persist into a disordered cubic phase above the charge-ordering transition at T_{CO} = 415 K. Furthermore, quasi-elastic neutron scattering indicates that the disordered clusters remain well-defined and static to 1100 K.

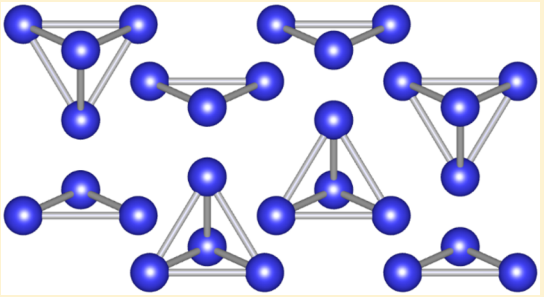

INTRODUCTION

The notable electronic properties of vanadium oxides have led to these materials finding numerous applications. Several systems, such as layered $Li_{1+x}V_{1-x}O_2$[1] and Na_xVO_2[2] phases and nanostructured V_2O_5,[3] are being investigated as battery electrode materials. Nanospheres of the spinel ZnV_2O_4 have promising supercapacitance and hydrogen storage properties;[4] BIMEVOX phases derived from γ-$Bi_4V_2O_{11}$ are a prominent family of oxide ion conductors;[5] and many vanadium oxides are used as catalysts.[6]

In some vanadium oxides, functionality is the result of an electronic ordering transition. A prominent example is VO_2, which undergoes an ultrafast metal−insulator transition at 340 K.[7] There is considerable interest in developing technology that exploits the dramatic change in properties associated with this transition, ranging from electronic switches to chemical sensors and thermochromic window coatings.[8,9]

At the metal−insulator transition, VO_2 undergoes changes to both its electronic and crystallographic structure. In the high-temperature metallic phase there is a single V−V nearest-neighbor distance (2.87 Å), found along chains of edge-sharing VO_6 octahedra, but this splits into alternatingly short (2.65 Å) and long (3.12 Å) separations in the low-temperature insulating regime.[10] This is an example of an orbital molecule state—the short V−V separations in insulating VO_2 define spin-singlet $(V^{4+})_2$ dimers. Orbital molecules are clusters of transition-metal cations formed when orbital ordering localizes electrons into directly interacting d orbitals,[11] and they are found in the ground states of many vanadium oxides. Mixed-valence oxides such as V_4O_7, which are structurally related to VO_2, also exhibit metal−insulator transitions accompanied by V−V dimerization.[12] Triangular $(V^{3+})_3$ spin-singlet trimers form in $LiVO_2$, $Li_{1+x}V_{1-x}O_2$ ($x \leq 0.1$),[13] and $BaV_{10}O_{15}$.[14] $NaVO_2$ undergoes orbital ordering without forming orbital molecules,[15] but interestingly the ground states of different polymorphs of $Na_{0.5}VO_2$, corresponding to different arrangements of the Na-site vacancies, exhibit different vanadium clusterings, and both dimer and trimer ground states have been found.[16] In all of these materials the formation of orbital molecules coincides with dramatic changes to their electronic structure, and hence to their electrical and magnetic properties.

Understanding the microscopic mechanism of orbital molecule formation is desirable for developing this behavior into functionality. Typically, V−V bonds emerge when a uniform structure distorts below an electronic transition temperature. In both VO_2 and $LiVO_2$, the distortion is driven by orbital polarizations that result in significant d−d σ-bonding interactions.[17,18] This is similar to the orbitally induced Peierls transition used to describe the formation of orbital dimer states in the spinels $CuIr_2S_4$ and $MgTi_2O_4$.[19]

However, we recently found a very different type of orbital molecule behavior in the spinel AlV_2O_4.[20] Investigation of the local structure of this material through analysis of the pair distribution function (PDF) revealed ordered $(V^{3+})_3$ trimers and $(V^{2+})_4$ tetramers—the largest known orbital molecules—in the distorted $R\bar{3}m$ ground state, and not V_7^{17+} heptamers as previously proposed.[21] This ground state is the result of long-range orbital- and charge-ordering, corresponding to the electronic description $Al_4[V_4^{8+}V_3^{9+}V^{3+}]O_{16}$. Above the transition temperature T_{CO} = 700 K this long-range order is lost, and the material has a cubic $Fd\bar{3}m$ average structure with uniform V−V nearest-neighbor distances. However, short-range order is retained, and the trimers and tetramers persist in a structurally disordered phase to at least 1100 K ($1.6T_{CO}$). This is consistent with magnetization and resistivity measurements,

Received: December 21, 2017
Published: February 21, 2018

DOI: 10.1021/acs.inorgchem.7b03221
Inorg. Chem. 2018, 57, 2815−2822

which show very little change across the transition temperature.[22] The stability of V−V bonding well above the long-range ordering temperature indicates a fundamentally different mechanism of orbital molecule formation in AlV_2O_4 than is found in other vanadium oxides—in the high-temperature phase of VO_2, the dimers do not persist on either the long-range or local scale.[23]

Here we report the synthesis and characterization of GaV_2O_4, a new vanadium oxide spinel. It exhibits the complex orbital molecule behavior found in isoelectronic AlV_2O_4 but with a lower T_{CO} of 415 K; hence, we demonstrate the persistence of disordered orbital molecules to the relatively higher temperature of $2.7T_{CO}$. Furthermore, we used quasi-elastic neutron scattering (QENS) to investigate whether the orbital molecules have static or dynamic disorder at high temperatures.

EXPERIMENTAL SECTION

Synthesis. Polycrystalline GaV_2O_4 was synthesized by a high-temperature solid-state reaction. Powdered Ga_2O_3 (Sigma-Aldrich, 99.99%), V (Alfa Aesar, 99.5%), and V_2O_5 (Alfa Aesar, 99.6%) in the stoichiometric ratio were ground together, pressed into pellets, and sealed in an evacuated quartz ampule, which was heated at 1000 °C for 48 h.

Structural Characterization. High-resolution powder X-ray diffraction data were collected at beamline ID22 at the European Synchrotron Radiation Facility, using a multianalyzer stage detector and 27.5 keV radiation (λ = 0.450 842 Å). Data were collected on warming, with the sample loaded in a 0.5 mm diameter borosilicate capillary and heated from room temperature to 500 K using a nitrogen cryostream. X-ray total scattering data were also collected at ID22. To access the high momentum transfers Q needed to generate good quality PDFs, a PerkinElmer XRD1611 2D detector and 60 keV radiation (λ = 0.206 547 Å) were used. The sample was held in a 0.7 mm diameter quartz capillary and heated from 300 to 1100 K using a hot air blower, with measurements made on warming. 201 exposures were collected at each temperature step and averaged to give a total scattering pattern. Rietveld analysis was performed using GSAS.[24] Total scattering functions $S(Q)$ were transformed to PDFs $G(r)$ using PDFgetX3,[25] for $0.5 \leq Q$ (Å^{-1}) ≤ 25.8, after making suitable background corrections. Structural models were refined against $G(r)$ using PDFgui,[26] which includes simulation of termination ripples, for interatomic distances $1.5 \leq r$ (Å) ≤ 12.

Powder neutron diffraction was performed with the HRPD beamline at the ISIS pulsed neutron and muon source. A 2.7 g sample in a vanadium can was loaded into a furnace and heated to 550 K, and data were collected on cooling to room temperature. Diffraction patterns collected by the 168° detectors were analyzed by Rietveld refinement using GSAS.

Magnetic and Transport Property Measurements. The magnetic behavior of GaV_2O_4 was measured using a Quantum Design SQUID MPMS XL. Measurements were made over the temperature range of 2−300 K in an applied field of 100 Oe, under zero-field cooled and field cooled conditions, and on heating from 300 to 600 K in an applied field of 5000 Oe. The electrical resistivity of a sintered pellet of GaV_2O_4 was measured over the range of 300−800 K by a conventional four-probe technique, using in-house apparatus.

Quasi-Elastic Neutron Scattering. QENS data were collected with the time-of-flight spectrometer IN6 at the Institut Laue Langevin. The sample was loaded into a niobium can in a furnace, and spectra were collected between 400 and 1100 K using neutrons with incident wavelength λ = 5.12 Å. Eight spectra were collected at each temperature, and averaged scattering functions $S(Q,E)$, where E is the energy transfer, were generated with vanadium normalization and corrections for the empty can background.

RESULTS AND DISCUSSION

Average Structure. High-resolution powder X-ray diffraction was used to study the average structure of GaV_2O_4, and a distortion analogous to that found in AlV_2O_4[20] is observed. At room temperature, GaV_2O_4 has an $R\bar{3}m$ unit cell (Figure 1):

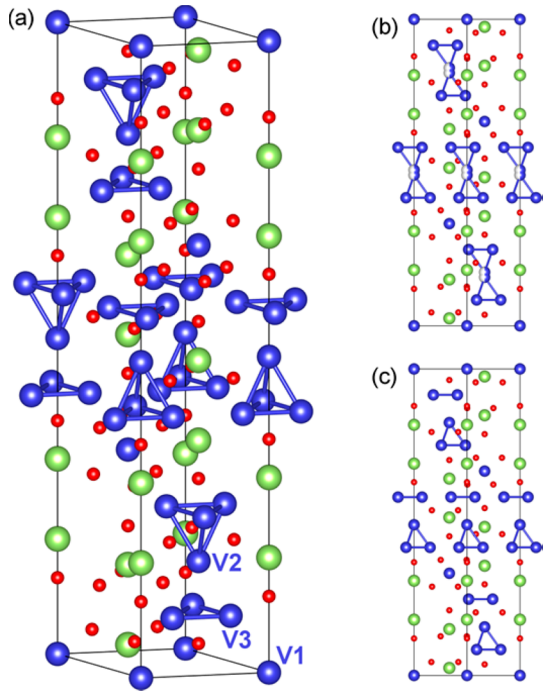

Figure 1. (a) Local structure in the $R\bar{3}m$ phase of GaV_2O_4. Ga (green), V (blue), and O (red) are shown, with the three different vanadium sites labeled and the short (~2.80 Å) V−V separations defining the V_3 trimers and V_4 tetramers shown. One local configuration of each orbital molecule pair is shown here, but these are disordered over two possible configurations (trimer-tetramer or tetramer-trimer) in the average structure, shown in (b), which is modeled by splitting the z-coordinate of the V2 site in Rietveld refinements. (c) The $R3m$ structure that was used for PDF fits, in which all orbital molecule pairs have the same orientation.

Rietveld analysis (Figure 2a) gives lattice parameters a_H = 5.862 07(4) Å and c_H = 28.982 69(37) Å, and the refined atomic parameters are given in Table 1. Bond distances and angles are provided in the Supporting Information. There are three vanadium crystallographic sites, and refinement of their positions defines V_3 trimers and V_4 tetramers through short (~2.80 Å) V−V nearest-neighbor distances. Tetramers are formed by the V2 site and half of the V3 site cations; the remaining V3 cations form trimers, and the V1 site is nonbonding (Figure 1a). In this low-temperature phase, pairs of a V_3 cluster and V_4 cluster have long-range structural order, but there are two possible configurations of the clusters within each pair. This disorder in the average structure is modeled by splitting the V2 site (Figure 1b). An impurity phase, V_2O_3, with weight fraction 5.3%, was also found in the Rietveld fits.

When heated, a structural phase transition from the $R\bar{3}m$ superstructure to the cubic $Fd\bar{3}m$ normal spinel arrangement is observed. Within this average structure there is only a single $V^{2.5+}$ crystallographic site, and all V−V nearest-neighbor distances are equivalent (~2.95 Å). However, as found for AlV_2O_4, Rietveld fits are improved by letting seven-eighths of the vanadium (the proportion of vanadium cations involved in

DOI: 10.1021/acs.inorgchem.7b03221
Inorg. Chem. 2018, 57, 2815−2822

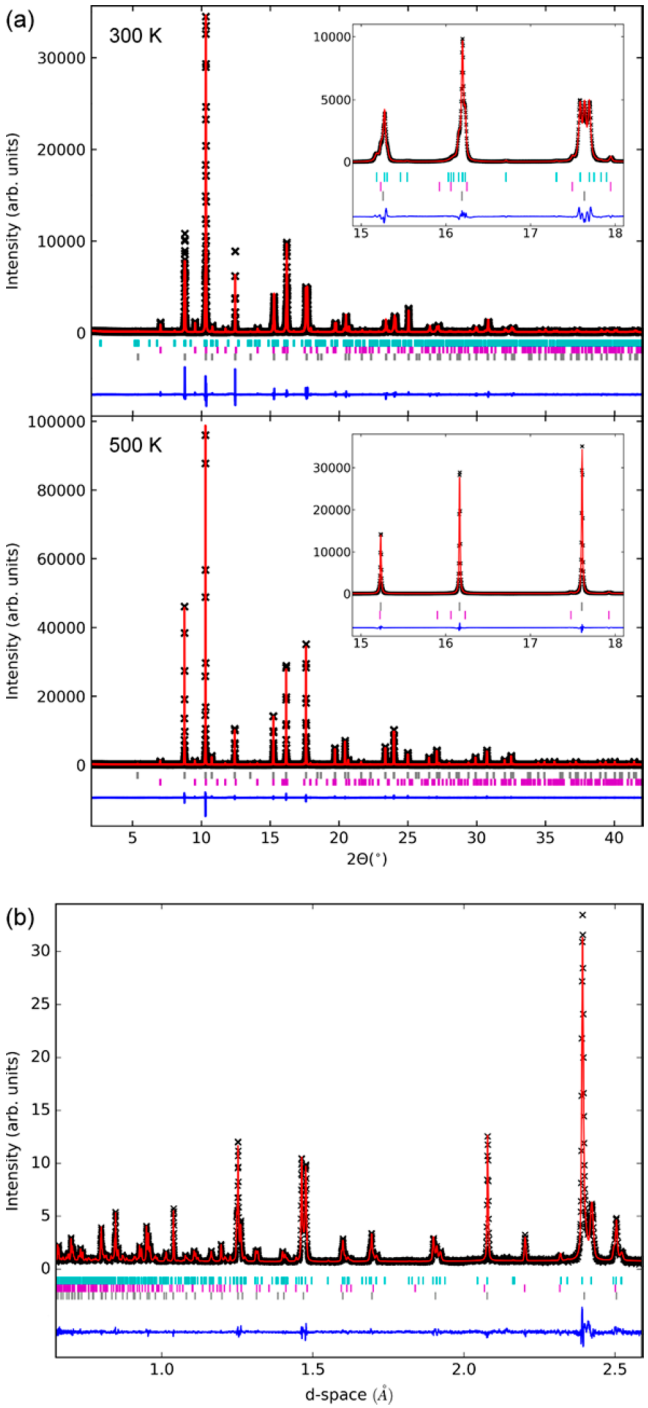

Figure 2. Rietveld analyses of GaV_2O_4. Tick marks correspond to the $R\bar{3}m$ (blue) and $Fd\bar{3}m$ (gray) phases of GaV_2O_4, and a V_2O_3 impurity (pink). (a) Fits to high-resolution powder X-ray diffraction data collected at room temperature (upper, R_w = 12.3%) and 500 K (lower, R_w = 9.0%), with insets showing the peak splitting associated with the rhombohedral distortion in an expanded region. (b) Fit to powder neutron diffraction data collected at room temperature (R_w = 5.7%).

orbital molecule bonding) displace away from this ideal position as a split site, indicating disorder in the high-temperature phase.

Conversion of the high-temperature $Fd\bar{3}m$ structure into the low-temperature $R\bar{3}m$ structure is evident as a splitting of the Bragg peaks of the cubic phase (Figure 2a, insets), as the rhombohedral distortion causes the lattice parameters a_H and c_H to deviate from metrically cubic values $a_H = a_C/\sqrt{2}$ and $c_H = \sqrt{12}\,a_C$. The thermal variation of an order parameter-like quantity X below the long-range ordering transition temperature T_{CO} can be described by the critical equation:

$$X = X_{CO} + (X_0 - X_{CO})\tanh(W_X t^{1/2})/\tanh(W_X) \quad (1)$$

where X takes values X_0 and X_{CO} at $T = 0$ and $T = T_{CO}$, respectively; the reduced temperature is $t = (T_{CO} - T)/T_{CO}$; and $W_X \approx 2$ is a fitting parameter. Equation 1 has been used to describe the behavior of structural quantities below the Verwey transition in magnetite.[27] Applying eq 1 to the thermal variation of the reduced lattice parameters of GaV_2O_4, $\sqrt{2}\,a_H$ and $c_H/\sqrt{12}$, taken from Rietveld refinements, gives good fits and determines T_{CO} = 415 K (Figure 3a).

Powder neutron diffraction (Figure 2b) corroborates the above structural characterization, although as a result of poor thermal equilibration of the large sample used for this experiment the value of T_{CO} appears as 465 K. As vanadium scatters neutrons very weakly no site splitting to describe disordered orbital molecules was included in the refinement models. However, the high neutron scattering contrast between Ga and V confirms that there is no antisite disorder.

Both the X-ray and neutron refinements reveal that a proportion of GaV_2O_4 remains cubic below T_{CO}. This is most likely due to microstructural stresses that prevent some regions of the polycrystalline sample from converting to rhombohedral below the transition. A similar suppression of the orbital molecule ordering transition in strained crystallites has been observed in magnetite.[27] The fractions of the two GaV_2O_4 phases were extracted through Rietveld refinement, and the decreasing fraction of the $R\bar{3}m$ phase on warming is described well by eq 1 (Figure 3b).

Rietveld fits to neutron diffraction data collected in the critical region were used to determine the lattice parameters of the rhombohedral (a_H and c_H) and cubic (a_C) phases, and the spontaneous strains for the low-temperature phase were calculated as:

$$s_a = \frac{\sqrt{2}\,a_H - a_C}{a_C} \quad (2)$$

$$s_c = \frac{c_H/\sqrt{12} - a_C}{a_C} \quad (3)$$

Spontaneous strain is an order parameter and for a (near) second-order transition close to the transition temperature the variation:

$$s^2 = s_0^2\left(1 - \frac{T}{T_{CO}}\right) \quad (4)$$

is expected. Plots of s_a^2 and s_c^2 against T/T_{CO} confirm the quasi-continuous nature of the structural transition (Figure 3c).

Local Structure. X-ray total scattering data were used to characterize the local V−V interactions in GaV_2O_4. Rietveld analyses of these data, using the split-site $R\bar{3}m$ and $Fd\bar{3}m$ models described previously, are consistent with those using the high-resolution powder diffraction data. Analysis of the PDFs generated from the total scattering data shows that the real-space structure described by the PDFs is consistent with that determined from Rietveld refinement below T_{CO}, with ordered pairs of V_3 and V_4 orbital molecules (Figure 4a). A modified model was used to fit these PDFs—instead of $R\bar{3}m$

DOI: 10.1021/acs.inorgchem.7b03221
Inorg. Chem. 2018, 57, 2815−2822

Table 1. Atomic Parameters of $R\bar{3}m$ GaV_2O_4 at Room Temperature, from Rietveld Refinement against the High-Resolution Powder X-ray Diffraction Data

atom	site	x	y	z	occupancy	U_{iso} (Å^2)
Ga1	6c	0	0	0.184 89(9)	1	0.0069(1)
Ga2	6c	0	0	0.310 51(9)	1	0.0069(1)
V1	3a	0	0	0	1	0.0059(2)
V2	6c	0	0	0.495 37(32)	0.5	0.0059(2)
V3	18h	0.839 82(19)	0.160 18(19)	0.416 68(9)	1	0.0059(2)
O1	6c	0	0	0.124 68(44)	1	0.0103(4)
O2	6c	0	0	0.374 86(40)	1	0.0103(4)
O3	18h	0.836 14(70)	0.163 86(70)	0.541 52(29)	1	0.0103(4)
O4	18h	0.827 58(70)	0.172 42(70)	0.288 84(28)	1	0.0103(4)

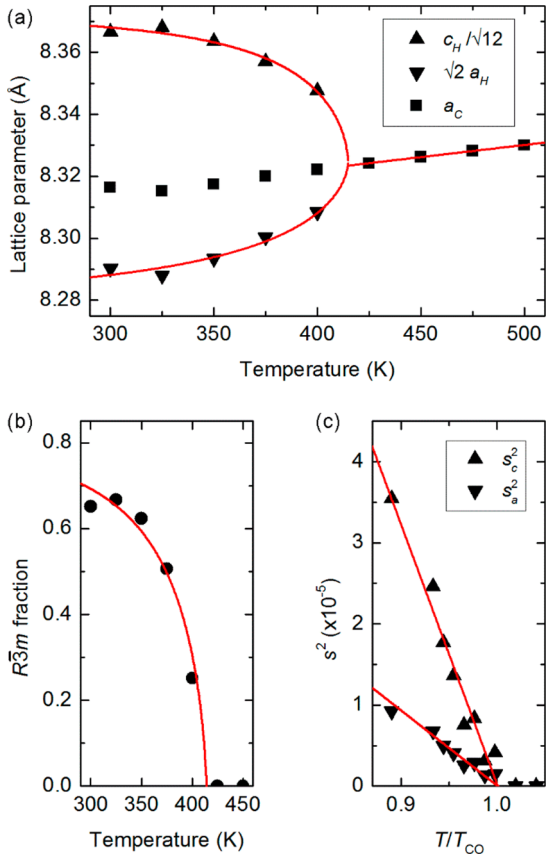

Figure 3. (a) Lattice parameters of the rhombohedral and cubic phases of GaV_2O_4 and (b) the rhombohedral phase fraction, from high-resolution powder X-ray diffraction showing fits of eq 1 below T_{CO} = 415 K. (c) Squared spontaneous lattice strains of rhombohedral GaV_2O_4 from powder neutron diffraction decrease linearly to zero at $T = T_{CO}$, in keeping with eq 4 for a continuous transition.

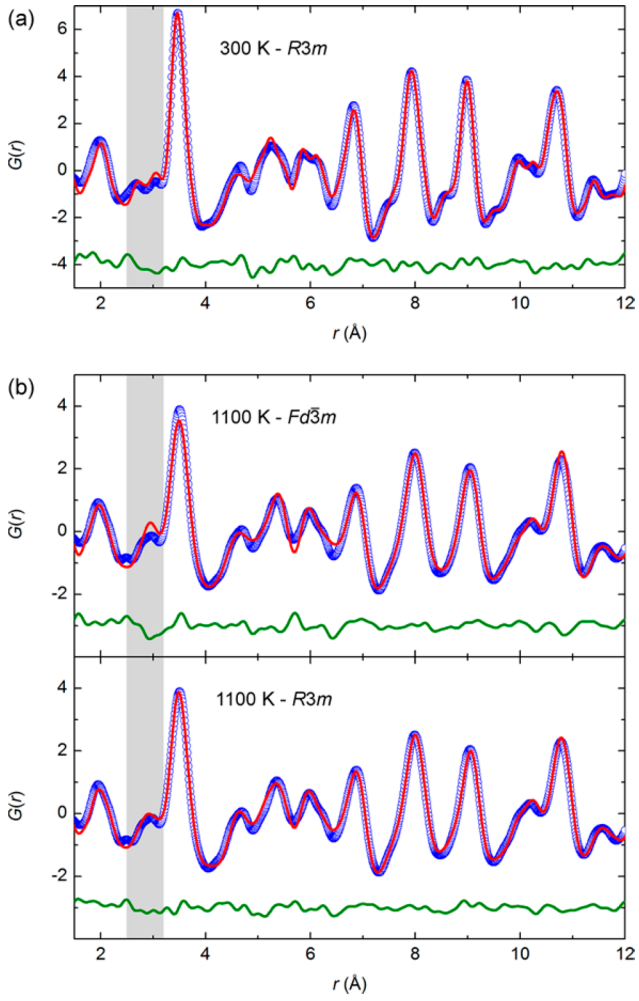

Figure 4. (a) Fit of the $R3m$ model, featuring V_3 and V_4 orbital molecules, to the 300 K PDF of GaV_2O_4 (R_w = 11.9%), where the presence of short and long V−V distances gives rise to two peaks in the shaded region. (b) Fits to the 1100 K PDF using the $Fd\bar{3}m$ average structure model (upper, R_w = 13.5%), in which all V−V nearest-neighbor distances are equal, and the $R3m$ model representing disordered orbital molecules (lower, R_w = 10.3%).

symmetry with a split V2 site a lower symmetry $R3m$ model, in which the V2 site displaces with full occupancy, was used (though constraints consistent with $R\bar{3}m$ symmetry were applied to all other sites to reduce the number of refined variables).

Both the $R\bar{3}m$ and $R3m$ models feature V_3−V_4 orbital molecule pairs, so the local structural correlations in both are the same. However, while in the $R\bar{3}m$ model different pairs adopt different configurations and are disordered, in the $R3m$ model all pairs have the same orientation. The two models therefore represent different average structures (Figure 1b,c). As the $R\bar{3}m$ model gives a better Rietveld fit than the $R3m$ model, the disordered pairs scenario is a better overall description of the structure of rhombohedral GaV_2O_4, as was also found for AlV_2O_4.[20] The $R3m$ model was used for the PDF fits as the half-occupied split-site used to model the disorder in the $R\bar{3}m$ model, while suitable for describing the average atomic distribution, does not meaningfully represent the local structure.

DOI: 10.1021/acs.inorgchem.7b03221
Inorg. Chem. 2018, 57, 2815−2822

Above 415 K, the PDFs are not well fit by an ideal cubic spinel model in which the V−V nearest-neighbor distances are equal (Figure 4b). This is particularly evident in the first V−V coordination shell, which corresponds to the PDF intensity in the range of $2.5 \leq r$ (Å) ≤ 3.2 (the shaded region in Figure 4), indicative of local V site displacements. A much better fit is achieved using the same $R3m$ model as used to fit the PDFs below T_{CO}. a_H and c_H were constrained in the metrically cubic ratio, consistent with the average structure, and the V2 and V3 site displacements were constrained to be equal to improve refinement stability (consequently, the two short bonding V−V distances are equal). V site displacements of ∼0.1 Å, consistent with those found through split-site Rietveld refinements, are present to 1100 K (Figure 5a), and result in short V−V distances corresponding to locally ordered V_3 and V_4 orbital molecules (Figure 5b). The V−V distances determined at 300 and 1100 K are tabulated in the Supporting Information. The residual cubic phase below T_{CO} was not included in the analysis of the X-ray total scattering data: the resolution of the diffraction patterns is insufficient for it to be included in Rietveld fits, and as both phases of GaV_2O_4 are likely to have the same local structure it does not need to be accounted for separately in the PDF analysis.

The persistence of the orbital molecules to high temperatures in GaV_2O_4, with T_{CO} indicating their order−disorder transition, is consistent with the orbital molecule behavior found in AlV_2O_4,[20] though the value of T_{CO} = 415 K in GaV_2O_4 is substantially lower than that for AlV_2O_4 (700 K). This is likely due to Ga^{3+} having a larger ionic radius than Al^{3+}, so the average lattice V−V separation—2.96 Å in GaV_2O_4 at 1100 K, compared to 2.92 Å in AlV_2O_4—is correspondingly larger. This weakens the tendency of orbital molecules to long-range order and hence suppresses T_{CO}. Furthermore, the larger average separation weakens the interactions within the orbital molecules. Not only are the bonding V−V distances in GaV_2O_4 (both 2.72 Å at 300 K) not as short as those in AlV_2O_4 (2.59 and 2.65 Å) but the difference between bonding and nonbonding distances (2.72−3.13 Å in GaV_2O_4, 2.59−3.17 Å in AlV_2O_4) is less. The smaller spin-gap energy, discussed in the following section, also evidences weaker bonding interactions in GaV_2O_4.

A lower T_{CO} does, however, allow the temperature scale over which local orbital molecule interactions are found to be extended. The total scattering analysis demonstrates the persistence of structurally disordered orbital molecules in GaV_2O_4 to 1100 K, which is $2.7T_{CO}$, far above the critical regime.

Magnetic and Transport Properties. Although the presence of orbital molecules in GaV_2O_4 was deduced through structural analysis and the identification of unusually short V−V distances, their presence impacts on, and can be corroborated by characterizing, the material's magnetic and electrical properties. The formation of orbital molecules requires electrons to be paired in V−V bonds, and the properties of GaV_2O_4 are based on the electronic description $Ga_4[V_4^{8+}V_3^{9+}V^{3+}]O_{16}$. For every eight vanadium atoms, which have an average oxidation state of 2.5, a V_4^{8+} tetramer and a V_3^{9+} trimer are formed by the two-center two-electron bonding of four V^{2+} and three V^{3+}, respectively. These are both spin-paired (S = 0) species, but the remaining vanadium is a monomeric and paramagnetic (S = 1) V^{3+} cation.

Equation 5, used previously to characterize the magnetic behavior of AlV_2O_4,[21] treats the total susceptibility as the sum

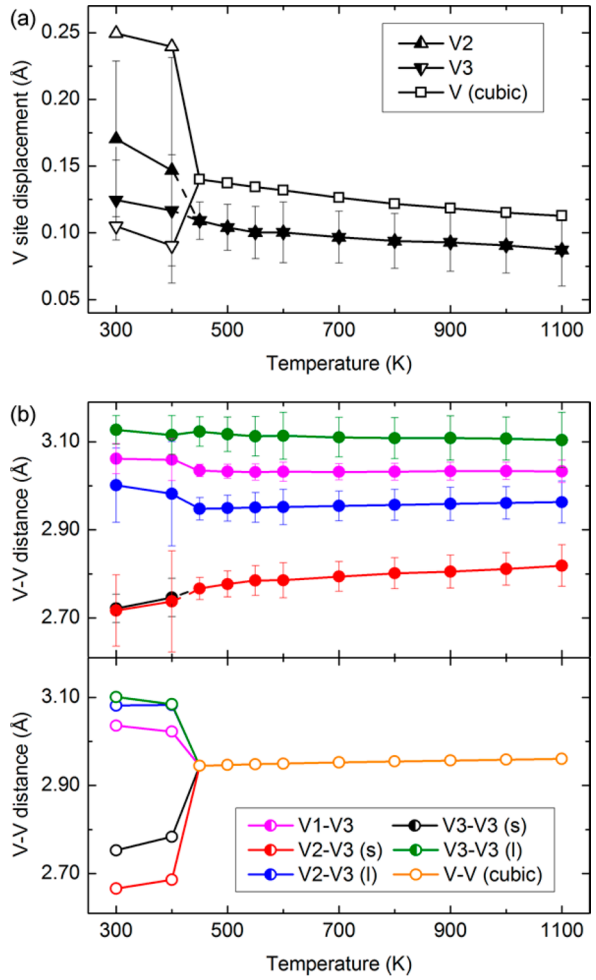

Figure 5. Structural parameters extracted from PDF (filled symbols) and Rietveld (open symbols) analyses of the X-ray total scattering data, evidencing the persistence of disordered orbital molecules to 1100 K. (a) V−V bonding causes the vanadium atoms to be displaced from ideal spinel positions. The V2 and V3 sites displace independently below T_{CO}, with the split-site $R\bar{3}m$ model used for Rietveld fits and the $R3m$ model for PDF fits. Above T_{CO} Rietveld analysis using the split-site $Fd\bar{3}m$ model reveals significant displacement of vanadium away from its ideal site, and PDF fits using the $R3m$ model yield similar displacements (for refinement stability, the V2 and V3 site displacements were constrained to be equal). (b) PDF fits reveal that the short V−V distances that define the ordered V_3 and V_4 orbital molecules in the ground state evolve continuously through T_{CO}, though Rietveld analysis of the cubic average structure gives only a single V−V distance.

of a Curie−Weiss term for the monomeric V^{3+} cations, and a generic spin-gap term for the spin-singlet clusters, which can be thermally excited to a triplet state:

$$\chi = \frac{C}{T-\theta} + \frac{D}{T\left[1+\frac{1}{3}\exp\left(\frac{E_g}{k_B T}\right)\right]} \quad (5)$$

Equation 5 gives a reasonable fit to the measured susceptibility of GaV_2O_4, with parameters C = 0.225 emu K mol^{-1}, θ = −25.4 K, D = 0.662 emu K mol^{-1}, and E_g/k_B = 416.2 K (Figure 6a). These values are in keeping with those determined for AlV_2O_4 and give a paramagnetic moment μ_{eff} = 2.68 μ_B (the predicted values for a d^2 cation are C = 0.25 emu K mol^{-1} and μ_{eff} = 2.83 μ_B). The average spin-gap energy E_g/k_B

DOI: 10.1021/acs.inorgchem.7b03221
Inorg. Chem. 2018, 57, 2815−2822

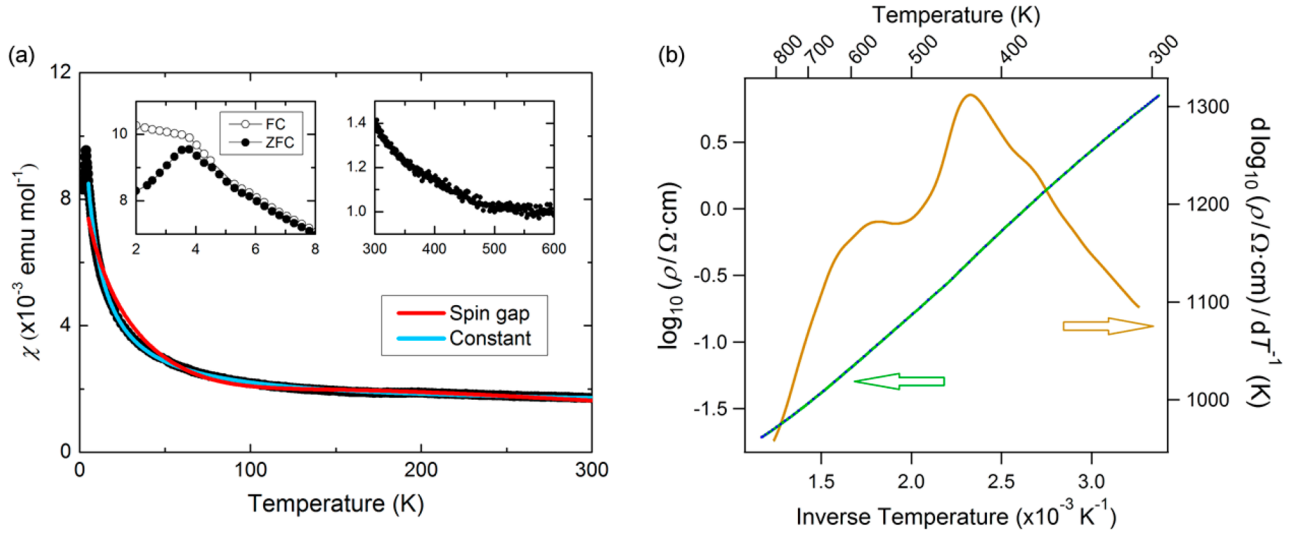

Figure 6. (a) The zero-field cooled magnetic susceptibility of GaV_2O_4. Fits of eq 5 and eq 6, which use a spin-gap term and a constant, respectively, to account for the susceptibility contributions of the spin-singlet clusters, are shown over the range of 5−300 K. (left inset) A cusp, resulting from freezing or ordering of paramagnetic V^{3+} spins not involved in orbital molecule bonding, at 3.8 K. (right inset) The high-temperature susceptibility measured on warming, with no pronounced anomaly at T_{CO} = 415 K. (b) Logarithmic plot of the high-temperature resistivity against inverse temperature showing continuous variation through T_{CO}, but with a change of slope at T_{CO} = 415 K evident in the derivative.

= 416 K shows that strong spin pairing is present, though a smaller value than for AlV_2O_4 (844 K) is consistent with GaV_2O_4 having weaker bonding interactions. An improved fit to the low-temperature susceptibility is, however, obtained by using a temperature-independent constant to account for the susceptibility contributions of the orbital molecules:

$$\chi = \frac{C}{T - \theta} + A \tag{6}$$

with fitting parameters C = 0.0793 emu K mol^{-1}, θ = −6.2 K, and A = 1.46 × 10^{-3} emu mol^{-1}. A negative value of θ, indicating antiferromagnetic correlations of the V^{3+} spins, is again obtained, though the value of C gives a moment μ_{eff} = 1.59 μ_B that is smaller than expected for S = 1 V^{3+}. A sharp cusp in the susceptibility, below which the zero-field cooled and field cooled susceptibilities diverge, is observed at 3.8 K (Figure 6a, left inset) and is attributed to the freezing or ordering of the monomeric V^{3+} spins.

Although a structural distortion occurs in GaV_2O_4 at T_{CO} = 415 K, no corresponding change in the high-temperature susceptibility is observed (Figure 6a, right inset). This is consistent with the structural description of local V_3 and V_4 orbital molecules persisting above T_{CO}, as the breakup of these spin-singlet clusters should lead to large increases of the susceptibility—complete decomposition would lead to C = 2.88 emu K mol^{-1} for paramagnetic $GaV^{2+}V^{3+}O_4$. Similarly, there is no change in resistivity that might arise if the bonding electrons became delocalized (Figure 6b). GaV_2O_4 is a semiconductor with an activation energy of 0.24 eV, and only a slight change of slope is observed around T_{CO}. Equivalent measurements of the properties of AlV_2O_4 also only show small changes to the susceptibility and resistivity on crossing T_{CO}.[22] Hence the physical properties of these materials are consistent with a change from ordered to disordered orbital molecules at the transition, rather than any changes in the V−V bonding.

Quasi-Elastic Neutron Scattering. The total scattering analysis and property measurements described previously demonstrate the persistence of structurally disordered orbital molecules in GaV_2O_4 (as in AlV_2O_4) to 1100 K. However, from these analyses it is not clear whether the disordered orbital molecules in these materials are static (glass-like) or dynamic (liquid-like). QENS was used to investigate whether dynamical motion or interchange of V atoms between orbital molecules in GaV_2O_4 becomes evident at high temperatures. Dynamic behavior would result in quasi-elastic scattering, which would appear as a broadening of the elastic scattering line.

QENS data were collected from 400 K, at which temperature the orbital molecule pairs have long-range order and are expected to be static, to 1100 K. The scattering functions $S(Q,E)$ at 400 and 1100 K are provided in the Supporting Information, and the integrated functions $S(E)$ for all measured temperatures are plotted in Figure 7. Although the intensity of the elastic line decreases on heating, due to the Debye−Waller effect, no broadening of the elastic line is observed. This linewidth establishes that in GaV_2O_4 any dynamic behavior must be

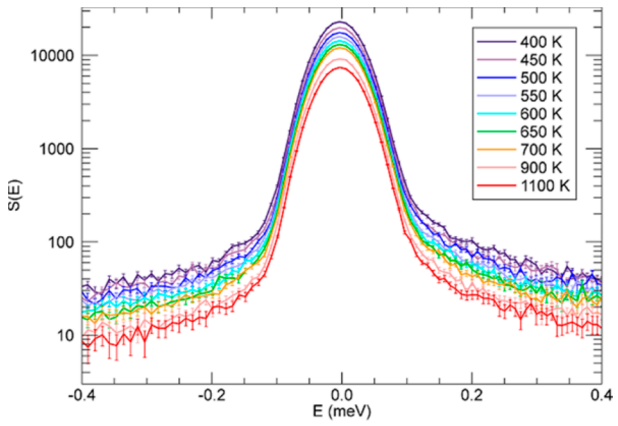

Figure 7. Thermal variation of the QENS scattering function $S(Q,E)$ of GaV_2O_4, integrated over the full measured range of Q. Quasi-elastic scattering from orbital molecule dynamics that would broaden the elastic line is not seen, showing that the disordered orbital molecules remain static up to 1100 K.

DOI: 10.1021/acs.inorgchem.7b03221
Inorg. Chem. 2018, 57, 2815−2822

slower than ~1×10^{-11} s, indicating that the clusters are well-defined and statically disordered even at 1100 K.

CONCLUSION

GaV_2O_4, a new oxide spinel, has been synthesized. Long-range orbital- and charge-ordering in the ground state results in a structural distortion and pairwise order of V_3^{9+} and V_4^{8+} orbital molecules. Above T_{CO} = 415 K long-range order is lost but short-range order remains, and the orbital molecules persist in a statically disordered phase to at least $2.7T_{CO}$.

The orbital molecules in GaV_2O_4 and AlV_2O_4 are found to be stable to temperatures well above that at which they lose long-range structural order, unlike those in VO_2, which do not persist above the metal−insulator transition. This implies that the electronic interactions that result in V−V bonding in vanadium oxides can vary considerably, from real-space (molecular) to momentum-space (Fermi surface) electronic instabilities. To explore these variations of orbital molecule bonding, further investigations of the local and long-range structures of vanadium oxides will be required.

ASSOCIATED CONTENT

Supporting Information

The Supporting Information is available free of charge on the ACS Publications website at DOI: 10.1021/acs.inorgchem.7b03221.

Metal−oxygen bond distances and angles in the room-temperature structure; V−V distances at 300 and 1100 K; and QENS scattering functions at 400 and 1100 K (PDF)

AUTHOR INFORMATION

Corresponding Author

*E-mail: j.p.attfield@ed.ac.uk.

ORCID

Alexander J. Browne: 0000-0002-1458-8066

J. Paul Attfield: 0000-0001-9763-3987

Author Contributions

A.J.B., S.A.J.K., and J.P.A. designed the concept for this study. A.J.B. performed the experimental work and data analysis, and C.L. made the resistivity measurement. A.J.B. and J.P.A. wrote the manuscript with inputs from all authors.

Funding

This work was supported by the ERC (Advanced Grant No. EC339312), and access to facilities was provided by the STFC. This manuscript has been authored by UT-Battelle, LLC, under Contract No. DE-AC05-00OR22725 with the U.S. Department of Energy (DOE). The United States Government retains and the publisher, by accepting the article for publication, acknowledges that the United States Government retains a nonexclusive, paid-up, irrevocable, worldwide license to publish or reproduce the published form of this manuscript, or allow others to do so, for United States Government purposes. The DOE will provide public access to these results of federally sponsored research in accordance with the DOE Public Access Plan (http://energy.gov/downloads/doe-public-access-plan).

Notes

The authors declare no competing financial interest.

Open data for this article are at http://dx.doi.org/10.7488/ds/2308.

ACKNOWLEDGMENTS

We thank M. Coduri (ESRF), K. Knight (ISIS), and M. Koza (ILL) for help with data collection; K. H. Hong for assistance at ESRF; and J. Cumby and P. M. Sarte for assistance with data analysis.

REFERENCES

(1) Armstrong, A. R.; Lyness, C.; Panchmatia, P. M.; Islam, M. S.; Bruce, P. G. The lithium intercalation process in the low-voltage lithium battery anode $Li_{1+x}V_{1-x}O_2$. *Nat. Mater.* **2011**, *10*, 223−229.

(2) Guignard, M.; Didier, C.; Darriet, J.; Bordet, P.; Elkaïm, E.; Delmas, C. P2-Na_xVO_2 system as electrodes for batteries and electron-correlated materials. *Nat. Mater.* **2013**, *12*, 74−80.

(3) Wang, Y.; Cao, G. Developments in Nanostructured Cathode Materials for High-Performance Lithium-Ion Batteries. *Adv. Mater.* **2008**, *20*, 2251−2269.

(4) Butt, F. K.; Tahir, M.; Cao, C.; Idrees, F.; Ahmed, R.; Khan, W. S.; Ali, Z.; Mahmood, N.; Tanveer, M.; Mahmood, A.; Aslam, I. Synthesis of Novel ZnV_2O_4 Hierarchical Nanospheres and Their Applications as Electrochemical Supercapacitor and Hydrogen Storage Material. *ACS Appl. Mater. Interfaces* **2014**, *6*, 13635−13641.

(5) Sammes, N. M.; Tompsett, G. A.; Näfe, H.; Aldinger, F. Bismuth Based Oxide Electrolytes − Structure and Ionic Conductivity. *J. Eur. Ceram. Soc.* **1999**, *19*, 1801−1826.

(6) Wachs, I. E. Catalysis science of supported vanadium oxide catalysts. *Dalton Trans.* **2013**, *42*, 11762−11769.

(7) Morin, F. J. Oxides which show a metal-to-insulator transition at the Neel temperature. *Phys. Rev. Lett.* **1959**, *3*, 34−36.

(8) Yang, Z.; Ko, C.; Ramanathan, S. Oxide Electronics Utilizing Ultrafast Metal-Insulator Transitions. *Annu. Rev. Mater. Res.* **2011**, *41*, 337−367.

(9) Wang, S.; Liu, M.; Kong, L.; Long, Y.; Jiang, X.; Yu, A. Recent progress in VO_2 smart coatings: Strategies to improve the thermochromic properties. *Prog. Mater. Sci.* **2016**, *81*, 1−54.

(10) Goodenough, J. B. The Two Components of the Crystallographic Transition in VO_2. *J. Solid State Chem.* **1971**, *3*, 490−500.

(11) Attfield, J. P. Orbital molecules in electronic materials. *APL Mater.* **2015**, *3*, 041510.

(12) Marezio, M.; McWhan, D. B.; Dernier, P. D.; Remeika, J. P. Structural Aspects of the Metal-Insulator Transition in V_4O_7. *J. Solid State Chem.* **1973**, *6*, 419−429.

(13) Pourpoint, F.; Hua, X.; Middlemiss, D. S.; Adamson, P.; Wang, D.; Bruce, P. G.; Grey, C. P. New Insights into the Crystal and Electronic Structures of $Li_{1+x}V_{1-x}O_2$ from Solid State NMR, Pair Distribution Function Analyses, and First Principles Calculations. *Chem. Mater.* **2012**, *24*, 2880−2893.

(14) Kajita, T.; Kanzaki, T.; Suzuki, T.; Kim, J. E.; Kato, K.; Takata, M.; Katsufuji, T. Opening of a charge gap with V trimerization in $BaV_{10}O_{15}$. *Phys. Rev. B: Condens. Matter Mater. Phys.* **2010**, *81*, 060405R.

(15) McQueen, T. M.; Stephens, P. W.; Huang, Q.; Klimczuk, T.; Ronning, F.; Cava, R. J. Successive Orbital Ordering Transitions in $NaVO_2$. *Phys. Rev. Lett.* **2008**, *101*, 166402.

(16) Guignard, M.; Delmas, C. Using a Battery to Synthesize New Vanadium Oxides. *ChemistrySelect* **2017**, *2*, 5800−5804.

(17) Haverkort, M. W.; Hu, Z.; Tanaka, A.; Reichelt, W.; Streltsov, S. V.; Korotin, M. A.; Anisimov, V. I.; Hsieh, H. H.; Lin, H. J.; Chen, C. T.; Khomskii, D. I.; Tjeng, L. H. Orbital-assisted metal-insulator transition in VO_2. *Phys. Rev. Lett.* **2005**, *95*, 196404.

(18) Jin-no, T.; Shimizu, Y.; Itoh, M.; Niitaka, S.; Takagi, H. Orbital reformation with vanadium trimerization in d^2 triangular lattice $LiVO_2$ revealed by ^{51}V NMR. *Phys. Rev. B: Condens. Matter Mater. Phys.* **2013**, *87*, 075135.

(19) Khomskii, D. I.; Mizokawa, T. Orbitally Induced Peierls State in Spinels. *Phys. Rev. Lett.* **2005**, *94*, 156402.

(20) Browne, A. J.; Kimber, S. A. J.; Attfield, J. P. Persistent three- and four-atom orbital molecules in the spinel AlV_2O_4. *Phys. Rev. Mater.* **2017**, *1*, 052003R.

DOI: 10.1021/acs.inorgchem.7b03221
Inorg. Chem. 2018, 57, 2815−2822

(21) Horibe, Y.; Shingu, M.; Kurushima, K.; Ishibashi, H.; Ikeda, N.; Kato, K.; Motome, Y.; Furukawa, N.; Mori, S.; Katsufuji, T. Spontaneous Formation of Vanadium "Molecules" in a Geometrically Frustrated Crystal: AlV_2O_4. *Phys. Rev. Lett.* **2006**, *96*, 086406.
(22) Matsuno, K.; Katsufuji, T.; Mori, S.; Moritomo, Y.; Machida, A.; Nishibori, E.; Takata, M.; Sakata, M.; Yamamoto, N.; Takagi, H. Charge Ordering in the Geometrically Frustrated Spinel AlV_2O_4. *J. Phys. Soc. Jpn.* **2001**, *70*, 1456−1459.
(23) Corr, S. A.; Shoemaker, D. P.; Melot, B. C.; Seshadri, R. Real-Space Investigation of Structural Changes at the Metal-Insulator Transition in VO_2. *Phys. Rev. Lett.* **2010**, *105*, 056404.
(24) Larson, A. C.; Von Dreele, R. B. *General Structure Analysis System (GSAS),* Report LAUR 86-748; Los Alamos National Laboratory, 2004.
(25) Juhás, P.; Davis, T.; Farrow, C. L.; Billinge, S. J. L. PDFgetX3: A rapid and highly automatable program for processing powder diffraction data into total scattering pair distribution functions. *J. Appl. Crystallogr.* **2013**, *46*, 560−566.
(26) Farrow, C. L.; Juhas, P.; Liu, J. W.; Bryndin, D.; Božin, E. S.; Bloch, J.; Proffen, Th.; Billinge, S. J. L. PDFfit2 and PDFgui: computer programs for studying nanostructure in crystals. *J. Phys.: Condens. Matter* **2007**, *19*, 335219.
(27) Senn, M. S.; Wright, J. P.; Cumby, J.; Attfield, J. P. Charge localization in the Verwey structure of magnetite. *Phys. Rev. B: Condens. Matter Mater. Phys.* **2015**, *92*, 024104.

DOI: 10.1021/acs.inorgchem.7b03221
Inorg. Chem. 2018, 57, 2815−2822